UCGE Reports
Number 20346

Department of Geomatics Engineering

Quality Assurance of Multi-Sensor Systems

(URL: http://www.geomatics.ucalgary.ca/graduatetheses)

by

Ana Paula Baungarten Kersting

December, 2011

UNIVERSITY OF CALGARY

Quality Assurance of Multi-Sensor Systems

by

Ana Paula Baungarten Kersting

A THESIS
SUBMITTED TO THE FACULTY OF GRADUATE STUDIES
IN PARTIAL FULFILMENT OF THE REQUIREMENTS FOR THE
DEGREE OF DOCTOR OF PHILOSOPHY

DEPARTMENT OF GEOMATICS ENGINEERING

CALGARY, ALBERTA

DECEMBER, 2011

ABSTRACT

The demand for fast and cost-effective geo-spatial data collection along with technological advances in the last few decades have triggered considerable changes in the mapping survey practices. Currently, modern mapping systems consist of multi-sensor systems, typically encompassing navigation sensors and two types of imaging sensors: digital camera (one or multiple) and a laser scanning system. In order to fully attain the potential accuracy of the system sensors and guarantee accurate multi-sensor integration, careful system Quality Assurance (QA) should be carried out. Although several activities are involved in the QA of a multi-sensor system, the system calibration is the crucial activity to ensure the attainment of the expected accuracy and the most complex activity as well. System calibration involves individual sensor calibration and the mounting parameters calibration (i.e., lever arm offset and boresight angles) relating the system components such as the Global Positioning System (GPS), the Inertial Navigation System (INS), and the imaging sensors. In this research work, new calibration procedures for photogrammetric and Light Detection and Ranging (LiDAR) systems are introduced. The proposed procedures are based on similar point positioning equations and the system parameters are estimated while minimizing flight and control requirements. More specifically, a rigorous analysis, based on the mathematical analysis of the GPS/INS-assisted photogrammetric/LiDAR point positioning equation, is carried out to devise the minimum control and flight configuration requirements for the calibration of airborne single-camera photogrammetric and LiDAR systems. The proposed photogrammetric system calibration is a single-step procedure, which can be used for airborne/terrestrial directly geo-referenced single or multi-camera systems. The proposed procedure also has the ability to estimate the Relative Orientation Parameters (ROP) among the cameras in the absence of GPS/INS data. Furthermore, a general model, which allows for the incorporation of prior information about the ROP among the cameras in the calibration process, is devised. From such general model, the previous models (calibration without prior ROP information and the estimation of the ROP among the cameras) can be derived as special cases. The proposed LiDAR system calibration is an automated procedure and doesn’t require specific features (e.g., planes or lines) in the covered area. Suitable primitives, which do not involve pre-processing of the data, are implemented. The correspondence between conjugate primitives is determined using a robust matching procedure. A modification to the Gauss Markov model is introduced to keep the implementation of the calibration procedure simple while utilizing higher order primitives. Experimental results using simulated and real datasets have demonstrated the feasibility/effectiveness of the proposed methodologies for the calibration of photogrammetric and LiDAR systems.

ACKNOWLEDGEMENTS

I would like to express my gratitude to my supervisor Dr. Ayman Habib, who was abundantly helpful and offered invaluable assistance, support and guidance. He has been an example of dedication and professionalism.

Many thanks also to my colleagues at the Digital Photogrammetry Research Group (DPRG) for all their invaluable help. I would also like to convey thanks to McElhanney Consulting Services Ltd, for providing airborne single-camera system dataset; the National Cheng-Kung University, for providing the land-based multi-camera system dataset; and the École Polytechnique Fédérale de Lausanne (EPFL), for providing the LiDAR dataset utilized in this research work. I am also indebted to Mr. Dan Tresa, Dr. Jiann-Yeou Rau, and Dr. Jan Skaloud for their valuable feedback on the provided real datasets. Also, many thanks to GEOmatics for Informed DEcisions (GEOIDE) for the support on this research work.

I wish to thank Dr. Derek Lichti, Dr. Naser El-Sheimy, Dr. John Yackel, and Dr. Steve Liang for carefully reading and providing valuable comments on this dissertation.

Finally, I take this opportunity to express my profound gratitude to my son Lucas and my husband Juliano for filling my heart with joy and love, for the care, support, and understanding during the difficult days of this journey. I would also like to thank my parents Ivone and Mario, and my siblings. I really appreciate how much they have helped me with my life, love, and career and given me all of the things that have gotten me here.

DEDICATION

To my son Lucas, my husband Juliano, and my family in Brazil.

TABLE OF CONTENTS

LIST OF TABLES

LIST OF FIGURES

NOTATION

1. Vector notation:

The vector notation r_a^b stands for the coordinates of point a relative to point b – this vector is defined relative to the coordinate system associated with point b.

When the vector is not defined by the coordinates of two points the notation used to represent such vector will be lower case letter with an arrow $\vec{r}$.

2. Rotation matrix notation:

The rotation matrix notation R_a^b stands for the rotation matrix that transforms a vector defined relative to the coordinate system denoted by a into a vector defined relative to the coordinate system denoted by b.

COORDINATE SYSTEMS

- Camera coordinate system (c): 3D Cartesian coordinate system associated with the camera unit.
- Laser unit coordinate system: 3D Cartesian coordinate system associated with the laser unit.
- Laser beam coordinate system: 3D Cartesian coordinate system associated with the laser beam, with the z-axis defined along the laser beam.
- IMU coordinate system (b): 3D Cartesian coordinate system associated with the IMU body frame. In this dissertation, it is assumed that the position and orientation information from the GPS/INS integration process is defined relative to the IMU body frame (i.e., the GPS/INS integration process is performed while considering the lever arm offset between the IMU body frame and the phase center of the GPS antenna).
- Mapping Frame (m): In this dissertation, the mapping frame (i.e., the coordinate system associated with the object space) is assumed to be a 3D Cartesian coordinate system (topocentric coordinate system).

LIST OF ACRONYMS

AGL	Above Ground Level
AT	Aerial Triangulation
DGPS	Differential Global Positioning System
EOP	Exterior Orientation Parameters
EuroSDR	European Spatial Data Research
GCP	Ground Control Points
GPS	Global Positioning System
IMU	Inertial Measurement Unit
INS	Inertial Navigation System
IOP	Interior Orientation Parameters
ISO	Integrated Sensor Orientation
LASER	Light Amplification by Stimulated Emission of Radiation
LiDAR	Light Detection And Ranging
MFDC	Medium Format Digital Camera
MMS	Mobile Mapping Systems
MPiA	Multiple Pulses in Air
NRCan	Natural Resources Canada
OEEPE	European Organization for Experimental Photogrammetric Research
PC	Perspective Center
PDOP	Position Dilution of Precision
POS	Position and Orientation System
PRF	Pulse Repetition Frequency
QA	Quality Assurance
RMSE	Root Mean Squared Error
ROC	Relative Orientation Constraints
ROP	Relative Orientation Parameters
SMAC	Simultaneous Multi-frame Analytical Calibration
TIN	Triangular Irregular Network

2D	Two Dimensional
3D	Three Dimensional
USGS	U. S. Geological Survey

CHAPTER 1

INTRODUCTION

1.1 Motivation

In the last few decades, there has been a significant advancement in the remote sensing and mapping technology, which has led to considerable changes in the mapping practices. The evolution of the photogrammetric mapping practices has been described by several authors (Skaloud, 1999; Cramer, 1999; Jacobsen, 2000; Csanyi, 2008). Traditionally, image-based topographic mapping has been performed using a single sensor, more specifically a large format analogue camera. The concept of sensor orientation, crucial for the object space reconstruction from overlapping images, has relied on the availability of Ground Control Points (GCP) in the survey area. The development of bundle adjustment or Aerial Triangulation (AT) procedure reduced considerably the amount of GCP to orient each image. Although reduced, the required amount is still significant in a conventional bundle adjustment. With the advent of Global Positioning System (GPS), the position of the exposure station is obtained directly while its orientation can be determined in a GPS-assisted AT procedure. Nonetheless, the complete elimination of GCP in a GPS-assisted AT would still require block structure and a considerable number of tie points. Direct sensor orientation, without the need for GCP and AT, became possible with the introduction of Inertial Navigation System (INS) allowing the evolvement of GPS/INS-assisted photogrammetric systems. The integration of GPS and inertial systems has been stimulated by their complementary error behaviour. GPS offer high absolute accuracy position and velocity information, but its relative accuracy (i.e., short term noise) is dependent on the data quality and observation approach. Inertial systems, on the other hand, provide very high relative accuracy for position, velocity and attitude information, but the absolute accuracy decreases with time (Schwarz, 1995).

The advent of GPS/INS stimulated the emergence of the concept of Mobile Mapping Systems (MMS) as a cost-effective methodology for the collection of geo-spatial information. MMS can be defined as moving platforms which integrate a set of imaging sensors and a Position and Orientation System (POS). Although the MMS concept was first utilized and commonly associated with land-based systems, such concept might involve any moving platform (e.g., terrestrial, airborne, or satellite). Land-based MMS came out as an alternative to terrestrial surveying techniques, which are considered quite intrusive and inefficient, allowing for fast collection of dense information to feed mapping and Geographic Information System (GIS) applications. The first operational land-based MMS was developed in the late 1980s by the Center for Mapping at the Ohio State University. The developed system, named GPSVan™, consisted of a code-only GPS receiver, two digital CCD cameras, two colour video cameras, and dead-reckoning sensors (two gyroscopes and an odometer on each of the front wheels) mounted on a van (Goad, 1991; Novak, 1991, He et al., 1992). The GPSVan™ was a good starting point to demonstrate how land-based MMS could improve the mapping efficiency although the accuracy was still not at the level of competing technologies (Ellum, 2001). Improvements in the GPSVan™ system, such as the use of full inertial navigation system (low cost Inertial Measurement Unit – IMU) tightly coupled with the GPS receiver and the integration of digital cameras, led to the development of more accurate systems such as the GIM™ (GPS/lnertial Mapping) (Coetsee et al., 1994) and the GPSVision™ system (He et al., 1996). Several other similar systems were developed worldwide by the mid-1990s, e.g., the VISAT™ (Schwarz et al., 1993; El-Sheimy, 1996b), the KiSS™ (Hock et al., 1995), and the GI-EYE™ (Sullivan and Brown, 1996) systems. Further progress on those systems includes the use of dual frequency carrier phase differential GPS, more accurate IMUs, more sophisticated processing techniques, and larger number of imaging sensors. A comprehensive review of land-based MMS is provided in El-Sheimy (2008). By the late 1990s, improvements in GPS/INS technology attained an adequate accuracy level for supporting direct sensor orientation of photogrammetric airborne systems (Scherzinger, 1997; Grejner-Brzezinska, 1997; Toth, 1998). Moreover, the development of technologies where direct sensor orientation is essential, such as airborne Light Detection and Ranging (LiDAR) systems, became possible. LiDAR is an active remote sensing system, based on the Light Amplification by Stimulated Emission of Radiation (LASER) technology, capable of directly obtaining high density 3D point cloud of the object space through range measurements. Airborne LiDAR systems have undergone significant advances since its introduction (pulse repetition rate, multi-pulse technology, multiple returns, full-waveform digitization) and have been receiving wide acceptance in airborne mapping as a standard tool for the fast acquisition of high quality topographic data (Toth, 2010).

Besides the economical advantage, due to the possibility of an almost control-free mapping environment, the direct sensor orientation overcome existing limitations of the conventional image-based AT, such as mapping of coastal regions, forests, deserts and mountainous areas where ground control points are not easy to obtain and conjugate points in overlapping images are difficult to identify. Currently, modern airborne/terrestrial mapping systems consist of multi-sensor systems, typically encompassing a GPS/INS and either one or two types of imaging sensors: digital cameras and a laser scanning system. The use of multi-camera systems, to obtain larger object space coverage, is also a trend in the modern photogrammetric mapping scenario.

Besides all benefits of GPS/INS-assisted systems, a common reference frame for all the imaging sensors is established at a very early stage. However, in order to fully explore the potential accuracy of the system sensors and guarantee accurate multi-sensor integration, careful system Quality Assurance (QA) should be carried out. In this research work, the term "Quality Assurance" is used to denote pre-mission activities focusing on ensuring that a process will provide the quality needed by the user. QA mainly deals with creating management controls including the calibration, planning, implementation, and review of data collection activities. Several activities are involved in the QA of GPS/INS-assisted (directly geo-referenced) systems such as planning for the appropriate mission time, i.e., planning for good satellite availability and distribution (e.g., number of satellites > 4 and Position Dilution of Precision – PDOP < 4), GPS base station distance, among others. However, the system calibration is the crucial activity to ensure the attainment of the expected accuracy and the most complex activity as well.

System calibration involves individual sensor calibration and the mounting parameters calibration (i.e., lever arm offset and boresight angles) relating the system components such as the GPS, INS, and the imaging sensors (i.e., laser scanner and digital cameras). The lever arm offset is usually measured using traditional surveying techniques, while approximate values for the boresight angles are known from the mechanical alignment. Since these initial mounting parameters might be biased, they should be refined through a system calibration. Without proper system calibration, for the photogrammetric and LiDAR system, the quality of the final product cannot be guaranteed.

The photogrammetric system calibration involves the camera and the mounting parameters calibration (i.e., the lever arm offset and boresight angles relating the camera and the navigation sensors). In the camera calibration procedure, the internal characteristics of a camera, which are defined by its Interior Orientation Parameters (IOP), are determined. The camera IOP include the principal distance, the coordinates of the principal point, and the distortion model parameters. For traditional large format analogue cameras, the well defined laboratory calibration process is executed to determine the camera IOP. The laboratory calibration is usually performed by system manufacturers and dedicated organizations, such as the U.S. Geological Survey (USGS) and the Natural Resources Canada (NRCan), where trained professionals ensure that high calibration quality is upheld. Due to its decreasing cost and increasing resolution, digital cameras are rapidly replacing the need for the conventional large format analogue cameras. Also, the utilization of a larger number of cameras onboard the mapping platform is a tendency in some of recent photogrammetric mapping projects (El-sheimy, 2005). The airborne digital cameras that are currently available can be grouped into two main categories: the first group includes large format digital cameras, such as line cameras (e.g., ADS80 from Leica Geosystems) and large format frame cameras (e.g., DMC^{TM} from Zeiss/Intergraph); while the second group includes medium to small-format digital cameras (e.g., Rollei-P65). In contrast to the standard analogue cameras, the calibration process for digital cameras is a more complex task. The difficulty is attributed to the large variety of camera designs available in the market, which would demand different facilities and calibration approaches (Cramer, 2004). This is not critical for large format digital cameras that are specifically built for mapping applications. For these cameras, the calibration process is conducted by the system manufacturer (e.g., Leica or Z/I). This is not the case for Medium Format Digital Cameras (MFDCs), which are not manufactured for photogrammetric purposes and have been increasingly used in photogrammetric activities. The increased use of MFDCs by the photogrammetric community is noticeable, especially in conjunction with LiDAR systems and in smaller coverage flight blocks. The preference given by some data providers to MFDCs is attributed to its lower cost when compared with large format digital cameras. The wide spectrum of existing designs for MFDCs coupled with the large number of this type of camera in use by the photogrammetric community make it impracticable for the system manufacturer and/or few specialized organizations to execute the laboratory calibration. In addition, the stability of MFDCs is also a concern, given the fact that these cameras are not manufactured for photogrammetric purposes. Therefore, it has become more practical for the data providers to perform their own calibration and stability analysis of the utilized cameras. In this context, more attention should be placed towards the method and quality of the camera calibration. More specifically, the appropriate calibration procedure and stability analysis as well as the adequate model to represent the inherent distortions in the implemented camera should be carefully investigated. For GPS/INS-assisted photogrammetric systems, accurate estimation of the camera IOP plays a more important role than for the traditional indirect geo-referencing procedure since biases in the camera IOP are not compensated by the estimated Exterior Orientation Parameters (EOP) (Habib and Schenk, 2001). The development of a methodology for determining the adequacy of a distortion model is one of the goals of this research work. On the other hand, the optimum flight configuration for refining the principal point coordinates and the principal distance during the in-flight calibration will be devised since such parameters are more susceptible to changes under operational conditions (Jacobsen, 2003).

The mounting parameters calibration of photogrammetric systems has been the focus of several research groups in the past few years. Mounting parameters calibration of land-based photogrammetric system has been investigated by several authors (e.g., He et al., 1992; El-Sheimy, 1996a). For airborne systems, most of the research work took place in the years 1999-2002, more intensively when the former European Organization for Experimental Photogrammetric Research (OEEPE) – now European Spatial Data Research (EuroSDR) – started its test on “Integrated Sensor Orientation (ISO)” (Heipke et al., 2001; Heipke et al., 2002). Two main approaches for system mounting parameters calibration can be found in the literature. The first approach consists of a two-step procedure, while the second one consists of a single-step procedure. In the two-step procedure, the system mounting parameters are estimated by comparing the GPS/INS-derived position and orientation results with the EOP determined from an independent AT (bundle adjustment) solution (Toth, 1998; Toth, 1999; Cramer, 1999; Jacobsen, 1999; Skaloud, 1999; Grejner-Brzezinska, 2001; Cramer and Stallmann, 2001; Yastikli and Jacobsen, 2005; Casella et al., 2006). Such approach relies on the availability of a calibration site with ground control points and a strong data acquisition geometry to perform the bundle adjustment procedure. Moreover, correlations among the EOP and among the EOP and IOP of the imaging sensor are ignored. In the single-step procedure, the mounting parameters and additional parameters (e.g., camera self-calibration parameters) can be estimated in the bundle adjustment procedure (Cramer and Stallmann, 2002; Wegmann, 2002, Honkavaara et al., 2003; Honkavaara, 2004; Smith et al., 2006; Yuan, 2008). Besides less strict flight/data acquisition configuration and control requirements, the single-step is considered a more robust method to handle the dependencies among the EOP and IOP parameters, since the IOP can be refined along with the mounting parameters, if needed. Some authors have empirically investigated flight and control requirements for the in-flight single-step photogrammetric system calibration using real and/or simulated datasets (Pinto and Forlani, 2002; Honkavaara, 2003; Yuan, 2008). However, a rigorous analysis has not been presented yet and is the focus of this research work. The commonly used single-step procedure in previous work consists of extending existing bundle adjustment procedures with additional observation equations. Although for single-camera systems such approach is appropriate, when dealing with multi-camera systems dependent observation equations are introduced, which increases the complexity of the adjustment procedure. For multi-camera systems in the absence of GPS/INS data, Relative Orientation Constraints (ROC) can be included in the bundle adjustment procedure to enforce the invariable relationship among the cameras. Such procedure involves complicated implementation, e.g., extensive partial derivatives as well as manual formatting of the camera pairs to be utilized in the ROC. These complexities are intensified as the number of cameras onboard gets larger. In this work, a novel single-step procedure, which is suitable for single and multi-camera systems in the presence or absence of GPS/INS data, is proposed. The proposed method utilizes the concept of modified collinearity equations, which has already been used by some authors in ISO procedures involving single-camera systems (Ellum, 2001; Pinto and Forlani, 2002).

LiDAR system calibration involves the laser ranging and scanning unit calibration along with the mounting parameters calibration. The overall process to calibrate a LiDAR system involves several steps such as the calibration of the individual system components in a laboratory, which is performed by the system manufacturer, and a platform calibration to determine the system mounting parameters (Schenk, 2001). An in-flight system calibration is usually needed to refine the parameters determined in the laboratory and in the platform calibrations. Compared to the photogrammetric system calibration, a rigorous in-flight LiDAR calibration is a more challenging task due to the irregular nature of the LiDAR point cloud, which demands appropriate primitives and mechanism for using them. Extensive research has been carried out on in-flight LiDAR system calibration in the past few years (Burman, 2000; Filin, 2001; Morin, 2002; Toth, 2002; Skaloud and Lichti, 2006; Friess, 2006; Habib et al. 2010b; Bang, 2010). Some of the existing approaches either rely on primitives, which are not suitable to deal with the irregular nature of LiDAR surfaces (Morin, 2002) or deal with appropriate primitives while requiring specific features in the calibration site (planar or linear features) and/or pre-processing of the LiDAR point cloud, i.e., classification of LiDAR data into terrain/off-terrain features or segmentation of planar patches (Skaloud and Lichti, 2006;

Friess, 2006) or even the requirement for control surfaces (Filin, 2001). Moreover, in some of the methods, the number of unknowns changes with the number of primitives used in the calibration procedure (Burman, 2000; Skaloud and Lichti, 2006). In addition, some procedures rely on interpolation techniques where the explicit link between the surface representation scheme and the LiDAR equation is not preserved (Burman, 2000; Toth, 2002). In terms of data requirement, existing methods demand the system's raw measurements (Filin, 2001; Skaloud and Lichti, 2006; Friess, 2006) or at least the trajectory and time-tagged point cloud (Burman, 2000; Toth, 2002; Morin, 2002) for the estimation of biases in the system parameters with the help of the LiDAR point positioning equation. Recently, two calibration methods that overcome the limitation in terms of data requirements for the LiDAR system calibration faced by most users have been proposed in Habib et al. (2010b) and Bang (2010). One of the methods, denoted as "Simplified Calibration", only requires the LiDAR point cloud coordinates. This relaxed data requirement is enabled by the use of a simplified LiDAR point positioning equation. The underlying assumptions to simplify the LiDAR point positioning equation and to derive the calibration mathematical model limit its use to datasets following a strict flight configuration and terrain characteristics, i.e., parallel flight lines acquired by fixed wing platforms (small pitch and roll angles) over an area with moderately varying elevation (minor terrain elevation variations compared to the flying height above ground). On the other hand, the second method proposed in Habib et al. (2010b) and Bang (2010), denoted as "Quasi-Rigorous Calibration", is more flexible in terms of the required flight configuration (i.e., it can be used in datasets consisting of non-parallel flight lines) and has no restriction in terms of the terrain characteristics. However, this method is only suitable for datasets acquired by steady platforms (small pitch and roll angles) and requires time-tagged point cloud and the trajectory position. With the widespread adoption of LiDAR systems and efforts in developing standards for the delivery of the LiDAR data, it is expected that access to the LiDAR system raw measurements will not be an issue in the near future. Therefore, the implementation of accurate rigorous calibration procedures would benefit not only system manufactures (and some data providers) but the whole LiDAR data user community. One should note that access to the system raw measurements is not the only requirement for having a rigorous calibration that can be easily adopted by end-users. A flexible calibration procedure that can be executed without strict requirements (e.g., flight, terrain coverage, control, and pre-processing requirements such as classification of the LiDAR point cloud into terrain/off-terrain features or segmentation of planar features) as well as with a high level of automation would also be essential. The implementation of a rigorous calibration procedure while having such characteristics is one of the goals of this research work.

1.2 Research Objectives

The goal of this research work is to fill in some of the gaps in the quality assurance of multi-sensor systems encompassing GPS/INS unit and two types of imaging sensors: digital cameras (single or multi-camera systems) and a laser scanning system. The objectives of this research work can be summarized as follows:

- General Research Objectives
    - I. Propose methodologies for the calibration of GPS/INS-assisted photogrammetric and LiDAR systems with the following characteristics:
        - i. Practical, cost-effective, reliable, and without strict flight, control and ground coverage requirements.
    - II. Utilization of a unified mathematical model, i.e., point-positioning equation, for the calibration of GPS/INS-assisted photogrammetric and LiDAR systems.

- Specific Research Objectives
    - I. Propose a rigorous analysis of flight and control requirements for the system calibration of airborne GPS/INS-assisted single-camera photogrammetric and LiDAR systems:
        - i. Analyze the recoverability of the investigated parameters, i.e., check whether these parameters are correlated or not;
        - ii. Propose a rigorous analysis of control and flight configuration (e.g., flight pattern, flight height, overlap percentage) for reliable estimation of these

parameters. In other words, the optimum flight configuration that maximizes the impact of biases in the system parameters on the derived surface and decouples correlated parameters using minimum control requirement will be investigated.

II. Photogrammetric System Calibration:

  i. Methodology for determining the adequacy of the distortion model for the calibration of MFDCs. One should note that inappropriate distortion model will negatively affect the estimation of the mounting parameters. This in turn will affect the quality of the object space reconstruction.

  ii. Propose a single-step photogrammetric system calibration with the following characteristics:
    a. Suitable for single and multi-camera systems;
    b. Simple implementation;
    c. Flexible: The developed procedure can also be used for the estimation of the Relative Orientation Parameters (ROP) among the cameras in the absence of GPS/INS. Furthermore, a general model, which allows for the incorporation of prior information about the ROP among the cameras in the calibration process, is devised. Such model should have the ability of deriving the previous models as special cases (ISO without prior ROP information and the estimation of the ROP among the cameras).

III. LiDAR System Calibration

Propose a rigorous system calibration with the following characteristics:

  a. Fully automated method that does not require specific features in the covered area (e.g., planar or linear features);
  b. Suitable primitives are utilized, which can deal with the irregular nature of the LiDAR point cloud while not involving pre-processing of the data (i.e., classification or segmentation of the dataset);

c. The parameters associated with the utilized primitives are not part of the unknowns, which significantly decreases the storage and execution time requirements due to the manageable size of the normal equation matrix;
d. Control and tie features can be equally utilized in the calibration procedure without enforcing any constraints about the nature of the control data (i.e., a collection of control points that need not be physically identified in the LiDAR data can be incorporated);
e. The correspondence between conjugate primitives is determined in the calibration procedure using a robust automated matching procedure;
f. While utilizing higher order primitives, simplicity in the implementation of the method is maintained by utilizing point-based observation equations. For that purpose, a modification to the traditional Gauss Markov stochastic model is introduced.

1.3 Thesis Outline

This thesis is structured as follows:

- Chapter 2 provides an overview of the photogrammetric principles and modern photogrammetric mapping systems while focusing on presenting the state-of-the-art on photogrammetric system mounting parameters calibration. LiDAR principles are described next while also focusing on the review of existing methods for the LiDAR system calibration.

- Chapter 3 discusses the photogrammetric/LiDAR system parameters involved in the system calibration. More specifically, the parameters involved in the individual sensor calibration, i.e., camera/laser unit parameters, while focusing on an adequate selection, are reviewed. In addition, a methodology for determining the adequate distortion model for the calibration of MFDC is introduced.

- Chapter 4 presents a rigorous analysis of flight and control requirements for the calibration of airborne GPS/INS-assisted single-camera photogrammetric and LiDAR systems. Such investigation is performed through the mathematical analysis of the GPS/INS-assisted photogrammetric/LiDAR point positioning equations and verified through simulations.

- Chapter 5 introduces a novel single-step procedure for the calibration of single or multi-camera systems. For multi-camera systems, besides the estimation of the mounting parameters relating the cameras and the navigation sensors, the proposed single-step procedure has the capability of estimating the ROP among the cameras. A general mathematical model is devised to allow for the incorporation of prior information on the ROP among the cameras in the ISO procedure. The introduced general model has the ability of deriving the previous models as special cases (the estimation of the mounting parameters relating the cameras and the navigation sensors – without prior ROP information – and estimation of the ROP among the cameras).
- Chapter 6 presents a novel rigorous LiDAR system calibration, which is fully automated and does not require pre-processing or specific features in the calibration site.
- Chapter 7 presents experimental results to demonstrate the feasibility of the proposed methodologies for the photogrammetric and LiDAR system calibration.
- Chapter 8 finally presents the conclusions of the presented research work and recommendations for future investigations.

CHAPTER 2

BACKGROUND

2.1 Photogrammetric Systems

2.1.1 Photogrammetric Principles

Photogrammetry focuses on accurate derivation of spatial and descriptive information from imagery to satisfy the needs of several applications. Photogrammetric object space reconstruction is obtained through intersection of conjugate light rays from overlapping imagery (Figure 2.1). Therefore, the conjugate bundle of light rays must be defined and their position and orientation in space should be known. A bundle of light ray is defined by having the image point measurements and the internal characteristics of the camera. The camera internal characteristics, i.e., the camera Interior Orientation Parameters (IOP), are determined through a camera calibration process while the position and orientation of the bundles in space, which are known as the Exterior Orientation Parameters (EOP) or image geo-referencing parameters, are obtained through a geo-referencing procedure.

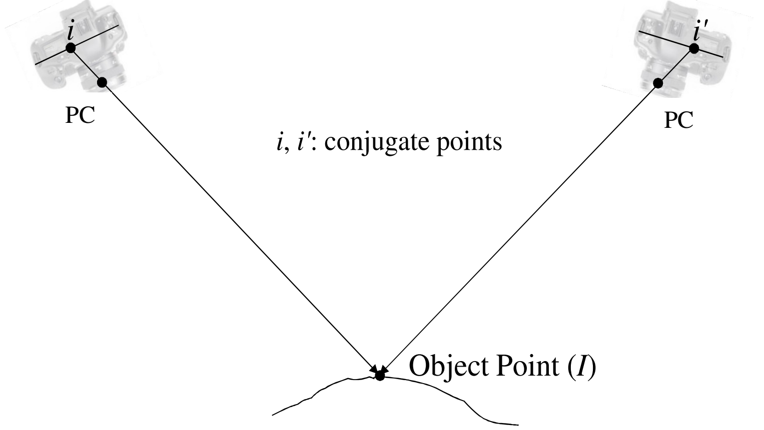

Figure 2.1. Photogrammetric surface reconstruction principle based on the intersection of conjugate light rays (Adapted Habib et al., 2006).

The mathematical model for the photogrammetric point positioning is based on the collinearity of the camera's perspective center (PC), the object point (*I*), and the corresponding image point (i). The classical derivation of the collinearity equations is based on the concept that the vector from the perspective center to the image point (r_i^c) is co-aligned with the vector from the perspective center to the corresponding object point (r_I^c) (Krauss, 1993). The mathematical relationship between these two vectors is expressed in Equation 2.1. The final form of the collinearity equations, shown in Equations 2.2a and 2.2b, can be obtained by moving the term r_i^c to the left side of the equation while dividing the first two rows by the third one. One should note that the scale factor (λ_i) is eliminated through the division process.

$$r_I^c = R_m^c \begin{bmatrix} X_I - X_o \\ Y_I - Y_o \\ Z_I - Z_o \end{bmatrix} = \lambda_i r_i^c = \lambda_i \begin{bmatrix} x_i - x_p - \Delta_x \\ y_i - y_p - \Delta_y \\ -c \end{bmatrix} \tag{2.1}$$

where:

- X_I, Y_I, Z_I: the coordinates of the object point (I) defined relative to the mapping frame;
- X_o, Y_o, Z_o: the coordinates of the camera perspective center defined relative to the mapping frame;
- λ_i: represents the ration between the magnitudes of the vector connecting the perspective center and the object point and the vector connecting the perspective center and the image point;
- R_c^m: the rotation matrix relating the mapping frame and the camera coordinate systems, defined by the rotation angles ω , φ , and κ and the elements $(r_{11}, r_{12}, r_{13}, \cdots, r_{33})$;
- x_i, y_i: image coordinates of an image point (i);
- x_p , y_p , c , and the coefficients describing Δ_x and Δ_y : the camera interior orientation parameters, which will be described in more details in Chapter 3.

$$x_i = x_p - c\,\frac{N_x}{D} + \Delta_x \tag{2.2a}$$

$$y_i = y_p - c\,\frac{N_y}{D} + \Delta_y \tag{2.2b}$$

where:

- $N_x = r_{11}(X_I - X_o) + r_{21}(Y_I - Y_o) + r_{31}(Z_I - Z_o)$;
- $N_y = r_{12}(X_I - X_o) + r_{22}(Y_I - Y_o) + r_{32}(Z_I - Z_o)$;
- $D = r_{13}(X_I - X_o) + r_{23}(Y_I - Y_o) + r_{33}(Z_I - Z_o)$.

The photogrammetric point positioning mathematical model can be alternatively derived through the summation of the vectors illustrated in Figure 2.2. As demonstrated in this figure, the position of an object point (*I*) relative to the mapping frame (r_I^m) can be expressed by the summation of two vectors: r_c^m and r_i^c after applying the rotation R_c^m and the scale factor (λ_i) as presented in Equation 2.3. In this equation, r_c^m represents the vector from the origin of the mapping frame to the camera perspective center, i.e., the ground coordinates of the perspective center (X_o, Y_o, Z_o). The term r_c^m and the rotation angles defining R_c^m represent the EOP of the exposure station (position and orientation of the bundles in space). As already mentioned, the term r_i^c represents the vector from the perspective center to the image point with respect to the camera coordinate system. The magnitude of the vector r_i^c, after applying the scale factor (λ_i), corresponds to the distance from the camera perspective center to the object point. Equation 2.3 can be rearranged to produce the form in Equation 2.4, by moving the term r_i^c to the left side of the equation. Equation 2.4 can be reduced to the traditional form of the collinearity equations (Equation 2.2) after dividing the first two rows by the third one.

$$r_I^m = \begin{bmatrix} X_I \\ Y_I \\ Z_I \end{bmatrix} = r_c^m + \lambda_i R_c^m \, r_i^c = \begin{bmatrix} X_o \\ Y_o \\ Z_o \end{bmatrix} + \lambda_i R_c^m \begin{bmatrix} x_i - x_p - \Delta_x \\ y_i - y_p - \Delta_y \\ -c \end{bmatrix} \tag{2.3}$$

$$\begin{bmatrix} x_i - x_p - \Delta_x \\ y_i - y_p - \Delta_y \\ -c \end{bmatrix} = \frac{1}{\lambda_i} \, R_m^c \begin{bmatrix} X_I - X_o \\ Y_I - Y_o \\ Z_I - Z_o \end{bmatrix} \tag{2.4}$$

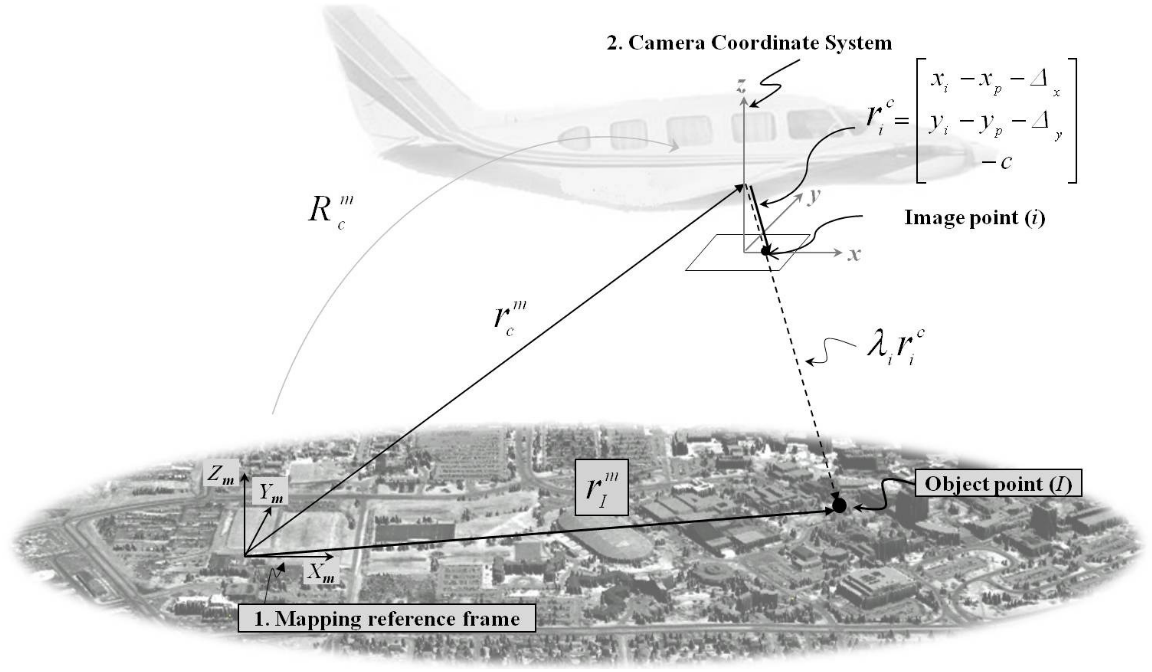

Figure 2.2. Alternative derivation of the collinearity equation through a vector summation process.

As already mentioned, the camera IOP (i.e., $x_p, y_p, c,$ and the coefficients describing Δ_x, and Δ_y) are determined through a camera calibration process. Methods for camera calibration can be categorized into two groups: laboratory and analytical calibration methods. The laboratory calibration is carried out under controlled conditions using specially designed devices (e.g., multi-collimator). This type of calibration is usually conducted by the camera manufacturer or a certified organization (e.g., the USGS in USA or NRCan in Canada). The analytical camera calibration utilizes bundle adjustment with self-calibration (Kenefick et al., 1972; Fraser, 1997), in which the collinearity equations and control information are usually utilized. There are two types of analytical calibration: indoor and in-flight/in-situ. The indoor calibration has been conventionally done using a test field, which can be either two dimensional (2D) (e.g., calibration wall) or three dimensional (3D) (e.g., calibration cube) with precisely surveyed GCP (or using an arbitrary reference frame while having distance measurements to define the scale) and convergent images (in case of 2D test fields). The in-flight/in-situ calibration, on the other hand, is performed under operational conditions (Merchant, 1974).

Traditionally, the image geo-referencing parameters have been estimated indirectly with the help of a set of GCP and identified tie points in a bundle adjustment procedure, i.e., through an indirect geo-referencing procedure, as illustrated in Figure 2.3a. Currently, modern mapping systems incorporate a GPS/INS unit to directly obtain the position and orientation of the mapping platform (Figure 2.3b) (Toth, 1998, Cramer, 1999, Skaloud, 1999). Also, there is a trend for the utilization of multi-camera systems (El-sheimy, 2005). Aspects related to modern photogrammetric mapping systems are discussed in more details in the following section.

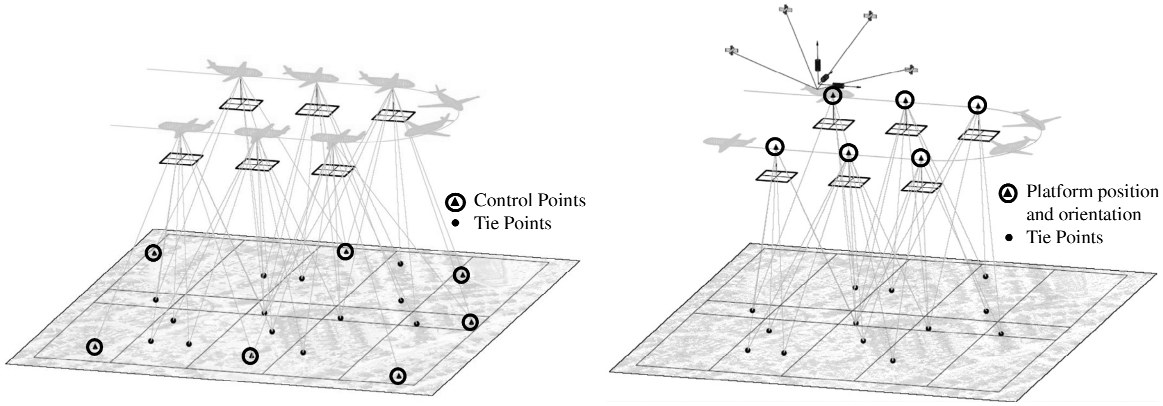

(a) (b)

Figure 2.3. Geo-referencing methodologies: indirect geo-referencing (a) and direct sensor orientation (b) (Adapted Habib et al., 2006).

2.1.2 Modern Photogrammetric Mapping Systems

The use of integrated GPS/INS for direct sensor orientation has received increasing attention from the photogrammetric survey community in the past few years. In airborne mapping, a transition from large format analogue cameras to digital cameras, which has been facilitated by the increased resolution and more affordable cost associated with latter ones, is noticeable. Also, the utilization of larger number of cameras onboard the mapping platform (airborne/terrestrial), to obtain larger object space coverage, is a trend in modern photogrammetric mapping systems.

The inclusion of navigation sensors increases the complexity of the photogrammetric reconstruction process since for photogrammetric geo-referencing, the position and orientation of the camera coordinate system relative to the mapping reference frame is of interest. However, the position and orientation information derived from the integration of the GPS/INS observations would provide the position and orientation of the IMU body frame relative to the mapping frame. Therefore, the mounting parameters relating the system's sensors must be known. Different from the indirect geo-referencing, where only the camera calibration is involved in the photogrammetric system calibration, direct sensor orientation also involves the mounting parameters calibration. Moreover, camera calibration plays a more important role in the direct sensor orientation than in the indirect geo-referencing. This is mainly due to the fact that direct sensor orientation is an extrapolation procedure and errors are directly propagated to the object space (Habib and Shenk, 2001). For instance, errors in the calibration parameters cannot be compensated by the EOP. Therefore, reliable camera and mounting parameters calibration are essential to obtain accurate object space reconstruction.

In the next sections, a review of the implementation approaches for the utilization of the GPS/INS-derived position and orientation in the photogrammetric reconstruction along with related work on the photogrammetric system calibration are presented.

2.1.2.1 Direct Sensor Orientation: Implementation Approaches

Direct sensor orientation can be performed in two different ways: (i) Direct geo-referencing and (ii) Integrated Sensor Orientation (ISO) (Jacobsen, 2004). In the direct geo-referencing, the EOP of the camera at the moments of exposure are derived from the GPS/INS-derived position and orientation using the time tags associated with the exposure stations and the system calibration parameters. The EOP are then used to derive the object coordinates of points of interest through a simple intersection procedure. In the ISO, on the other hand, the GPS/INS-derived position and orientation information are used as prior information in the bundle adjustment procedure along with the image coordinates of tie points. This simultaneous adjustment of a number of tie points within a bundle adjustment procedure allows for further improvement in the EOP. Several authors have investigated/compared the performance of the direct geo-referencing and the ISO procedures (e.g., Jacobsen, 2000; Habib and Schenk, 2001; Heipke et al., 2002; Wegman, 2002; Khoshelham et al., 2007). In investigations on the direct geo-referencing performance, large remaining *y*-parallaxes in the photogrammetric model have been noticed, which makes the use of direct geo-referencing for stereo plotting not always possible. The use of the ISO procedure, on the other hand, eliminates these remaining parallaxes. In Khoshelham et al. (2007), it was demonstrated that although the object space accuracy is not significantly improved (when compared with the direct geo-referencing), regardless of the number and distribution the tie points in the ISO procedure, significant reduction of the *y*-parallax in the photogrammetric model is obtained. Different from the traditional bundle adjustment procedure (without GPS/INS information) and a GPS-assisted AT, in the ISO fewer tie points are required. Khoshelham et al. (2007) has investigated the influence of the number and distribution of tie points on ISO procedures. In that work, it was demonstrated that one tie point per model would be sufficient to reduce the remaining *y*-parallaxes.

The main limiting factor of the direct sensor orientation, regardless of performing ISO or direct geo-referencing, is the stability of the system mounting parameters and the camera IOP. Any error in such parameters will propagate directly to the ground coordinates. In contrast to the traditional bundle adjustment, in the ISO procedure, errors in the IOP are not absorbed by the EOP. It should be noted that, in the presence of appropriate flight and control configuration, which allows the recovery of the camera IOP and the system mounting parameters, the ISO provide the most reliable solution for high accuracy applications since such system calibration parameters can be estimated/refined (Cramer et al., 1999). Related work on photogrammetric system calibration is discussed in the next section.

2.1.2.2 Related Work on Photogrammetric System Calibration

There exist several factors that might have an impact on the performance of the direct sensor orientation, e.g., the quality of photogrammetric system calibration (i.e., camera and mounting parameters calibration), the GPS data quality (which is mainly dependent on the distance from the base station, satellite geometry, and continuity of the GPS lock), the type of the IMU system used, and the quality of the GPS/INS integration process. Moreover, the stability of the parameters determined in the calibration procedure is also an issue. Over the last few years, extensive investigations on the performance of GPS/INS-assisted photogrammetric systems have been carried out (e.g., Toth, 1998; Toth, 1999; Jacobsen, 2000; Cramer et al., 2000; Habib and Schenk, 2001; Wegmann, 2002; Baron et al., 2003). The results from the performed investigations, especially the results from the OEEPE test on "Integrated Sensor Orientation" (Heipke et al., 2002), have demonstrated that the achievement of the potential accuracy of direct sensor orientation is mainly limited by the quality of the photogrammetric system calibration, which is, as already mentioned, composed by the camera and the system mounting parameters calibration.

For single-camera systems, the mounting parameters include the boresight angles and the lever arm offset relating the camera and the IMU body frame. For multi-camera systems, on the other hand, the mounting parameters encompass two sets of Relative Orientation Parameters (ROP) (El-Sheimy, 1996a): the ROP among the cameras as well as the ROP between the cameras and the navigation sensors (i.e., the IMU body frame as the navigation solution usually refers to its coordinate frame). One should note that these two sets of ROP are not independent. The calibration of the mounting parameters relating the cameras and the IMU body frame is necessary for GPS/INS-assisted systems. In the absence of GPS/INS data, accurate estimation of the ROP among the cameras is important since they can be utilized as prior information in future survey projects. Moreover, the knowledge of the cameras' ROP can be also useful for directly geo-referenced systems since they can be used as prior information in the calibration of the mounting parameters between the cameras and the IMU body frame to improve the accuracy of the estimated parameters (as will be proposed in this research work). One should note that since the cameras and the navigation sensors are rigidly mounted on a platform, their geometric relationships (mounting parameters) are assumed to be invariant.

Two main approaches can be distinguished in the literature for the estimation of the system mounting parameters: two-step or single-step procedures. In the two-step procedure, the system mounting parameters are estimated by comparing the GPS/INS-derived position and orientation results with the EOP determined from a conventional bundle adjustment solution. The estimated EOP from the bundle adjustment procedure, i.e., $r_c^m(t)$ and $R_c^m(t)$, and the GPS/INS-derived position and orientation (w.r.t. the IMU body frame), i.e., $r_b^m(t)$ and $R_b^m(t)$, are usually utilized in Equations 2.5 and 2.6 to come up with estimates for the lever arm offset r_c^b and the boresight angles defining the boresight matrix R_c^b, respectively (Figure 2.4). One should be noted that the derived mounting parameters in Equations 2.5 and 2.6 are expressed for a time instance *t* since each exposure instance will give an estimate for mounting parameters relating the cameras and the IMU body frame. An averaging process is usually performed to obtain mean values for the mounting parameters as well as their standard deviation. Due to the lower accuracy of the estimated EOP, the images located in the extremities of the flight lines are usually disregarded from the analysis in airborne single-camera systems (e.g., Skaloud, 1999; Jacobsen, 1999). In Skaloud (1999) the mounting parameters are estimated for each image separately and then the results undergo an average weighting procedure. In Grejner-Brzezinska (2001), the resulting linear system from Equation 2.5 and 2.6 are solved using a least squares adjustment procedure to derive an estimate of the system mounting parameters.

$$r_c^b|_t = R_m^b(t)(r_c^m(t) - r_b^m(t)) \tag{2.5}$$

$$R_c^b|_t = R_m^b(t)\, R_c^m(t) \tag{2.6}$$

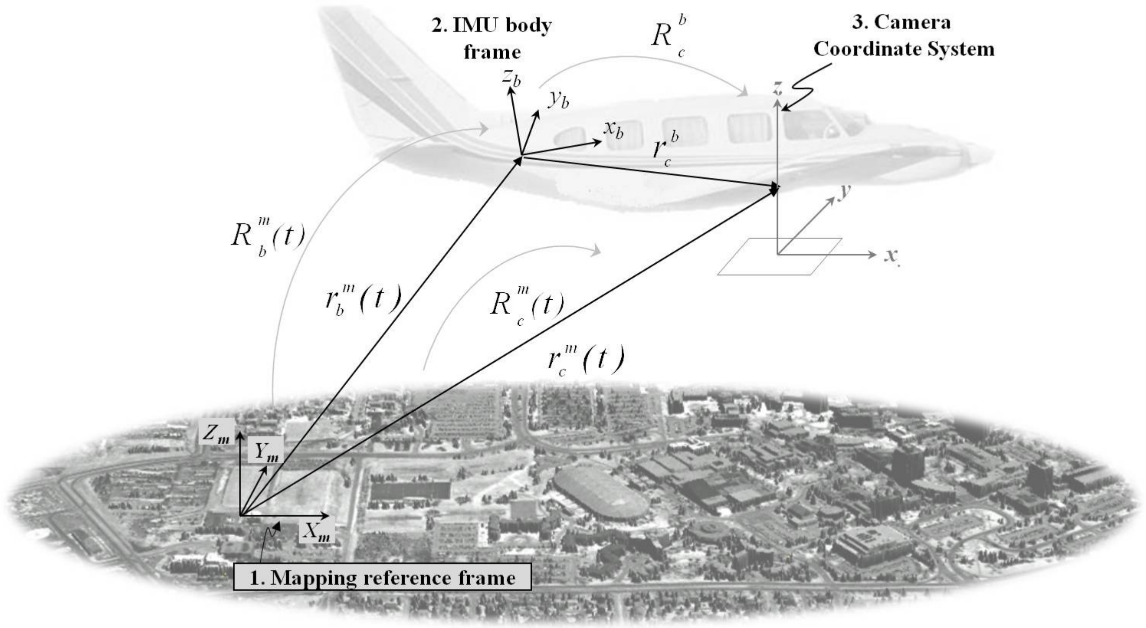

Figure 2.4. Involved quantities in the two-step procedure for the estimation of the mounting parameters.

When dealing with multi-camera systems, "c" in Equations 2.5 and 2.6 should be regarded as "cj", denoting the j^{th} camera coordinate system. The EOP ($r_{cj}^m(t)$ and $R_{cj}^m(t)$) are also obtained through a traditional bundle adjustment procedure (Figure 2.5). To derive estimates for the system mounting parameters, the derived EOP along with the GPS/INS-derived position and orientation information are utilized in Equations 2.7 and 2.8.

$$r_{cj}^b\big|_t = R_m^b(t)\big(r_{cj}^m(t) - r_b^m(t)\big) \tag{2.7}$$

$$R_{cj}^b\big|_t = R_m^b(t)\, R_{cj}^m(t) \tag{2.8}$$

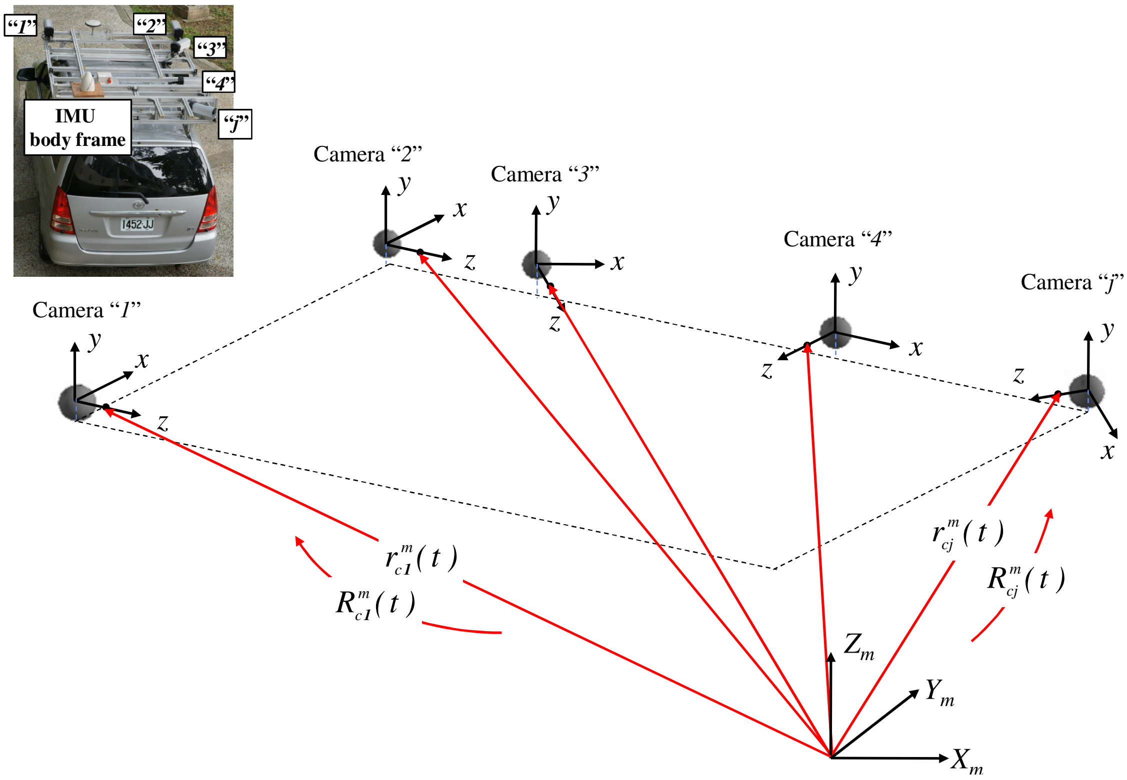

Figure 2.5. EOP of the images captured by a multi-camera system through a traditional indirect geo-referencing procedure.

Similarly, in the absence of GPS/INS data, the ROP of the cameras w.r.t. a reference camera can be determined by comparing the cameras EOP (i.e., $r_{cj}^{m}(t)$ and $R_{cj}^{m}(t)$) with the EOP of the reference one (i.e., $r_{cr}^{m}(t)$ and $R_{cr}^{m}(t)$), which are the outcome from a traditional indirect geo-referencing (bundle adjustment) solution (Figure 2.5). To come up with an estimate for the ROP of the cameras w.r.t. the reference one, Equations 2.9 and 2.10 can be utilized.

$$r_{cj}^{cr}\big|_{t} = R_{m}^{cr}(t)\left(r_{cj}^{m}(t) - r_{cr}^{m}(t)\right) \tag{2.9}$$

$$R_{cj}^{cr}\big|_{t} = R_{m}^{cr}(t)\, R_{cj}^{m}(t) \tag{2.10}$$

Here again, it should be noted that the derived mounting parameters in Equations 2.7 – 2.10 are expressed for a time instance *t* since each exposure instance will give an estimate for the ROP between any of the utilized cameras and the IMU body frame or the reference camera. An averaging process is usually performed to obtain mean values for the mounting parameters as well as their standard deviation.

Due to its simplicity (i.e., any bundle adjustment software can provide the EOP values for the system calibration) the two-step procedure has been extensively used by several authors (Toth, 1998; Toth, 1999; Cramer, 1999; Jacobsen, 1999; Skaloud, 1999; Cramer and Stallmann, 2001; Yastikli and Jacobsen, 2005; Casella et al., 2006). However, the two-step approach presents several drawbacks. One of the disadvantages of this method is that it demands a calibration site with ground control points and a data acquisition configuration with very strong geometry to perform the bundle adjustment procedure. Moreover, correlations among the EOP and among the EOP and IOP of the imaging sensor are ignored (Cramer and Stallmann, 2002), which is a concern especially for aerial vertical imagery over relatively flat terrain. In Jacobsen (1999), high correlation among the EOP was observed due to insufficient flight configuration. In Cramer et al. (2000), correlations among the EOP and IOP resulted in systematic vertical offsets in the derived photogrammetric product.

In the single-step procedure, on the other hand, the system mounting parameters are estimated in the bundle adjustment procedure (i.e., through an ISO procedure). There are two approaches for the single-step procedure, which differ on how the GPS/INS-derived position and orientation and the system mounting parameters are incorporated in the ISO procedure. In the commonly used approach, denoted in this dissertation as “added observations method”, the traditional bundle adjustment procedure is extended by adding the observations equations shown in Equations 2.11 and 2.12. In Equation 2.11, the term r_b^c represents the lever arm offset describing the position of the IMU body frame relative to the camera coordinate system. The rotation matrix R_b^c in Equation 2.12 represents the boresight matrix (rotation matrix) relating the IMU and the camera coordinate systems. It should be noted that the rotation matrix $R_b^m(t)$ has nine dependent elements (i.e., they should satisfy six orthogonality conditions). Therefore, only three independent elements should be utilized as part of the additional observations. The elements r_{12}, r_{13}, and r_{23} are usually selected due to the simplicity and independency of the derived observation equations (Equations 2.13 – 2.15). The noise associated with the observations can be obtained through error propagation (using the noise of the GPS/INS-derived orientation information). Therefore, six equations will be added for the GPS/INS-derived position (three as per Equation 2.11) and orientation (Equations 2.13 – 2.15) information for each image within the dataset.

$$r_b^m(t) = r_c^m(t) + R_c^m(t)\, r_b^c \tag{2.11}$$

$$R_b^m(t) = R_c^m(t)\, R_b^c \tag{2.12}$$

where:

$$R_b^m(t) = \begin{bmatrix} cos\varphi_b cos\kappa_b & \boldsymbol{-cos\varphi_b sin\kappa_b} & \boldsymbol{sin\varphi_b} \\ cos\varphi_b sin\kappa_b + sin\omega_b sin\varphi_b cos\kappa_b & cos\omega_b cos\kappa_b - sin\omega_b sin\varphi_b sin\kappa_b & \boldsymbol{-sin\omega_b cos\varphi_b} \\ sin\omega_b sin\kappa_b - cos\omega_b sin\varphi_b cos\kappa_b & sin\omega_b cos\kappa_b + cos\omega_b sin\varphi_b sin\kappa_b & cos\omega_b cos\varphi_b \end{bmatrix}$$

$$R_c^m(t) = \begin{bmatrix} cos\varphi cos\kappa & \boldsymbol{-cos\varphi sin\kappa} & \boldsymbol{sin\varphi} \\ cos\varphi sin\kappa + sin\omega sin\varphi cos\kappa & cos\omega cos\kappa - sin\omega sin\varphi sin\kappa & \boldsymbol{-sin\omega cos\varphi} \\ sin\omega sin\kappa - cos\omega sin\varphi cos\kappa & sin\omega cos\kappa + cos\omega sin\varphi sin\kappa & cos\omega cos\varphi \end{bmatrix}$$

$$R_b^c(t) = \begin{bmatrix} cos\Delta\varphi cos\Delta\kappa & \boldsymbol{-cos\Delta\varphi sin\Delta\kappa} & \boldsymbol{sin\Delta\varphi} \\ cos\Delta\varphi sin\Delta\kappa + sin\Delta\omega sin\Delta\varphi cos\Delta\kappa & cos\Delta\omega cos\Delta\kappa - sin\Delta\omega sin\Delta\varphi sin\Delta\kappa & \boldsymbol{-sin\Delta\omega cos\Delta\varphi} \\ sin\Delta\omega sin\Delta\kappa - cos\Delta\omega sin\Delta\varphi cos\Delta\kappa & sin\Delta\omega cos\kappa + cos\Delta\omega sin\Delta\varphi sin\Delta\kappa & cos\Delta\omega cos\Delta\varphi \end{bmatrix}$$

$$-cos\varphi_b sin\kappa_b = \quad \begin{aligned} & cos\varphi cos\kappa(-cos\Delta\varphi sin\Delta\kappa) + \\ & -cos\varphi sin\kappa(cos\Delta\omega cos\Delta\kappa - sin\Delta\omega sin\Delta\varphi sin\Delta\kappa) + \\ & sin\varphi(sin\Delta\omega cos\Delta\kappa + cos\Delta\omega sin\Delta\varphi sin\Delta\kappa) \end{aligned} \tag{2.13}$$

$$sin\varphi_b = \quad \begin{aligned} & cos\varphi cos\kappa(sin\Delta\varphi) + \\ & -cos\varphi sin\kappa(-sin\Delta\omega cos\Delta\varphi) + \\ & sin\varphi(cos\Delta\omega cos\Delta\varphi) \end{aligned} \tag{2.14}$$

$$-sin\omega_b cos\varphi_b \quad \begin{aligned} & (cos\varphi sin\kappa + sin\omega sin\varphi cos\kappa)(sin\Delta\varphi) + \\ & (cos\omega cos\kappa - sin\omega sin\varphi sin\kappa)\,(-sin\Delta\omega cos\Delta\varphi) + \\ & -sin\omega cos\varphi(cos\Delta\omega cos\Delta\varphi) \end{aligned} \tag{2.15}$$

Although this approach might be suitable for single-camera systems (Cramer and Stallmann, 2002; Wegmann, 2002; Honkavaara et al., 2003; Honkavaara, 2004; Smith et al., 2006; Yuan, 2008), when dealing with multi-camera systems (Equations 2.16 and 2.17), dependent observations are introduced. More specifically, the same observation will be used n_{cam} times in the Least Squares Adjustment (LSA), where n_{cam} denotes the number of cameras. The dependency among the observations are ignored in the adjustment procedure. Figure 2.6 illustrates the parameters involved in the added observations method for a multi-camera system.

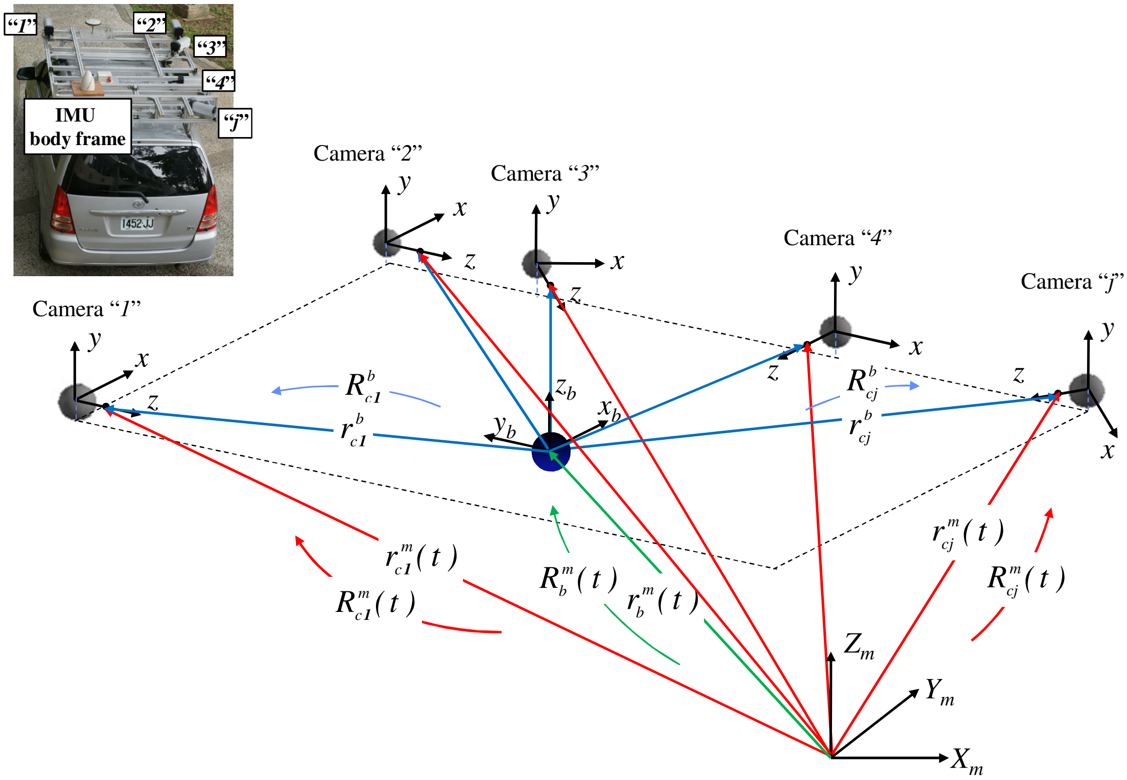

Figure 2.6. Involved parameters in the added observations method for multi-camera systems.

$$r_b^m(t)\{j\} = r_{cj}^m(t) + R_{cj}^m(t)\, r_b^{cj} \qquad j: 1 - n_{cam} \tag{2.16}$$

$$R_b^m(t)\{j\} = R_{cj}^m(t)\, R_b^{cj} \qquad j: 1 - n_{cam} \tag{2.17}$$

For multi-camera systems, the single-step approach used to enforce the invariant geometric relationship, i.e., the ROP, among the cameras in the absence of GPS/INS data, consists of expanding traditional bundle adjustment procedures with constraint equations (e.g., He et al., 1992; King, 1992; El-Sheimy, 1996a; Lerma et. al, 2010) (Figure 2.7). Constraint equations have been extensively used in analytical photogrammetry to enforce geometric or physical relationships that exist between parameters of an adjustment to obtain a solution of higher quality. For instance, King (1992) has proposed the optimization of conventional bundle adjustment procedures by constraining the base distance and the convergence angles of the camera axes (dot products of each pair of *X*, *Y* and *Z* axes) to the mean computed for all stereo-pairs taken from two cameras rigidly fixed. Similarly, in El-Sheimy (1996a), constraint equations are added to enforce the invariance of the base distance and the boresight matrix among the cameras for different epochs in the mounting parameters calibration. The base distance constraint is also used by Lerma et al. (2010) to improve the self-calibration quality.

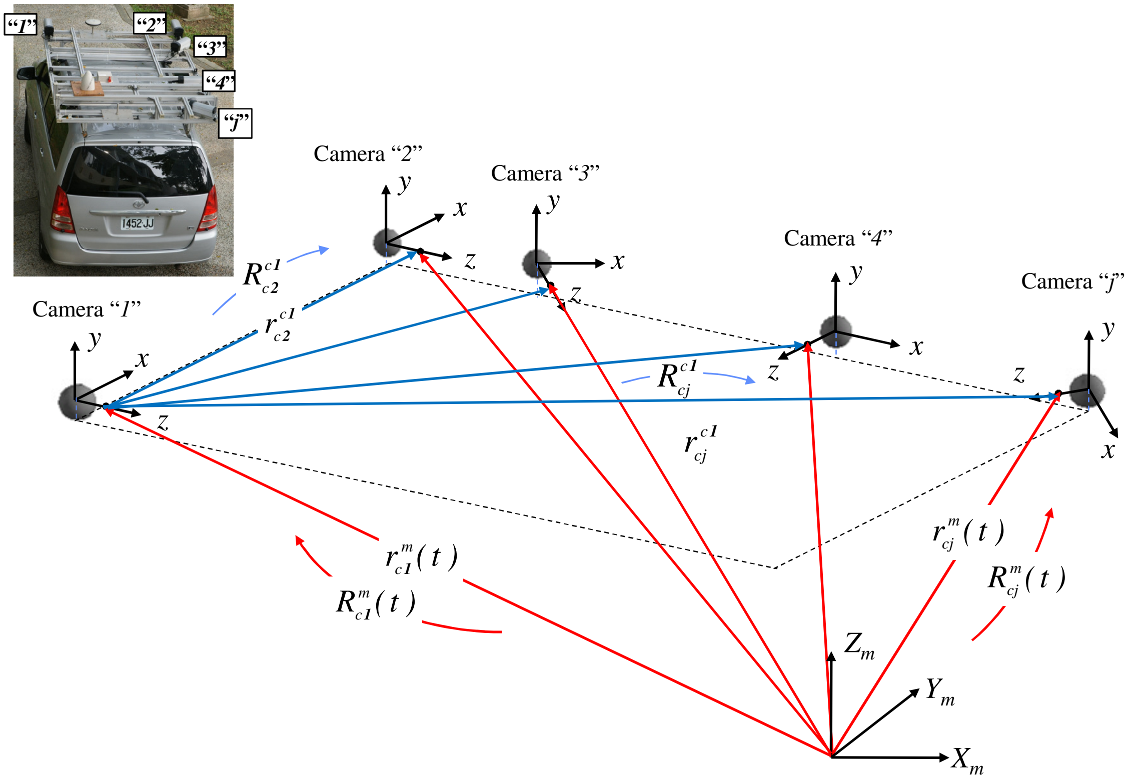

Figure 2.7. EOP (in red) and the constrained ROP among the cameras and a reference camera (in blue).

Table 2.1 shows constraint equations to enforce the invariance of the lever arm offset among the cameras (illustrated in Figure 2.7) in the bundle adjustment procedure. Note that in Table 2.1, *n_cam* represents the total number of cameras while *n_epoch* represents the total number of epochs. Similarly, constraints equations to enforce the invariance of the boresight matrix relating the cameras (illustrated in Figure 2.7) in the bundle adjustment procedure are shown in Table 2.2. The drawback of incorporating constraint equations to enforce consistent ROP among the sensors is the associated complicated procedure for doing that (e.g., extensive partial derivatives as well as manual formatting of the camera pairs to be utilized in the ROC). One should note that these complexities are intensified as the number of cameras onboard gets larger.

Table 2.1. Constraint equations to enforce the invariance of the lever arm offset among the cameras in the bundle adjustment procedure.

Constraints to enforce the invariance of the lever arm offset between the reference camera c_1 and cameras c_2 to c_{n_cam} at epochs t_1 and t_2
$r^{c1}_{c2} = R^{c1}_{m}(t_1)[r^{m}_{c2}(t_1) - r^{m}_{c1}(t_1)] = R^{c1}_{m}(t_2)[r^{m}_{c2}(t_2) - r^{m}_{c1}(t_2)]$ $r^{c1}_{c3} = R^{c1}_{m}(t_1)[r^{m}_{c3}(t_1) - r^{m}_{c1}(t_1)] = R^{c1}_{m}(t_2)[r^{m}_{c3}(t_2) - r^{m}_{c1}(t_2)]$ … $r^{c1}_{cn\_cam} = R^{c1}_{m}(t_1)\left[r^{m}_{cn\_cam}(t_1) - r^{m}_{c1}(t_1)\right] = R^{c1}_{m}(t_2)\left[r^{m}_{cn\_cam}(t_2) - r^{m}_{c1}(t_2)\right]$
Constraints to enforce the invariance of the lever arm offset between the reference camera c_1 and cameras c_2 to c_{n_cam} at epochs t_1 and t_3
$r^{c1}_{c2} = R^{c1}_{m}(t_1)[r^{m}_{c2}(t_1) - r^{m}_{c1}(t_1)] = R^{c1}_{m}(t_2)[r^{m}_{c2}(t_3) - r^{m}_{c1}(t_3)]$ $r^{c1}_{c3} = R^{c1}_{m}(t_1)[r^{m}_{c3}(t_1) - r^{m}_{c1}(t_1)] = R^{c1}_{m}(t_2)[r^{m}_{c3}(t_3) - r^{m}_{c1}(t_3)]$ … $r^{c1}_{cn\_cam} = R^{c1}_{m}(t_1)\left[r^{m}_{cn\_cam}(t_1) - r^{m}_{c1}(t_1)\right] = R^{c1}_{m}(t_2)\left[r^{m}_{cn\_cam}(t_3) - r^{m}_{c1}(t_3)\right]$
Constraints to enforce the invariance of the lever arm offset between the reference camera c_1 and cameras c_2 to c_{n_cam} at epochs t_1 and t_{n_epoch}
$r^{c1}_{c2} = R^{c1}_{m}(t_1)[r^{m}_{c2}(t_1) - r^{m}_{c1}(t_1)] = R^{c1}_{m}(t_2)\left[r^{m}_{c2}\left(t_{n\_epochs}\right) - r^{m}_{c1}\left(t_{n\_epoch}\right)\right]$ $r^{c1}_{c3} = R^{c1}_{m}(t_1)[r^{m}_{c3}(t_1) - r^{m}_{c1}(t_1)] = R^{c1}_{m}(t_2)\left[r^{m}_{c3}\left(t_{n\_epochs}\right) - r^{m}_{c1}\left(t_{n\_epoch}\right)\right]$ … $r^{c1}_{cn\_cam} = R^{c1}_{m}(t_1)\left[r^{m}_{cn\_cam}(t_1) - r^{m}_{c1}(t_1)\right] = R^{c1}_{m}(t_2)\left[r^{m}_{cn\_cam}\left(t_{n\_epoch}\right) - r^{m}_{c1}\left(t_{n\_epoch}\right)\right]$

Table 2.2. Constraint equations to enforce the invariance of the boresight angles among the cameras in the bundle adjustment procedure.

Constraints to enforce the invariance of the boresight matrix relating the reference camera c_1 and cameras c_2 to c_{n_cam} at epochs t_1 and t_2
$R_{c2}^{c1} = R_m^{c1}(t_1)R_{c2}^{m}(t_1) = R_m^{c1}(t_2)R_{c2}^{m}(t_2)$ $R_{c3}^{c1} = R_m^{c1}(t_1)R_{c3}^{m}(t_1) = R_m^{c1}(t_2)R_{c3}^{m}(t_2)$ $\ldots$ $R_{cn\_cam}^{c1} = R_m^{c1}(t_1)R_{cn\_cam}^{m}(t_1) = R_m^{c1}(t_2)R_{cn\_cam}^{m}(t_2)$
Constraints to enforce the invariance of the boresight matrix relating the reference camera c_1 and cameras c_2 to c_{n_cam} at epochs t_1 and t_3
$R_{c2}^{c1} = R_m^{c1}(t_1)R_{c2}^{m}(t_1) = R_m^{c1}(t_3)R_{c2}^{m}(t_3)$ $R_{c3}^{c1} = R_m^{c1}(t_1)R_{c3}^{m}(t_1) = R_m^{c1}(t_3)R_{c3}^{m}(t_3)$ $\ldots$ $R_{cn\_cam}^{c1} = R_m^{c1}(t_1)R_{cn\_cam}^{m}(t_1) = R_m^{c1}(t_3)R_{cn\_cam}^{m}(t_3)$
Constraints to enforce the invariance of the boresight matrix relating the reference camera c_1 and cameras c_2 to c_{n_cam} at epochs t_1 and t_{n_epoch}
$R_{c2}^{c1} = R_m^{c1}(t_1)R_{c2}^{m}(t_1) = R_m^{c1}\left(t_{n\_epoch}\right)R_{c2}^{m}\left(t_{n\_epoch}\right)$ $R_{c3}^{c1} = R_m^{c1}(t_1)R_{c3}^{m}(t_1) = R_m^{c1}\left(t_{n\_epoch}\right)R_{c3}^{m}\left(t_{n\_epoch}\right)$ $\ldots$ $R_{cn\_cam}^{c1} = R_m^{c1}(t_1)R_{cn\_cam}^{m}(t_1) = R_m^{c1}\left(t_{n\_epoch}\right)R_{cn\_cam}^{m}\left(t_{n\_epoch}\right)$

An alternative approach for implementing the single-step procedure consists of directly incorporating GPS/INS-derived position and attitude information and the system mounting parameters in the collinearity equations, denoted as "direct incorporation method". In this approach, the point positioning equation (Equation 2.18), i.e., the modified collinearity equations, can be derived through the summation of three vectors after applying the appropriate rotation matrices, and scale factor (Figure 2.8). The vector r_c^b is the lever arm offset representing the position of the camera relative to the IMU body frame, while the rotation matrix R_c^b stands for the boresight rotation matrix relating the camera and IMU coordinate systems. The concept of modified collinearity equations has been used by few authors for single-camera systems (Elhum, 2001; Pinto and Forlani, 2002). In the current research work, the concept of modified collinearity equations is utilized to devise a photogrammetric system calibration suitable for single and multi-camera systems.

$$r_I^m = r_b^m(t) + R_b^m(t)\, r_c^b + \lambda_i R_b^m(t) R_c^b r_i^c \tag{2.18}$$

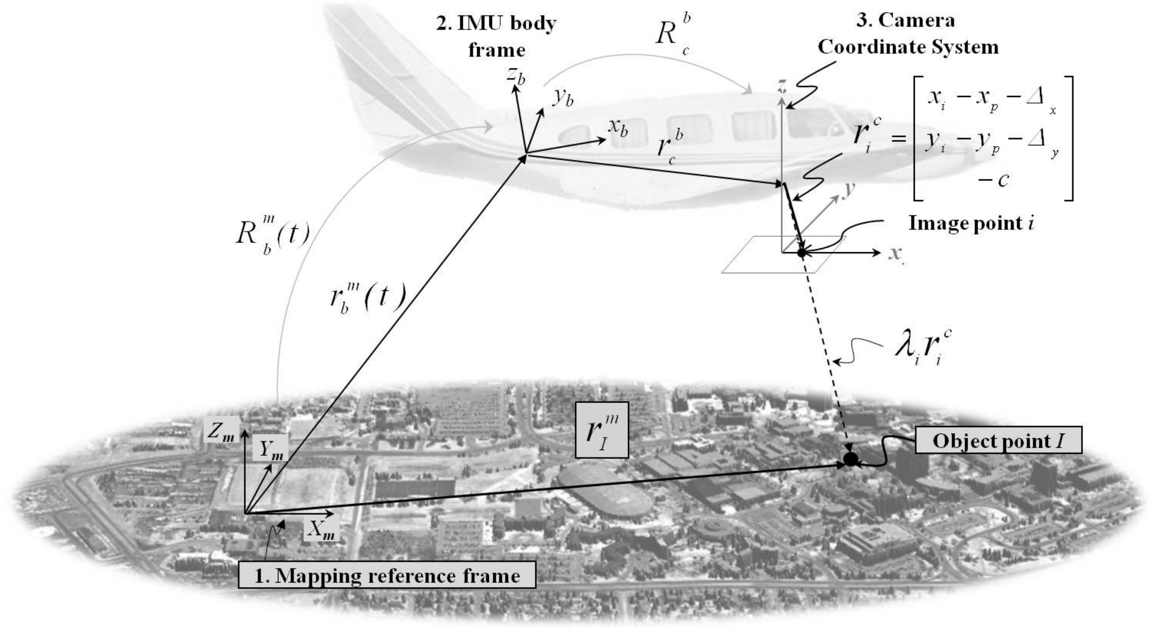

Figure 2.8. Coordinate systems and involved quantities in the point positioning equation based on GPS/INS-assisted photogrammetric system.

When compared to the two-step procedure, the single-step procedure, either for the estimation of the mounting parameters relating the camera (s) and the IMU body frame or for the estimation of the ROP among the cameras, is the most appropriate solution since a less strict flight/data acquisition configuration and control requirements is required. Moreover, for vertical airborne single-camera systems (over a relatively flat terrain), the single-step procedure is considered a more robust method to handle the dependencies among the EOP and IOP parameters, since some of the IOP can be estimated along with the mounting parameters if an appropriate flight/data acquisition configuration is available (Cramer and Stallmann, 2002). The flight and control requirements for the single-step calibration of vertical airborne single-camera systems have already been investigated by some authors. A review of the performed investigations is presented in the next section.

2.1.2.3 Flight and Control Configuration Requirements for the Single-Step Calibration of Airborne Single-Camera Systems

In the last few years, the flight and/or control configuration requirements to perform the calibration of vertical airborne single-camera systems have been the focus of study of some authors. In Jacobsen (2001), a flight configuration for the estimation of the camera principal distance along with the system mounting parameters (i.e., lever arm offset and boresight angles) is suggested and tested. According to Jacobsen (2001), in order to decouple the vertical lever arm offset from the camera principal distance, the calibration must be done using two different flying heights with the GPS/INS position and attitude, or at least the position incorporated in the bundle adjustment procedure and control points. The separation between the principal distance and the vertical lever arm offset component is possible since the effect of vertical lever arm offset component will be the same for different flying heights while the impact of principal distance will change. The two flight scales used were 1:5,000 and 1:10,000. The configuration of the flight lines flown using the scale 1:5,000 consisted of two flight lines flown in opposite directions (100% side lap) and one crossing flight line while the 1:10,000 configuration consisted of a conventional block structure with four parallel and one crossing flight lines. In Wegmann (2002), significant improvement in the object space reconstruction accuracy is observed when the principal distance and principal point coordinates camera are estimated along with the mounting parameters in the system calibration. For the system calibration, Wegman (2002) utilizes strips from two different calibration flights performed using different flying heights (800 and 1600 m above ground level (AGL) – flight scales 1:5,000 and 1:10,000, respectively) and 51 well signalized ground control points. The flight performed at 800 m consisted of four strips flown in opposite and in cross direction. The strips in opposite flight directions are recommended to decouple of the lever arm offsets from the camera principal point coordinates. The flight at 1600 m consisted of four parallel strips and one cross strip. Wegmann (2002) suggests that, in case of non-feasibility of having two flights at significantly different flying heights, the system calibration should be carried out at the same height (and thus the same scale) as the actual project.

Honkavaara (2003) evaluated through simulations the recoverability of the boresight angles and the camera interior orientation parameters (principal point coordinates and principal distance) under several block structures and GCP configurations. On the other hand, in Honkavaara et al. (2004), several block configurations and control requirements for the system calibration were investigated empirically using real data. In addition, the inclusion of several camera interior orientation parameters in the system calibration was investigated. The significance of the studied parameters was assessed by comparing the parameter value to its standard deviation. To be considered as significant, the parameter had to be at least two times larger than its standard deviation. Also, the correlations of the calibration parameters should be evaluated. The addition of image distortion parameters was not appropriate due to their high correlations with other parameters. The principal distance was not included since only one flying height was available for the calibration procedure. The parameters considered significant were the principal point coordinates and the boresight angles. To solve for such parameters, a minimal block geometry consisting of two flight lines flown in opposite directions with 100% side lap and no ground control points were necessary in the calibration procedure. With the objective of finding a minimal sufficient configuration for the calibration of the system mounting parameters, Pinto and Forlani (2002) have investigated through simulated and real datasets several block configurations with varying number and location of ground control points.

Although some authors have empirically investigated flight and/or control requirements for the single-step in-flight photogrammetric system calibration using real and/or simulated datasets (e.g., Jacobsen, 2003, Honkavaara, 2003; Honkavaara et al., 2004;

Pinto and Forlani, 2002; Yuan, 2008), a rigorous analytical analysis has not been presented yet and is one of the objectives of this research work.

2.2 LiDAR Systems

2.2.1 LiDAR Principles

In contrast to photogrammetric systems, LiDAR is an active remote sensing technique, which is based on the laser technology. LiDAR systems are capable of directly providing the 3D coordinates of a surface at high density. The basic principle of operation relies on range measurements, i.e., the determination of the distance between the laser firing point and the footprint on the ground. Range measurements can be performed using Continuous Wave (CW) laser systems or pulsed laser systems. In CW laser systems, the range is determined by measuring the phase difference between the transmitted and the received signal. CW laser systems are usually used in terrestrial LiDAR systems aiming to measure relatively short distances. Most of commercially available airborne LiDAR systems are pulsed lasers, which are usually solid-state pumped lasers since they can provide very short pulses with large peak power at high repetition rate (Toth, 2010). A common type is the Nd: YAG laser, with pulse widths ranging from 4 to 10 ns and 1.064 μm wavelength (Wehr and Lohr, 1999). In such systems, the range measurement is based on the laser pulses' time-of-flight, i.e., elapsed time between the emitted and backscattered laser pulses (Figure 2.9).

Besides a laser ranging unit, LiDAR systems also entail a scanning unit allowing the data collection in a strip-wise fashion. The scanning mechanism (i.e., opto-mechanical scanning assemblies) usually consists of an oscillating mirror, which produces a zigzag pattern (Figure 2.9). Examples of other scanning mechanisms are palmer scan, rotating polygon, and fiber scanner (Wehr and Lohr, 1999). The geo-referencing of the sensor platform, which is crucial for deriving the coordinates of the scanned object points relative to the mapping frame, is enabled by the GPS/INS unit onboard the platform. A GPS base station is utilized for differential GPS positioning (DGPS). Figure 2.9 illustrates the basic LiDAR system components and its operational principles.

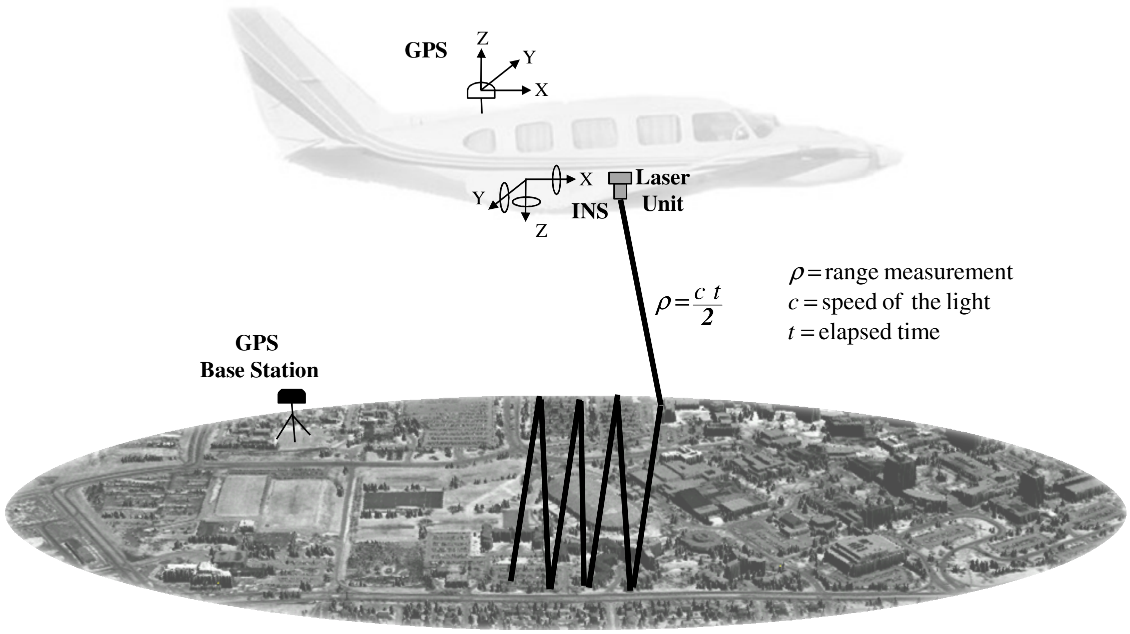

Figure 2.9. Basic LiDAR system components and its operational principles.

Figure 2.10 illustrates the configuration parameters involved in the LiDAR mapping. The swath width of a LiDAR strip depends on the total scan angle and the flying height above ground. The scan frequency defines the number of whole scans per second, while the Pulse Repetition Frequency (PRF) signifies the number of laser pulses emitted per second. Current systems can reach up to 500 kHz of pulse repetition frequency. The limiting factor for the achievement of very high pulse rates is the laser pulse travel time. For instance, for a flying height of 1500m, the laser pulse travel time is approximately 10μs. In such a case, the PRF would have to be less than 100 kHz. The increase in the PRF in current commercial systems is achieved through the use of one of two solutions. The first solution, called as Multiple Pulses in Air (MPiA), consists of emitting the laser pulse without having to wait for the return of the previous pulse, i.e., several pulses can simultaneously travel from the sensor to the mapped object while resolving the ambiguity of the measured range (multi-pulse technology). Such solution is used, for instance, in the Reigl LMS-Q680i system. A more robust solution to overcome the PRF limitation consists of the use of multiple laser sensors. Such systems are known as multi-channel

LiDAR systems. Some of the current systems combine the two solutions to allow for an even higher PRF (e.g., Optech Pegazus 500 kHz).

The density of the collected point cloud will depend on the PRF, the scan frequency, and several other factors such as the flying speed, scan angle, flying height, terrain topography, and surface reflectance properties. The emitted laser beam is not perfectly cylindrical; instead, it has a conical shape since the beam diverges by an angle γ, which is known as the beam divergence angle. The beam divergence angle typically varies from 0.2 to 1.0 mrad (Toth, 2010). The diameter of the footprint will be mainly dependent on the beam divergence angle and flying height. Other factors such as the scan angle of the laser beam and the slope of the terrain will also have an influence on the shape and size of the footprint.

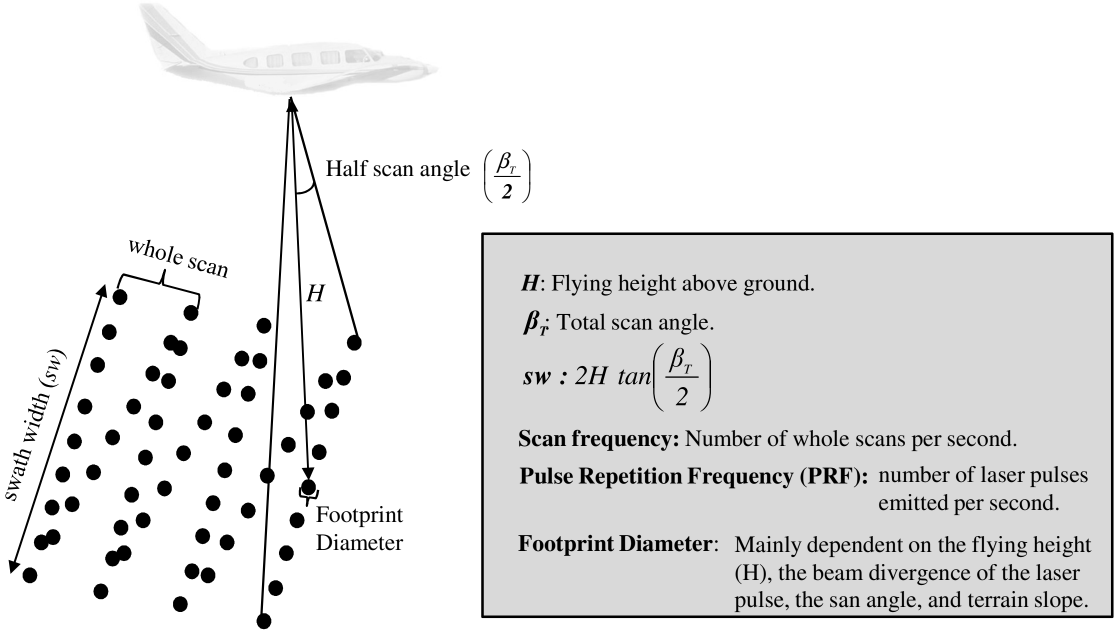

Figure 2.10. Involved configuration parameters in the LiDAR mapping.

In addition to the geometric information (i.e., the 3D coordinates of the mapped points), LiDAR systems also record the intensity (amplitude) of the backscattered signal. Figure 2.11a shows the LiDAR points represented by triangular patches using a Triangular Irregular Network (TIN) generation procedure while Figure 2.11b shows an interpolated image generated using the intensity information of the backscattered signal. Figure 2.11c shows an interpolated image using the elevation and the intensity information.

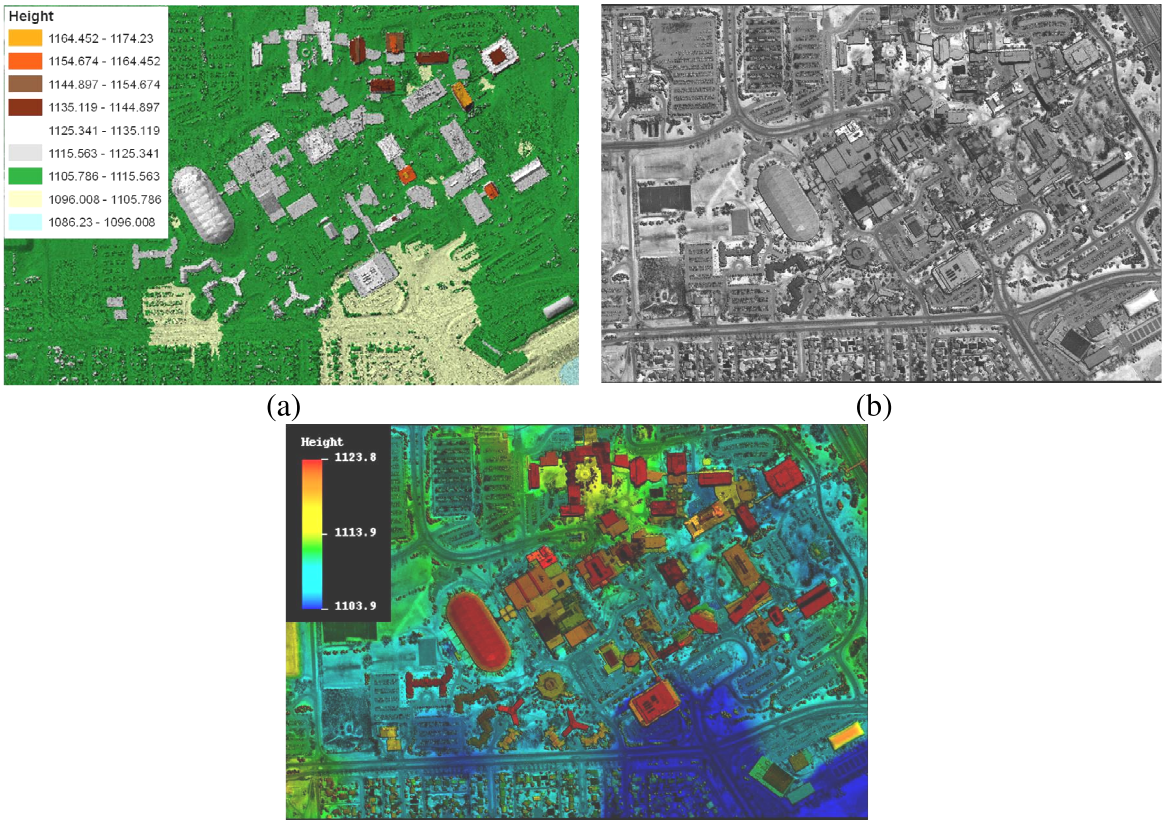

(a) (b)

(c)

Figure 2.11. LiDAR points represented by triangular patches using a Triangular Irregular Network (TIN) generation procedure (a), interpolated image using the intensity information (b), and interpolated image using the intensity and height information (c).

The intensity information can be quite useful for several applications such as land cover classification, change detection, among others. One should note that the amplitude of the backscattered signal is not only affected by the reflectance properties of the mapped surface but it is also affected by atmospheric parameters, energy loss, system parameters such as the range and incidence angle, and by the automatic gain control (for some systems only). Therefore, prior to the use of the intensity values in any particular application an appropriate radiometric calibration/correction must be carried out (Vain et al. 2010). Radiometric calibration/correction has been the subject of study of several authors (e.g., Coren and Sterzai, 2006; Höfle and Pfeifer, 2007; Kaasalainen et al., 2007, Yan et al., 2011).

In its travel path from the laser firing point to the Earth surface, the emitted laser pulse might encounter several objects of different ranges within its diffraction cone that generate individual backscatter returns (echoes). Modern commercial systems are capable of recording up to six echoes for each emitted laser pulse. Moreover, during the last years, a new generation of LiDAR systems, which are able to digitize the signal of the entire backscattered laser pulse, have been developed (Figure 2.12). Such systems are called full waveform systems. One of the benefits from those systems is that the post-processing of the received signal can be used to obtain all individual echoes, i.e., they allow for a higher range resolution than that obtained from the systems' real time pulse detection methods, which typically operate with analog threshold detection (e.g., peak detection, leading edge detection, constant fraction detection) (Jutzi and Stilla, 2003). Therefore, a point cloud with a higher point density can be obtained. Moreover, through the modelling of the received waveforms, besides the amplitude (intensity) of the signal, additional features can be obtained such as the pulse width, which might also be helpful for land-cover classification and object recognition (Wagner et al., 2006; Chauve et al., 2008).

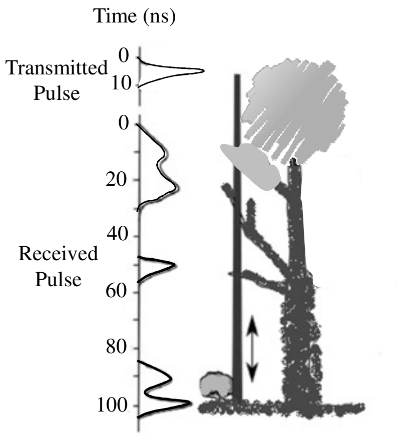

Figure 2.12. Transmitted and received waveform using a small footprint full waveform LiDAR system (Adapted Bretar et al., 2008).

The coordinates of the LiDAR points are computed using the derived measurements from each of the system components as well as the mounting parameters relating such components. The relationship between the LiDAR point coordinates, the system measurements, and parameters is expressed through the LiDAR point positioning equation (Schenk, 2001; El-Sheimy et al., 2005), Equation 2.19. As illustrated in Figure 2.13, the position of the laser point (r_I^m) is derived through the summation of three vectors, $r_b^m(t), r_{lu}^b$, and r_I^{lb}, after applying the appropriate rotation matrices: $R_b^m(t)$, R_{lu}^b, and R_{lb}^{lu}. In this equation, $r_b^m(t)$ is the vector from the origin of the ground reference frame to the origin of the IMU coordinate system, r_{lu}^b $(\Delta X, \Delta Y, \Delta Z)$ – lever arm offset – is the vector from the origin of the IMU coordinate system to the origin of the laser unit coordinate system (defined relative to the IMU body frame), and r_I^{lb} is the laser range vector whose magnitude (ρ) is equivalent to the distance from the laser firing point to its footprint. It should be noted that $r_b^m(t)$ is derived through the GPS/INS integration process while considering the lever arm offset between the IMU body frame and the phase center of the GPS antenna. The term $R_b^m(t)$ stands for the rotation matrix relating the ground and IMU coordinate systems, which is derived through the GPS/INS integration process. The term R_{lu}^b represents the rotation matrix relating the IMU and laser unit coordinate systems, which is defined by the boresight angles $(\Delta\omega, \Delta\varphi, \Delta\kappa)$. The term R_{lb}^{lu} refers to the rotation matrix relating the laser unit and laser beam coordinate systems, which is defined by the mirror scan angle (i.e., the spatial direction of the laser beam w.r.t. the laser unit coordinate system).

$$r_I^m = r_b^m(t) + R_b^m(t) r_{lu}^b + R_b^m(t) R_{lu}^b R_{lb}^{lu} r_I^{lb} \qquad (2.19)$$

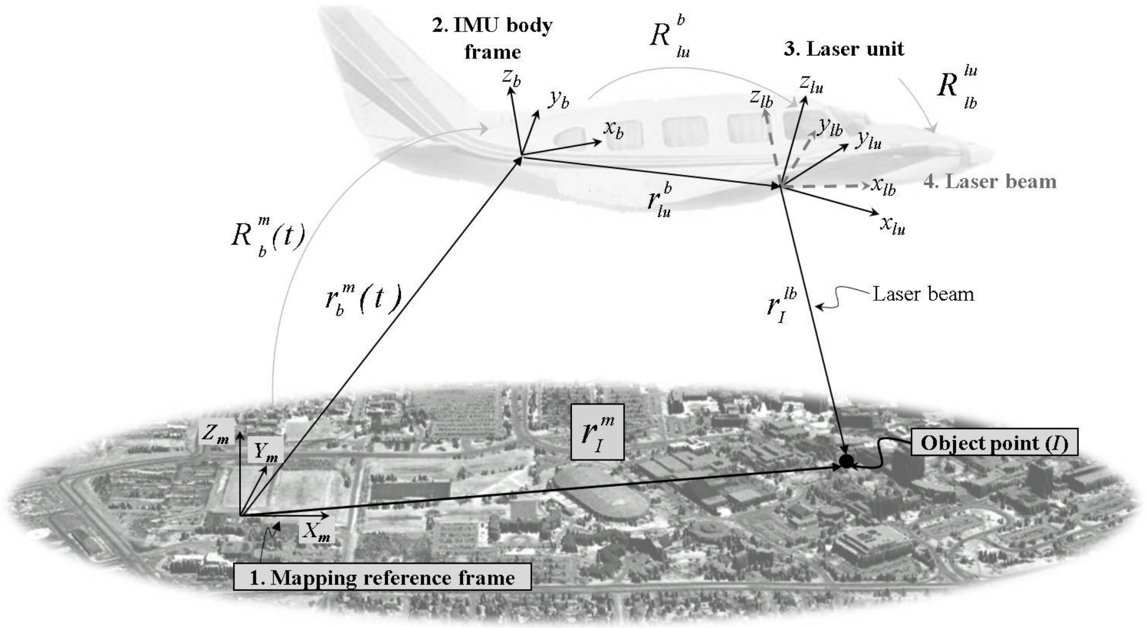

Figure 2.13. Coordinate systems and involved quantities in the LiDAR point positioning equation.

The accuracy of the derived point cloud from a LiDAR system depends on the random and systematic errors in the system measurements and parameters. A detailed description of LiDAR random and systematic errors can be found in Huising and Pereira (1998), Baltsavias (1999), Schenk (2001), Csanyi (2008), and Bang (2010). The magnitude of the random errors depends on the precision of the system's measurements, which include position and orientation information from the GPS/INS unit, mirror angles, and ranges. Systematic errors, on the other hand, are mainly caused by biases in the mounting parameters relating the system components, biases in the system measurements (e.g., ranges and mirror angles), and biases in the GPS/INS-derived position and attitude information. GPS/INS position and orientation errors are mission, strip, or even strip-segment dependent. In contrast, systematic errors in the system parameters (i.e., systematic errors in the mounting parameters, measured ranges, and mirror angles) are global parameters, i.e., not mission, strip or strip-segment dependent. The elimination of the latter systematic errors, in a way that only random errors are left, can be achieved through a calibration procedure, which is discussed in the next section.

2.2.2 LiDAR System Calibration Overview

The LiDAR system calibration is usually accomplished in several steps: (i) Laboratory calibration, (ii) Platform calibration, and (iii) In-flight calibration. In the laboratory calibration, which is conducted by the system manufacturer, the individual system components are calibrated. In addition, the lever arm offset and boresight angles between the laser unit mirror and the IMU as well as the lever arm offset between the IMU and the sensor reference point are determined (Figure 2.14). In the platform calibration, the lever arm offset between the sensor reference point and the GPS antenna is determined (Figure 2.14).

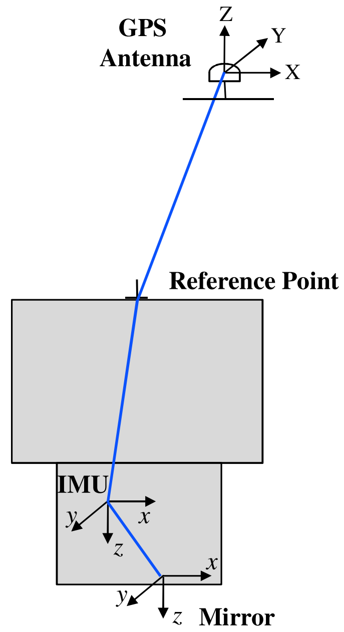

Figure 2.14. Lever arm offsets determined in the laboratory and platform calibrations.

Since the parameters determined in the laboratory and platform calibrations might be biased and/or not stable over time, an in-flight calibration should be carried out to refine such parameters. When the LiDAR systems became commercially available in the late 90's and until very recently, the in-flight methods which have been used by some of the data providers have several drawbacks such as (i) the use of manual and empirical procedures, (ii) time consuming and expensive, (iii) the use of complicated and sequential procedures, and (iv) strong dependence on control surfaces. Moreover, until now there is no commonly accepted methodology since the calibration techniques are usually based on a manufacturer-provided software package and the expertise of the LiDAR data provider. As a result of the non-transparent and sometimes empirical calibration procedures, considerable systematic discrepancies between conjugate surface elements in overlapping strips have been observed in the collected LiDAR data. Besides significantly reducing the accuracy of the point cloud, these discrepancies degrade the homogeneity of the dataset. As a result, the post-processing of the data (i.e., segmentation and classification of the point cloud) is adversely affected. This problem has stimulated extensive research for the development of methods for the elimination/reduction of the impact of systematic errors in the LiDAR system parameters on the derived point cloud in the past few years. A review of existing approaches for the elimination/reduction of the impact of systematic errors in the LiDAR system parameters on the derived point cloud is presented in the next section.

2.2.3 Approaches for Elimination/Reduction of the Impact of Systematic Errors in the LiDAR System Parameters on the Derived Point Cloud

Existing approaches for the elimination/reduction of the impact of systematic errors in the LiDAR system parameters on the derived point cloud have been categorized into two classes depending on the nature of the utilized data: data-driven or system-driven methods. Data-driven methods utilize the LiDAR point cloud coordinates only. They are usually based on arbitrary coordinate transformation model between the laser strip coordinate system and the reference data coordinate system. System-driven methods, on the other hand, utilize the system raw measurements or at least the trajectory (i.e., position and orientation of the platform) and time-tagged point cloud coordinates. Then, such dataset is used in conjunction with the LiDAR geometric model (i.e., the LiDAR point positioning equation) to estimate the biases in the system parameters. In this research work, the term “raw measurements” is used to denote all the involved quantities in the LiDAR equation (i.e., platform position and orientation as well as the measured range and scan angle for each pulse). Clearly, system-driven approaches are the most accurate/appropriate option to eliminate the impact of systematic errors in the LiDAR system parameters on the derived point cloud. The development of data-driven methods (e.g., Kilian et al., 1996; Crombaghs et al., 2000; Kager and Krauss, 2001; Maas, 2002; Filin and Vosselman, 2004) has been motivated by the difficulty in accessing the system raw measurements. Data-driven methods are also known as strip adjustment procedures since they aim at improving the compatibility between overlapping strips by estimating local transformation parameters between the laser strips coordinate system and the reference one. Some of the early data-driven strip adjustment methods aimed at reducing vertical discrepancies only (e.g., Crombaghs et al., 2000; Kager and Krauss, 2001). Such methods are not appropriate since planimetric discrepancies, which have larger magnitude when compared with vertical discrepancies, are not minimized. In Kilian et al. (1996), an adjustment procedure similar to the photogrammetric strip adjustment was introduced for detecting discrepancies and improving the compatibility between overlapping strips. The drawback of this approach is relying on distinct points to relate overlapping LiDAR strips and control surfaces. Due to the irregular nature of the LiDAR points, the identification of distinct points (for example, building corners) is quite difficult and not reliable. More suitable primitives have been suggested by Kager (2004), where planar features are used in the strip adjustment procedure, and in Maas (2002), where a least squares matching procedure is proposed to derive the correspondence between discrete points in one LiDAR strip and TIN patches in the other one. The focus of the method proposed by Maas (2002) relies on detecting the discrepancies between conjugate surface elements rather than improving the compatibility between neighboring strips or analyzing the detected discrepancies. The shortcoming of this work is that simple shifts were used as the transformation function relating conjugate point-patch pairs. The validity of the utilized mathematical model is not completely justified. In Habib et al. (2009) and Habib et al. (2010a), it is demonstrated through mathematical analysis of the LiDAR point positioning equation and through simulations that three shifts and a rotation angle around the flight direction can be used to model the discrepancies between conjugate surface elements in parallel overlapping strips. In Bretar (2004), an alternative methodology for improving the quality of LiDAR data using derived surfaces from photogrammetric procedures is proposed. The main disadvantage, which limits the practicality of this methodology, is relying on having aerial imagery over the same area.

The major drawback of data-driven methods is that the utilized transformation function might not be appropriate depending on the nature of the inherent biases in the LiDAR system parameters and the adopted flight configuration. Recently, Habib et al. (2009) and Bang (2010) have proposed a data-driven method based on a more appropriate mathematical model, which makes use of a simplified LiDAR equation. Different from the previous data-driven strip adjustment procedures, the method proposed by Habib et al. (2009) and Bang (2010) derives an estimate of biases in the system parameters. Therefore, this method can be categorized as a data-driven calibration procedure. The underlying assumptions to simplify the LiDAR equation limit its use to datasets following a strict flight configuration and terrain characteristics; i.e., parallel flight lines acquired by fixed wing platforms (small pitch and roll angles) over an area with moderately varying elevation (i.e., minor terrain elevation variations compared to the flying height above ground).

System-driven (or calibration) methods can be classified as rigorous or quasi-rigorous approaches. Rigorous approaches utilize the system raw measurements (e.g., Filin, 2001; Skaloud and Lichti, 2006; Friess, 2006) while the quasi-rigorous approaches utilize the trajectory and time-tagged point cloud coordinates (Burman, 2000; Toth, 2002; Morin, 2002, Habib et al., 2010b, Bang, 2010) for the estimation of biases in the system parameters with the help of the LiDAR equation. In Filin (2001), natural and man-made control surfaces, represented by a set of planar surfaces, are utilized to determine the system calibration parameters. More specifically, the system parameters are estimated by constraining the LiDAR points to the control surfaces they belong to. Since the initial correspondence might not be correct due to the presence of systematic errors, the method iteratively converges to an accurate estimate of the system parameters. Although this method proposes appropriate primitives and mechanism of using such primitives to deal with the irregular nature of the LiDAR point cloud, it only works if control surfaces are available. The control requirement is circumvented in Burman (2000), Toth (2002), Morin (2002), Skaloud and Lichti (2006), Friess (2006), and Habib et al. (2010b) where the system parameters can be estimated using LiDAR overlapping strips only. It is important to note that not all systematic errors can be detected without control information. For instance, biases in the vertical lever arm offset and range measurements would require control information. The method proposed by Skaloud and Lichti (2006) estimates the calibration parameters by enforcing a group of points to lie on a common plane. The utilized planes are selected manually and its parameters are determined along with the calibration parameters. The drawback of this approach is relying on the availability of large planar patches with varying slopes and aspects, which can be only available in LiDAR data over urban areas. Moreover, the number of unknowns changes with the number of planes used in the calibration procedure. The same shortcomings are associated with the approach proposed by Friess (2006). In spite of the fact that in the method proposed by Friess (2006) the planes are automatically segmented, pre-processing of the LiDAR point cloud may negatively affect the quality of the calibration procedure if the segmentation is not properly implemented. In the work proposed by Morin (2002), point primitives are utilized to establish the correspondence between overlapping strips. Due to the irregular nature of the LiDAR points, the identification of distinct points is quite difficult and not reliable. Moreover, this method relies on the assumption that the average of the coordinates of tie points in overlapping strips corresponds approximately to the ground truth. However, this is not always true depending on the nature of the biases present in the investigated system and the utilized flight configuration. In the calibration methods proposed by Burman (2000) and Toth (2002), only biases in the boresight angles are considered in the calibration procedure. Furthermore, in Burman (2000), the surface model is also considered as an unknown. Therefore, the amount of unknown parameters changes with the extent of the area or the number of primitives being utilized in the calibration procedure. In Toth (2002), the boresight angles are estimated using identified discrepancies between conjugate surface elements in overlapping LiDAR strips. The discrepancies are obtained through a matching procedure that works on interpolated regions. Due to the poor reliability of the matching outcome, the determined planimetric offsets are of low accuracy. Therefore, the estimated biases in the boresight pitch and heading angles have lower accuracy than the boresight roll angle. Such limitations are overcome in the quasi-rigorous method presented in Habib et al. (2010b) and Bang (2010). This method assumes that we are dealing with a linear scanner and that the laser unit is nearly vertical (i.e., small pitch and roll angles). These assumptions lead to a more relaxed data requirement in the sense that only the trajectory position and time-tagged point cloud coordinates are required. This flexibility is quite useful especially in cases where the sequence of the rotation angles defining the system attitude is not provided. However, one should note that for datasets captured by unsteady platforms (e.g., helicopters), where significant pitch and roll angles take place, the quality of the estimated parameters using this procedure might be negatively affected.

With the widespread adoption of LiDAR systems and efforts in developing standards for the delivery of the LiDAR data, it is expected that access to the LiDAR system raw measurements will not be an issue in the near future. Therefore, the implementation of accurate rigorous calibration procedures would benefit not only system manufactures (and some data providers) but the whole LiDAR data user community. One should note that access to the system raw measurements is not the only prerequisite to have a rigorous calibration, which can be easily performed by end-users. A flexible calibration procedure that can be executed without strict requirements (e.g., flight, terrain coverage, control, and preprocessing requirements) and with a high level of automation would also be essential. Moreover, a rigorous analysis of the necessary flight and control configuration requirements for reliable estimation of the system parameters is vital for a successful calibration. Few authors have investigated the necessary flight and control configuration for LiDAR system calibration. A review of some of the existing works in this area is provided in the next section.

2.2.4 Flight and Control Requirements for LiDAR System Calibration

Few authors have discussed the necessary flight and control configuration requirements to perform the calibration of LiDAR systems. Burman (2000) has presented an analytical analysis of the recoverability of the boresight angles, datum shifts, and the elevation and intensity values at the interpolated grid cells, using different configurations. The following configurations were investigated: one LiDAR strip, two LiDAR strips flown in opposite directions, and three LiDAR strips (i.e., two strips in opposite directions and one strip perpendicular to them). The analysis is performed with and without elevation and intensity gradients and with control information. The possibility of the estimation of each of the investigated parameters is analyzed for each scenario. The final recommended flight configuration, to give enough redundancy, consists of four strips flown in opposite and in cross direction (Figure 2.15) along with control information.

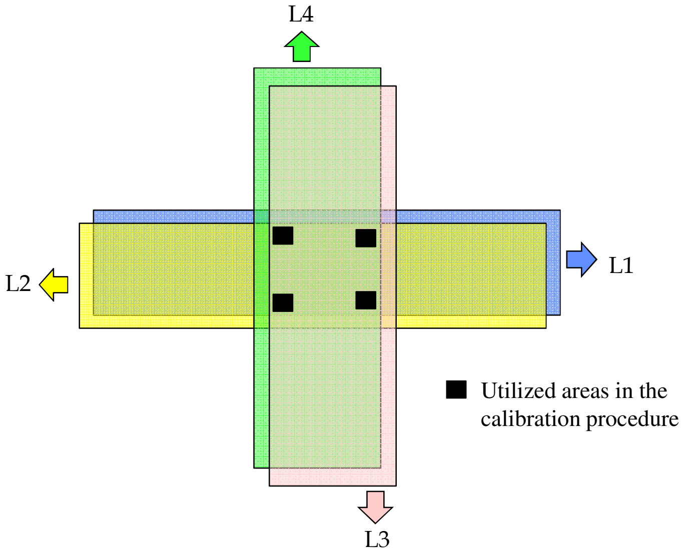

Figure 2.15. Recommended flight configuration for the LiDAR system calibration by Burman (2000) (Adapted Burman, 2000).

The use of a calibration site with sloped terrain as well as the selection of regions close to the edges of the strips for the calibration procedure is suggested by Burman (2000). In the performed analysis, high correlation among the parameters was still observed, e.g., the vertical datum shift and the elevation values at the grid cells, due to the nature of the proposed calibration procedure (the primitives are considered unknowns). The recoverability of the lever arm offset and systematic errors in the measured range and scan angle is not investigated.

The flight configuration suggested by Morin (2002) was devised for the recoverability of the boresight angles and the scale factor in the measured mirror angle while considering a flat calibration site. It is also based on the assumption that tie points can be identified in overlapping strips. The recommended flight configuration is illustrated in Figure 2.16. The different flying heights were recommended to recover the boresight pitch angle. A bias in the boresight pitch angle ($\delta\Delta\omega$) cause a vertical discrepancy (Δh) between overlapping strips flown at different flying heights as shown in Equation 2.20 (Morin, 2002). One should note that for small values of $\delta\Delta\omega$ the vertical discrepancy will be very small, which might affect the reliability of the estimated parameter.

$$\Delta h = (H_1 - H_2)\left(\frac{1}{cos\delta\Delta\omega} - 1\right) \tag{2.20}$$

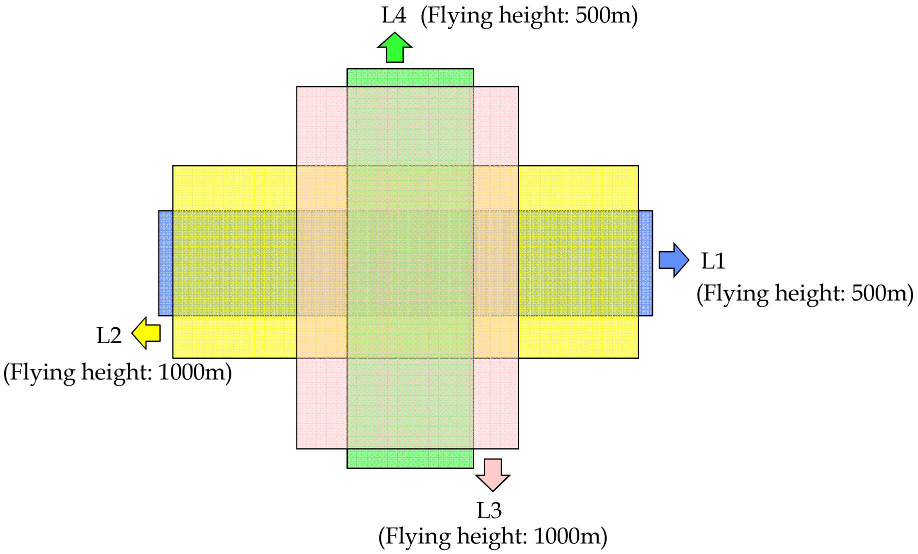

Figure 2.16. Recommended flight configuration for the LiDAR system calibration Morin (2002) (Adapted Morin, 2002).

Filin (2001) provides an analytical analysis of the terrain geometry, i.e., the surface slopes and aspects, to investigate how they affect the recoverability of the estimated parameters. However, the flight configuration has not been investigated.

CHAPTER 3

SYSTEM PARAMETERS INVOLVED IN THE CALIBRATION OF PHOTOGRAMMETRIC AND LIDAR SYSTEMS

3.1 Introduction

The calibration process aims at estimating the system parameters. For a multi-sensor system, the system parameters entail the parameters associated with the individual system components, which are determined in the individual sensor calibration, as well as the mounting parameters relating such components. The individual sensor calibration involves the calibration of the imaging sensors, i.e., the camera (for a photogrammetric system) and the laser unit (for a LiDAR system), as well as the calibration of the navigation sensors (GPS antenna and INS). The calibration of the navigation sensors goes beyond the scope of this dissertation, and therefore will not be discussed. The camera parameters involve the principal distance, the principal point coordinates, and the distortion parameters that compensate for the deviation from the collinearity assumption. The laser unit parameters, on the other hand, include errors in the ranging and scanning components.

Adequate selection of the system parameters, which are the outcome of an error modeling, is crucial for a successful system calibration. Insufficient or over-parameterized models should be avoided since they might have adverse impact on the quality of the estimated system parameters and the quality of the reconstruction outcome. There exist numerous sources of errors that might affect the performance of the system’s imaging sensors. This doesn’t mean that all these errors should be included in the error model. For instance, if two individual errors have the same impact for whatever data acquisition configuration is used, such errors are totally dependent (i.e., 100% correlated) and therefore cannot be estimated separately. On the other hand, if an insufficient error model is used, systematic errors in the calibrated data will still be present.

The following subsections will describe the system parameters involved in the calibration process of photogrammetric and LiDAR systems that will be investigated in this research. Moreover, a methodology for determining the adequate distortion model for the calibration of MFDCs will be proposed.

3.2 Photogrammetric System Parameters

The parameters of GPS/INS-assisted photogrammetric systems are illustrated in Table 3.1. They include the camera IOP and the mounting parameters relating the camera coordinate system and the IMU body frame. Approximate (nominal) values for the boresight angles $\Delta\omega, \Delta\varphi$, and $\Delta\kappa$ relating the camera coordinate system and the IMU body frame are known from the mechanical alignment while initial values for the lever arm offset components $\Delta X, \Delta Y$, and ΔZ can be obtained through field surveying. Such parameters are usually provided by the system manufacturer. These approximate values should be then refined in the photogrammetric system calibration. For multi-camera systems, the mounting parameters involve besides the lever arm offset and boresight angles relating the cameras and the IMU body frame, the ROP among the cameras.

Table 3.1. Photogrammetric system parameters.

Camera Parameters (IOP)	Mounting Parameters	
	Single-Camera System	Multi-Camera System
Principal point coordinates Principal distance Distortion parameters	Lever arm offset and boresight angles relating the camera coordinate system and the IMU body frame	Lever arm offset and boresight angles relating the cameras coordinate systems and the IMU body frame as well as the ROP among the cameras (these two sets of parameters are not independent)

The camera IOP comprises the principal distance (c) and the principal point coordinates (x_p and y_p), which define the coordinates of the perspective center relative to the camera coordinate system, along with the distortion model parameters. A distortion model is the mathematical representation of the corrections that compensate for various deviations from the assumed collinearity condition. There exist several variations of the distortion models that can be used to model inherent distortions such as the Brown-Conrady model (Brown, 1966; Brown 1971) (Equations 3.1a and 3.1b) and the USGS Simultaneous Multi-frame Analytical Calibration (SMAC) model (USGS, 2008) (Equations 3.2a and 3.2b). In Habib et al. (2008), the equivalency between these distortion models has been tested. In this research work, the Brown-Conrady distortion model (Equations 3.1a and 3.1b) will be used.

$$\Delta_x = K_1(r^2 - R_o^2)\bar{x} + K_2(r^4 - R_o^4)\bar{x} + P_1(r^2 + 2\bar{x}^2) + 2P_2\bar{x}\bar{y} - A_1\bar{x} + A_2\bar{y} \tag{3.1a}$$

$$\Delta_y = K_1(r^2 - R_o^2)\bar{y} + K_2(r^4 - R_o^4)\bar{y} + P_2(r^2 + 2\bar{y}^2) + 2P_1\bar{x}\bar{y} + A_1\bar{y} \tag{3.1b}$$

where:

- $\bar{x} = x - x_p$ and $\bar{y} = y - y_p$ are the image coordinates reduced to the principal point,
- $r = \sqrt{(x - x_p)^2 + (y - y_p)^2}$ is the radial distance between the point in question and the principal point,
- K_1 and K_2 are the radial lens distortion parameters,
- R_o is a camera-specific constant,
- P_1 and P_2 are the de-centering lens distortion parameters, and
- A_1 and A_2 are the affine deformation parameters.

$$\Delta_x = \bar{x}(K_0 + K_1 r^2 + K_2 r^4 + K_3 r^6) + (1 + P_3 r^2)[P_1(r^2 + 2\bar{x}^2) + 2P_2\bar{x}\bar{y}] \tag{3.2a}$$

$$\Delta_y = \bar{y}(K_0 + K_1 r^2 + K_2 r^4 + K_3 r^6) + (1 + P_3 r^2)[2P_1\bar{x}\bar{y} + P_2(r^2 + 2\bar{y}^2)] \tag{3.2b}$$

where:

- $\bar{x} = x - x_p$ and $\bar{y} = y - y_p$ are the image coordinates reduced to the principal point,

- $r = \sqrt{(x - x_p)^2 + (y - y_p)^2}$ is the radial distance between the point in question and the principal point,
- K_0 , K_1 , K_2, and K_3 are the radial lens distortion parameters,
- P_1 , P_2 , and P_3 are the de-centering lens distortion parameters, and

The camera IOP are determined through a camera calibration process. As already mentioned, methods for camera calibration can be categorized into two groups: laboratory and analytical calibrations methods. The analytical camera calibration might involve an indoor calibration or an in-situ calibration under operational conditions. For airborne systems, due to variations in the external conditions (such as pressure, temperature, humidity, among others), some of the calibration parameters determined through a laboratory or indoor procedure might experience variations under operational conditions (Merchant, 2004). The importance of refining the camera calibration parameters during the in-flight system calibration has been highlighted by several authors (Jacobsen, 2001; Wegmann, 2002; Jacobsen, 2003; Honkavaara et al., 2003; Honkavaara et al., 2004). One of the conclusions and recommendations of the OEEPE test (Heipke et al., 2002) is that the interior orientation parameters should be included in the system calibration whenever possible. The principal distance and the principal point coordinates are the parameters most susceptible to variations while the camera inherent distortions are usually stable over longer time (Jacobsen, 2003). One should note that in direct sensor orientation, errors in the principal point coordinates and in the principal distance cannot be compensated by the EOP.

Most of current photogrammetric mapping systems are mainly relying on metric large-format analog or digital cameras that have been specifically designed for this purpose. The calibration of metric large format analog cameras is usually established by a certified government agency (e.g., the USGS in USA or NRCan in Canada) through a laboratory calibration. In contrast to the standard analogue cameras, the calibration process for digital cameras is a more complex task. The difficulty is attributed to the large variety of camera designs available in the market, which would demand different facilities and calibration approaches. This is not critical for large format digital cameras that are specifically built for mapping applications. For these cameras, the calibration process is conducted by the system manufacturer (e.g., Leica or Z/I). This is not the case for MFDCs, which are not manufactured for photogrammetric purposes and have been increasingly used in photogrammetric activities, especially in conjunction with LiDAR systems and in smaller coverage flight blocks. This scenario has been stimulated by the reduced cost and improved resolution associated with this type of camera. Due to the wide spectrum of existing designs for MFDCs coupled with the large number of this type of camera in use by the photogrammetric community, it has become more practical for the data providers to perform their own calibrations and stability analysis of the utilized cameras. As such, the camera calibration task has been shifted to the hands of the mapping data providers. The crucial step when designing an indoor camera calibration procedure for a MFDC is the selection of the appropriate distortion model and the investigation of the adequacy of such model. This is especially critical for direct sensor orientation. In contrast to the traditional indirect geo-referencing procedure, errors in the distortion parameters cannot be fully or partially compensated by the EOP in the direct sensor orientation. Moreover, inappropriate distortion model will negatively affect the estimation of the mounting parameters. This in turn will affect the quality of the object space reconstruction (this hypothesis will be tested/verified in the experimental results section). In this research work, a methodology for evaluating the distortion model adequacy for MFDCs is introduced. The proposed methodology is described in the following subsection.

3.2.1 Distortion Model Adequacy

An adequate distortion model has the minimum number of distortion parameters needed to sufficiently describe the inherent distortions in the implemented camera. Insufficient and over-parameterized distortion models should be avoided since they will have an adverse effect on the system mounting parameters calibration as well as on the reconstructed object space. The adequacy of a model with a set of parameters can be carried out by adding one parameter at a time until the minimum number of parameters that is capable of properly representing the phenomenon under investigation is determined. In this work, the adequacy of the distortion model is evaluated by incrementally increasing the model parameters while checking:

I. The outcome of the bundle adjustment with self-calibration procedure: A reduction in the a-posteriori variance factor (which represents the quality of fit between the observations and estimated parameters as represented by the mathematical model) indicates a transition from an insufficient distortion model to a better one. On the other hand, insignificant change in the a-posteriori variance factor indicates a transition from an adequate distortion model to an over-parameterized one. In terms of the accuracy of the estimated distortion parameters, poor accuracy should be expected for insufficient and over-parameterized models. In addition, higher correlations among the elements of the IOP and EOP are expected for over-parameterized models.

II. Analysis of the bundle similarity: The bundles defined by each of the distortion models will be checked for similarity. For that purpose, bundle similarity methods previously used for camera stability analysis will be employed (Habib et al., 2006). Three bundle similarity methods will be utilized in this work: the Zero Rotation (ZROT), Rotation (ROT), and Single Photo Resection (SPR) methods. The ZROT and ROT procedures evaluate the similarity between the shapes of the defined bundles. The main difference is that the ZROT procedure evaluates the degree of similarity between the defined bundles while sharing the same position and orientation in space. The drawback of the ZROT method is that correlations between the IOP and EOP are not considered. The SPR procedure, on the other hand, does not evaluate the degree of similarity between the shapes of the involved bundles. It just evaluates the quality of fit between these bundles at a given object space (for specific flight height and terrain height variation). In the SPR procedures, the bundles are allowed to freely shift and rotate in space to assure the best fit at the given object space. The ROT procedure is the most suitable bundle similarity method. It evaluates the similarity of the bundles while sharing only the same position in space. In other words, the ROT procedure allows for relative rotations between the two bundles to assure the best similarity possible. To evaluate the degree of similarity between two defined bundles, a similarity measure ($\text{RMSE}_{\text{offset}}$) value is computed. The $\text{RMSE}_{\text{offset}}$ is a global measure that describes the average offset along the image plane between conjugate light rays in two bundles, which are derived from two IOP sets (Figure 3.1). The two bundles are deemed similar if the computed $\text{RMSE}_{\text{offset}}$ is within the range defined by the expected standard deviation of the image coordinate measurements (i.e., 1/2 pixel). For details on how the $\text{RMSE}_{\text{offset}}$ is computed in each of the bundle similarity methods, interested readers can refer to Habib et al. (2006) and Habib et al. (2008). The adequacy of the distortion model using the bundle similarity methods will be checked as follows:

a. The transition from insufficient to adequate models should be manifested in a change in the shape of the reconstructed bundles.

b. The transition from adequate to over-parameterized models should be manifested in having bundles with similar shapes.

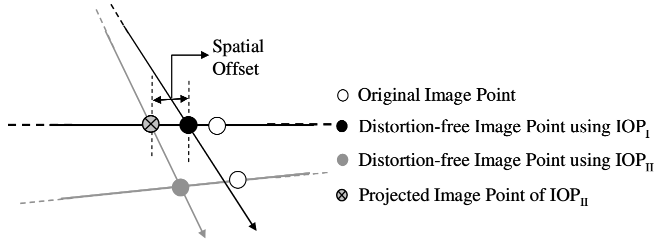

Figure 3.1. Illustration of how the spatial offset is computed in the image space between two bundles defined by two different calibration datasets.

III. Verification of the adequate model through system calibration: the adequate model according to 1) and 2) will be verified/confirmed by analyzing the validity of the estimated lever arm offset, i.e., the proximity of the physically measured lever arm offset to the estimated one in the system calibration.

3.3 LiDAR System Parameters

The LiDAR system parameters include parameters associated with the laser unit measurements as well as the mounting parameters (i.e., the lever arm offset and boresight angles relating the laser unit and the IMU body frame). As for GPS/INS-assisted photogrammetric systems, initial (nominal values) for the boresight angles $\Delta\omega, \Delta\varphi,$ and $\Delta\kappa$ are known from the mechanical alignment while initial values for the lever arm offset components $\Delta X, \Delta Y,$ and ΔZ can be obtained through field surveying. Such parameters are usually provided by the system manufacturer. These initial values should be then refined during the in-flight LiDAR system calibration along with the parameters associated with the laser unit measurements.

As already mentioned, the laser unit comprises a ranging and a scanning unit. The ranging component measures the ranges (distance from the laser firing point to the laser footprint) while the scanning unit provides the spatial direction of the laser beam with respect to the laser unit coordinate system. There are several sources that can lead to errors in the range measurements (Baltsavias, 1999). Although complex, the contribution of range errors to 3D coordinate errors is the minimum among the major error sources (Baltsavias, 1999). The systematic error in the range measurements have been satisfactorily explained by a constant bias $(\Delta\rho)$ (Filin, 2001; Shenk, 2001; Skaloud and Litchi, 2006; Csany, 2008).

Systematic errors in the measured scan angles can be caused by an index error, i.e., the "0" direction and the vertical axis may not coincide (Shenk, 2001). The index error and some other possible errors sources (errors in the scan plane and in the scan angle) are discussed in Shenk (2001). Such errors translates to angular biases, which will have the same impact as the boresight angles regardless of the flight configuration and terrain topography, and therefore, cannot be simultaneously included in the error model. A more significant error, which will be investigated in this research work, is a scale factor (S) in the measured angles also known as “smiley error” due to its non-linear impact on the vertical coordinates (Morin, 2002; Optech, 2002; Csany, 2008). Table 3.2 presents the LiDAR system parameters, which will be investigated in this research work.

Table 3.2. LiDAR system parameters.

Laser Unit Systematic Errors	Mounting Parameters
Constant bias in the range Scale in the mirror scan angle	Lever arm offset and boresight angles relating the laser unit and the IMU body frame

Equation 3.3 shows the LiDAR point positioning equation now with all the considered system parameters: $\Delta X, \Delta Y, \Delta Z, \Delta\omega, \Delta\varphi, \Delta\kappa, \Delta\rho,$ and S. Note that Equation 3.3 assumes that we are dealing with a linear scanner (only one scan angle) and that the *y*-axis of the laser unit coordinate system, which considers the convention right-forward-up, is aligned along the flying direction (refer to Figure 3.2 for the definition of the laser unit and laser beam coordinate systems). In the next chapter, the optimum flight and control configuration requirements for the estimation of such parameters are investigated.

$$r_I^m = r_b^m + R_b^m(t) r_{lu}^b + R_b^m(t) R_{lu}^b R_{lb}^{lu} r_I^{lb} \tag{3.3}$$

where:

- $R_{lb}^{lu} = \begin{bmatrix} cos\,S\beta & 0 & sin\,S\beta \\ 0 & 1 & 0 \\ -sin\,S\beta & 0 & cos\,S\beta \end{bmatrix}$; and
- $r_I^{lb} = \begin{bmatrix} 0 \\ 0 \\ -(\rho + \Delta\rho) \end{bmatrix}$.

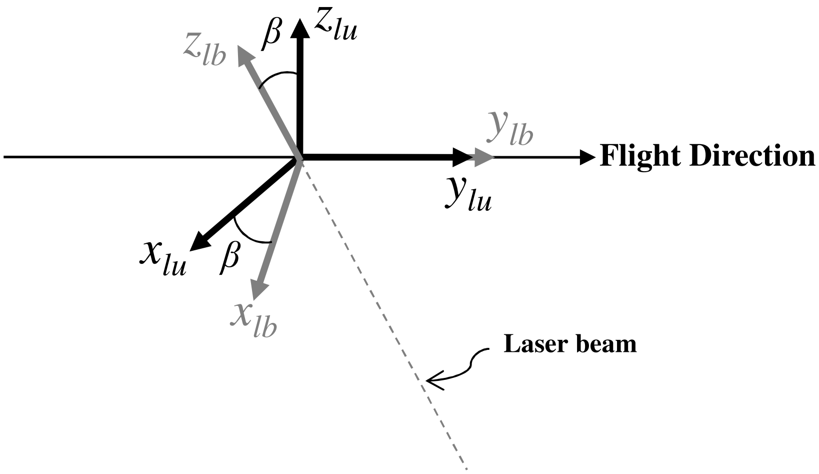

Figure 3.2. Definition of the laser unit and the laser beam coordinate systems.

3.4 Summary

The contributions to the research objectives presented in this chapter as well as the hypothesis that will be tested/verified in the experimental results chapter are listed below:

- Photogrammetric Systems:
  - Contribution: Methodology for determining the adequacy of the distortion model based on the analysis of the outcome from the bundle adjustment with self-calibration and bundle similarity methods previously developed for camera stability analysis.
  - Hypothesis: Inappropriate distortion model will negatively affect the estimation of the mounting parameters. This in turn will affect the quality of the object space reconstruction (this hypothesis will be tested/verified in Chapter 7 with experimental results using a real dataset). On the other hand, inaccurate estimates of the principal point coordinates and principal distance will be refined through the proposed in-flight/in-situ system calibration procedure (since they are susceptible to changes under operational conditions).

- LiDAR systems:
    - Contribution: A review of the system parameters commonly employed in previous research work have been presented.
    - Hypothesis: It is hypothesized that it is possible to devise a flight/control configuration to simultaneously and reliably estimate all these parameters.

CHAPTER 4

ANALYSIS OF FLIGHT AND CONTROL REQUIREMENTS FOR THE CALIBRATION OF AIRBORNE GPS/INS-ASSISTED SINGLE-CAMERA PHOTOGRAMMETRIC AND LIDAR SYSTEMS

4.1 Introduction

A cost-effective, reliable, practical, and accurate in-flight system calibration for the estimation of the photogrammetric and LiDAR system parameters requires a rigorous analysis of the optimum flight and control requirements. In this research work, such analysis is carried out for airborne GPS/INS-assisted vertical single-camera photogrammetric and airborne vertical LiDAR systems since these represent the most critical/weak geometry. The devised flight/control configuration for such systems will be sufficient for systems with stronger geometry (e.g., airborne oblique multi-camera systems and airborne oblique LiDAR systems). In this research work, the term “optimum” for flight and control requirements means:

- Minimum number of flight lines for accurate/reliable estimation of the parameters. In other words, the minimum flight configuration (e.g., flight pattern, flight height, overlap percentage) that maximizes the impact of biases in the system parameters on the derived point cloud and decouples correlated parameters.
- Minimum control for accurate/reliable estimation of the parameters.

By rigorous analysis, it is meant that it is based on the rigorous mathematical model for the point positioning process. The rationale/conceptual basis behind the proposed rigorous analysis to devise the optimum flight configuration requiring minimum control is as follows:

I. Check whether inaccurate/biased parameters would have an impact on the reconstruction process. For instance, photogrammetric object space reconstruction is obtained through the intersection of conjugate light rays from overlapping imagery. Therefore, a rigorous analysis for photogrammetric systems should first check whether conjugate light would intersect, i.e., check whether *y*-parallax would be introduced in the presence of biases in the system parameters.

   - If that is the case, the system parameters can be estimated by minimizing their impact on the reconstruction process.

II. Check whether inaccurate/biased parameters would lead to biases in the derived object points, whose magnitudes and directions depend on the flight configuration. One can devise a flight configuration that maximizes the impact of biases in the system parameters on the derived object space.

   - If that is the case, using the devised configuration, the system parameters can be estimated while reducing the discrepancy among the derived object points from different flight lines (i.e., achieving the best precision of the derived object points).

III. Finally, for the system parameters, which will not have an impact on the reconstruction process or will not cause discrepancies between reconstructed points from different flight lines in a given flight configuration, control points will be required to estimate such parameters.

   - If that is the case, the system parameters can be estimated while reducing the discrepancy among the derived object points and the control data (i.e., achieving the best accuracy of the derived object points).

In the next subsections, the proposed analyses for photogrammetric and LiDAR systems are presented.

4.2 Flight and Control Requirements: GPS/INS-Assisted Photogrammetric Systems

In this section, the proposed rigorous analysis of flight and control requirements for the calibration of airborne GPS/INS-assisted vertical single-camera photogrammetric systems is presented. The conceptual basis/rationale behind the proposed rigorous analysis has been presented in section 4.1 and is now explicitly discussed for photogrammetric systems:

I. Impact on the reconstruction process: If the photogrammetric system is properly calibrated and geo-referenced, conjugate light rays should intersect (i.e., no *y*-parallax is introduced). Therefore, a rigorous analysis should first check whether biases in the system parameters will introduce *y*-parallax. If that is the case, the system parameters can be estimated through the elimination/minimization of the *y*-parallax among conjugate light rays in stereo-imagery (Figure 4.1a). Parameters falling in this category would affect the precision of the reconstructed photogrammetric model. Such parameters can be estimated using a stereo-image pair without the need for any ground control points. In the literature, the parallax, which contributes towards the parameter estimation, is usually referred to as "*y*-parallax" due to the fact that the *x*-direction of the camera coordinate system is usually defined along the baseline direction. One should note that, although here forth the parallax contributing towards the parameters' estimation will be denoted as "*y*-parallax", the baseline might not be always aligned along the *x*-axis.

II. Impact on the precision of the object space reconstructed from different flight lines: If the photogrammetric system is properly calibrated and geo-referenced, conjugate surface elements from different flight lines should coincide with each other (regardless of the flight direction/configuration). Therefore, one should analyze whether inaccurate/biased parameters would lead to biases in the derived object points, whose magnitudes and directions depend on the flight configuration. In such a case, one can devise a flight configuration that maximizes the impact of biases in the system mounting parameters on the derived object space. Therefore, using such a configuration, the system parameters can be estimated while reducing the discrepancy among the derived object points from the overlapping imagery (i.e., achieving the best precision of the derived object points) from different flight lines (Figure 4.1b). The parameters falling in this category can be estimated without the need for any ground control points.

III. Impact on the accuracy of the reconstructed object space: If the photogrammetric system is properly calibrated and geo-referenced, conjugate surface elements from different flight lines should coincide with the ground truth (control surface). For biased system parameters, which will not introduce *y*-parallax between conjugate light rays or discrepancies between derived points from different flight lines in a given flight configuration, control points will be utilized to estimate such parameters. In other words, the parameters falling in this category will be estimated while reducing the discrepancy between the derived object space from the directly geo-referenced imagery and the provided control (i.e., achieving the best accuracy of the derived object points) (Figure 4.1c).

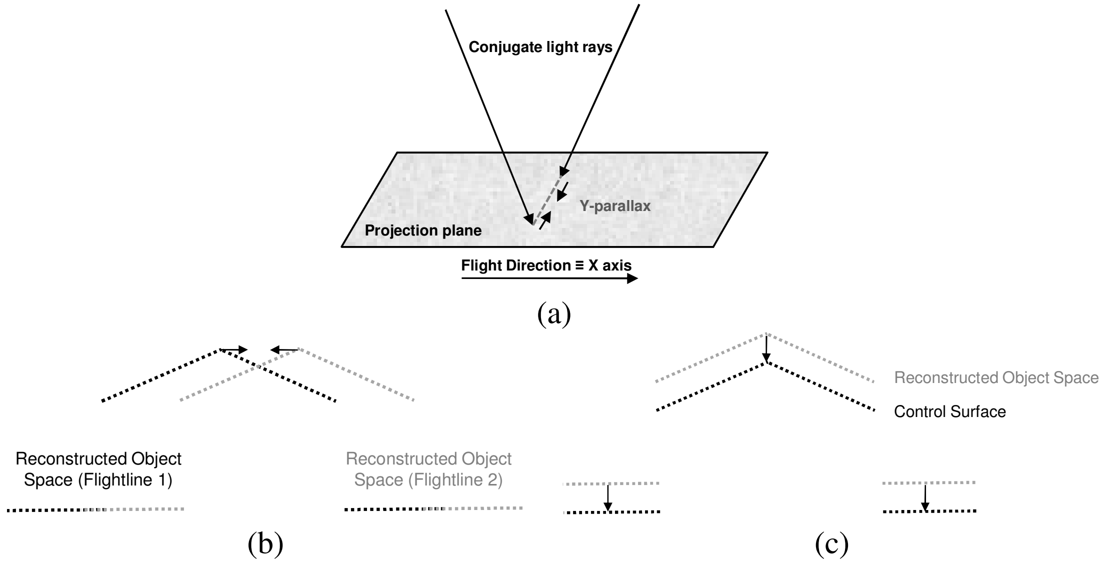

Figure 4.1. Estimation of the system parameters through minimization of the *y*-parallax (a), minimization of the discrepancy among the derived object points from different flight lines (b), and minimization of the discrepancy among photogrammetric and control surfaces (c).

Two mathematical analyses are introduced in this research work. The first analysis investigates which biased system parameters under different flight configurations would introduce *y*-parallax (i.e., impact on the reconstruction process). This analysis is presented first since it would lead to the most cost-effective/practical calibration (theoretically, the calibration can be conducted using stereo-imagery). The second analysis is restricted to stereo-pairs from the same flight line for the *y*-parallax analysis but allows for the investigation of the impact of biases in the system parameters on the reconstructed object space. In other words, the second analysis allows for the analysis of the impact of biased system parameters on the reconstruction process as well as on the reconstructed object space (precision and accuracy). The mathematical analysis is verified through a simulation process. In the simulation process, biases are added to the system parameters, which are used to reconstruct the surface using an intersection procedure. To check whether the biases in the system parameters will have an impact on the reconstruction process (i.e., whether *y*-parallax is introduced) the precision of the photogrammetric model produced by a stereo-pair is analysed. On the other hand, the differences between the bias-contaminated and true coordinates of the reconstructed points from different flight lines are used to represent the impact of a given bias in the system parameters on the reconstructed object space. The two proposed analyses are presented in the next subsections.

4.2.1 First Proposed Analysis (impact on the reconstruction process under different flight configurations)

The objective of the first analysis is to determine which biased system parameters will introduce *y*-parallax under different flight configurations. The analysis is built on the concept that biases in the system parameters, which cause variation in the spatial offset and/or rotational offset matrix relating two camera stations (i.e., camera position and orientation at two different epochs – t_1 and t_2), will introduce *y*-parallax while assuming a properly geo-referenced system. One should note that the components of the variations in the spatial offset, which will introduce *y*-parallax, are the ones not aligned along the baseline connecting the two camera stations in question. Also, any variation in the elements of the rotational offset matrix relating the two camera stations will introduce *y*-parallax.

The assumptions considered in the proposed analysis are as follows: (i) The mathematical derivations consider the convention right-forward-up (right-handed) for the camera, IMU, and ground coordinate systems; (ii) The *x*-axes of the camera and IMU coordinate systems are aligned along the flight direction; (iii) The ground coordinate system (mapping frame) is defined parallel to the IMU body frame at time t_1; (iv) The camera coordinate system is considered almost parallel to the IMU coordinate system (i.e., small boresight angles are considered); and (v) In the mathematical derivation, the variations in the spatial offset and rotational offset matrix will be defined w.r.t the camera coordinate system of the first camera station (i.e., c_1).

The EOP of the camera stations, i.e., the position and orientation of the camera station c_1 $(r_{c_1}^m, R_{c_1}^m)$ and camera station c_2 $(r_{c_2}^m, R_{c_2}^m)$, can be expressed by Equations 4.1 and 4.2, respectively (see Figure 4.2).

$$r_{c_1}^m = r_{b_1}^m + R_{b_1}^m r_c^b = r_{b_1}^m + R_{b_1}^m \begin{bmatrix} \Delta X \\ \Delta Y \\ \Delta Z \end{bmatrix} \tag{4.1a}$$

$$R_{c_1}^m = R_{b_1}^m R_c^b = R_{b_1}^m \begin{bmatrix} 1 & -\Delta\kappa & \Delta\varphi \\ \Delta\kappa & 1 & -\Delta\omega \\ -\Delta\varphi & \Delta\omega & 1 \end{bmatrix} \tag{4.1b}$$

$$r_{c_2}^m = r_{b_2}^m + R_{b_2}^m r_c^b = r_{b_2}^m + R_{b_2}^m \begin{bmatrix} \Delta X \\ \Delta Y \\ \Delta Z \end{bmatrix} \tag{4.2a}$$

$$R_{c_2}^m = R_{b_2}^m R_c^b = R_{b_2}^m \begin{bmatrix} 1 & -\Delta\kappa & \Delta\varphi \\ \Delta\kappa & 1 & -\Delta\omega \\ -\Delta\varphi & \Delta\omega & 1 \end{bmatrix} \tag{4.2b}$$

where:

- $r_{c_1}^m$ and $r_{c_2}^m$: vectors from the origin of the ground coordinate system (mapping frame) to the camera perspective center at times t_1 and t_2, respectively;
- $R_{c_1}^m$ and $R_{c_2}^m$: rotation matrix relating the ground and the camera coordinate systems at times t_1 and t_2, respectively;
- $r_{b_1}^m$ and $r_{b_2}^m$: vectors from the origin of the ground coordinate system to the origin of the IMU coordinate system at times t_1 and t_2, respectively (derived through the GPS/INS integration process);

- $R_{b_1}^{m}$ and $R_{b_2}^{m}$: rotation matrices relating the ground and IMU coordinate systems at times t_1 and t_2, respectively (derived through the GPS/INS integration process);
- $r_c^b = \begin{bmatrix} \Delta X \\ \Delta Y \\ \Delta Z \end{bmatrix}$ lever arm offset relating the camera and the IMU coordinate systems (defined relative to the IMU body frame);
- $R_c^b = \begin{bmatrix} 1 & -\Delta\kappa & \Delta\varphi \\ \Delta\kappa & 1 & -\Delta\omega \\ -\Delta\varphi & \Delta\omega & 1 \end{bmatrix}$: rotation matrix (boresight matrix) relating the camera and the IMU coordinate systems, defined by the boresight roll ($\Delta\omega$), pitch ($\Delta\varphi$) and yaw ($\Delta\kappa$) angles.

The spatial offset $r_{c_2}^{c_1}$ and the rotational offset matrix $R_{c_2}^{c_1}$ (illustrated in Figure 4.2) relating the camera coordinate systems of camera stations at times t_1 and t_2 (i.e., c_1 and c_2) are defined by Equations 4.3 and 4.4, respectively.

$$r_{c_2}^{c_1} = R_m^{c_1}\left(r_{c_2}^{m} - r_{c_1}^{m}\right) \tag{4.3}$$

$$R_{c_2}^{c_1} = R_m^{c_1} R_{c_2}^{m} \tag{4.4}$$

By substituting the EOP of the camera stations c_1 and c_2, as defined in Equations 4.1a, 4.1b, and 4.2a, in Equation 4.3 one can get the form in Equation 4.5 for the spatial offset relating the two camera stations. Similarly, by substituting the terms $R_m^{c_1}$ and $R_{c_2}^{m}$ as defined in Equations 4.1b and 4.2b, in Equation 4.4 one can get the form in Equation 4.6 for the rotational offset relating the two camera stations.

$$r_{c_2}^{c_1} = R_m^{c_1}\left[r_{b_2}^{m} + R_{b_2}^{m} r_c^b - r_{b_1}^{m} - R_{b_1}^{m} r_c^b\right] = R_b^c R_m^{b_1}\left[r_{b_2}^{m} - r_{b_1}^{m} + \left(R_{b_2}^{m} - R_{b_1}^{m}\right) r_c^b\right] \tag{4.5}$$

$$R_{c_2}^{c_1} = R_b^c R_m^{b_1} R_{b_2}^{m} R_c^b \tag{4.6}$$

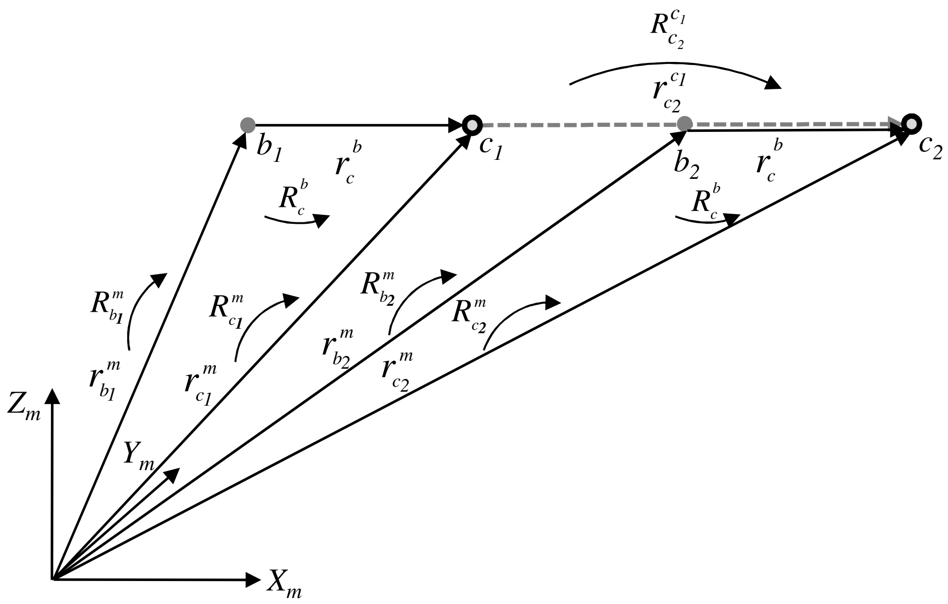

Figure 4.2. Spatial offset ($r_{c_2}^{c_1}$) and rotational offset matrix ($R_{c_2}^{c_1}$) relating two camera stations (c_1 and c_2).

In order to investigate which biases in the system parameters will cause variation in the spatial offset and/or in the rotational offset matrix relating two camera stations (i.e., $r_{c_2}^{c_1}$ and $R_{c_2}^{c_1}$), the spatial offset and the rotational offset matrix relating the two cameras stations will be differentiated with respect to the system parameters. One should note that only the system mounting parameters can be analyzed since the principal point coordinates (x_p and y_p) and the principal distance (c) are not involved in the developed mathematical expressions (Equations 4.5 and 4.6). The spatial offset ($r_{c_2}^{c_1}$) is function of the lever arm offset (r_c^b) and the boresight matrix (R_c^b) (Equation 4.7). Therefore, variations in the spatial offset ($\delta r_{c_2}^{c_1}$) can be caused by biases in the lever arm offset (δr_c^b) and/or biases in the boresight matrix (δR_c^b) (Equations 4.8 and 4.9). Since the rotational offset matrix ($R_{c_2}^{c_1}$) is only a function of the boresight matrix (R_c^b) (Equation 4.10), variations in the rotational offset ($\delta R_{c_2}^{c_1}$) can only be caused by biases in the boresight matrix (δR_c^b) (Equation 4.11).

$$r_{c_2}^{c_1} = f(r_c^b,\ R_c^b) \qquad (4.7)$$

$$\delta r_{c_2}^{c_1}(\delta r_c^b) = \frac{\partial r_{c_2}^{c_1}}{\partial r_c^b}\delta r_c^b \tag{4.8}$$

$$\delta r_{c_2}^{c_1}(\delta R_c^b) = \frac{\partial r_{c_2}^{c_1}}{\partial R_c^b}\delta R_c^b \tag{4.9}$$

$$R_{c_2}^{c_1} = f(R_c^b) \tag{4.10}$$

$$\delta R_{c_2}^{c_1}(\delta R_c^b) = \frac{\partial R_{c_2}^{c_1}}{\partial R_c^b}\delta R_c^b \tag{4.11}$$

The analysis is carried out for the following scenarios:

I. Stereo-pair from the same flight line or from parallel flight lines flown in the same direction with constant attitude;
II. Stereo-pair from flight lines flown in opposite direction with constant attitude;
III. Stereo-pair from flight lines flown in cross-direction with constant attitude.

The investigated scenarios are illustrated in Figure 4.3. In this figure, b_x and b_y represent the baselines in the x and y directions, respectively, of the IMU body frame at time t_1 (b_1). One should note that there might be cases where the baseline is not aligned either along the x or the y-axis of b_1 for all the three scenarios. For such cases, the baseline will have components in the x and y-axes. Figure 4.4 illustrates that situation for scenario I. This scenario is valid only if proper overlap/side lap between the images of the stereo-pair under consideration is available. Table 4.1 shows the form of the rotation matrices $R_{b_1}^m$ and $R_{b_2}^m$ for the different scenarios.

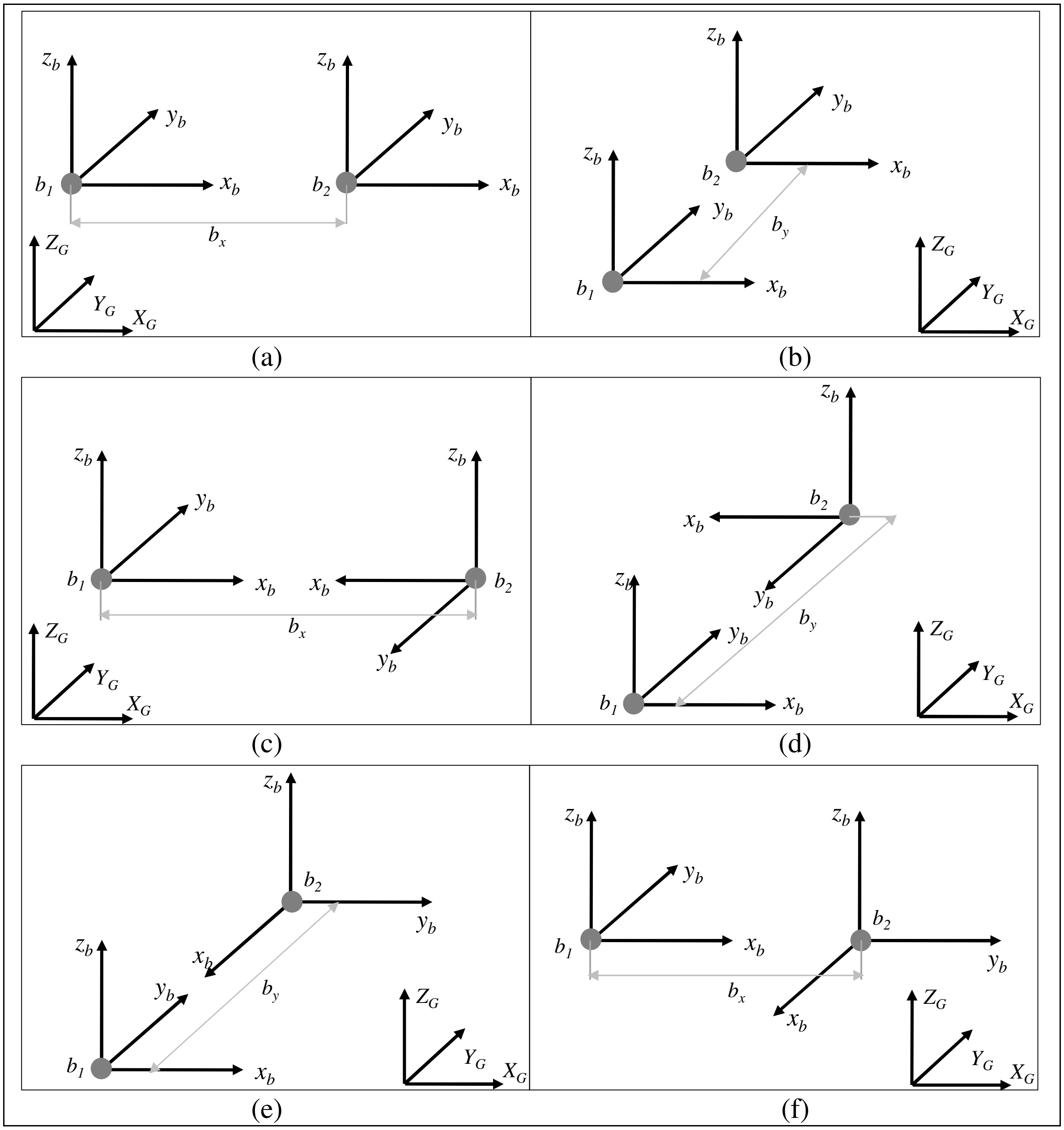

Figure 4.3. Scenario I-A: stereo-pair from the same flight line (baseline along the x-axis of b_1) (a), I-B: stereo-pair from parallel flight lines (same direction) with side lap (> 50%) (baseline along the y-axis of b_1) (b), II-A: stereo-pair from opposite flight lines with 100% side lap (baseline along the x-axis of b_1) (c), II-B: stereo-pair from opposite flight lines with some side lap (> 50%) (baseline along the y-axis of b_1) (d), III-A: stereo-pair from cross flight lines (baseline along the y-axis of b_1) (e), III-B: stereo-pair from cross flight lines (baseline along the x-axis of b_1) (f).

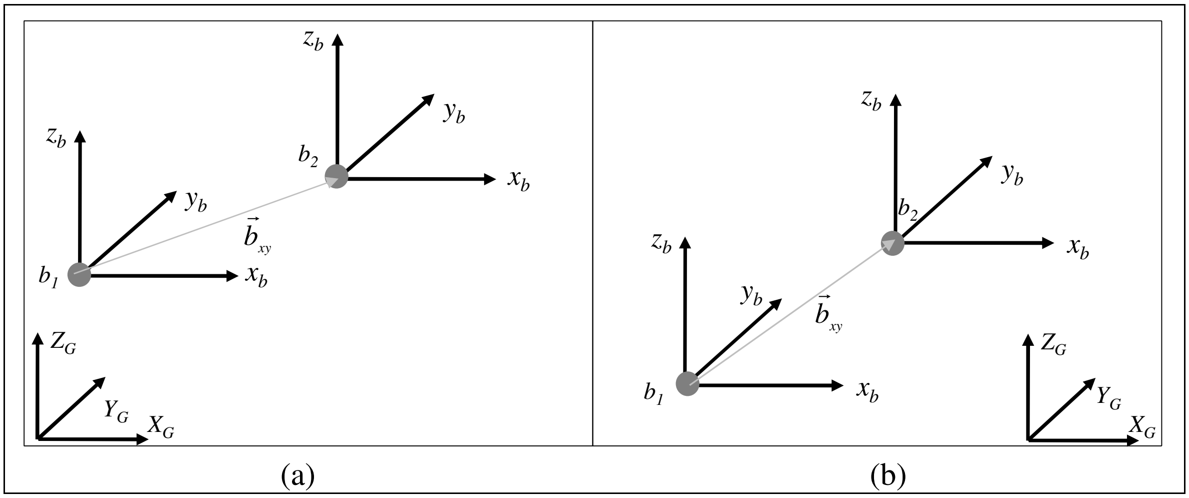

Figure 4.4. Examples of cases where the baseline is not aligned either along the *x* or the *y* axis of b_1 (IMU body frame at time t_1) for scenarios I-A (a) and I-B (b).

Table 4.1. Rotation matrices $\boldsymbol{R_{b_1}^m}$ and $\boldsymbol{R_{b_2}^m}$ for the different investigated scenarios.

	$R_{b_1}^m$	$R_{b_2}^m$
Scenario I-A and I-B	$\begin{bmatrix}1 & 0 & 0\\0 & 1 & 0\\0 & 0 & 1\end{bmatrix}$	$\begin{bmatrix}1 & 0 & 0\\0 & 1 & 0\\0 & 0 & 1\end{bmatrix}$
Scenario II-A and II-B	$\begin{bmatrix}1 & 0 & 0\\0 & 1 & 0\\0 & 0 & 1\end{bmatrix}$	$\begin{bmatrix}-1 & 0 & 0\\0 & -1 & 0\\0 & 0 & 1\end{bmatrix}$
Scenario III-A and III-B	$\begin{bmatrix}1 & 0 & 0\\0 & 1 & 0\\0 & 0 & 1\end{bmatrix}$	$\begin{bmatrix}0 & 1 & 0\\-1 & 0 & 0\\0 & 0 & 1\end{bmatrix}$

By utilizing Equations 4.8 and 4.9 (i.e., after differentiating Equation 4.5 with respect to the lever arm offset and boresight angles) one can get Equations 4.12 and 4.13, respectively. These equations represent the variations in the spatial offset relating the two cameras stations ($\delta r_{c_2}^{c_1}$) caused by biases in the lever arm offset (r_c^b) and boresight matrix (R_c^b).

$$\delta r_{c_2}^{c_1}(\delta r_c^b) = R_b^c R_m^{b_1}\left(R_{b_2}^m - R_{b_1}^m\right)\delta r_c^b \tag{4.12}$$

$$\delta r_{c_2}^{c_1}(\delta R_c^b) = \delta R_b^c\left[r_{b_2}^{b_1} + R_m^{b1}\left(R_{b_2}^m - R_{b_1}^m\right)r_c^b\right] \tag{4.13}$$

where:

- $r_{b_2}^{b_1} = R_m^{b1}\left(r_{b_2}^m - r_{b_1}^m\right) = \begin{bmatrix} b_x \\ b_y \\ b_z \end{bmatrix}$: is the vector from the origin of the IMU coordinate system at time t_1 to the origin of the IMU coordinate system at time t_2.

Similarly, by utilizing Equation 4.11 (i.e., after differentiating Equation 4.6 with respect to the boresight angles) one can get Equation 4.14. Such equation represents the variation in the rotational offset matrix relating the two cameras stations ($\delta R_{c_2}^{c_1}$) originated by biases in the boresight matrix (δR_c^b).

$$\delta R_{c_2}^{c_1}(\delta R_c^b) = R_b^c R_m^{b_1} R_{b_2}^m [\delta R_c^b] + [\delta R_b^c] R_m^{b_1} R_{b_2}^m R_c^b \tag{4.14}$$

Table 4.2 shows the variation in the spatial offset relating the two cameras stations ($\delta r_{c_2}^{c_1}$) for the different scenarios. The expressions in Table 4.2 are obtained by expanding Equations 4.12 and 4.13 according to the specified scenarios while ignoring terms from the multiplication of two small quantities (such as the multiplication of the boresight angles by the biases in the lever arm offset components). The highlighted terms in Table 4.2 are the components of the variations, which will cause *y*-parallax among conjugate light rays in overlapping imagery. Also, one should note that the variations in the spatial offset relating the two cameras stations caused by biases in the boresight matrix ($\delta r_{c_2}^{c_1}(\delta R_c^b)$) are the same for the 3 scenarios. This happens due to the fact that the additional terms for scenarios II and III get cancelled out in the mathematical manipulation.

Table 4.2. Variation in the spatial offset relating the two camera stations ($\delta r^{c_1}_{c_2}$) caused by biases in the lever arm offset (δr^b_c) and biases in the boresight matrix (δR^b_c) for the different scenarios.

Scenario		Baseline Direction	$\delta r^{c_1}_{c_2}(\delta r^b_c)$	$\delta r^{c_1}_{c_2}(\delta R^b_c)$
I	A	along the *x*-axis of b_1 (Figure 4.3a)	0(*)	$\begin{bmatrix} 0 \\ -\delta\Delta\kappa\ b_x \\ \delta\Delta\varphi\ b_x \end{bmatrix}$
	B	along the *y*-axis of b_1 (Figure 4.3b)	0(*)	$\begin{bmatrix} \delta\Delta\kappa\ b_y \\ 0 \\ -\delta\Delta\omega\ b_y \end{bmatrix}$
II	A	along the *x*-axis of b_1 (Figure 4.3c)	$\begin{bmatrix} -2\delta\Delta X \\ -2\delta\Delta Y \\ 0 \end{bmatrix}$	$\begin{bmatrix} 0 \\ -\delta\Delta\kappa\ b_x \\ \delta\Delta\varphi b_x \end{bmatrix}$
	B	along the *y*-axis of b_1 (Figure 4.3d)	$\begin{bmatrix} -2\delta\Delta X \\ -2\delta\Delta Y \\ 0 \end{bmatrix}$	$\begin{bmatrix} \delta\Delta\kappa\ b_y \\ 0 \\ -\delta\Delta\omega b_y \end{bmatrix}$
III	A	along the *x*-axis of b_1 (Figure 4.3e)	$\begin{bmatrix} -\delta\Delta X + \delta\Delta Y \\ -\delta\Delta X - \delta\Delta Y \\ 0 \end{bmatrix}$	$\begin{bmatrix} 0 \\ -\delta\Delta\kappa\ b_x \\ \delta\Delta\varphi b_x \end{bmatrix}$
	B	along the *y*-axis of b_1 (Figure 4.3f)	$\begin{bmatrix} -\delta\Delta X + \delta\Delta Y \\ -\delta\Delta X - \delta\Delta Y \\ 0 \end{bmatrix}$	$\begin{bmatrix} \delta\Delta\kappa\ b_y \\ 0 \\ -\delta\Delta\omega b_y \end{bmatrix}$

(*)Note that in the scenario where there is variation in the attitude, the term $\left(R^m_{b_2} - R^m_{b_1}\right)$ will not be zero and therefore there will be variation in the spatial offset relating the cameras (i.e., $\delta r^{c_1}_{c_2}(\delta r^b_c) \neq 0$). Significant attitude variation would contribute towards the estimation of all the parameters including the vertical lever arm offset component. However, in most cases, the available attitude variations are very small and do not allow for reliable estimation of the parameters.

Table 4.3 presents the variations in the rotational offset matrix relating the cameras stations c_1 and c_2 $\left(\delta R_{c_2}^{c_1}\right)$ for the different scenarios. The expressions in Table 4.3 are obtained by expanding Equation 4.14 according to the specified scenarios while ignoring terms from the multiplication of two small quantities in the mathematical manipulation (such as the multiplication of the biases in the boresight angles by the boresight angles).

Table 4.3. Variation in the rotational offset matrix relating the two camera stations $(\delta R_{c_2}^{c_1})$ caused by biases in the boresight matrix (δR_c^b) for the different scenarios.

Scenario	$\delta R_{c_2}^{c_1}(\delta R_c^b)$
I	0
II	$\begin{bmatrix} 0 & 0 & -2\delta\Delta\varphi \\ 0 & 0 & 2\delta\Delta\omega \\ -2\delta\Delta\varphi & 2\delta\Delta\omega & 0 \end{bmatrix}$
III	$\begin{bmatrix} 0 & 0 & -\delta\Delta\omega - \delta\Delta\varphi \\ 0 & 0 & \delta\Delta\omega - \delta\Delta\varphi \\ \delta\Delta\omega - \delta\Delta\varphi & \delta\Delta\omega + \delta\Delta\varphi & 0 \end{bmatrix}$

Table 4.4 presents a summary of the biases in the system mounting parameters which introduce *y*-parallax under the different investigated scenarios. Note that the only bias that will not introduce *y*-parallax, under any scenario (assuming constant attitude), is the bias in the vertical component of the lever arm offset. One should note that by having significant attitude variation in the flight will contribute towards the estimation of the parameters including the vertical lever arm offset component. However, the attitude variation is usually not significant enough to enable reliable estimation of the parameters.

Table 4.4. Biases in the system mounting parameters, which will introduce *y*-parallax for the different investigated scenarios.

Bias	Scenario				
	I-A	I-B	II-A	II-B	III-A or III-B
$\delta\Delta X$	No	No	Yes	No	Yes
$\delta\Delta Y$	No	No	No	Yes	Yes
$\delta\Delta Z$	No	No	No	No	No
$\delta\Delta\omega$	No	Yes	Yes	Yes	Yes
$\delta\Delta\varphi$	Yes	No	Yes	Yes	Yes
$\delta\Delta\kappa$	Yes	Yes	Yes	Yes	Yes

The following conclusions can be drawn from the presented analysis:

- For a stereo-pair from the same flight line, biases in the boresight pitch ($\delta\Delta\varphi$) and yaw ($\delta\Delta\kappa$) angles will introduce *y*-parallax. This means that in the presence of biases in the boresight pitch and yaw angles, conjugate light rays will not intersect. These findings reveal the possibility of estimating the boresight pitch and yaw angles using a single flight line. More specifically, the minimum requirement for estimating such parameters would be a control-free stereo-pair. By having adjacent flight lines flown in the same direction will contribute for the estimation of all the boresight angles.
- By having well tied parallel flight lines in opposite directions with side lap percentages ranging from 50% to 100% will contribute towards the estimation of all parameters except the vertical component of the lever arm offset.
- By having flight lines flown in cross directions will contribute towards the estimation of all the system mounting parameters except the vertical component of the lever arm.

4.2.2 Second Proposed Analysis (impact on the reconstruction process and the reconstructed object space – precision and accuracy)

The objective of the second proposed analysis is to investigate the impact of biases in the system parameters on the reconstruction process as well as on the reconstructed object space. The proposed analysis utilizes the GPS/INS-assisted photogrammetric point positioning equation in the form presented in Equation 4.15. All vectors are the same as in Equation 2.18 except the lever arm offset, which is now defined as the vector from the camera perspective center to the origin of the IMU coordinate system (defined relative to the camera coordinate system) (r_b^c), as illustrated in Figure 4.5. This alternative equation will be used to make the analysis clearer.

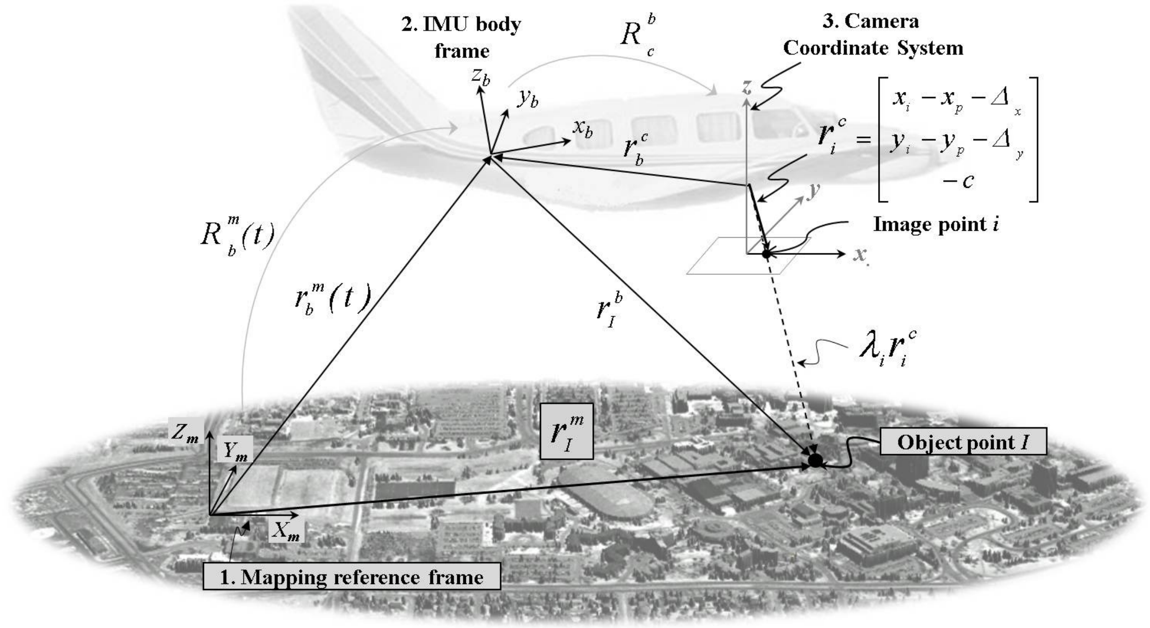

Figure 4.5. Involved quantities and coordinate systems in the second proposed analysis.

$$r_I^m = r_b^m(t) + R_b^m(t) R_c^b \left(\lambda_i \begin{bmatrix} x_i - x_p - \Delta_x \\ y_i - y_p - \Delta_y \\ -c \end{bmatrix} - r_b^c \right) \tag{4.15}$$

The following assumptions will be considered in the proposed analysis: (i) After the GPS/INS integration, the position refers to the origin of the IMU coordinate system and the attitude refers to the orientation of the IMU body frame; (ii) The flight direction is parallel to the positive direction of the *x*-axis of the IMU coordinate system; (iii) The flight lines follow a straight-line trajectory with constant attitude; and (iv) The camera has relatively small boresight angles (w.r.t. the IMU body frame).

To analytically investigate whether biases in the system parameters will have an impact on the reconstruction process (i.e., whether they will introduce *y*-parallax), a pair of normalized images from the stereo-pair under consideration is generated. The utilized stereo-pair in this analysis is from the same flight line. The normalized image plane will be defined as being parallel to the *xy*-plane of the IMU body frame (Figure 4.6), and therefore, parallel to the baseline (refer to the assumption ii). In contrast to the traditional image normalization process, where the position of the perspective centers of the original images are preserved, in the presented analysis the perspective centers of the normalized images are shifted to the origin of the IMU coordinate system.

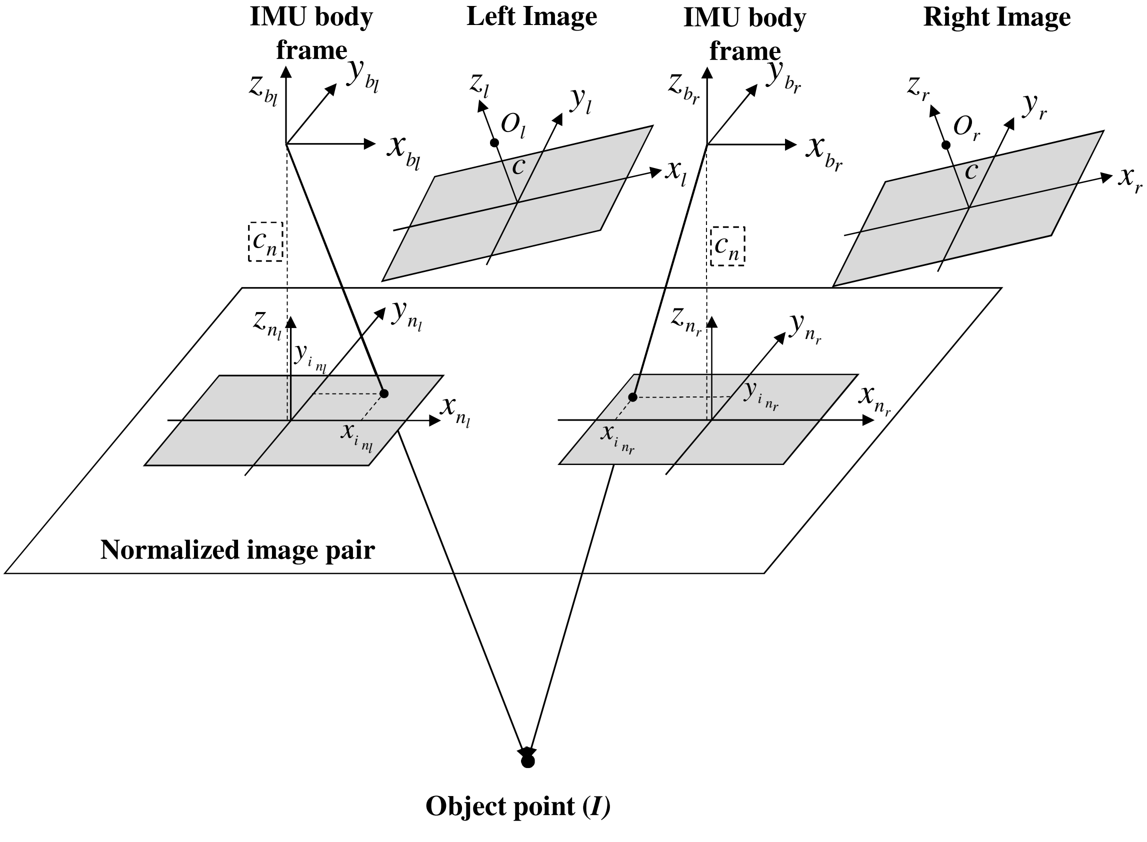

Figure 4.6. Original and normalized image pair.

After rearranging the terms in Equation 4.15, one can get the form in Equations 4.16, which represents the vector from the origin of the IMU body frame to the object point (*I*). In this analysis, it is assumed that the IMU body frame is parallel to the mapping frame. Equation 4.17 expresses the image normalization process. Since the normalized image coordinates (x_{i_n}, y_{i_n}) are defined relative to the IMU body frame, which is assumed to be parallel to the mapping frame, the normalization rotation matrix (R_n) becomes identity. After some mathematical manipulation, one can get the form in Equation 4.18. One should note that the normalized scale factor (λ_{i_n}), for a given normalized principal distance (c_n), represents the ration between the magnitudes of the vector connecting the origin of the IMU body frame (i.e., the shifted perspective center) and the object point and the vector connecting the origin of the IMU body frame (i.e., the shifted perspective center) and the normalized image point.

$$r_I^b = \begin{bmatrix} X_b \\ Y_b \\ Z_b \end{bmatrix} = R_m^b[r_I^m - r_b^m] = R_c^b\left(\lambda_i \begin{bmatrix} x_i - x_p - \Delta_x \\ y_i - y_p - \Delta_y \\ -c \end{bmatrix} - \begin{bmatrix} \Delta X' \\ \Delta Y' \\ \Delta Z' \end{bmatrix}\right) = \begin{bmatrix} X_b \\ Y_b \\ Z_b \end{bmatrix} \tag{4.16}$$

where:

- $\Delta X', \Delta Y', \Delta Z'$ are the components of the lever arm offset r_b^c.

$$\lambda_{i_n} R_n \begin{bmatrix} x_{i_n} \\ y_{i_n} \\ -c_n \end{bmatrix} = R_c^b\left(\lambda_i \begin{bmatrix} x_i - x_p - \Delta_x \\ y_i - y_p - \Delta_y \\ -c \end{bmatrix} - \begin{bmatrix} \Delta X' \\ \Delta Y' \\ \Delta Z' \end{bmatrix}\right) = \begin{bmatrix} 1 & -\Delta\kappa & \Delta\varphi \\ \Delta\kappa & 1 & -\Delta\omega \\ -\Delta\varphi & \Delta\omega & 1 \end{bmatrix} \begin{bmatrix} X_c \\ Y_c \\ Z_c \end{bmatrix} \tag{4.17}$$

where:

- $R_n = I$;
- $\begin{bmatrix} X_c \\ Y_c \\ Z_c \end{bmatrix} = \begin{bmatrix} \lambda_i(x_i - x_p - \Delta_x) - \Delta X' \\ \lambda_i\left(y_i - y_p - \Delta_y\right) - \Delta Y' \\ -\lambda_i c - \Delta Z' \end{bmatrix}$, are the coordinates of the object point w.r.t. the camera coordinate system shifted to the origin of the IMU coordinate system.

$$\lambda_{i_n} \begin{bmatrix} x_{i_n} \\ y_{i_n} \\ -c_n \end{bmatrix} = \begin{bmatrix} X_c - Y_c\Delta\kappa + Z_c\Delta\varphi \\ X_c\Delta\kappa + Y_c - Z_c\Delta\omega \\ -X_c\Delta\varphi + Y_c\Delta\omega + Z_c \end{bmatrix} = \begin{bmatrix} X_b \\ Y_b \\ Z_b \end{bmatrix} \tag{4.18}$$

One should note that in the normalized image pair $\left[\left(x_{i_{n_l}}, y_{i_{n_l}}\right), \left(x_{i_{n_r}}, y_{i_{n_r}}\right)\right]$, there will be no y-parallax (i.e., $P_y = y_{i_{n_l}} - y_{i_{n_r}} = 0$). To analyze the impact of the biases in the system parameters in the normalized image plane, Equations 4.19a and 4.19b (obtained by dividing the first two rows in Equation 4.18 by the third one) will be differentiated with respect to the system parameters.

$$x_{i_n} = -c_n \frac{X_c - Y_c\Delta\kappa + Z_c\Delta\varphi}{-X_c\Delta\varphi + Y_c\Delta\omega + Z_c} = -c_n \frac{X_b}{Z_b} \tag{4.19a}$$

$$y_{i_n} = -c_n \frac{X_c\Delta\kappa + Y_c - Z_c\Delta\omega}{-X_c\Delta\varphi + Y_c\Delta\omega + Z_c} = -c_n \frac{Y_b}{Z_b} \tag{4.19b}$$

The normalized image coordinates (x_{i_n}, y_{i_n}) are function of the system parameters ($\vec{x}$), as presented in Equations 4.20a and 4.20b. One should note that in contrast to the first proposed analysis, the utilized mathematical expression involves not only the mounting parameters but also the principal point coordinates (x_p and y_p) and the principal distance (c). In the presence of biases in the system parameters ($\delta\vec{x}$), the normalized image coordinates will experience displacements (δx_{i_n}, δy_{i_n}). The displacements in the normalized image coordinates are obtained using Equations 4.21a and 4.21b.

$$x_{i_n} = f_x(\vec{x}) \tag{4.20a}$$

$$y_{i_n} = f_y(\vec{x}) \tag{4.20b}$$

where:

- $\vec{x} = \left(\Delta X', \Delta Y', \Delta Z', \Delta\omega, \Delta\varphi, \Delta\kappa, x_p, y_p, c\right)$.

$$\delta x_{i_n} = \frac{\partial x_{i_n}}{\partial \vec{x}} \delta\vec{x} \tag{4.21a}$$

$$\delta y_{i_n} = \frac{\partial y_{i_n}}{\partial \vec{x}} \delta\vec{x} \tag{4.21b}$$

where:

- $\delta\vec{x} = \left(\delta\Delta X', \delta\Delta Y', \delta\Delta Z', \delta\Delta\omega, \delta\Delta\varphi, \delta\Delta\kappa, \delta x_p, \delta y_p, \delta c\right)$.

By expanding Equations 4.21a and 4.21b while ignoring higher order terms and the multiplication of two small quantities (e.g., the multiplication of biases in the lever arm offset components by the boresight angles), one can come up with the displacements in the normalized image coordinates caused by a bias in each of the system parameters, as presented in Table 4.5. To illustrate how the displacements in the normalized image coordinates have been derived, Equation 4.22 illustrates the expansion of Equation 4.21a for the bias in the lever arm offset component in the along flight direction ($\delta\Delta X'$).

$$\delta x_{i_n}(\delta\Delta X') = \frac{\partial x_{i_n}}{\partial \Delta X}\delta\Delta X' \tag{4.22a}$$

$$\delta x_{i_n}(\delta\Delta X') = -c_n \frac{Z_b(-\,\delta\Delta X') - X_b(\delta\Delta X'\Delta\varphi)}{{Z_b}^2} \tag{4.22b}$$

$$\delta x_{i_n}(\delta\Delta X') = -c_n \frac{Z_b(-\,\delta\Delta X') - 0}{{Z_b}^2} \tag{4.22c}$$

$$\delta x_{i_n}(\delta\Delta X') = -c_n \frac{-\,\delta\Delta X'}{-\lambda_{i_n} c_n} \tag{4.22d}$$

$$\delta x_{i_n}(\delta\Delta X') = -\frac{\delta\Delta X'}{\lambda_{i_n}} \tag{4.22e}$$

Table 4.5. Displacements in the normalized image coordinates caused by a bias in each of the system parameters.

	δx_{i_n}	δy_{i_n}
$\delta\Delta X'$	$-\frac{\delta\Delta X'}{\lambda_{i_n}}$	0
$\delta\Delta Y'$	0	$-\frac{\delta\Delta Y'}{\lambda_{i_n}}$
$\delta\Delta Z'$	$-\frac{x_{i_n}}{\lambda_{i_n} c_n}\delta\Delta Z'$	$-\frac{y_{i_n}}{\lambda_{i_n} c_n}\delta\Delta Z'$
$\delta\Delta\omega$	$\frac{x_{i_n} y_{i_n}}{c_n}\delta\Delta\omega$	$\left(c_n + \frac{{y_{i_n}}^2}{c_n}\right)\delta\Delta\omega$
$\delta\Delta\varphi$	$\left(-c_n - \frac{{x_{i_n}}^2}{c_n}\right)\delta\Delta\varphi$	$-\frac{x_{i_n} y_{i_n}}{c_n}\delta\Delta\varphi$
$\delta\Delta\kappa$	$-y_{i_n}\delta\Delta\kappa$	$x_{i_n}\delta\Delta\kappa$
δx_p	$-\frac{\lambda_i \delta x_p}{\lambda_{i_n}}$	0
δy_p	0	$-\frac{\lambda_i \delta y_p}{\lambda_{i_n}}$
δc	$-\frac{\lambda_i x_{i_n}}{\lambda_{i_n} c_n}\delta c$	$-\frac{\lambda_i y_{i_n}}{\lambda_{i_n} c_n}\delta c$

To this point, the impact of the biases on the normalized image coordinates has been derived. Now, one should check whether the displacements in these normalized image coordinates will introduce y-parallax or not. Figures 4.7, 4.8 and 4.9 show a pair of normalized images illustrating the displacements caused by biases in the lever arm offset components ($\delta\Delta X'$, $\delta\Delta Y'$, and $\delta\Delta Z'$), in the boresight angles ($\delta\Delta\omega$, $\delta\Delta\varphi$, and $\delta\Delta\kappa$), and in the principal point coordinates and the principal distance (δx_p, δy_p, and δc), respectively. It can be observed in Figures 4.7a and 4.7b that biases in the planimetric lever arm offset components ($\delta\Delta X'$ and $\delta\Delta Y'$), will not introduce parallax (neither *x*-parallax nor *y*-parallax). Therefore, in the presence of biases in the planimetric lever arm offset components, conjugate light rays will intersect and the elevation of the reconstructed point won't change. The bias in the vertical lever arm offset component ($\delta\Delta Z'$) (Figure 4.7c) will not cause *y*-parallax, but will introduce *x*-parallax. This means that conjugate light rays will intersect, but the elevation of the intersection point will change. Similar to the bias in the vertical lever arm offset component ($\delta\Delta Z'$), bias in the boresight roll angle ($\delta\Delta\omega$) will only cause *x*-parallax, as illustrated in Figure 4.8a. On the other hand, biases in the boresight pitch ($\delta\Delta\varphi$) and yaw ($\delta\Delta\kappa$) angles, as observed in Figures 4.8b and 4.8c, respectively, will introduce *y*-parallax. In other words, in the presence of biases in the boresight pitch and yaw angles, conjugate light rays will not intersect. These findings reveal the possibility of estimating the boresight pitch and yaw angles using a control-free stereo-pair, confirming the results obtained in the first proposed analysis (scenario I-A) (described in section 4.2.1). One can observe in Figures 4.9a and 4.9b that biases in the principal point coordinates (δx_p and δy_p) will not introduce parallax (neither *x*-parallax nor *y*-parallax). The bias in the principal distance (δc) (Figure 4.9c) will not cause *y*-parallax, but will introduce *x*-parallax. This means that conjugate light rays will intersect, but the elevation of the intersection point will change. Therefore, as the lever arm offset and the boresight roll angle, the principal point coordinates and the principal distance cannot be estimated by minimizing the *y*-parallax among conjugate light rays from stereo-pair captured in the same flight line.

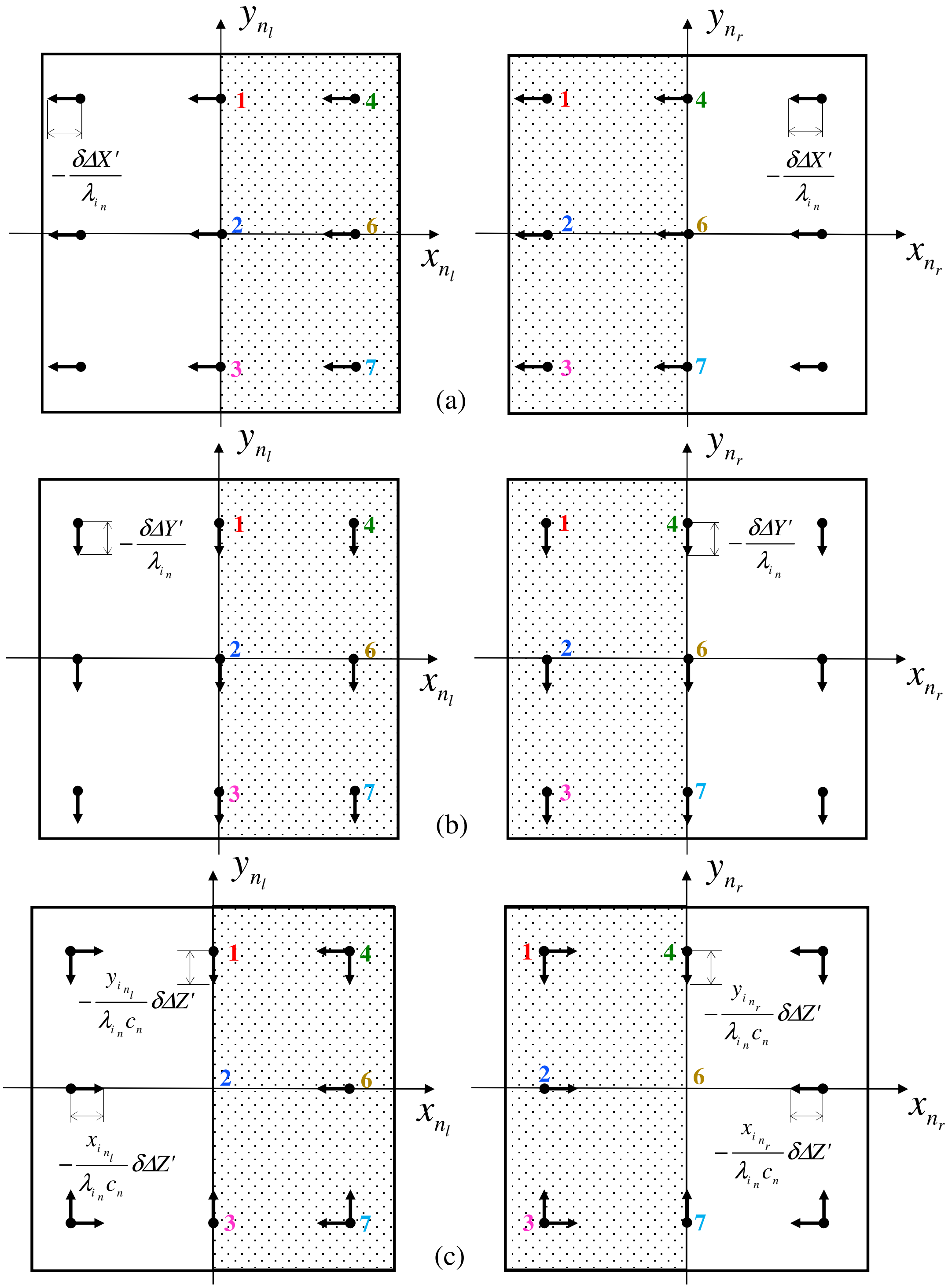

Figure 4.7. Pair of normalized images illustrating the displacements caused by biases in the lever arm offset components $\delta\Delta X'$ (a), $\delta\Delta Y'$ (b), and $\delta\Delta Z'$ (c).

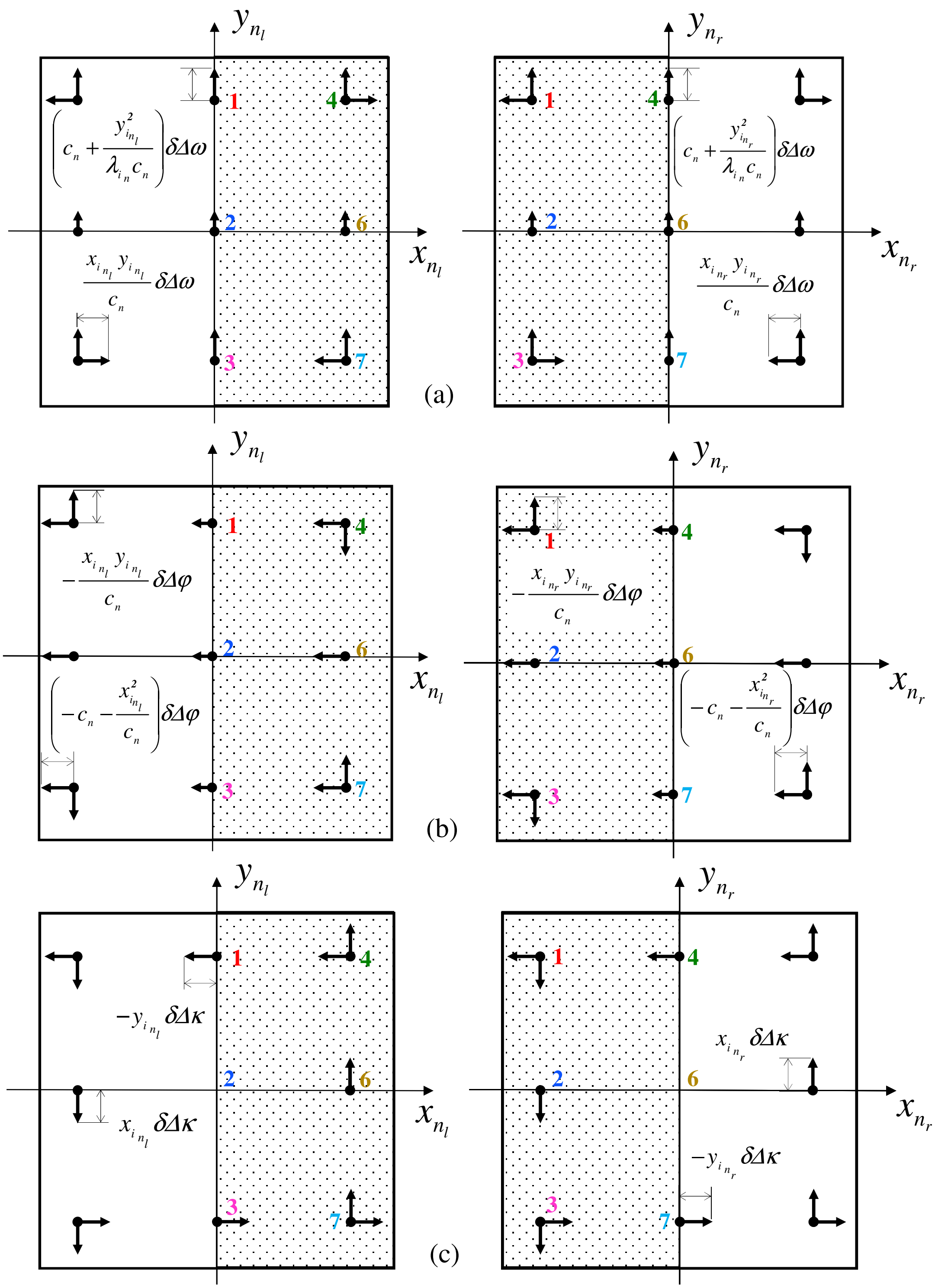

Figure 4.8. Pair of normalized images illustrating the displacements caused by biases in the boresight roll ($\delta\Delta\omega$) (a), pitch ($\delta\Delta\varphi$) (b), and yaw ($\delta\Delta\kappa$) (c) angles.

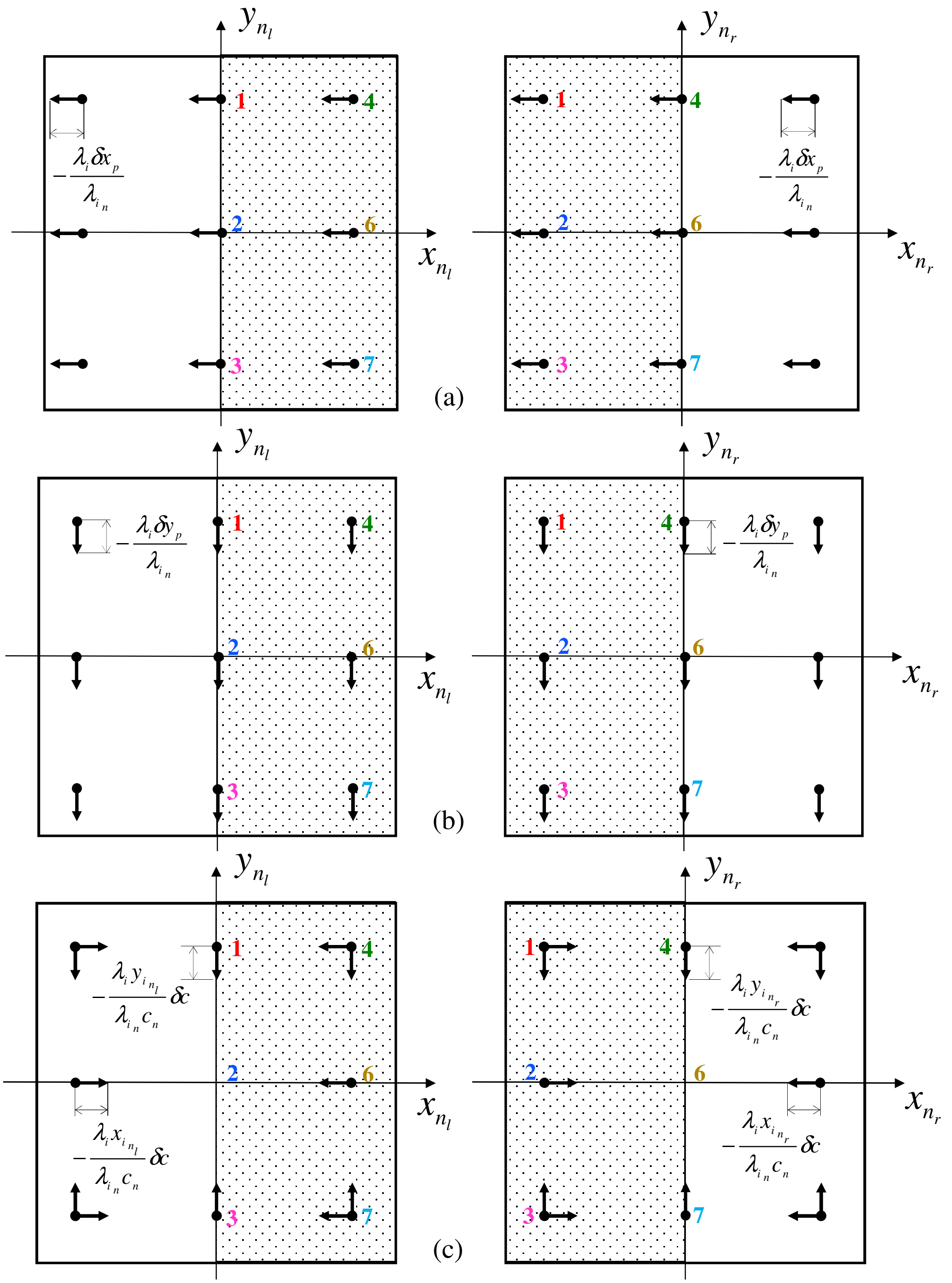

Figure 4.9. Pair of normalized images illustrating the displacements caused by biases in the principal point coordinates δx_p (a) and δy_p (b) and principal distance (δc) (c).

Now, the focus will be shifted to the impact of biases in the system parameters on the reconstructed object space. In other words, the impact of the introduced displacements in the normalized image pair on the reconstructed object space will be investigated. For that purpose, the normalized image pair illustrated in Figure 4.10 for forward and backward flight lines will be utilized. To simplify the analysis, the origin of the IMU coordinate system of the left image will be considered as coinciding with the origin of the mapping frame. The original (true) ground coordinates can be derived from the image pair through Equation 4.23.

$$r_I^b{}_{original} = \begin{bmatrix} X_b \\ Y_b \\ Z_b \end{bmatrix}_{original} = \begin{bmatrix} X_{b_o} \\ Y_{b_o} \\ Z_{b_o} \end{bmatrix} = \begin{bmatrix} 0 \\ 0 \\ 0 \end{bmatrix} + \lambda_{i_{n_l}} \begin{bmatrix} x_{i_{n_l}} \\ y_{i_{n_l}} \\ -c_n \end{bmatrix} = \begin{bmatrix} B \\ 0 \\ 0 \end{bmatrix} + \lambda_{i_{n_r}} \begin{bmatrix} x_{i_{n_r}} \\ y_{i_{n_r}} \\ -c_n \end{bmatrix} \tag{4.23}$$

From Equation 4.23, one can note that the left image scale ($\lambda_{i_{n_l}}$) and the right image scale ($\lambda_{i_{n_r}}$) are equivalent (i.e., $\lambda_{i_{n_l}} = \lambda_{i_{n_r}} = \lambda_{i_n}$) and equal to $-Z_{b_o}/c_n$. To derive the impact of the biases in the system parameters on the derived object space, one can introduce the displacements in the normalized image coordinates (δx_{i_n} and δy_{i_n}) caused by these biases in the normalized coordinates from the left and right images, as presented in Equation 4.24. Using this equation, one can compute the modified scale factor (λ_{i_n}'). Once the modified scale factor has been computed, the biased ground coordinates using the biased normalized image coordinates either from the left or from the right image can be derived (Equation 4.24). It should be noted that there will not be conjugate light rays intersecting for the biases that introduce *y*-parallax in the normalized image coordinates. In that case, the object coordinates computed using the normalized left image coordinates will be different from the object coordinates computed using the right normalized image coordinates. In other words, there will be *y*-parallax in the object space. Finally, the impact of the biases in the object space coordinates relative to the IMU body frame of the left camera station (δr_I^b) can be obtained through Equation 4.25. Table 4.6 presents, for each bias, the modified scale factor (λ_{i_n}') as well as the impact of such bias in the object space coordinates. One should note that the impact on the object space, computed using

Equations 4.23 – 4.25, is relative to the IMU coordinate system of the left camera station (i.e., $\delta X_b, \delta Y_b,$ and δZ_b). To have the impact w.r.t. the mapping frame (i.e.,δX_m, δY_m, and δZ_m), the rotation matrix relating the mapping frame and IMU coordinate systems must be applied ($\delta r_I^m = R_b^m \delta r_I^b$). The multiple signs ($\pm, \mp$) in Table 4.6 signify the impacts on forward and backward flight lines (illustrated in Figures 4.10a and 4.10b, respectively) with the top sign always corresponding to the forward flight line.

$$r_{I\ biased}^{b} = \begin{bmatrix} X_b \\ Y_b \\ Z_b \end{bmatrix}_{biased} = \begin{bmatrix} 0 \\ 0 \\ 0 \end{bmatrix} + \lambda_{i_n}' \begin{bmatrix} x_{i_{n_l}} + \delta x_{i_{n_l}} \\ y_{i_{n_l}} + \delta y_{i_{n_l}} \\ -c_n \end{bmatrix} =$$

$$= \begin{bmatrix} B \\ 0 \\ 0 \end{bmatrix} + \lambda_{i_n}' \begin{bmatrix} x_{i_{n_r}} + \delta x_{i_{n_r}} \\ y_{i_{n_r}} + \delta y_{i_{n_r}} \\ -c_n \end{bmatrix} \tag{4.24}$$

$$\delta r_I^b = \begin{bmatrix} \delta X_b \\ \delta Y_b \\ \delta Z_b \end{bmatrix} = r_{I\ biased}^{b} - r_{I\ original}^{b} = \begin{bmatrix} X_b \\ Y_b \\ Z_b \end{bmatrix}_{biased} - \begin{bmatrix} X_b \\ Y_b \\ Z_b \end{bmatrix}_{original} \tag{4.25}$$

One can note in Table 4.6 that biases in the principal point coordinates and in the principal distance (i.e., δx_p, δy_p , and δc) will produce similar impact on the object space as the biases in the lever arm offset components. The only difference is that the principal point coordinates and the principal distance are dependent on the flight scale as can be observed in Table 4.6 (the biases is multiplied by the scale factor λ_i).

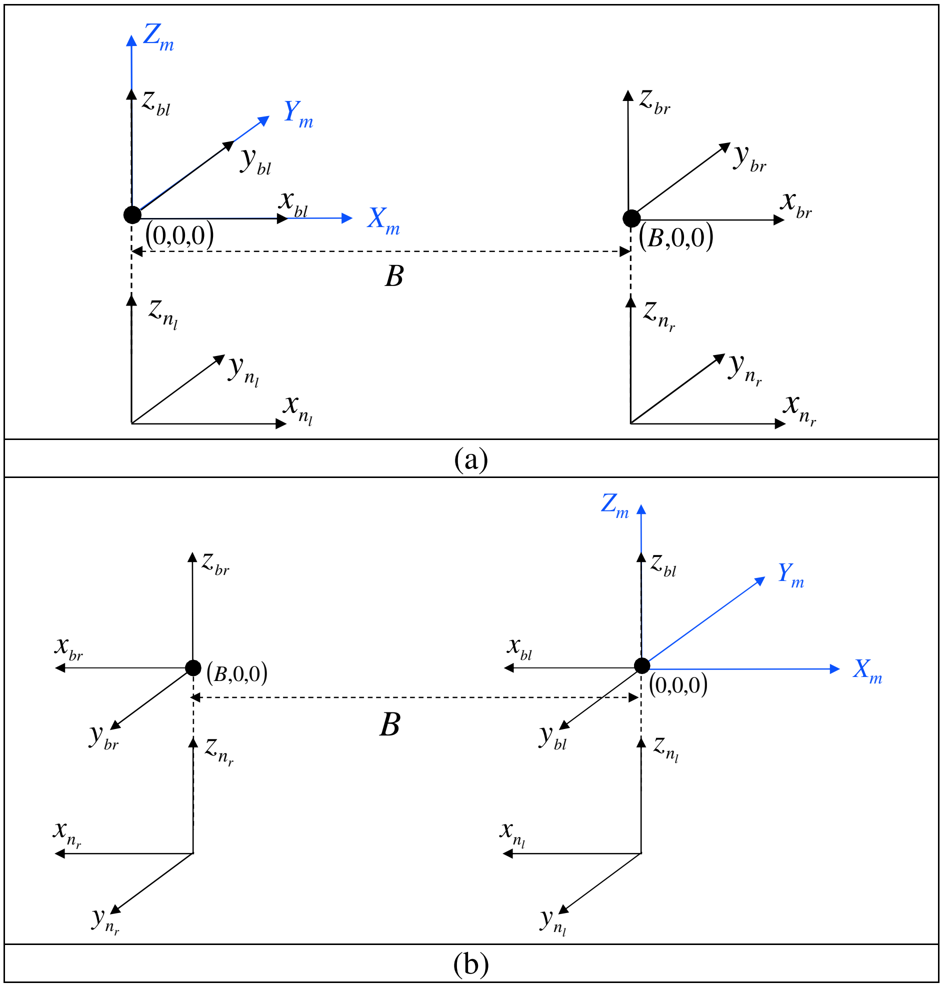

Figure 4.10. Normalized image pair utilized in the analysis of the impact of biases in the system parameters on the reconstructed object space, illustrated for forward (a) and backward (b) flight lines.

Table 4.6. Impact of biases in the system parameters on the derived object space coordinates.

	λ_{i_n}'	δX_m	δY_m	δZ_m
$\delta\Delta X'$	$\lambda_{i_n}' = \lambda_{i_n} = -Z_{b_o}/c_n$ (no scale change)	$\mp\delta\Delta X'$	0	0
$\delta\Delta Y'$	$\lambda_{i_n}' = \lambda_{i_n} = -Z_{b_o}/c_n$ (no scale change)	0	$\mp\delta\Delta Y'$	0
$\delta\Delta Z'$	$\lambda_{i_n}' = \frac{-Z_{b_o}/c_n}{1+\delta\Delta Z/Z_{b_o}}$ $\approx -Z_{b_o}/c_n\left(1-\delta\Delta Z/Z_{b_o}\right)$	0	0	$-\delta\Delta Z'$
$\delta\Delta\omega$	$\lambda_{i_n}' = -Z_{b_o}/c_n\left(1-y_{i_n}\delta\Delta\omega/c_n\right)$	0	$\mp Z_{b_o}\delta\Delta\omega$	$Y_{b_o}\delta\Delta\omega$
$\delta\Delta\varphi$	$\lambda_{i_n}' = -\frac{Z_{b_o}}{c_n}\left(1+\frac{x_{i_{n_l}}+x_{i_{n_r}}}{c_n}\delta\Delta\varphi\right)$	$\pm Z_{b_o}\delta\Delta\varphi$ $\pm\frac{X_{b_o}\left(B-X_{b_o}\right)}{Z_{b_o}}\delta\Delta\varphi$	left $\pm\frac{Y_{b_o}\left(B-X_{b_o}\right)}{Z_{b_o}}\delta\Delta\varphi$ right $\mp\frac{X_{b_o}Y_{b_o}}{Z_{b_o}}\delta\Delta\varphi$ $Y-parallax=$ $\pm\frac{BY_{b_o}}{Z_{b_o}}\delta\Delta\varphi$	$-2X_{b_o}\delta\Delta\varphi$ $+B\delta\Delta\varphi$
$\delta\Delta\kappa$	$\lambda_{i_n}' = \lambda_{i_n} = -Z_{b_o}/c_n$ (no scale change)	$\mp Y_{b_o}\delta\Delta\kappa$	left $\mp X_{b_o}\delta\Delta\kappa$ right $\mp\left(X_{b_o}-B\right)\delta\Delta\kappa$ $Y-parallax=$ $\pm B\delta\Delta\kappa$	0
δx_p	$\lambda_{i_n}' = \lambda_{i_n} = -Z_{b_o}/c_n$ (no scale change)	$\mp\lambda_i\delta x_p$	0	0
δy_p	$\lambda_{i_n}' = \lambda_{i_n} = -Z_{b_o}/c_n$ (no scale change)	0	$\mp\lambda_i\delta y_p$	0
δc	$\lambda_{i_n}' = \frac{-Z_{b_o}/c_n}{1+\lambda_i\delta c/Z_{b_o}}$ $\approx -Z_{b_o}/c_n\left(1-\lambda_i\delta c/Z_{b_o}\right)$	0	0	$-\lambda_i\delta c$

A simulation procedure was performed to verify the impact mathematically derived of the biases in system parameters on the reconstruction process as well as on the reconstructed object space. Stereo-pairs from parallel flight lines have been simulated using the following configurations:

- Stereo-pairs flown in opposite directions (i.e., forward and backward directions) with 100% side lap at a flying height of 1000 m;
- Stereo-pairs flown in opposite directions (i.e., forward and backward directions) with 100% side lap at a flying height of 1800 m;
- Stereo-pairs flown in the same direction with 50% side lap at a flying height of 1000 m.

One should note that parallel flight lines configuration is considered in the analysis since it is the most convenient/practical configuration for the survey missions. The configuration of the simulated photogrammetric stereo-pair and the magnitude of the introduced biases are reported in Table 4.7. The added noise in the image measurements was ±3 μm (half of the pixel size). To improve the clarity of the impact of the biases on the derived object space, a horizontal flat terrain was simulated.

Table 4.7. Simulated stereo-pair configuration.

Overlap:	50%
Flying height:	1000 m and 1800 m
Flying direction	along the X-axis
Principal Distance:	60.679 mm
Sensor size:	53.904 mm x 40.392 mm
Pixel size:	6 μm
$\delta\Delta X, \delta\Delta Y$ and $\delta\Delta Z$:	15 cm, 15 cm, and 15 cm
$\delta\Delta\omega, \delta\Delta\varphi$ and $\delta\Delta\kappa$:	720 sec, 720 sec, and 720 sec
δx_p , δy_p , and δc:	50 μm, 50 μm, and 50 μm

In the simulation process, the biases presented in Table 4.7 have been added in the system parameters. First, an intersection procedure using a single stereo-pair has been performed to check the impact of biased system parameters on the reconstruction process.

Table 4.8 reports the square root of the a-posteriori variance factor ($\hat{\sigma}_o$) of the intersection procedure with and without biases in the system parameters. The square root of the a-posteriori variance factor represents the quality of fit between the observations and the estimated parameters as represented by the mathematical model, which can be used as a measure to express the precision of the reconstructed object space. As expected, biases in the system parameters, which introduce *y*-parallax (boresight pitch ($\Delta\varphi$) and yaw ($\Delta\kappa$) angles), would affect the precision of the reconstructed object space (refer to the highlighted cells in Table 4.8). On the other hand, biases in the system parameters, which do not introduce *y*-parallax, would not affect the precision of the reconstructed object space. These results confirm the outcome from the mathematical analysis of the impact of the system biases on the reconstruction process.

Table 4.8. Precision of the generated photogrammetric model expressed through the squared root of the a-posteriori variance factor ($\boldsymbol{\hat{\sigma}_o}$) with and without biases in the system parameters utilized in the intersection procedure.

$\hat{\sigma}_o$ (mm)									
No bias	ΔX	ΔY	ΔZ	$\Delta\omega$	$\Delta\varphi$	$\Delta\kappa$	x_p	y_p	c
	15 cm bias			720 sec bias			50 μm bias		
0.003	0.003	0.003	0.003	0.003	0.011	0.016	0.003	0.003	0.003

Now, the impact of biases in the system parameters on the reconstructed object space will be verified by analyzing the differences between the bias-contaminated and the true coordinates of the reconstructed points through an intersection procedure. Such analysis is first conducted for reconstructed object space from parallel flight lines flown in opposite directions with 100% side lap at a flying height of 1000 m. In case such configuration does not allow for the estimation of the parameter in question, the other simulated flight configurations are analyzed (flight lines flown in the same direction with 50% side lap and flight lines flown at different flying heights).

To illustrate the simulation results, plots with the impact of biases in the system parameters in the *X*, *Y*, and *Z* coordinates of the reconstructed points are generated. In the

X and Y-axes of the produced plots, the true X and Y coordinates of the points are presented. On the other hand, the differences between the bias-contaminated and the true XYZ coordinates of the reconstructed points (using the stereo-pairs from the different flight lines such as forward and backwards strips or two flight lines in the same direction) are presented in the Z-axis of the produced plots. When only the impact of one of the flight lines is being displayed, means that its impact is identical to the impact of the other flight line and therefore the impact of one of the flight lines is hidden. To improve the clarity, the scale utilized to produce the plots is different for the considered biases and its impact in the X, Y, and Z directions.

The differences in the X, Y and Z directions between the reconstructed object space after the introduction of biases in the lever arm offset components $\delta\Delta X', \delta\Delta Y'$ and $\delta\Delta Z'$ and the true reconstructed object space are illustrated in Figures 4.11a – 4.11c, 4.12a – 4.12c, and 4.13a – 4.13c, respectively, for forward and backwards strips flown at a flying height of 1000 m. As can be observed in Figures 4.11, 4.12, and 4.13, biases in the lever arm offset components will lead to constant shifts in the derived object space. The magnitudes of these shifts are equivalent to the introduced biases in the lever arm offset components. Also, Figures 4.11a and 4.12b reveal that the horizontal impact of biases in the planimetric lever arm offset components are dependent on the flying direction, i.e., the effect is different for forward and backward strips. Such finding reveals the possibility of estimating the planimetric lever arm offset components by having flight lines in opposite directions (i.e., bias-contaminated coordinates from forward/backward flight lines are different). The vertical impact of a bias in the vertical lever arm offset component (Figure 4.13c), on the other hand, is independent of the flying direction (i.e., bias-contaminated coordinates from forward/backward flight lines are equivalent). The planimetric and vertical impacts of biases in the lever arm offset components are independent of the object point coordinates along and across the flight direction (as observed in Figures 4.11 – 4.13). Therefore, the vertical component of the lever arm offset cannot be estimated by minimizing the discrepancies between reconstructed points from different flight lines from a given flying height.

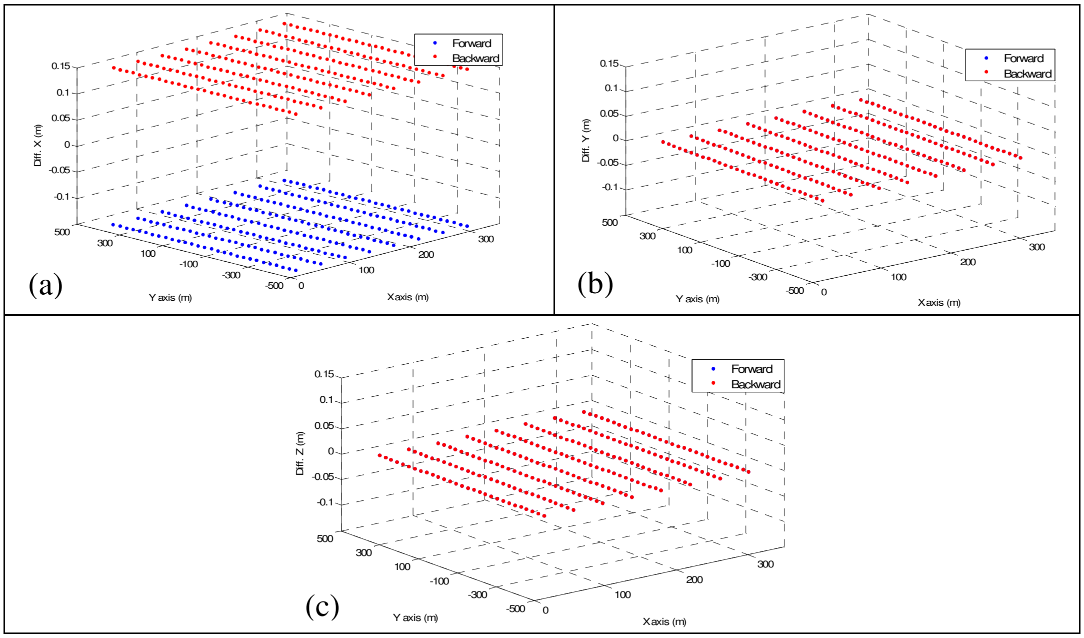

Figure 4.11. Differences between the bias-contaminated and true coordinates in the X (a), Y (b), and Z (c) directions after the introduction of a bias in the lever arm offset $\delta\Delta X'$ for forward and backward strips at 1000 m flying height.

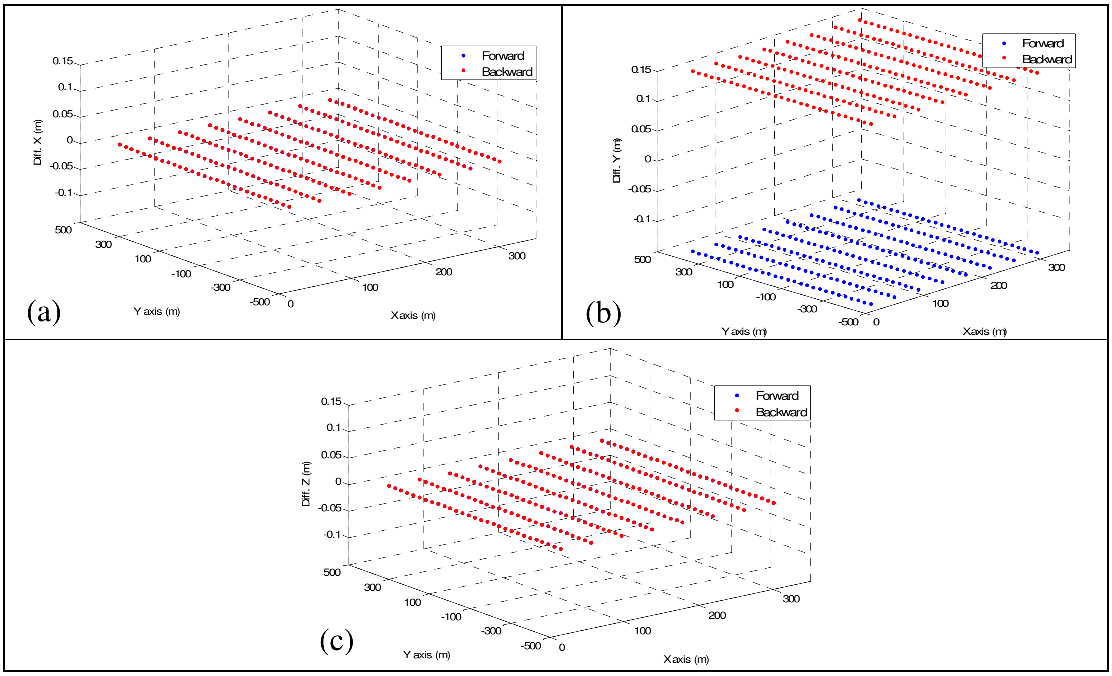

Figure 4.12. Differences between the bias-contaminated and true coordinates in the X (a), Y (b), and Z (c) directions after the introduction of a bias in the lever arm offset $\delta\Delta Y'$ for forward and backward strips at 1000 m flying height.

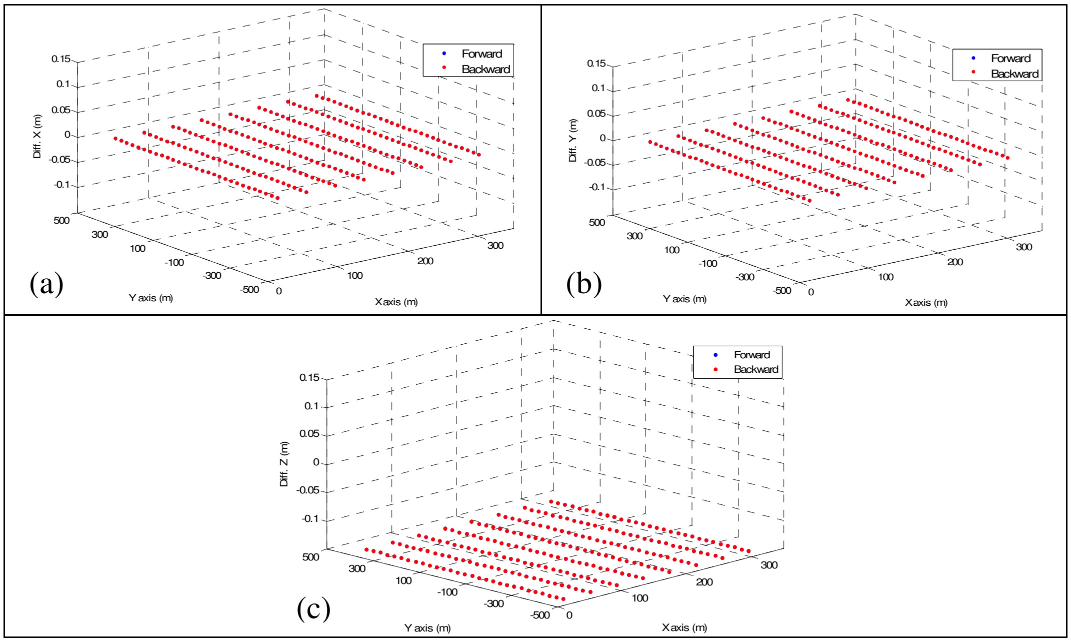

Figure 4.13. Differences between the bias-contaminated and true coordinates in the X (a), Y (b), and Z (c) directions after the introduction of a bias in the lever arm offset $\delta\Delta Z'$ for forward and backward strips at 1000 m flying height.

To check whether the impact of biases in the lever arm offset components are flying height dependent, the differences between the bias-contaminated and true coordinates of the reconstructed points from flight lines flown at a higher flying height (1800m) have been computed. Such differences are illustrated in Figures 4.14a – 4.14c, 4.15a – 4.15c, and 4.16a – 4.16c, for $\delta\Delta X', \delta\Delta Y'$ and $\delta\Delta Z'$, respectively. One can note in these figures that the impact of the lever arm offset components is independent of the flying height (i.e., the same impact was observed for flight lines flown at 1000m – refer to Figures 4.11 – 4.13). While the planimetric lever arm offset components can be recovered by having flight lines flown in opposite directions, the vertical component cannot be estimated by minimizing the discrepancies between reconstructed points from different flight lines since it will produce the same impact regardless of the utilized configuration. Therefore, vertical control point would be necessary for the estimation of such parameter.

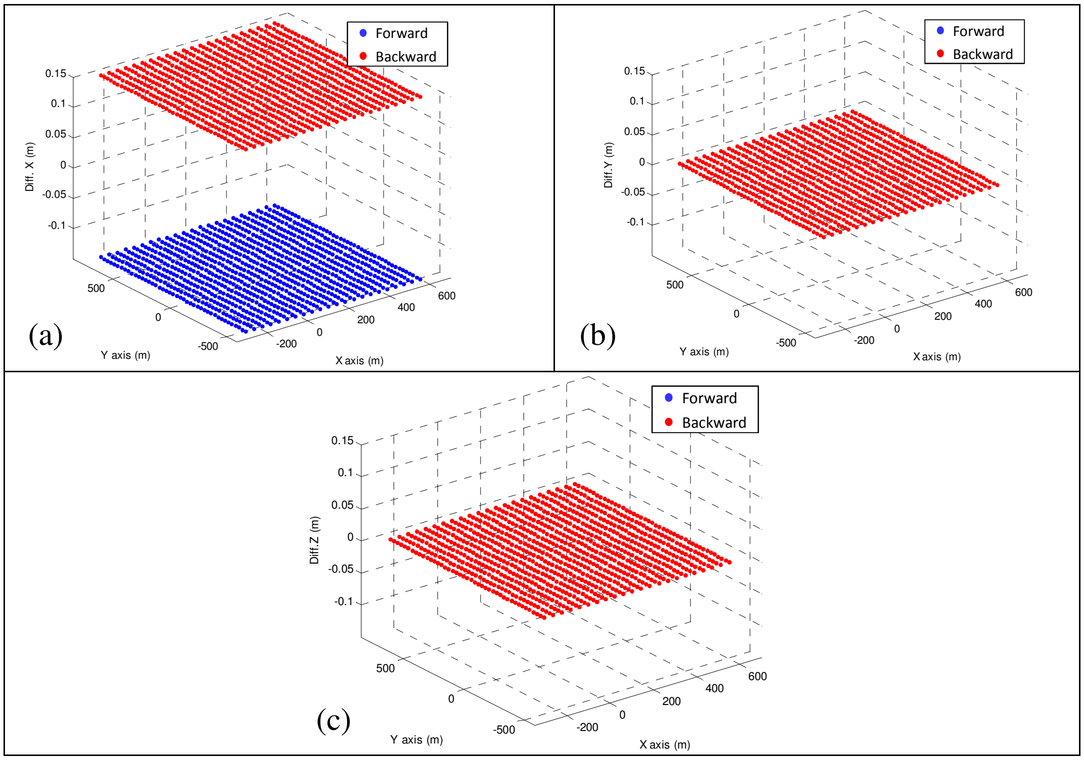

Figure 4.14. Differences between the bias-contaminated and true coordinates in the X (a), Y (b), and Z (c) directions after the introduction of a bias in the lever arm offset $\delta\Delta X'$ for forward and backward strips at 1800 m flying height.

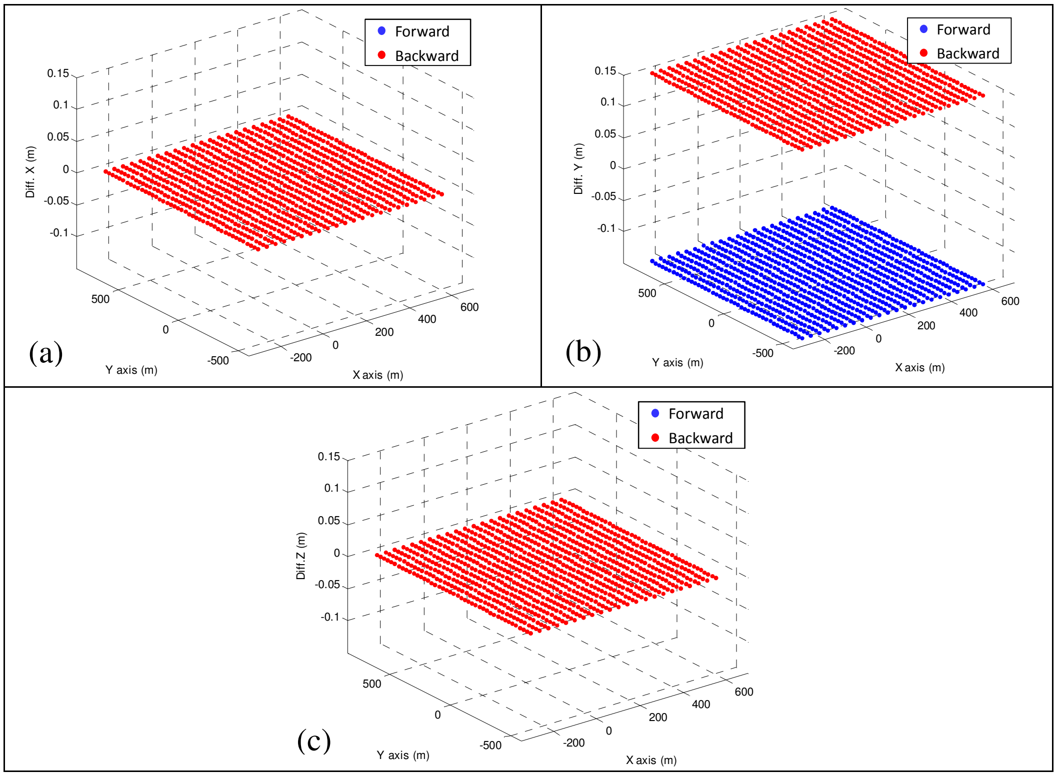

Figure 4.15. Differences between the bias-contaminated and true coordinates in the X (a), Y (b), and Z (c) directions after the introduction of a bias in the lever arm offset $\delta\Delta Y'$ for forward and backward strips at 1800 m flying height.

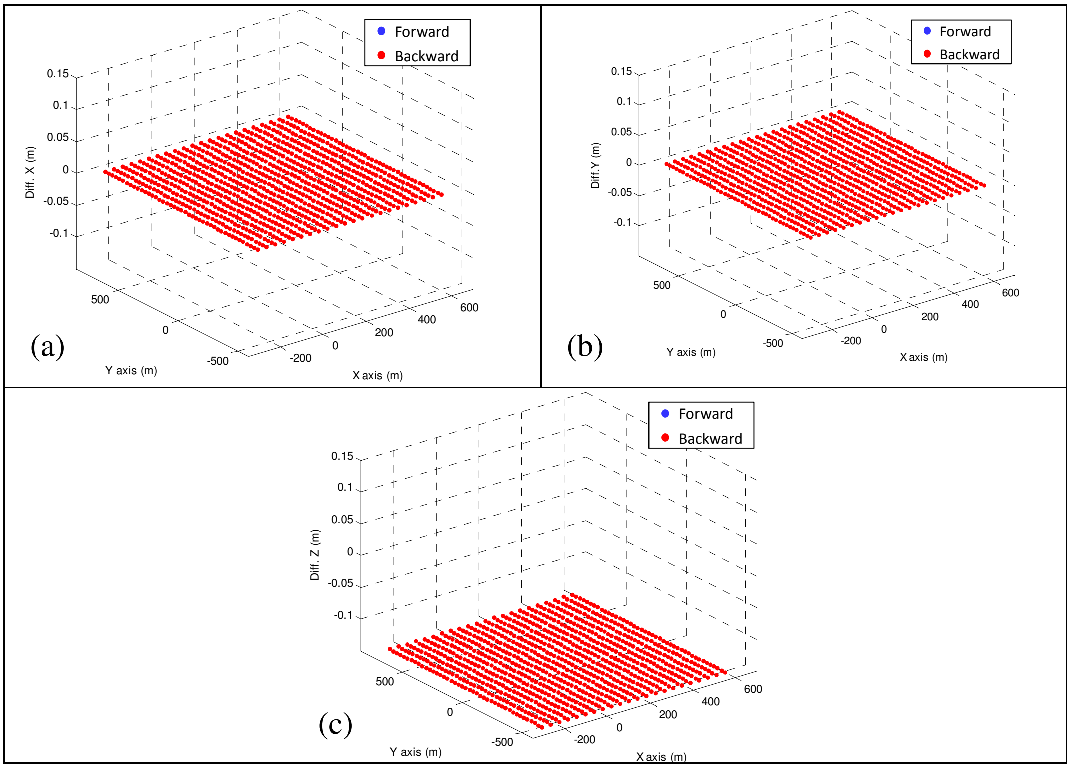

Figure 4.16. Differences between the bias-contaminated and true coordinates in the X (a), Y (b), and Z (c) directions after the introduction of a bias in the lever arm offset $\delta\Delta Z'$ for forward and backward strips at 1800 m flying height.

Now, the impact of biases in the boresight angles will be analyzed. The differences between the reconstructed object space after the introduction of biases in the boresight roll ($\delta\Delta\omega$), pitch ($\delta\Delta\varphi$), and yaw ($\delta\Delta\kappa$) angles and the true reconstructed object space are illustrated in Figures 4.17, 4.18 and 4.19, respectively, for forward and backward strips flown at a flying height of 1000m. Bias in the boresight roll angle does not affect the along flight direction as observed in Figure 4.17a. On the other hand, it will cause a constant shift across the flight direction (Figure 4.17b) and a shift in the Z direction with its magnitude varying linearly across the flying direction, i.e., the surface will be tilted (Figure 4.17c). The planimetric effect across the flight direction and vertical effect are dependent on the flying direction (as observed in Figures 4.17b and 4.17c). The planimetric effect across the flight direction is independent of the object point coordinates along and across the flight direction. The vertical effect, on the other hand, is dependent on the object point coordinates across the flight direction. One should note that the vertical effect decouples the boresight roll angle from the lever arm offset component in the across flight direction (i.e., it is possible to estimate those parameters simultaneously by having flight lines in opposite directions).

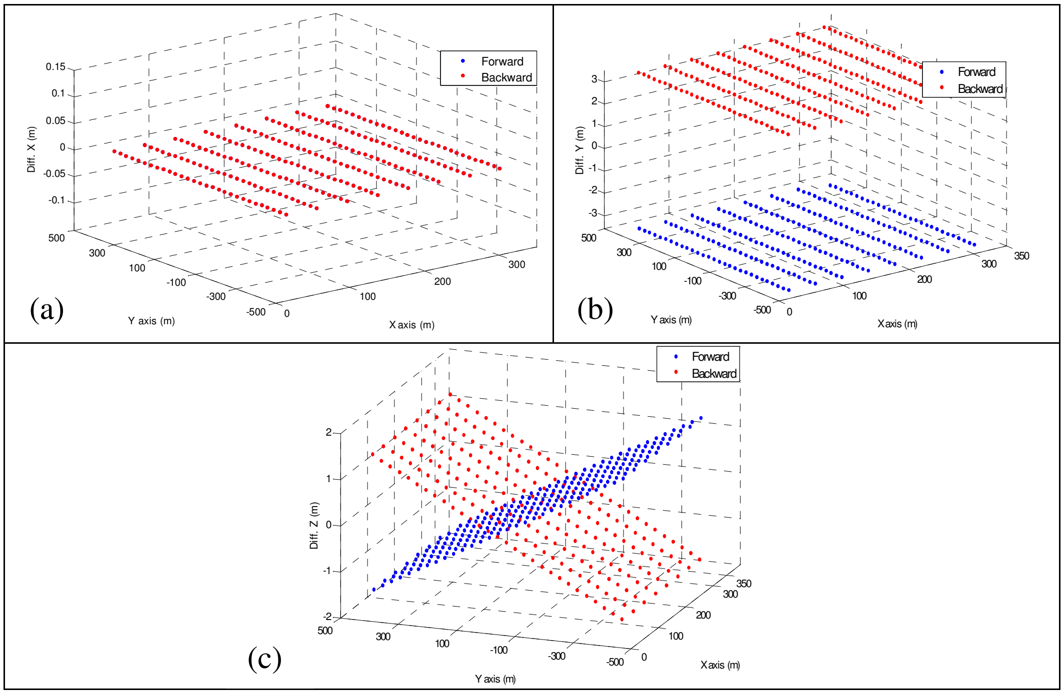

Figure 4.17. Differences between the bias-contaminated and true coordinates in the X (a), Y (b), and Z (c) directions after the introduction of a bias in the boresight roll angle ($\delta\Delta\omega$) for forward and backward strips at 1000 m flying height.

The boresight pitch angle (Figure 4.18) will cause a non-linear (almost constant) shift along the flight direction (Figure 4.18a) and a smaller non-linear shift in the across flight direction (Figure 4.18b). One can note in Figure 4.18c that a bias in the boresight pitch angle will also cause a shift in the Z direction with its magnitude varying linearly along the flying direction (the surface will be tilted). Here again, one can note that the vertical effect decouples the boresight pitch angle from the lever arm offset component in the along flight direction (i.e., it is possible to estimate those parameters simultaneously by having flight lines in opposite directions). The impact of the boresight pitch bias in the Z direction will produce a saw-tooth effect when we have 3 or more images with 50% overlap or less as illustrated in Figure 4.20. All these effects are dependent on the flying direction (as observed in Figure 4.18). The planimetric effect along the flight direction and the vertical effect are dependent on the object point coordinates in the along flight direction. The planimetric effect across the flight direction, on the other hand, is dependent on the object space coordinates along and across the flying direction.

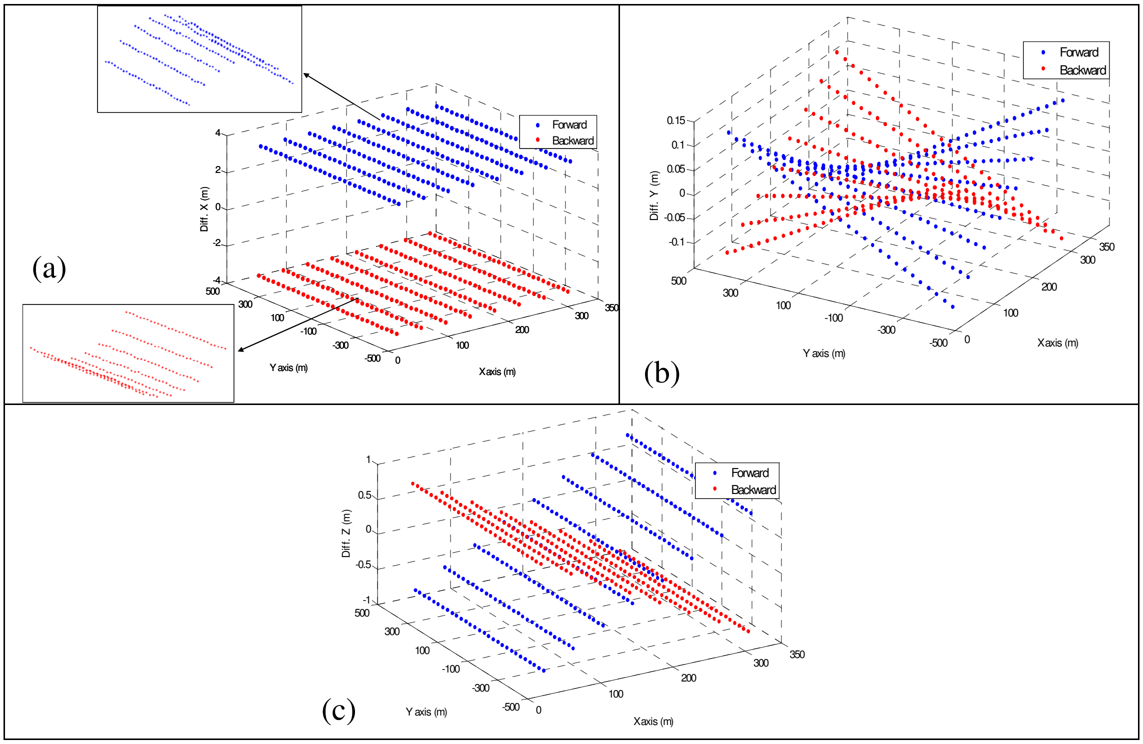

Figure 4.18. Differences between the bias-contaminated and true coordinates in the X (a), Y (b), and Z (c) directions after the introduction of a bias in the boresight pitch angle ($\delta\Delta\varphi$) for forward and backward strips at 1000 m flying height.

The boresight yaw angle (Figure 4.19) will cause a shift in the along flight direction with its magnitude varying linearly across the flight direction (Figure 4.19a). This effect is dependent on the object point coordinates across flight direction (as observed in Figure 4.19a). Also, it will cause a shift in the across flight direction with its magnitude varying linearly along the flight direction (Figure 4.19b). This effect is dependent on the object point coordinates along the flight direction (as observed in Figure 4.19b). Both effects are independent of the flying direction. This planimetric impact is equivalent to a shearing effect, i.e., the surface will be distorted, as illustrated in Figure 4.21. Based on the impact of biases in the boresight yaw angles one can note that by having parallel flight lines in opposite directions with 100% side lap, it is not possible to estimate such parameter.

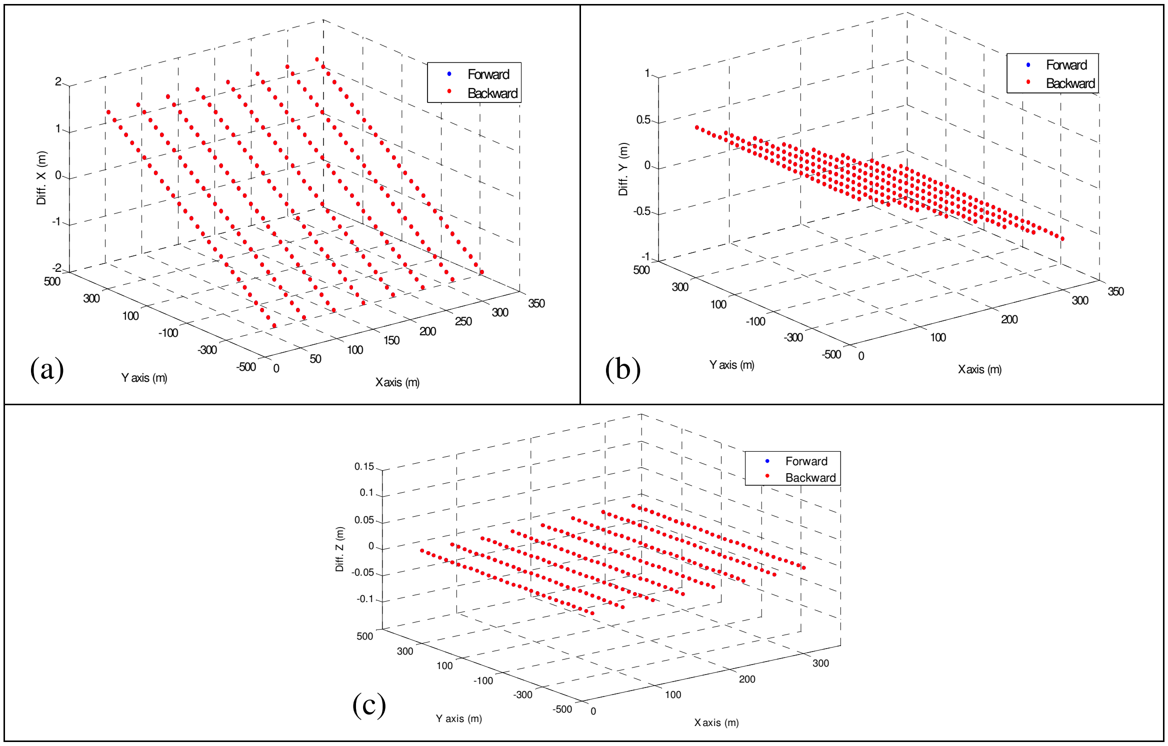

Figure 4.19. Differences between the bias-contaminated and true coordinates in the *X* (a), *Y* (b), and *Z* (c) directions after the introduction of a bias in the boresight yaw $\delta\Delta\kappa$ for forward and backward strips at 1000 m flying height.

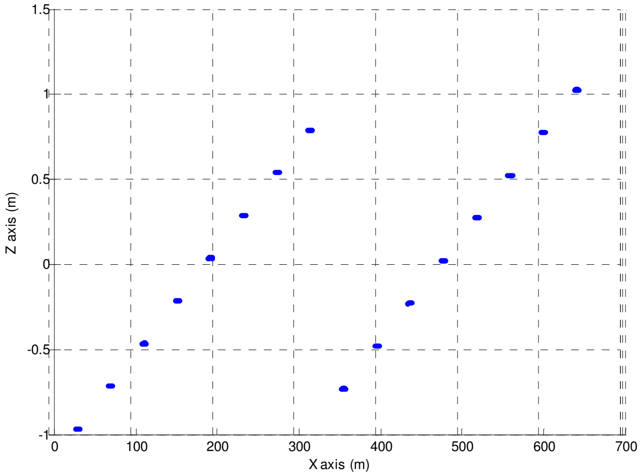

Figure 4.20. Saw-tooth effect in the *Z* direction when a bias in the boresight pitch angle is introduced for 3 or more images with 50% overlap or less.

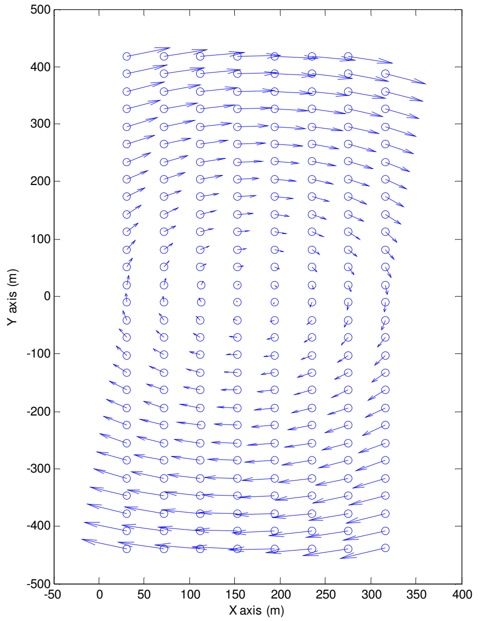

Figure 4.21. Shearing effect caused by the planimetric impact when a bias in the boresight yaw angle is introduced.

By having parallel flight lines with some side lap would lead to additional information for the estimation of the boresight yaw angle, as illustrated in Figure 4.22. Although the impact on strips flown in opposite directions is the same as the impact on the strips flown in parallel directions, strips flown in parallel directions are recommended since for such strips, the effect of biases in the planimetric lever arm offset is eliminated. Also, the impact of the biases in the boresight pitch and roll angles on the along and across flight direction, respectively, are eliminated as well.

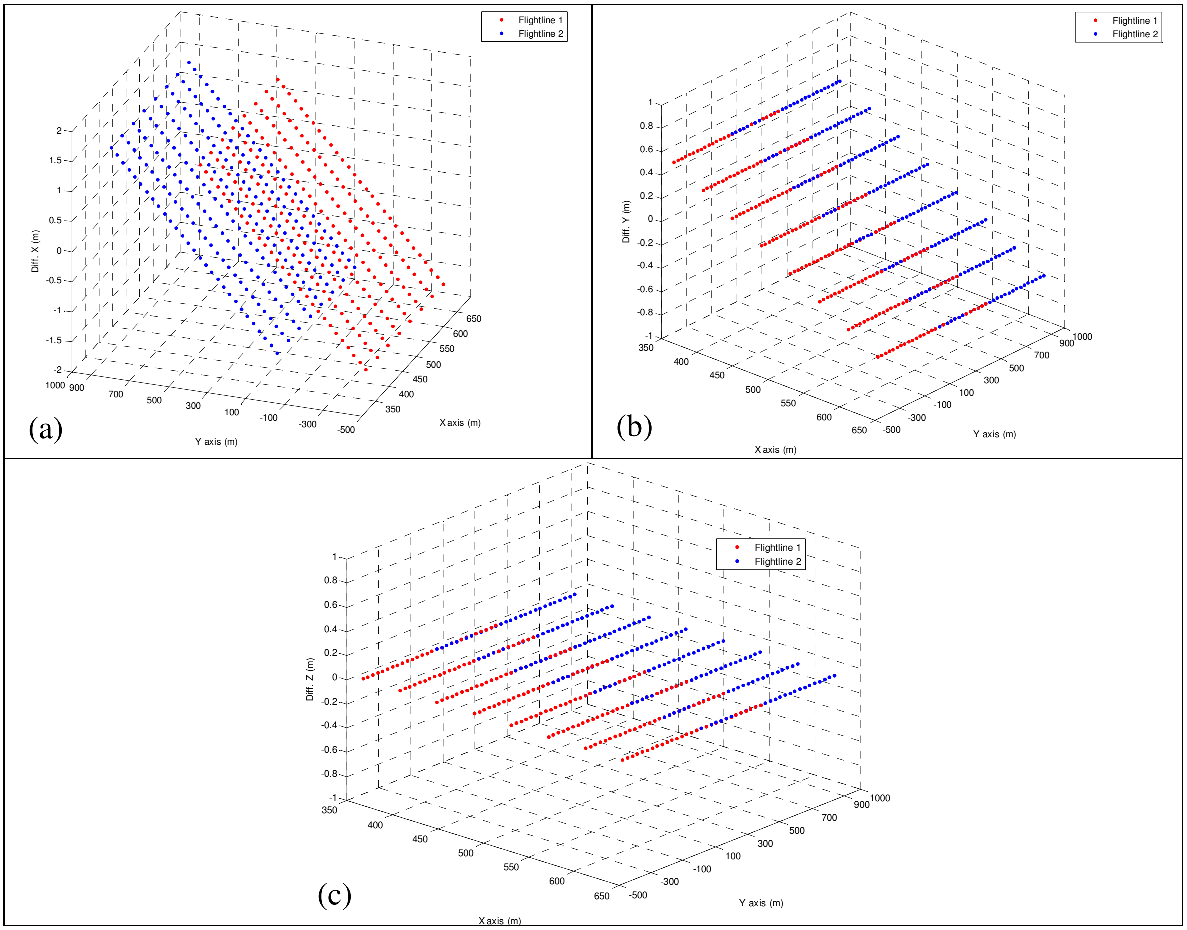

Figure 4.22. Differences between the bias-contaminated and true coordinates in the X (a), Y (b), and Z (c) directions after the introduction of a bias in the boresight yaw angle ($\delta\Delta\kappa$) for flight lines flown with 50% side lap at 1000 m flying height.

Finally, the differences between the reconstructed object space after the introduction of biases in the principal point coordinates and the principal distance (i.e., δx_p, δy_p, and δc) and the true reconstructed object space are illustrated in Figures 4.23, 4.24 and 4.25, respectively, for forward and backward flight lines flown at a flying height of 1000 m. As can be observed in these figures, biases in the principal point coordinates and the principal distance produce the same impact as the biases in the lever arm offset components for a given flying height. It has been already shown that the impact of the biases in the lever arm offset components is independent of the flying height. To check whether the impact of biases in the principal point coordinates and in the principal distance are flying height dependent, the differences between the bias-contaminated and true coordinates of the reconstructed points from flight lines flown at a higher flying height (1800m) have been computed. Such differences are illustrated in Figures 4.26, 4.27, and 4.28, for $\delta x_p, \delta y_p,$ and δc, respectively. One can note in these figures that the impact of the principal point coordinates and the principal distance are flying height dependent, i.e., the impact is amplified with an increase in the flying height. Therefore, to decouple the principal point coordinates from the planimmetric lever arm offset components and to estimate the principal distance, flight lines captured from two different flying heights should be available.

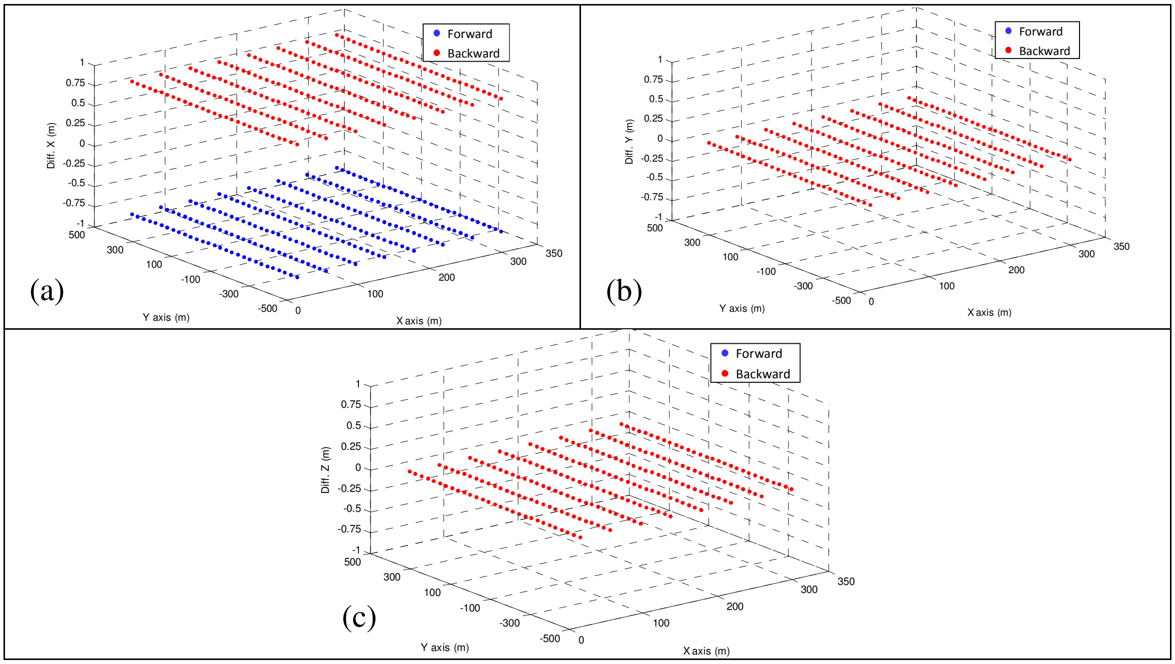

Figure 4.23. Differences between the bias-contaminated and true coordinates in the X (a), Y (b), and Z (c) directions after the introduction of a bias in the principal point coordinate δx_p for forward and backward strips at 1000 m flying height.

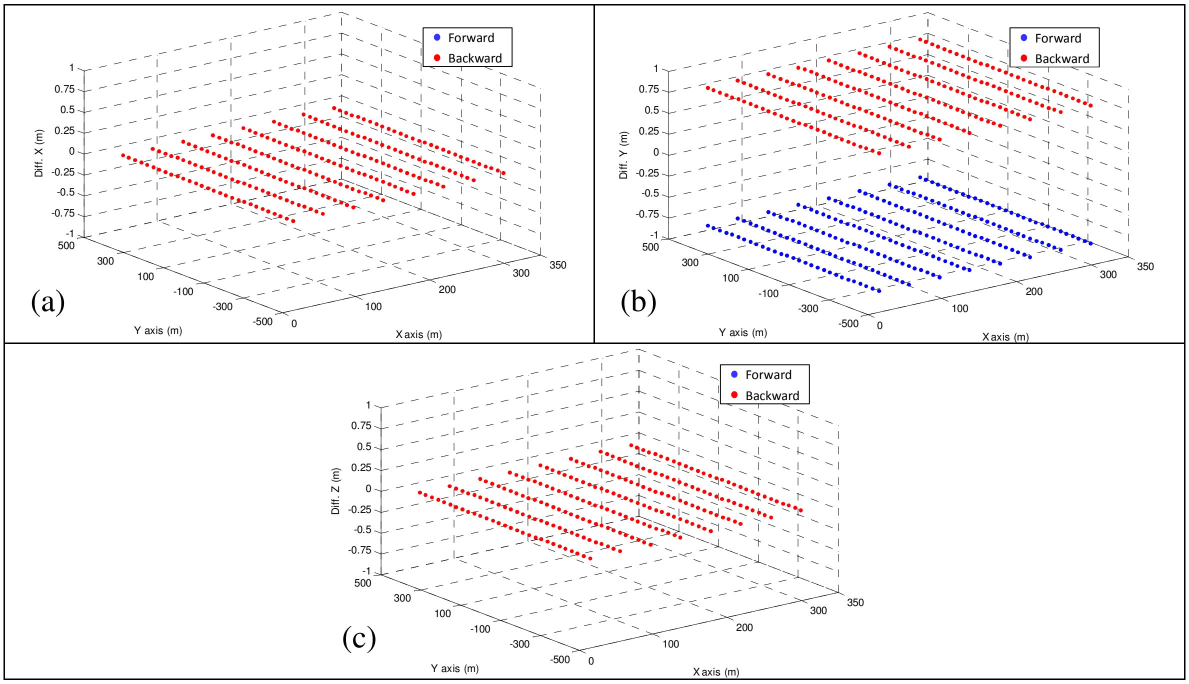

Figure 4.24. Differences between the bias-contaminated and true coordinates in the X (a), Y (b), and Z (c) directions after the introduction of a bias in the principal point coordinate δy_p for forward and backward strips at 1000 m flying height.

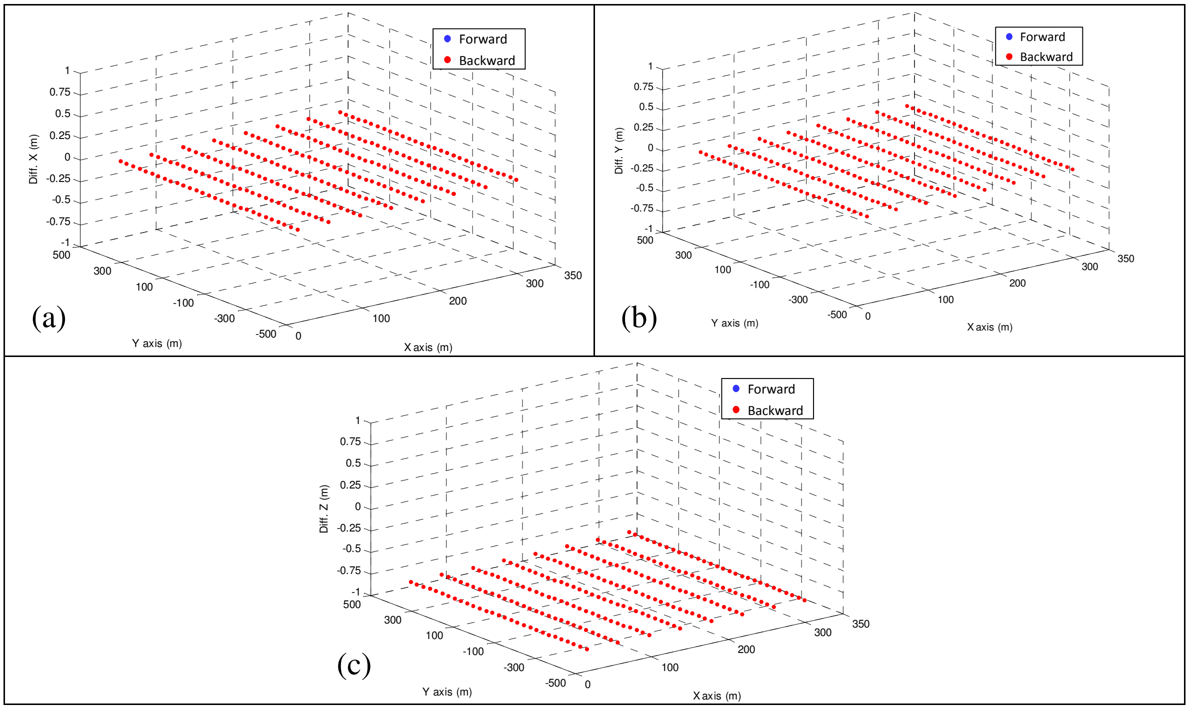

Figure 4.25. Differences between the bias-contaminated and true coordinates in the X (a), Y (b), and Z (c) directions after the introduction of a bias in the principal distance (δc) forward and backward strips at 1000 m flying height.

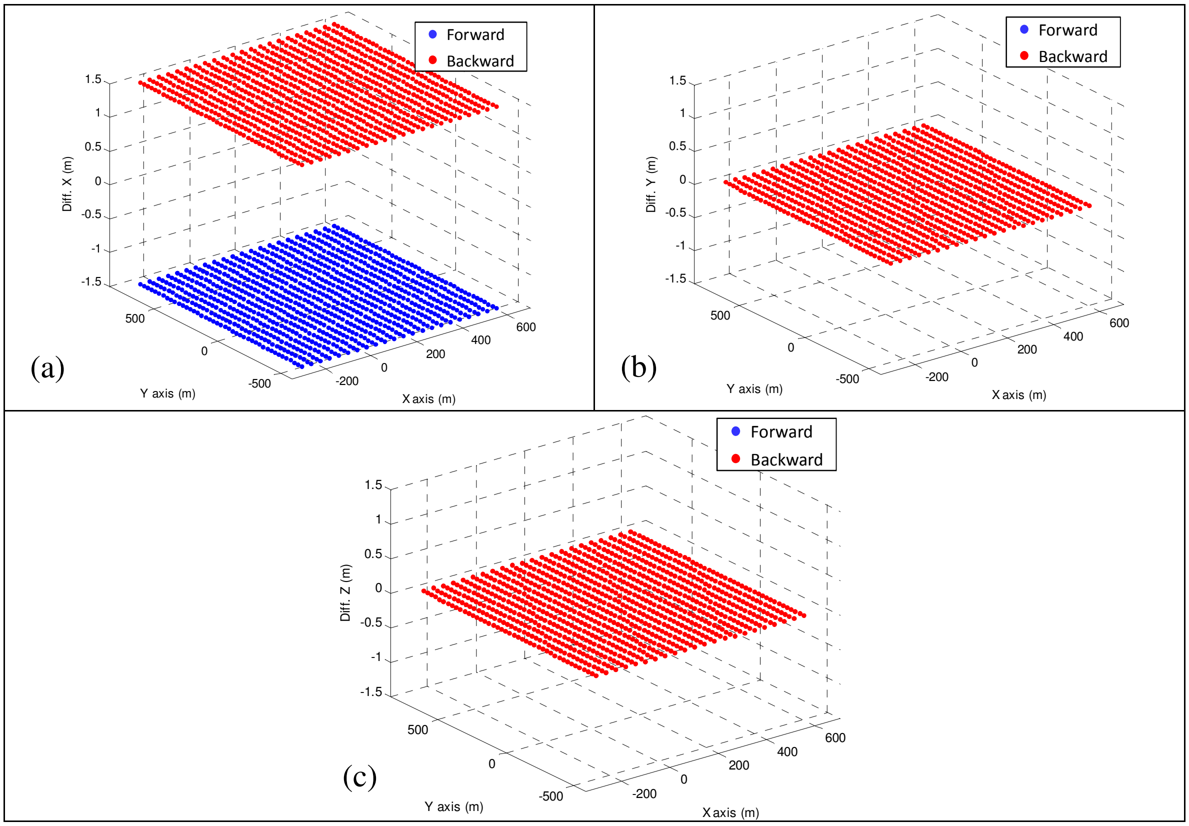

Figure 4.26. Differences between the bias-contaminated and true coordinates in the X (a), Y (b), and Z (c) directions after the introduction of a bias in the principal point coordinate δx_p for forward and backward strips at 1800 m flying height.

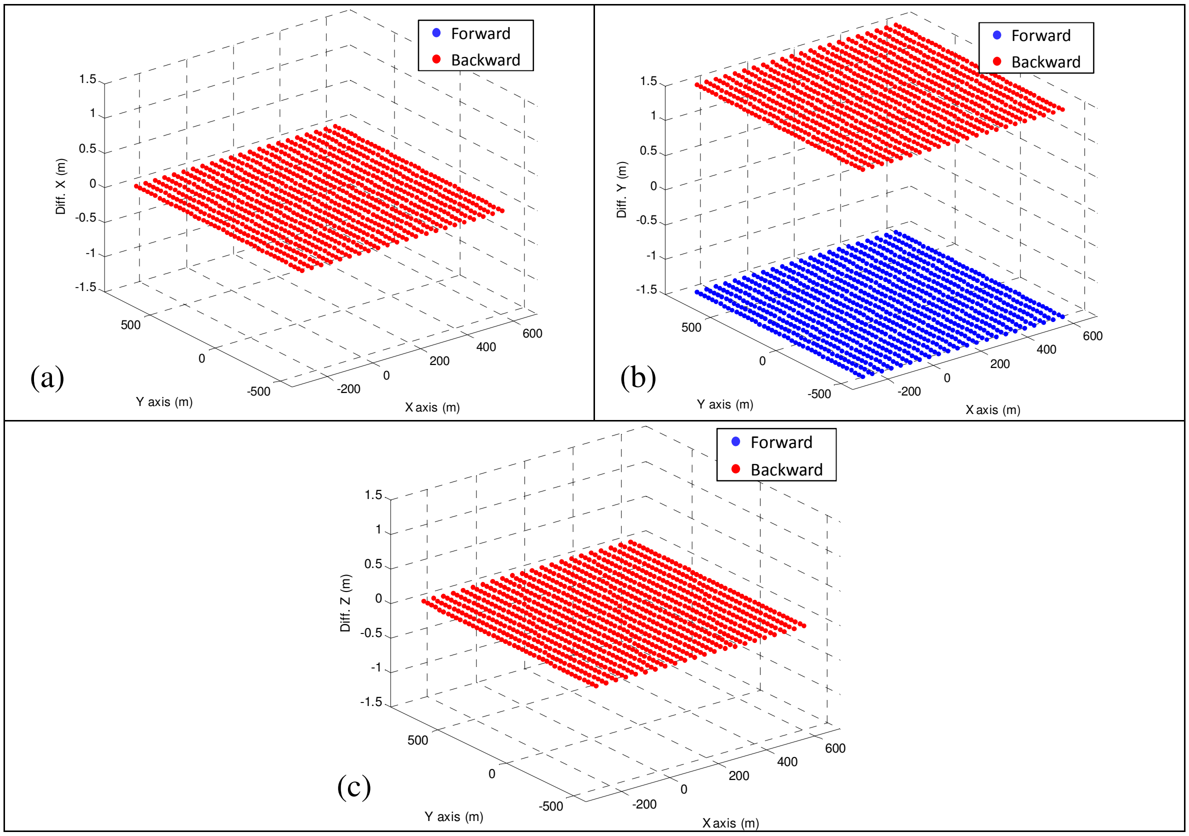

Figure 4.27. Differences between the bias-contaminated and true coordinates in the *X* (a), *Y* (b), and *Z* (c) directions after the introduction of a bias in the principal point coordinate δy_p for forward and backward strips at 1800 m flying height.

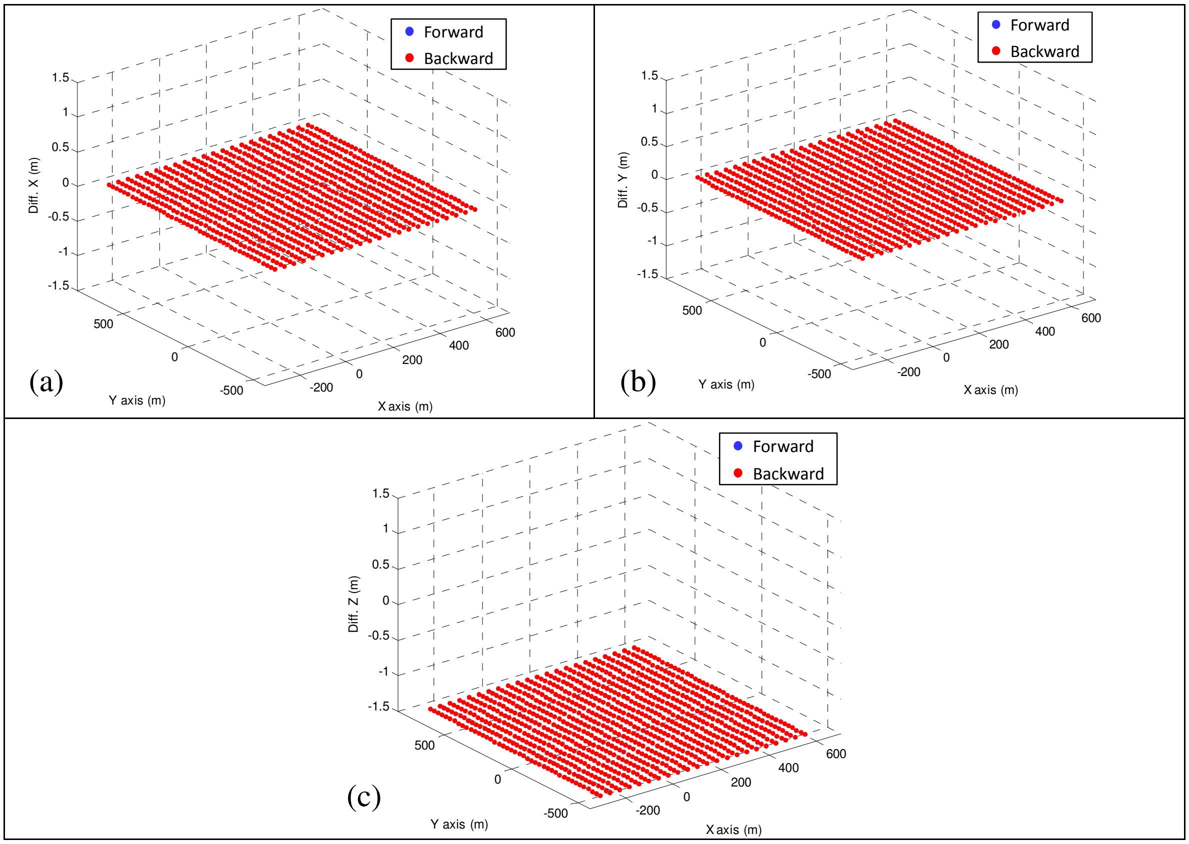

Figure 4.28. Differences between the bias-contaminated and true coordinates in the X (a), Y (b), and Z (c) directions after the introduction of a bias in the principal distance δc for forward and backward strips at 1800 m flying height.

A summary of the impacts of investigated biases on the reconstruction process (whether they introduce y-parallax among conjugate light rays from a stereo-pair from the same flight line) as well as on the reconstructed object space (as they relate to the flying direction, flying height, and point coordinates) is presented in Table 4.9. One can note that all parameters can be recovered either by minimizing the y-parallax among conjugate light rays in overlapping imagery or by minimizing the discrepancy between object points reconstructed from different flight lines except the vertical component of the lever arm offset, which requires control information.

Table 4.9. Summary of the impact of biases in the photogrammetric system parameters on the reconstruction process and on the reconstructed object space derived from the second proposed analysis (mathematical derivation and simulation process).

Parameter	y-parallax	Discrepancies: Flying Direction/ Flying Height/ Point Coord. Dependent	Control Requirement
planimetric lever arm offset components	No	Yes/No/No	No
vertical lever arm offset component	No	No/No/No	Yes
boresight roll	No	Yes/Yes/Yes	No
boresight Pitch	Yes	Yes/Yes/Yes	No
boresight yaw	Yes	No/Yes/Yes	No
principal point coordinates	No	Yes/Yes/No	No
principal distance	No	No/Yes/No	No

4.2.3 Concluding Remarks on the Flight and Control Configuration Requirements for Photogrammetric System Calibration

Based on the impact of the biases in the system parameters on the reconstruction process and the reconstructed object space, mathematically derived and verified through simulations, one could check whether the system parameters can be recovered and what would be the minimum requirements for that while considering parallel flight lines (since they are more convenient and practical to obtain when compared to cross flight lines). Also, the optimum flight configuration that maximizes the impact of biases in the system parameters and therefore increases the reliability of the estimated parameters can be devised as well. A summary of the outcome from the proposed analysis as well as the minimum and optimum requirements for the recovery of the system parameters are provided below:

- Planimetric lever arm offset components: the conducted analysis has shown that the biases in the planimetric lever arm offset components will not introduce *y*-parallax among conjugate light rays from directly geo-referenced stereo-imagery from the same flight line. On the other hand, biases in the planimetric lever arm offset components will cause discrepancies between the object space coordinates derived from flight lines captured in the opposite directions, and therefore control information is not needed.
    - Minimum requirement: two strips captured in opposite directions with some percentage of side lap.
    - Optimum requirement: two strips captured in opposite directions with 100% side lap (the impact of the biases in the boresight yaw angle is eliminated).
- Vertical lever arm offset component: the conducted analysis has shown that a bias in the vertical component of the lever arm offset will not introduce *y*-parallax among conjugate light rays from directly geo-referenced stereo-imagery from the same flight line. The conducted analysis has also shown that the vertical component of the lever arm offset cannot be estimated by observing discrepancies between the object space coordinates derived from different flight lines (assuming a vertical system/constant attitude). Such inability is caused by the fact that a vertical bias in the lever arm offset produces the same effect regardless of the flying direction, flying height, or image point coordinates. Therefore, control information is required.
    - Minimum requirement: one vertical control point.
    - Optimum requirement: one vertical control point that is visible in as many images as possible.
- Boresight roll angle: the conducted analysis has shown that a bias in the boresight

roll angle will not introduce *y*-parallax among conjugate light rays from directly geo-referenced stereo-imagery from the same flight line. On the other hand, the conducted analysis has shown that a bias in the boresight roll angle will cause discrepancies between the object space coordinates derived from different flight lines and therefore control information is not needed.

  - Minimum requirement: two strips with some percentage of side lap.
  - Optimum requirement: two strips captured in opposite directions with 100% side lap (the vertical discrepancy among reconstructed points from the flight lines caused by a bias in the boresight roll angle is maximized and the impact of a bias in the boresight yaw angle is eliminated).

- Boresight pitch angle: the conducted analysis has shown that a bias in the boresight pitch angle will lead to *y*-parallax between conjugate light rays from directly geo-referenced stereo-imagery from the same flight line. Therefore, the boresight pitch angle can be estimated through the elimination/minimization of the *y*-parallax among conjugate light rays in stereo-imagery. The conducted analysis has also shown that a bias in the boresight pitch angle will cause discrepancies between the object space coordinates derived from different flight lines.
  - Minimum requirement: stereo-imagery.
  - Optimum requirement: two strips captured in opposite directions with 100% side lap (the vertical discrepancy among reconstructed points from the flight lines caused by a bias in the boresight pitch angle is maximized and the impact of a bias in the boresight yaw angle is eliminated).

- Boresight yaw angle: the conducted analysis has shown that a bias in the boresight yaw angle will lead to *y*-parallax between conjugate light rays from directly georeferenced stereo-imagery from the same flight line. Therefore, this parameter can also be estimated through the elimination/minimization of the *y*-parallax among conjugate light rays in stereo-imagery. The conducted analysis has also shown that a bias in the boresight yaw angle will cause discrepancies between the object space coordinates derived from different flight lines (exception: strips with 100% side lap).

  - Minimum requirement: stereo-imagery.
  - Optimum requirement: two strips captured in the same direction with minimum side lap (while having proper tying among the images from the two flight lines). One can note that the impact on strips flown in opposite directions is the same as on those flown in the same direction. Strips flown in the same direction are recommended because in such strips, the effect of biases in the planimetric lever arm offset components is eliminated. Also, the impact of the biases in the boresight pitch and roll angles on the along and across flight direction, respectively, are eliminated as well. Using minimum side lap between the strips will maximize the discrepancy among conjugate reconstructed points (from the two strips) caused by a bias in the boresight yaw angle.

- Principal point coordinates: the conducted analysis has shown that biases in the principal point coordinates will not introduce *y*-parallax among conjugate light rays from directly geo-referenced stereo-imagery from the same flight line. On the other hand, biases in the principal point coordinates will cause discrepancies between the object space coordinates derived from different flight lines, except for strips captured in the same direction. However, for a given flying height, the principal point coordinates and the planimetric lever arm offset components are 100% correlated.

  - Minimum requirement to allow for simultaneous recovery of the planimetric lever arm offset components and the principal point coordinates: four strips (i.e., two strip pairs) captured from two different flying heights in opposite directions with some percentage of side lap.
  - Optimum requirement: four strips (i.e., two strip pairs) captured from two different flying heights in opposite directions with 100% side lap.

- Principal distance: the conducted analysis has shown that a bias in the principal distance will not introduce *y*-parallax among conjugate light rays from directly geo-referenced stereo-imagery from the same flight line. On the other hand, a bias in the principal distance can be detected by observing discrepancies between the object space coordinates derived from flight lines flown at different flying heights. Therefore, control information is not required.

- Minimum requirement: two strips flown at different flying heights.
- Optimum requirement: two strips flown at different flying heights.

In summary, the optimum flight and control configuration for reliable estimation of the mounting parameters consists of two side lap cases and one vertical control point. The first side lap case entails two strips captured in opposite directions with 100% side lap (as much overlap as possible), while the second side lap case consists of two strips, which are flown in the same direction with the least side lap possible (the minimum possible side lap where proper tying among the images from the two flight lines is still guaranteed) (Figure 4.29). On the other hand, the optimum flight and control configuration to reliably and simultaneously estimate the mounting parameters, the principal point coordinates, and the principal distance should consist of three side lap cases and one vertical control point as illustrated in Figure 4.30. As demonstrated in this figure, the optimum flight configuration consists of four strips which are captured from two flying heights in opposite directions with 100% side lap, and two strips, which are flown in the same direction with the least side lap possible (while having proper tying among the images from the two flight lines).

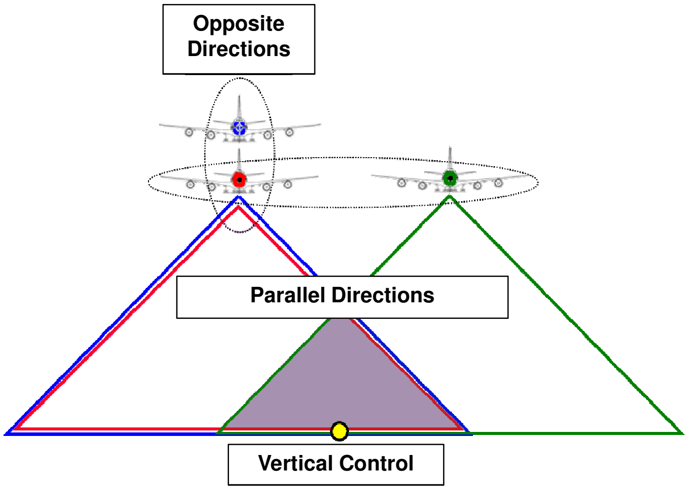

Figure 4.29. Optimum flight and control configuration for the estimation of the system mounting parameters.

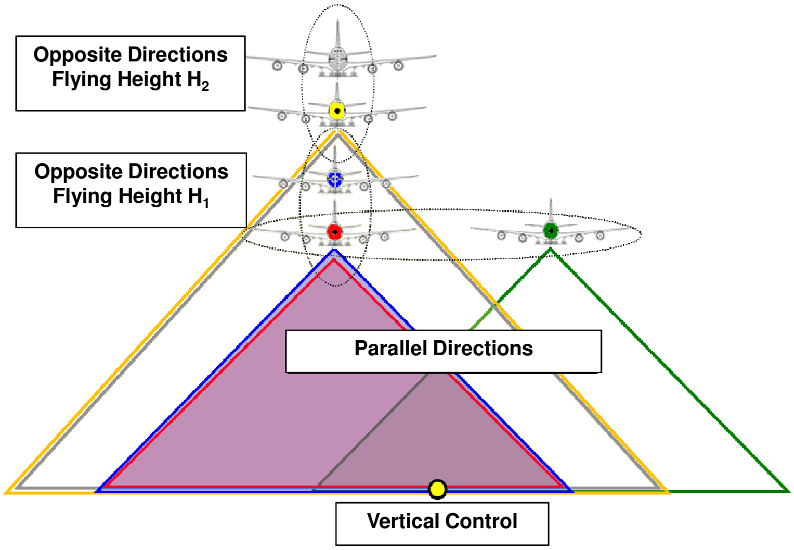

Figure 4.30. Optimum flight and control configuration for the estimation of the mounting parameters, the principal point coordinates, and the principal distance.

4.3 Flight and Control Requirements: LiDAR Systems

In this section, the proposed rigorous analysis of flight and control requirements for the calibration of airborne LiDAR systems is presented. The conceptual basis/rationale behind of the proposed rigorous analysis has been presented in section 4.1 and is now explicitly discussed for LiDAR systems:

I. Impact on the reconstruction process: For LiDAR systems, reconstruction will always occur regardless of the presence/absence of biases in the system parameters. More specifically, the LiDAR point reconstruction model is based on three equations and three unknowns for each laser pulse. Therefore, biases in the system parameters cannot be estimated by minimizing their impact on the reconstruction process.

II. Impact on the precision of the object space reconstructed from different flight lines: If the LiDAR system is properly calibrated and geo-referenced, conjugate surface elements from different flight lines should coincide with each other (regardless of the flight direction/configuration). Therefore, one should analyze whether inaccurate/biased parameters would lead to biases in the derived object points, whose magnitudes and directions depend on the flight configuration. In such a case, one can devise a flight configuration that maximizes the impact of biases in the system parameters on the derived point cloud. Therefore, using such a configuration, the system parameters can be estimated while reducing the discrepancy among the derived points from different flight lines (i.e., achieving the best precision of the derived object points). The parameters falling in this category can be estimated without the need for any ground control points.

III. Impact on the accuracy of the reconstructed object space: If the LiDAR system is properly calibrated and geo-referenced, conjugate surface elements from different flight lines should coincide with the ground truth (control surface). For biased system parameters, which will not cause discrepancies between derived points from different flight lines in a given flight configuration, control points will be utilized to estimate such parameters. In other words, the parameters falling in this category will be estimated while reducing the discrepancy between the derived point cloud and the provided control (i.e., achieving the best accuracy of the derived object points).

Similar to what was done for the photogrammetric system, the impact of biases in the system parameters on the derived point cloud will be derived by mathematical analysis of the LiDAR point positioning equation. Such analysis will be verified through a simulation process.

The following assumptions are considered in the proposed analysis: (i) Linear scanner; (ii) Flight lines follow a straight-line trajectory with constant attitude; (iii) LiDAR system is almost vertical; (iv) Flying directions parallel to the positive and negative directions of the *Y*-axis of the mapping frame; and (v) Small boresight pitch ($\delta\Delta\omega$), roll ($\delta\Delta\varphi$), and yaw ($\delta\Delta\omega$) angles.

After considering these assumptions, the LiDAR point positioning mathematical model presented in Equation 3.3 can be simplified to the form in Equation 4.26. The multiple signs ($\pm, \mp$) in Equation 4.26 signify the impacts on forward and backward strips with the top sign always corresponding to the forward strip (i.e., the system is flying along the positive direction of the *Y*-axis). One should note that the mathematical derivations consider the convention right-forward-up (right-handed) for the laser unit and IMU body frame coordinate systems with the *Y*-axis along the flight direction.

$$r_I^m = r_b^m + \begin{bmatrix} cos\kappa & -sink & 0 \\ sink & cos\,\kappa & 0 \\ 0 & 0 & 1 \end{bmatrix} \begin{bmatrix} \mathit{\Delta X} \\ \mathit{\Delta Y} \\ \mathit{\Delta Z} \end{bmatrix} + \begin{bmatrix} cos\kappa & -sink & 0 \\ sink & cos\kappa & 0 \\ 0 & 0 & 1 \end{bmatrix} \begin{bmatrix} 1 & -\mathit{\Delta}\kappa & \mathit{\Delta}\varphi \\ \mathit{\Delta}\kappa & 1 & -\mathit{\Delta}\omega \\ -\mathit{\Delta}\varphi & \mathit{\Delta}\omega & 1 \end{bmatrix} \begin{bmatrix} -(\rho + \Delta\rho)sin(S\beta) \\ 0 \\ -(\rho + \Delta\rho)cos(S\beta) \end{bmatrix} =$$

$$= r_b^m + \begin{bmatrix} \pm\Delta X \\ \pm\Delta Y \\ \Delta Z \end{bmatrix} + \begin{bmatrix} \pm 1 & \mp\Delta\kappa & \pm\Delta\varphi \\ \pm\Delta\kappa & \pm 1 & \mp\Delta\omega \\ \mp\Delta\varphi & \pm\Delta\omega & \pm 1 \end{bmatrix} \begin{bmatrix} x \\ 0 \\ z \end{bmatrix} \tag{4.26}$$

where:

- z is the vertical coordinate of the laser point with respect to the laser unit coordinate system; and
- x is the lateral coordinate of the laser point with respect to the laser unit coordinate system.

The LiDAR point coordinates (r_I^m) are function of the system parameters ($\vec{x}$), as presented in Equation 4.27. In the presence of biases in the system parameters ($\delta\vec{x}$), the LiDAR point coordinates will become biased. The impact of biases in the system parameters on the LiDAR point coordinates (δr_I^m) will be derived by differentiating the LiDAR point positioning equation (Equation 4.26) with respect to the system parameters as shown in Equation 4.28 while ignoring higher order terms. The impact of each of the investigated system parameters on the derived point cloud is presented in Table 4.10.

$$r_I^m = f(\vec{x}) \tag{4.27}$$

where:

- $\vec{x} = (\Delta X, \Delta Y, \Delta Z, \Delta\omega, \Delta\varphi, \Delta\kappa, \mathit{\Delta}\rho, S)$.

$$\delta r_I^m = \frac{\partial r_I^m}{\partial \vec{x}} \delta\vec{x} \tag{4.28}$$

where:

- $\delta\vec{x} = (\delta\Delta X, \delta\Delta Y, \delta\Delta Z, \delta\Delta\omega, \delta\Delta\varphi, \delta\Delta\kappa, \delta\mathit{\Delta}\rho, \delta S)$.

Table 4.10. Impact of the biases in the system parameters on the derived point cloud coordinates.

	δX_m	δY_m	δZ_m
$\delta\Delta X$	$\pm\delta\mathit{\Delta}X$	0	0
$\delta\Delta Y$	0	$\pm\delta\mathit{\Delta}Y$	0
$\delta\Delta Z$	0	0	$\delta\mathit{\Delta}Z$
$\delta\Delta\omega$	0	$\pm z\ \delta\mathit{\Delta}\omega$	0
$\delta\Delta\varphi$	$\mp z\ \delta\mathit{\Delta}\varphi$	0	$-x\ \delta\mathit{\Delta}\varphi$
$\delta\Delta\kappa$	0	$\pm x\ \delta\mathit{\Delta}\kappa$	0
$\delta\Delta\rho$	$\mp sin(S\beta)\ \delta\mathit{\Delta}\rho$	0	$-\ cos(S\beta)\ \delta\mathit{\Delta}\rho$
δS	$\mp z\ \beta\ \delta S$	0	$-x\ \beta\ \delta S$

A simulation procedure was performed to verify the mathematically derived impact (shown in Table 4.10) of the biases in the system parameters on the derived point cloud. The simulation process starts from a given surface and trajectory, which are then used to derive the system measurements (ranges, mirror angles, position and orientation information for each pulse). Then, biases are added to the system parameters, which are used to reconstruct the surface through the LiDAR equation. The differences between the bias-contaminated and true coordinates of the footprints for different strips are used to represent the impact of a given bias in the system parameters. The following LiDAR strips were simulated:

- Strips flown in opposite directions (i.e., forward and backward directions) with 100% side lap at a flying height of 1000 m;
- Strips flown in opposite directions (i.e., forward and backward directions) with 100% side lap at a flying height of 2000 m;
- Strips flown in the same direction with 50% side lap at a flying height of 1000 m.

The configuration of the simulated LiDAR strips and the magnitude of the introduced biases are reported in Table 4.11. To improve the clarity of the display of the biases' impact on the derived point cloud, a horizontal flat terrain was simulated.

Table 4.11. Simulated LiDAR data configuration.

Flying height:	1000 and 2000 m
Flying Direction:	along the *Y*-axis
PRF:	50 kHz
Scan Frequency:	33 Hz
Scan Angle:	-10° to $+10^{\circ}$
Lever arm biases $\delta\Delta X$, $\delta\Delta Y$ and $\delta\Delta Z$:	15cm, 15cm, and 15cm
Boresight angle biases $\delta\Delta\omega$, $\delta\Delta\varphi$ and $\delta\Delta\kappa$:	720sec, 720sec, and 720sec
Scan Angle Scale Bias δS:	0.01
Range Bias $\delta\Delta\rho$:	50 cm

To illustrate the simulation results, plots with the impact of biases in the system parameters in the *X*, *Y*, and *Z* coordinates of the derived points are generated. In the *X* and *Y*-axes of the produced plots, the true *X* and *Y* coordinates of the points are presented. On the other hand, the differences between the bias-contaminated and the true *XYZ* coordinates of the derived points from different LiDAR strips (such as forward and backward strips or two strips in the same direction) are presented in the *Z*-axis of the produced plots. When only the impact of one of the flight lines is being displayed, means that its impact is coincident with the impact of the other flight line and therefore the impact of one of the flight lines is hidden. To improve the clarity, the scale utilized to produce the plots is different for the considered biases and its impact in the X, Y, and Z directions.

The analysis is first conducted for the derived point cloud from parallel flight lines flown in opposite directions with 100% side lap at a flying height of 1000 m. In case such configuration does not allow for the estimation of the parameter in question, the other simulated flight configurations are analyzed (flight lines flown at a different flying height and flight lines flown in the same direction with 50% side lap).

The differences in the X, Y, and Z directions between the reconstructed point cloud after the introduction of biases in the lever arm offset components $\delta\Delta X$, $\delta\Delta Y$, and $\delta\Delta Z$ and the true point cloud are illustrated in Figures 4.31a – 4.31c, 4.32a – 4.32c, and 4.33a – 4.33c, respectively, for forward and backward strips flown at a flying height of 1000 m. As for the photogrammetric system, biases in the lever arm offset components of LiDAR systems will lead to constant shifts in the derived object space (refer to Figures 4.31, 4.32, and 4.33). The magnitudes of these shifts are equivalent to the introduced biases in the lever arm offset components. Also, Figures 4.31a and 4.32b reveal that the horizontal impact of biases in the planimetric lever arm offset components are dependent on the flying direction (i.e., the effect is different for backward and forward strips). Such finding reveals the possibility of estimating planimetric components of the lever arm offset by having flight lines in opposite directions. The vertical impact of the vertical lever arm offset component (Figure 4.33c), on the other hand, is independent of the flying direction (i.e., the effect is the same for backward and forward strips). Therefore, it is not possible to recover the vertical component of the lever arm offset by having flight lines flown in opposite directions at a given flying height. The planimetric and vertical impact of biases in the lever arm offset components are independent of the scan angle (as observed in Figures 4.31 – 4.33). A simulation using strips flown at a different flying height has been performed and the derived impact was the same as the one presented in Figures 4.31 –

4.33. Such simulation results confirm that the impact of the lever arm offset components is independent of the flying height. Since a bias in the vertical component of the lever arm offset will produce the same impact regardless of the flight configuration, vertical control would be required for the estimation of such parameter.

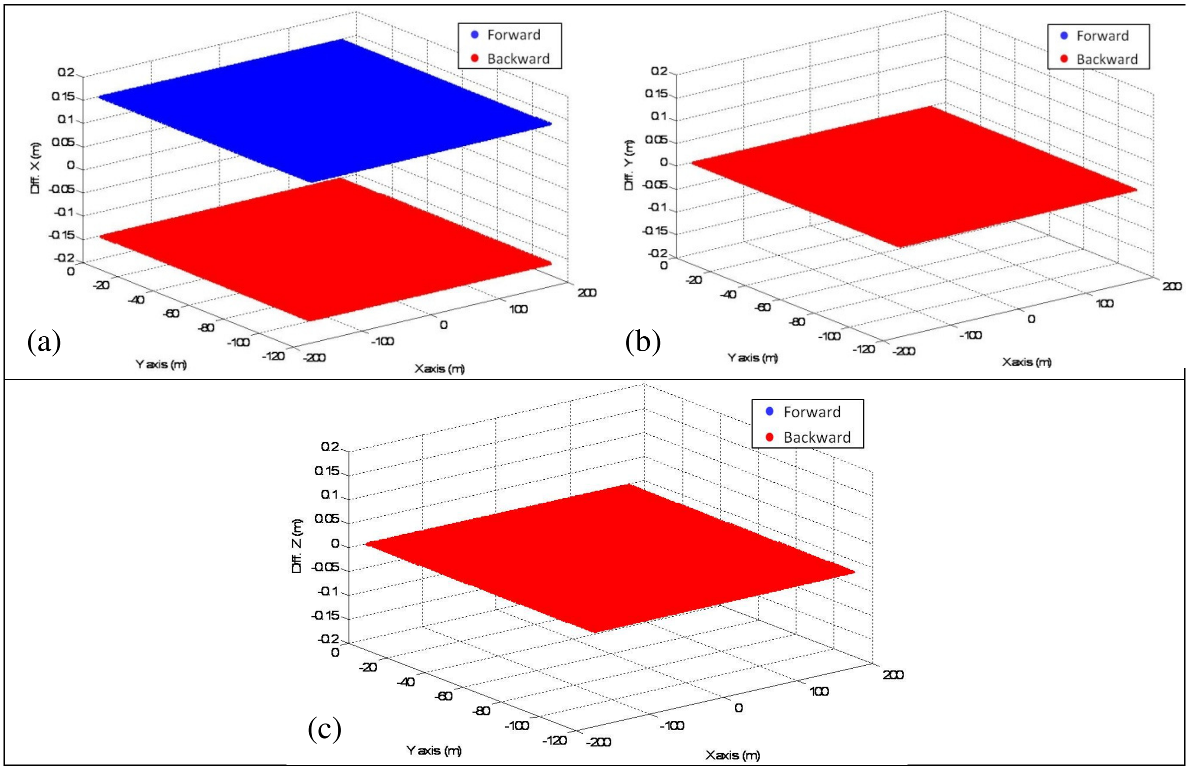

Figure 4.31. Differences between the bias-contaminated and true coordinates in the X (a), Y (b), and Z (c) directions after the introduction of a bias in the lever arm offset $\delta\Delta X$ for forward and backward strips at 1000 m flying height.

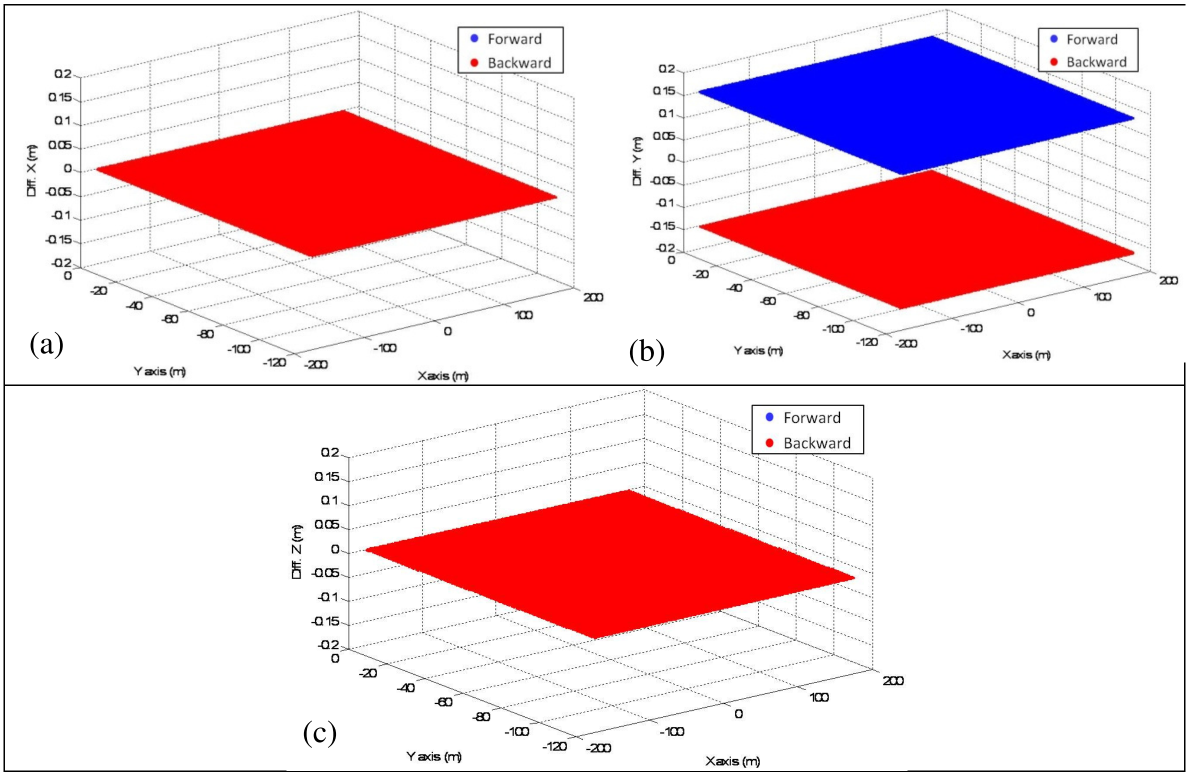

Figure 4.32. Differences between the bias-contaminated and true coordinates in the X (a), Y (b), and Z (c) directions after the introduction of a bias in the lever arm offset $\delta\Delta Y$ for forward and backward strips at 1000 m flying height.

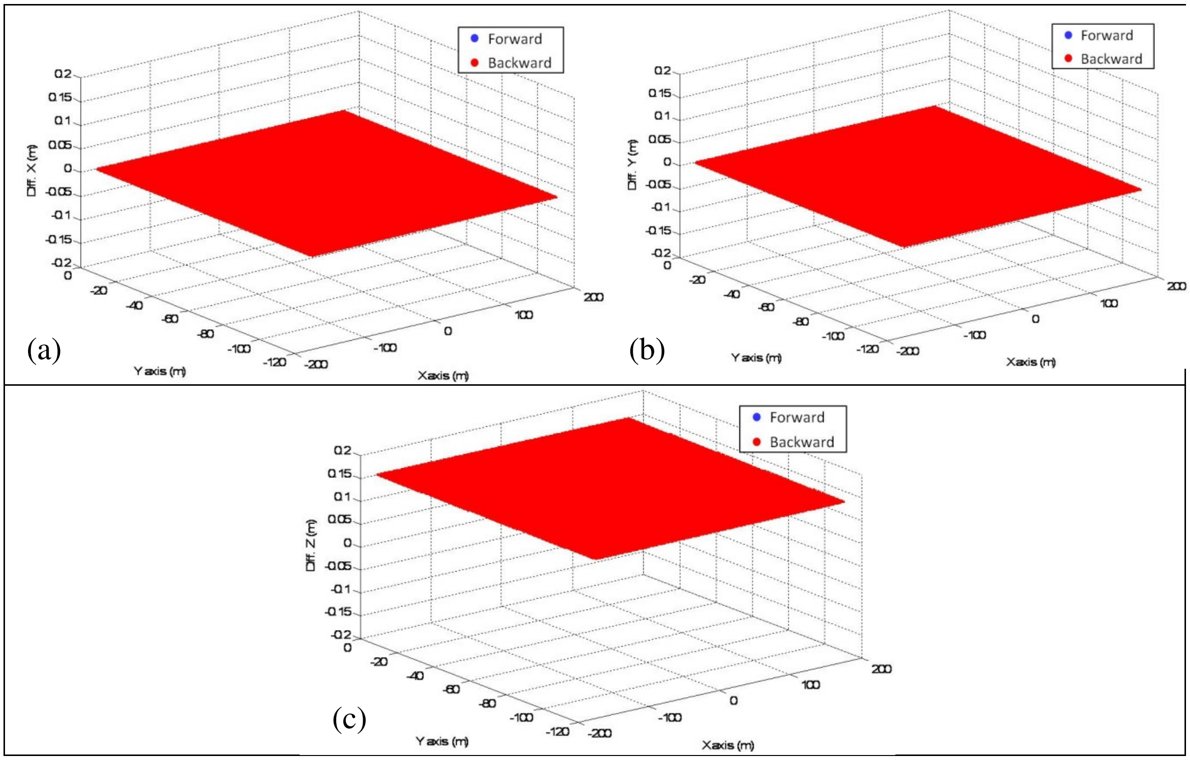

Figure 4.33. Differences between the bias-contaminated and true coordinates in the X (a), Y (b), and Z (c) directions after the introduction of a bias in the lever arm offset $\delta\Delta Z$ for forward and backward strips at 1000 m flying height.

Similarly, the differences between the reconstructed point cloud after the introduction of biases in the boresight pitch $(\delta\Delta\omega)$, roll $(\delta\Delta\varphi)$, and yaw $(\delta\Delta\kappa)$ angles and the true coordinates of the reconstructed point cloud are illustrated in Figures 4.34, 4.35 and 4.36, respectively. One can observe in Figure 4.34b that a bias in the boresight pitch angle $(\delta\Delta\omega)$ will cause a constant shift along the flight direction, which is dependent on the flying direction (different impact for forward and backward strips). Such finding reveals the possibility of estimating such parameter by having flight lines flown in opposite directions. Different from what was observed for photogrammetric systems, for LiDAR systems, the boresight pitch angle is 100% correlated with the lever am offset component in the along flight direction for a given flying height. It has already been demonstrated that the impact of the lever arm offset components is independent of the flying height. To check whether the impact of a bias in the boresight pitch angle is flying height dependent, the differences between the bias-contaminated and true coordinates of the reconstructed points from flight lines flown at a higher flying height (2000 m) have been computed. Such differences are illustrated in Figure 4.37. One can note in this figure that the impact of a bias in the boresight pitch angle is flying height dependent (i.e., the impact is amplified with an increase in the flying height). Therefore, to decouple the boresight pitch bias from the lever arm offset component in the along flight direction ($\delta\Delta Y$), flight lines captured from two different flying heights should be available.

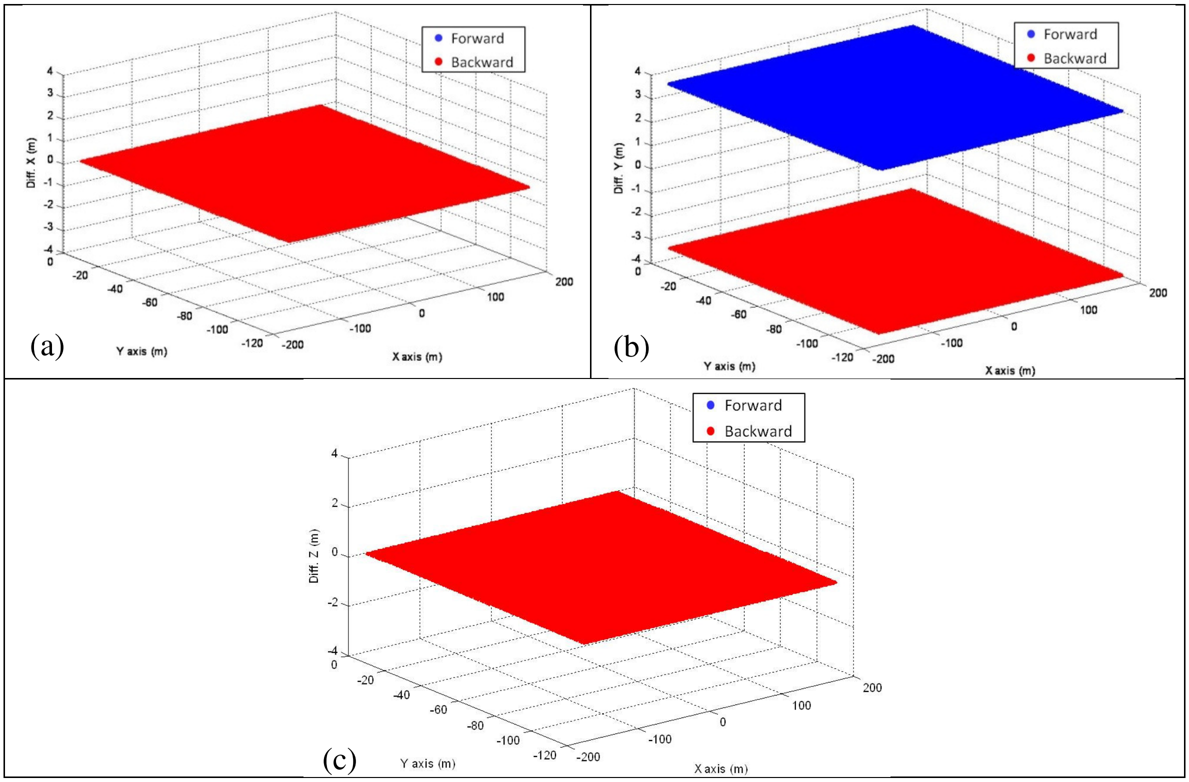

Figure 4.34. Differences between the bias-contaminated and true coordinates in the X (a), Y (b), and Z (c) directions after the introduction of a bias in the boresight pitch angle ($\delta\Delta\omega$) for forward and backward strips at 1000 m flying height.

A bias in the boresight roll angle, on the other hand, will cause a constant shift across the flight direction (i.e., the impact is scan angle independent) (Figure 4.35a) and a shift in the Z direction with its magnitude varying linearly across the flying direction (i.e., the impact is scan angle dependent) (Figure 4.35c). Both effects are dependent on the flying direction. One should note that the vertical effect decouples the boresight roll angle from the lever arm offset component in the across flight direction (i.e., it is possible to estimate those parameters simultaneously by having flight lines in opposite directions). Although for flight lines flown at the same direction, the impact in the across flight direction would be the same, the vertical impact would provide some information for the recovery of such parameter if the flight lines are flown with minimum percentage of side lap (while having enough conjugate surface elements among the strips) since its impact is dependent on the scan angle.

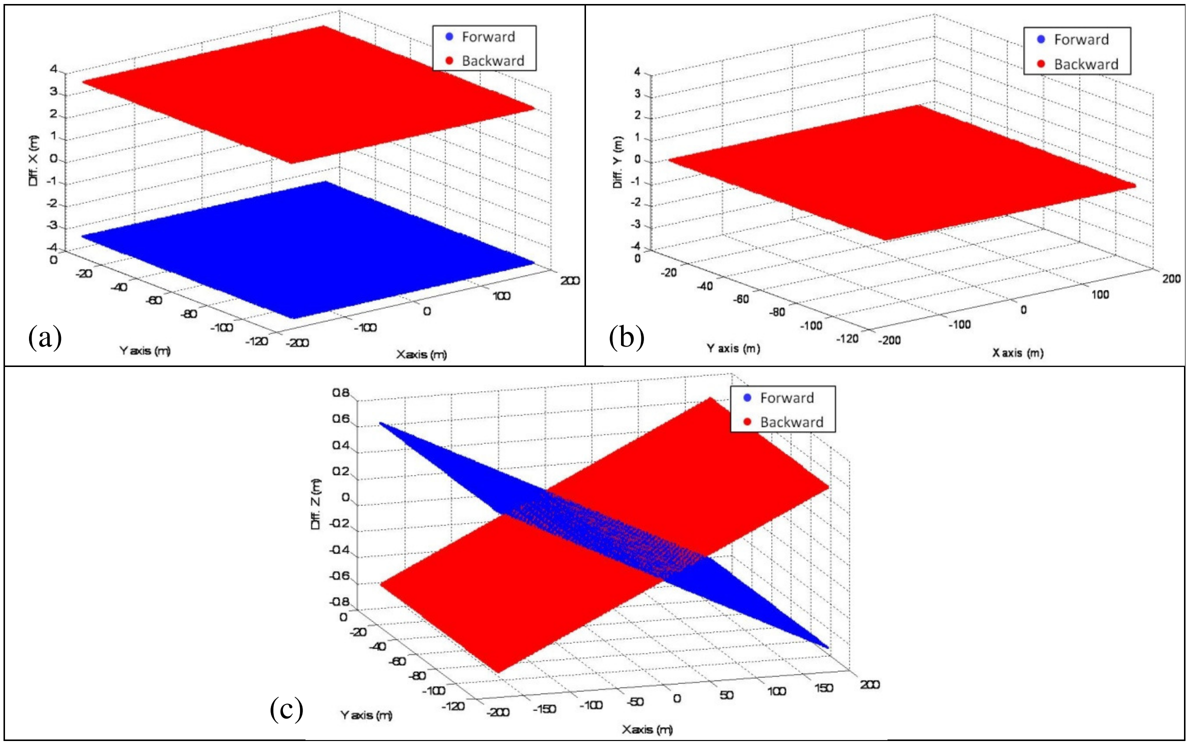

Figure 4.35. Differences between the bias-contaminated and true coordinates in the X (a), Y (b), and Z (c) directions after the introduction of a bias in the boresight roll angle ($\delta\Delta\varphi$) for forward and backward strips at 1000 m flying height.

The boresight yaw bias will only cause a shift along the flying direction with its magnitude varying linearly across the flight direction (i.e., the impact is scan angle dependent) (Figure 4.36b). This effect is independent of the flying direction. Therefore, it is not possible to estimate the boresight yaw angle by having flight lines flown with 100% side lap. However, since the impact is dependent on the scan angle, by having flight lines with minimum percentage of side lap (while having enough conjugate surface elements among the strips) will provide information for the recovery of such parameters as illustrated in Figure 4.38b.

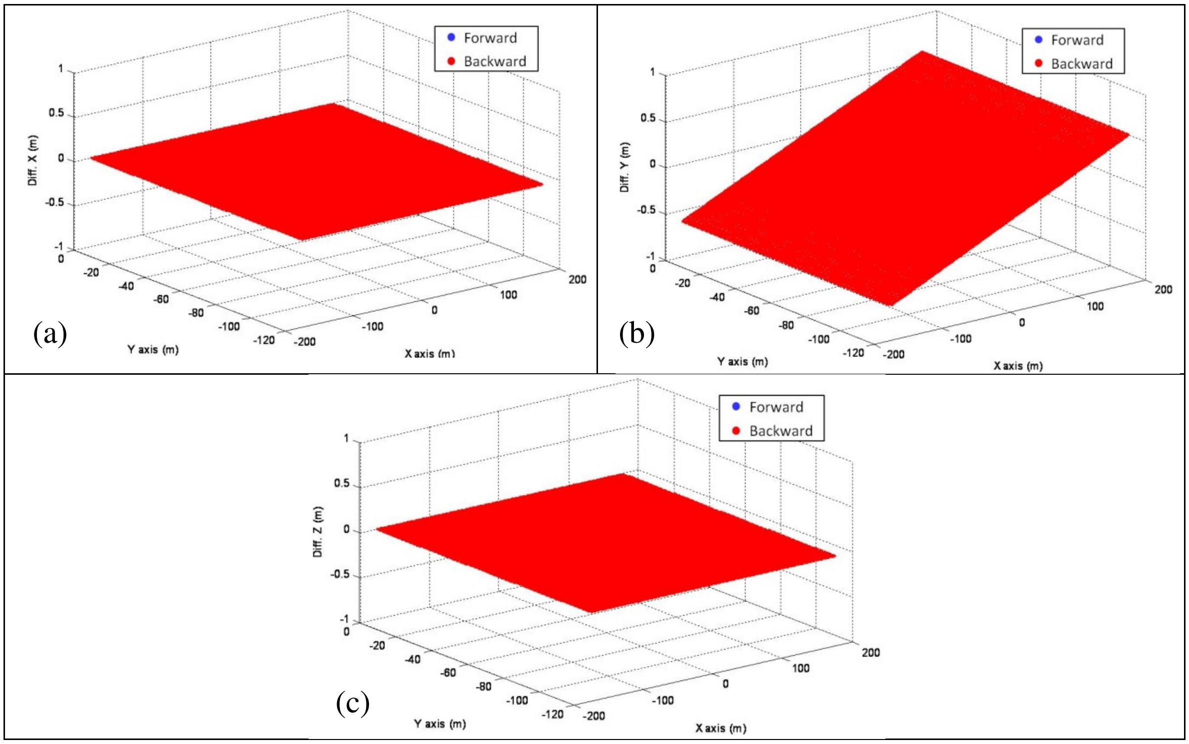

Figure 4.36. Differences between the bias-contaminated and true coordinates in the X (a), Y (b), and Z (c) directions after the introduction of a bias in the boresight yaw angle ($\delta\Delta\kappa$) for forward and backward strips at 1000 m flying height.

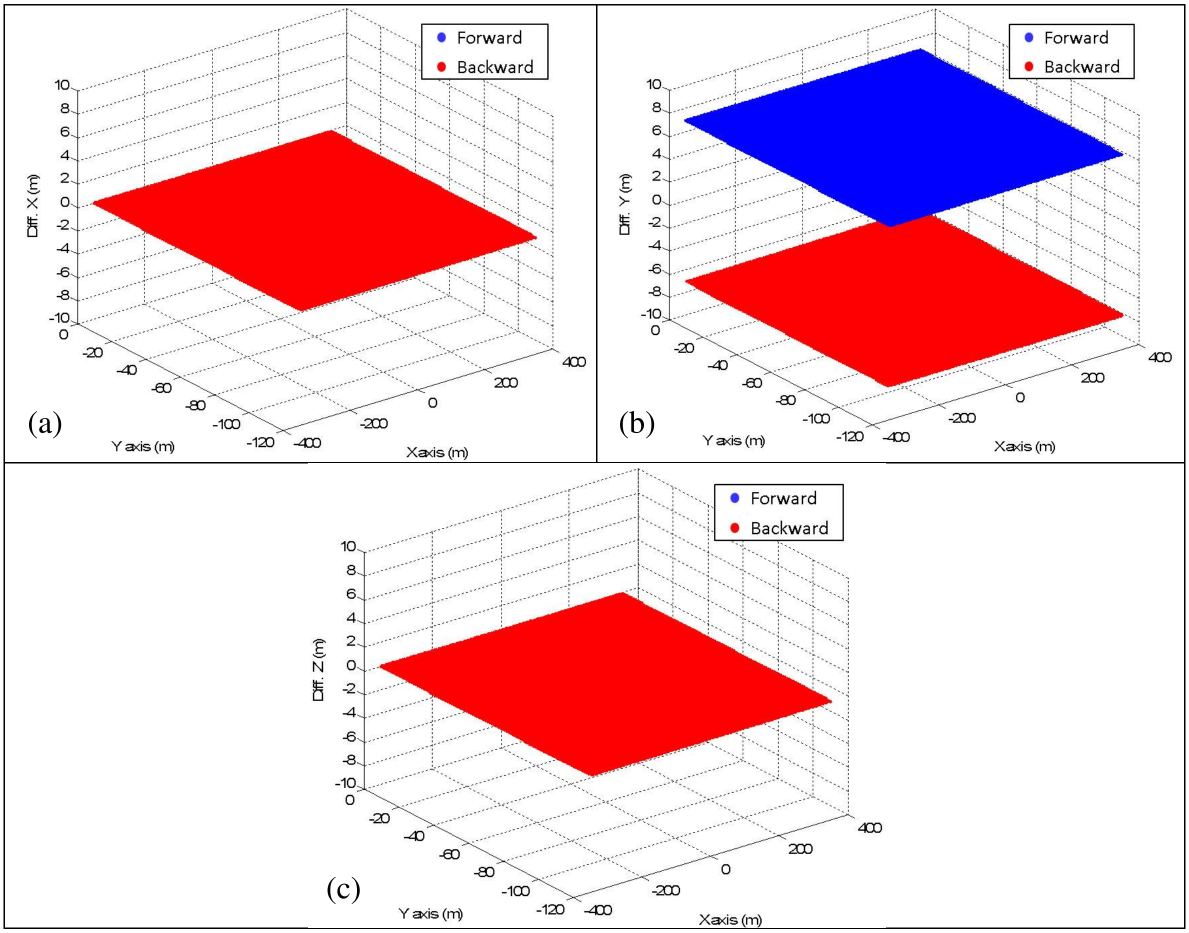

Figure 4.37. Differences between the bias-contaminated and true coordinates in the *X* (a), *Y* (b), and *Z* (c) directions after the introduction of a bias in the boresight pitch angle ($\delta\Delta\omega$) for forward and backward strips at 2000 m flying height.

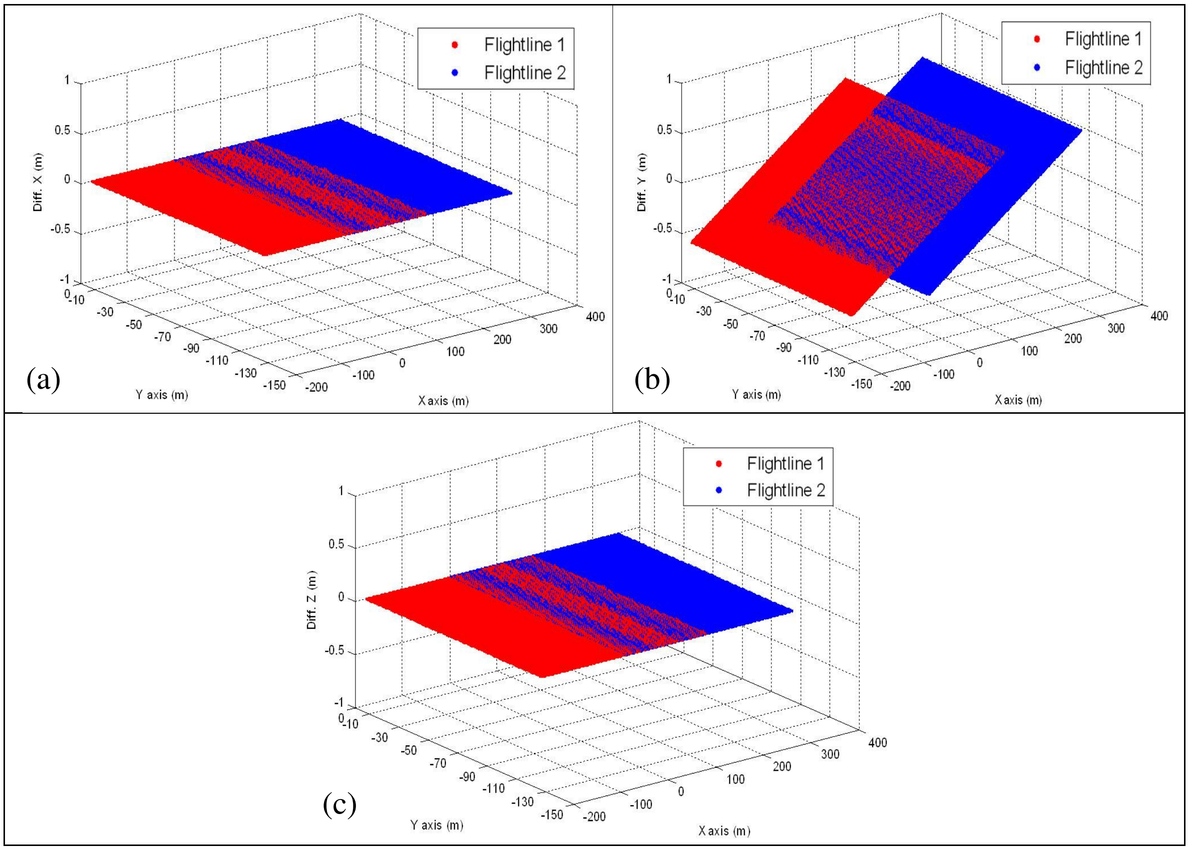

Figure 4.38. Differences between the bias-contaminated and true coordinates in the *X* (a), *Y* (b), and *Z* (c) directions after the introduction of a bias in the boresight yaw angle ($\delta\Delta\kappa$) for flight lines with 50% side lap at 1000 m flying height.

The range bias ($\delta\Delta\rho$) will cause a planimetric shift across the flying direction, whose magnitude varies almost linearly (small magnitude), as illustrated in Figure 4.39a. At the same time, the range bias will cause an almost constant vertical shift (major component), as shown in Figure 4.39c. Both effects are independent of the flying direction. Such finding reveals that it is not possible to estimate the range bias by having opposite flight lines with 100% side lap.

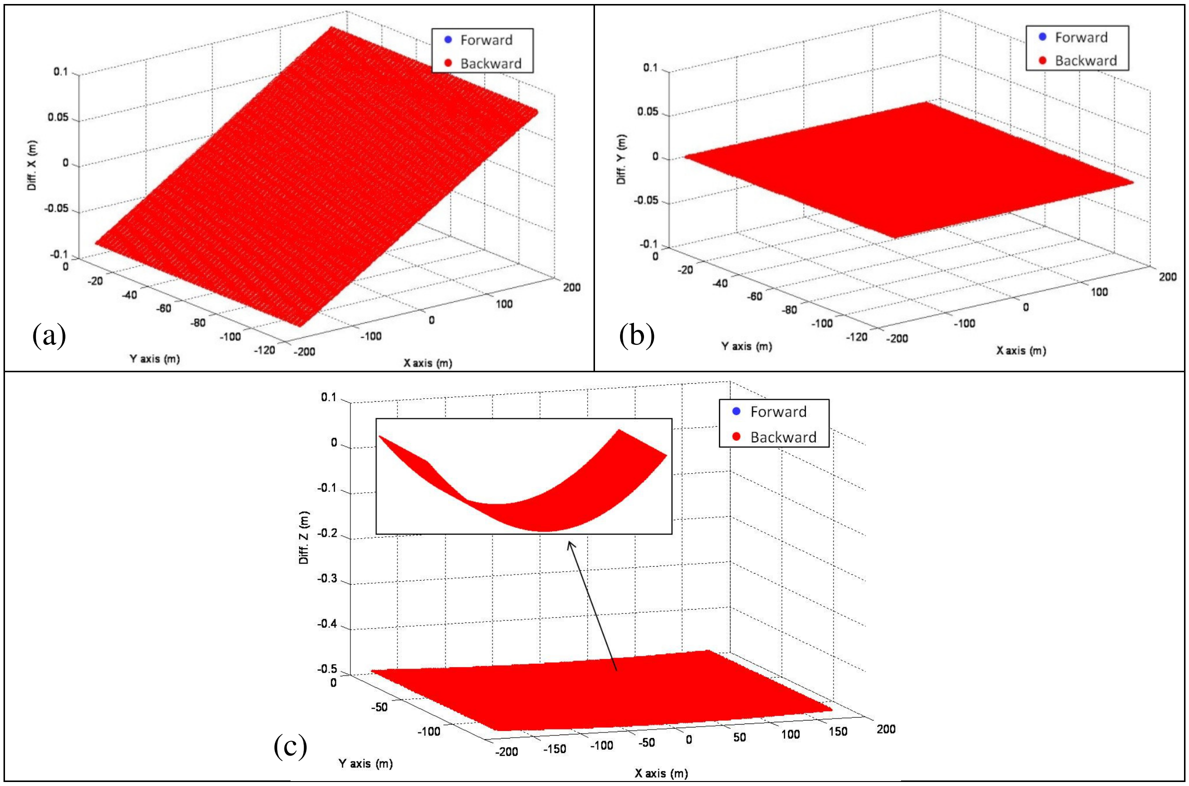

Figure 4.39. Differences between the bias-contaminated and true coordinates in the X (a), Y (b), and Z (c) directions after the introduction of a bias in the range ($\delta\Delta\rho$) for forward and backward strips at 1000 m flying height.

Figure 4.40 shows the impact of the range bias for flight lines flown with 50% side lap. One can see in Figure 4.40a that the planimetric impact is very small and as a consequence the discrepancies among conjugate surface elements would be very small, not allowing for reliable estimation of the range bias. Although the vertical impact is of higher magnitude (Figure 4.40c), the impact is almost constant (i.e., its dependency on the scan angle is not significant). As a consequence, the impact on the two strips will be almost the same, and therefore, will not provide enough information for reliable estimation of the range bias. In other words, the estimation of the range bias would be quite difficult to accomplish by evaluating/observing the discrepancies among conjugate surface elements from different strips for a given flying height. To check whether the impact of the range bias is flying height dependent, the differences between the bias-contaminated and true coordinates of the reconstructed points from flight lines flown at a higher flying height (2000m) have been computed. The impact for a given scan angle is the same for two strips flown at different flying heights as illustrated in Figure 4.41. On the other hand, the impact for conjugate points will be different. One should note that although for conjugate points there will be discrepancy, here again the magnitude of such discrepancy is very small (the impact is almost constant). Therefore, control information would be required for reliable estimation of such parameter. One should note that the range bias is highly correlated with the vertical bias in the lever arm offset component (i.e., they produce almost the same impact). As a result, such parameters cannot be estimated simultaneously.

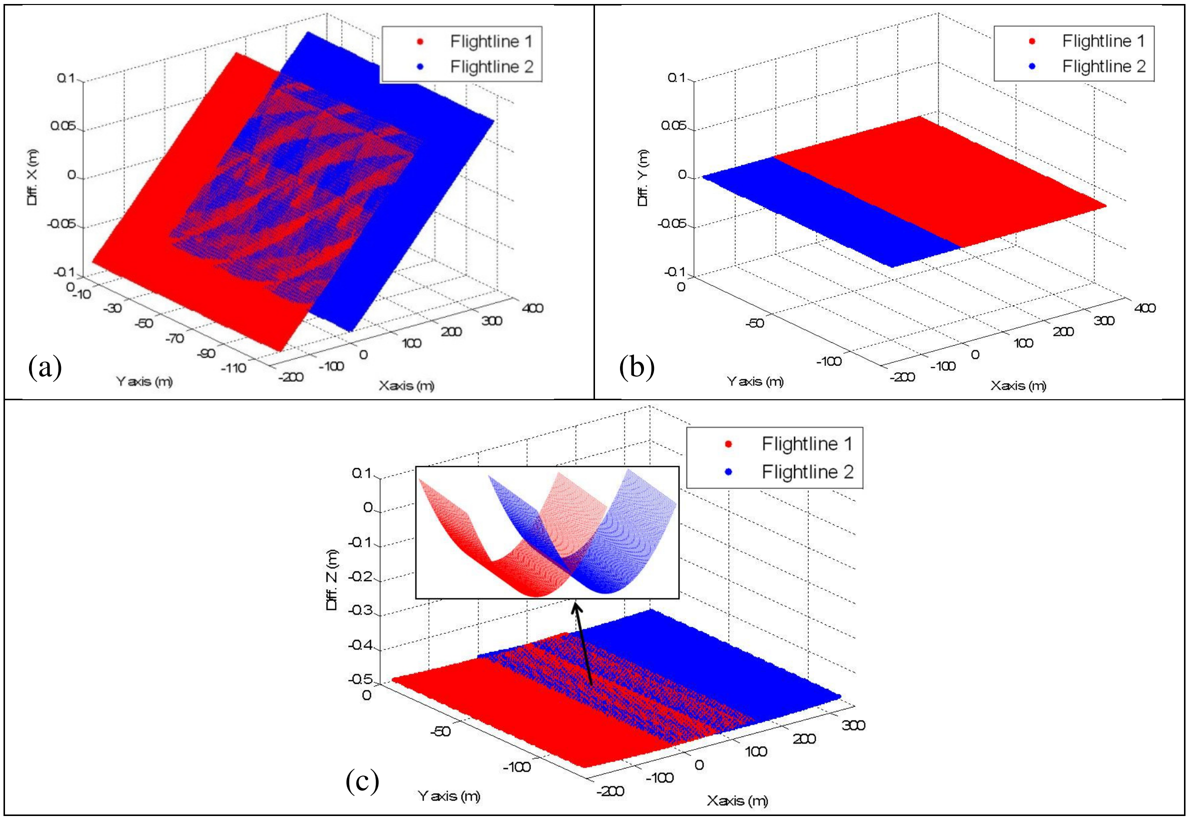

Figure 4.40. Differences between the bias-contaminated and true coordinates in the X (a), Y (b), and Z (c) directions after the introduction of a bias in the range ($\delta\Delta\rho$) for flight lines flown with 50% side lap at 1000 m flying height.

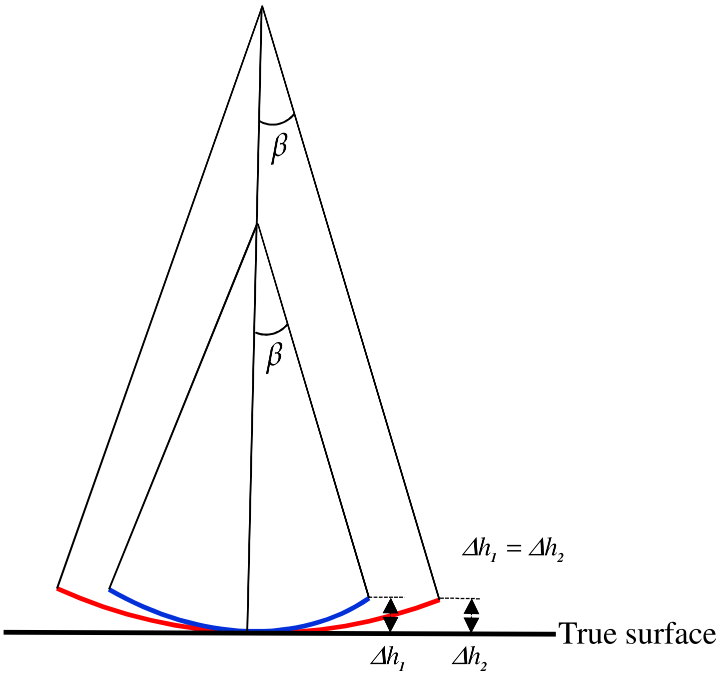

Figure 4.41. Vertical impact of the range bias on strips captured at different flying heights.

The mirror angle scale bias will cause a planimetric shift across the flying direction, whose magnitude varies linearly (Figure 4.42a). At the same time, it causes a vertical shift, whose magnitude varies non-linearly across the flying direction (Figure 4.42c). Both effects are independent of the flying direction. This reveals that it is not possible to estimate such a parameter by having opposite flight lines with 100% side lap. On the other hand, since the planimetric and the vertical impacts are dependent on the scan angle, by having flight lines with some percentage of side lap (while having enough conjugate surface elements among the strips) will allow for the parameter estimation as illustrated in Figures 4.43a and 4.43c. One should note that the magnitude of the planimetric and vertical discrepancies among conjugate surface elements caused by a bias in the mirror angle scale are of larger magnitude than that the discrepancies caused by a bias in the range. Therefore, such discrepancies allow for the estimation of the mirror angle scale. For reliable estimation of such parameter well distributed data in the across flight direction should be utilized.

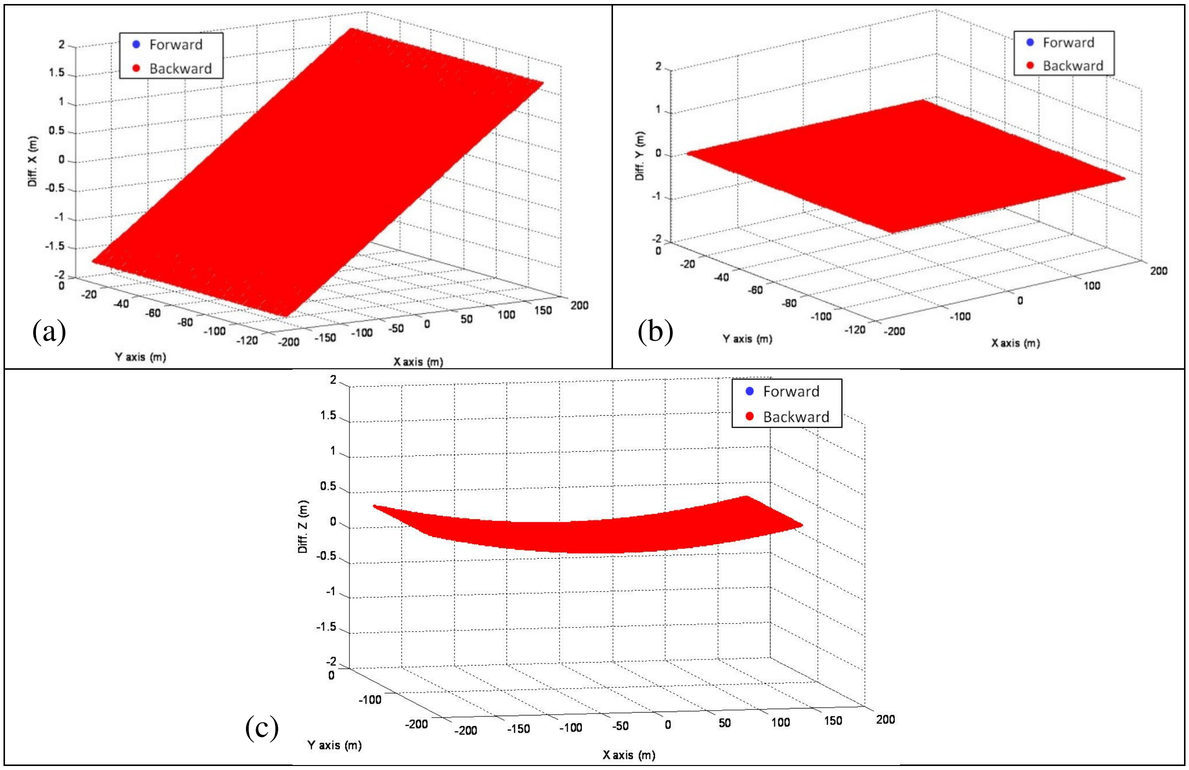

Figure 4.42. Differences between the bias-contaminated and true coordinates in the X (a), Y (b), and Z (c) directions after the introduction of a bias in the mirror angle scale (δS) for forward and backward strips at 1000 m flying height.

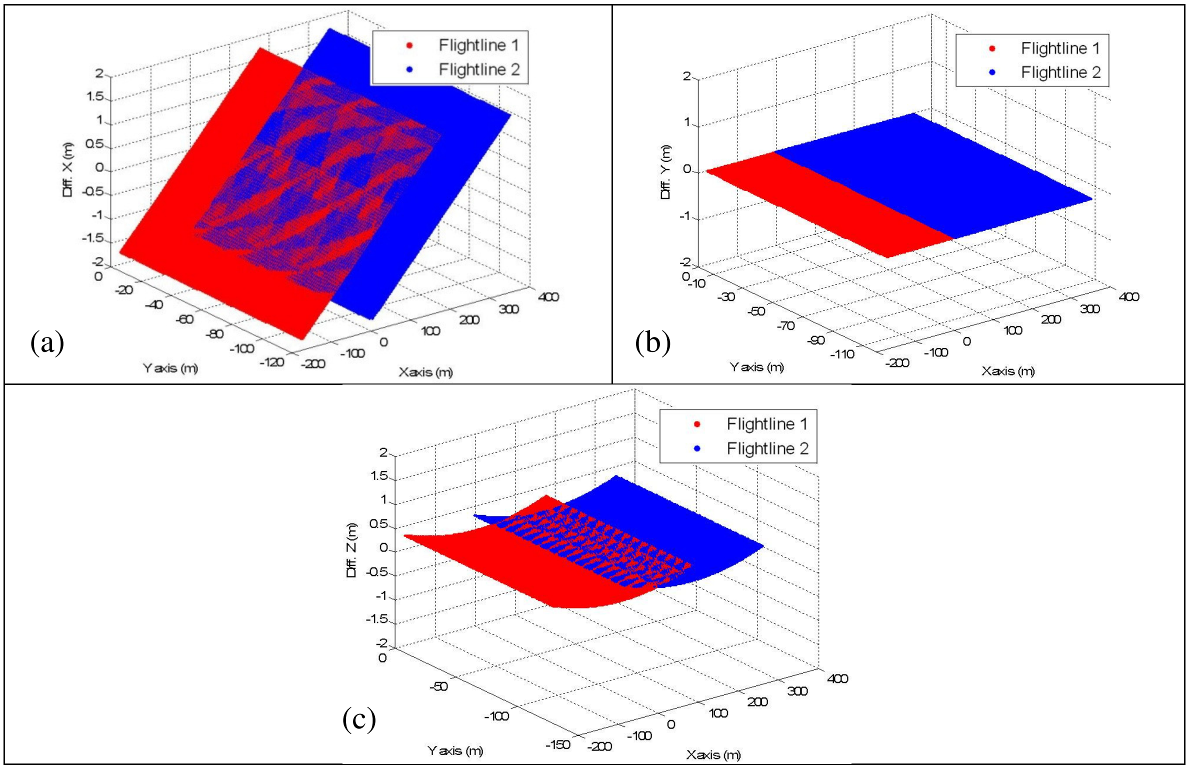

Figure 4.43. Differences between the bias-contaminated and true coordinates in the X (a), Y (b), and Z (c) directions after the introduction of a bias in the mirror angle scale (δS) for flight lines flown with 50% side lap at 1000 m flying height.

A summary of the impacts of the investigated biases (using the mathematical analysis and the simulation process) as they relate to the flying direction, flying height, and scan angle is presented in Table 4.12. One can note in Table 4.12 that all of the parameters can be recovered by minimizing the discrepancy between conjugate surface elements from different strips except the vertical component of the lever arm offset and the range bias. Such parameters require control information. Moreover, the vertical component of the lever arm offset and the range bias cannot be simultaneously recovered due to the high correlation between these parameters (i.e., they produce almost the same impact on the derived point cloud).

Table 4.12. Summary of the impacts of biases in the LiDAR system parameters on the reconstructed point cloud, as they relate to the flying direction, flying height, and scan angle, derived from the mathematical analysis and the simulation process.

Parameter	Discrepancies: Flying Direction/ Flying Height/ Scan Angle Dependent	Control Requirement
planimetric lever arm offset components	Yes/No/No	No
vertical lever arm offset component	No/No/No	Yes
boresight roll	Yes/Yes/Yes	No
boresight pitch	Yes/Yes/Yes	No
boresight yaw	No/No/Yes	No
range bias	No/Yes-No[*]/Yes	Yes
mirror scan angle scale	No/Yes/Yes	No

[*] The impact is flying height dependent for conjugate points (small discrepancies are generated among conjugate point) and independent when considering points mapped using the same scan angle (refer to Figure 4.41).

4.3.1 Concluding Remarks on the Flight and Control Configuration Requirements for LiDAR System Calibration

Based on the impact of the biases in the LiDAR system parameters on the reconstructed object space, mathematically derived and verified through simulations, one could check whether the system parameters can be recovered and what would be the minimum requirement for that while considering parallel flight lines (since they are more convenient and practical to obtain when compared to cross flight lines). Also, the optimum flight configuration that maximizes the impact of biases in the system parameters and therefore increases the reliability of the estimated parameters can be devised as well. A summary of the outcome from the proposed analysis as well as the minimum and optimum requirements for the recovery of the LiDAR system parameters are provided below:

- Planimetric lever arm offset components: the conducted analysis has shown that the biases in the planimetric lever arm offset components will cause discrepancies between conjugate surface elements from flight lines in opposite directions, and therefore control information is not needed.

  - Minimum requirement: two strips captured in opposite directions with some percentage of side lap.
  - Optimum requirement: two strips captured in opposite directions with 100% side lap (the impacts of the biases in the boresight yaw angle, the range bias, and the mirror scan angle scale are eliminated).

- Vertical lever arm offset component: the conducted analysis has shown that a vertical bias in the lever arm offset component cannot be detected by observing discrepancies between conjugate surface elements derived from different flight lines (assuming a vertical system with constant attitude). Such inability is caused by the fact that a vertical bias in the lever arm offset produces the same effect regardless of the flying direction, flying height, or scan angle. Therefore, control information is required.
  - Minimum requirement: one vertical control point.
  - Optimum requirement: one vertical control point.
- Boresight roll angle: the conducted analysis has shown that a bias in the boresight roll angle will cause discrepancies between conjugate surface elements from different flight lines, and therefore control information is not needed.
  - Minimum requirement: two strips with some percentage of side lap.
  - Optimum requirement: two strips captured in opposite directions with 100% side lap (the vertical discrepancy among conjugate reconstructed points from the flight lines caused by biases in the boresight roll angle is maximized and the impacts of the biases in the boresight yaw angle, the range, and the mirror scan angle scale are eliminated).
- Boresight pitch angle: the conducted analysis has shown that a bias in the boresight pitch angle will cause discrepancies between conjugate surface elements

from flight lines in opposite directions, and therefore control information is not needed.

  - Minimum requirement for simultaneous estimation with the lever arm offset component in the along flight direction: four strips (i.e., two strip pairs) captured in opposite directions at different flying heights.
  - Optimum requirement: four strips (i.e., two strip pairs) captured in opposite directions at different flying heights with 100% side lap (the impacts of the biases in the boresight yaw angle, the range, and the mirror scan angle scale are eliminated).

- Boresight yaw angle: the conducted analysis has shown that a bias in the boresight yaw angle will cause discrepancies between conjugate surface elements from different flight lines (except strips flown with 100% side lap), and therefore control information is not needed.
  - Minimum requirement: two strips with some percentage of side lap (exception: strips flown with 100% side lap).
  - Optimum requirement: two strips captured in the same direction with minimum side lap (while having enough conjugate surface elements among the strips). One can note that the impact on strips flown in opposite directions is the same as the impact on the strips flown in the same direction. Strips flown in the same direction are recommended because in such strips, the effect of biases in the planimetric lever arm offset components, the boresight pitch angle, and the boresight roll angle on the across flight direction are eliminated. Having minimum side lap between the strips will maximize the discrepancy among conjugate surface elements caused by the boresight yaw angle bias.

- Range bias: the conducted analysis has shown that the range bias will cause discrepancies of a very small magnitude between conjugate surface elements from different flight lines. These discrepancies do not allow for a reliable estimation of such a parameter. Therefore, control information is required. One should note that the range bias is highly correlated with the vertical component of the lever arm offset. Therefore, they cannot be reliably estimated at the same time. To avoid such a problem, one can rely on in-situ measurements of the vertical lever arm and only solve for the range bias during the calibration process.

  - Minimum requirement: one vertical control point.
  - Optimum requirement: one vertical control point.

- Mirror angle scale bias: the conducted analysis has shown that the mirror angle scale bias will cause discrepancies between conjugate surface elements from different flight lines (exception: strips flown with 100% side lap), and therefore control information is not needed.

  - Minimum requirement: two strips with some percentage of side lap (exception: strips flown with 100% side lap).
  - Optimum requirement: two strips captured in the same direction with minimum side lap (while having enough conjugate surface elements among the strips). Strips flown in the same direction are recommended since in such strips, the effect of biases in the planimetric lever arm offset components, the boresight pitch angle, and the boresight roll angle on the across flight direction are eliminated. Having minimum side lap between the strips will maximize the discrepancy among conjugate surface elements caused by the mirror angle scale bias.

In summary, the optimum flight and control configuration for reliable estimation of the system parameters (i.e., the planimetric lever arm offset components, the boresight angles, the range bias, and the mirror angle scale) should consist of three side lap cases and one vertical control point as illustrated in Figure 4.44. As demonstrated in this figure, the optimum flight configuration consists of four strips which are captured from two flying heights in opposite directions with 100 % side lap, and two flight lines, which are flown in the same direction with the least side lap possible (while having enough conjugate surface elements among the strips). One should note that the devised optimum flight and control configuration for the calibration of LiDAR systems is equivalent to the devised flight and control configuration for the calibration of GPS/INS-assisted photogrammetric systems. Such finding reveals the possibility of calibrating both systems using the same calibration flight.

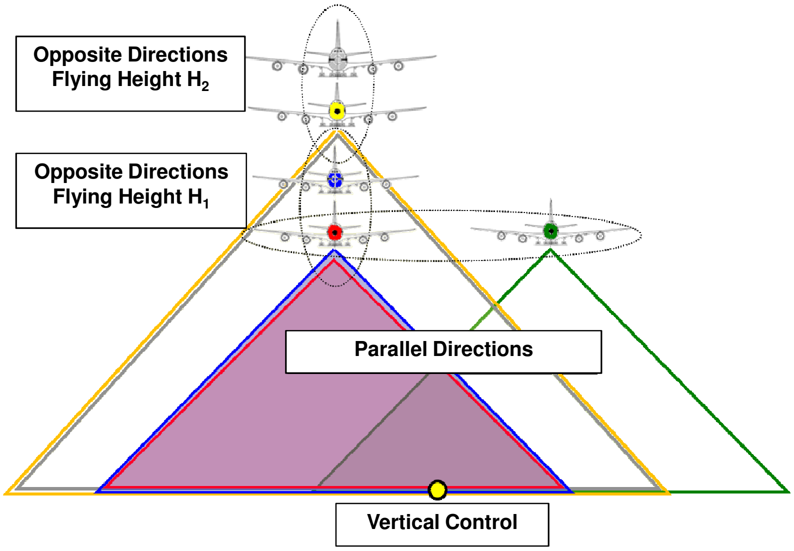

Figure 4.44. Optimum flight and control configuration for the estimation of the LiDAR system parameters.

4.4 Summary

In this chapter, the optimum flight and control configuration for the calibration of airborne GPS/INS-assisted single-camera photogrammetric and LiDAR and systems have been proposed. The general hypothesis that will be tested/verified in the experimental results is that the devised flight and control configuration will allow for reliable estimation of the system parameters. The specific hypotheses that will be tested/verified in the experimental results are as follows:

- Test whether adding more flight lines to the optimum recommended configuration would significantly improve the calibration results for photogrammetric and LiDAR systems;
- Test whether increasing the number of vertical ground control points would improve the calibration results for photogrammetric and LiDAR systems; and
- For photogrammetric systems, test the number of images that the utilized vertical control point should be visible/measured in.

CHAPTER 5

PHOTOGRAMMETRIC SYSTEM CALIBRATION

5.1 Introduction

In this chapter, a single-step photogrammetric system calibration, which is suitable for single and multi-camera systems, is introduced. As already mentioned for multi-camera systems, the mounting parameters involve two sets of ROP: the ROP among the cameras and the ROP between the cameras and the navigation sensors. One should note that these sets of ROP are not independent. The proposed method has the flexibility of estimating these sets of parameters using the same implementation. Moreover, a general mathematical model, which can incorporate prior information on the ROP among the cameras when estimating the mounting parameters relating the cameras and the navigation sensors, is devised. It will be demonstrated that the models for the estimation of the ROP among the cameras (in the absence of GPS/INS data) and for the estimation of the mounting parameters between the cameras and the navigation sensors can be derived as special cases of the general model.

5.2 Proposed Single-Step Photogrammetric System Calibration

The single-step estimation of the system parameters (i.e., the mounting parameters and the camera IOP) is performed through an ISO procedure. The incorporation of the GPS/INS position and orientation information as well as the mounting parameters in the ISO procedure can be established by including additional observation equations or by directly incorporating them in the collinearity equations. The latter method has been already used for single-camera systems and has been adapted in this research for use in systems composed of several synchronized cameras since it is the most appropriate solution and allows for easier implementation. The mathematical model for multi-camera systems is shown in Equation 5.1. Figure 5.1 illustrates the involved parameters and coordinate systems in the mathematical model.

$$r_I^m = \begin{bmatrix} X_I \\ Y_I \\ Z_I \end{bmatrix} = r_b^m(t) + R_b^m(t)\, r_{cj}^b + \lambda_i^{cj} R_b^m(t) R_{cj}^b\, r_i^{cj} \tag{5.1}$$

where:

- $r_i^{cj} = \begin{bmatrix} x_i^{cj} - x_p^{cj} - \Delta_x^{cj} \\ y_i^{cj} - y_p^{cj} - \Delta_y^{cj} \\ -c^{cj} \end{bmatrix}$: vector from the perspective center of the *j*th camera to the image point (*i*);
- λ_i^{cj}: represents the ration between the magnitudes of the vector connecting the perspective center of the j^{th} camera and the object point (*I*) and the vector connecting the perspective center of the j^{th} camera and the image point (*i*).

By rearranging the terms in Equation 5.1, i.e., moving the term r_i^{cj} to the left side of the equation, one can get the form in Equation 5.2. The observation equations in their final form, i.e., the modified collinearity equations, are shown in Equations 5.3a and 5.3b. These equations can be obtained by dividing the first two rows in Equation 5.2 by the third one while moving the terms x_p^{cj} , Δ_x^{cj}, y_p^{cj}, and Δ_x^{cj} to the left side of the equations. The scale factor (λ_i^{cj}) is eliminated through the division process. One should note that the right side of Equations 5.3a and 5.3b entails not only the system parameters but also observations (e.g., GPS/INS-derived position and orientation information, ground coordinates of control points). In this work, instead of using the Gauss-Helmert model to deal with mixed unknowns and observations in the mathematical model, the ISO is implemented through a general LSA procedure. In the general LSA, all the involved quantities in the mathematical model can be treated either as unknowns, unknowns with prior information, or error free (constant) parameters. Initially, all the quantities on the right side of Equations 5.3a and 5.3b are treated as unknowns (camera IOP, ground coordinates of control points, ground coordinates of tie points, position and orientation of the IMU body frame, mounting parameters). In order to include prior information regarding any of these parameters, pseudo-observation equations can be added for such parameters. Examples of pseudo-observation equations for adding prior information of the position and orientation of the IMU body frame relative to the mapping frame are shown in Equations 5.4a and 5.4b, respectively.

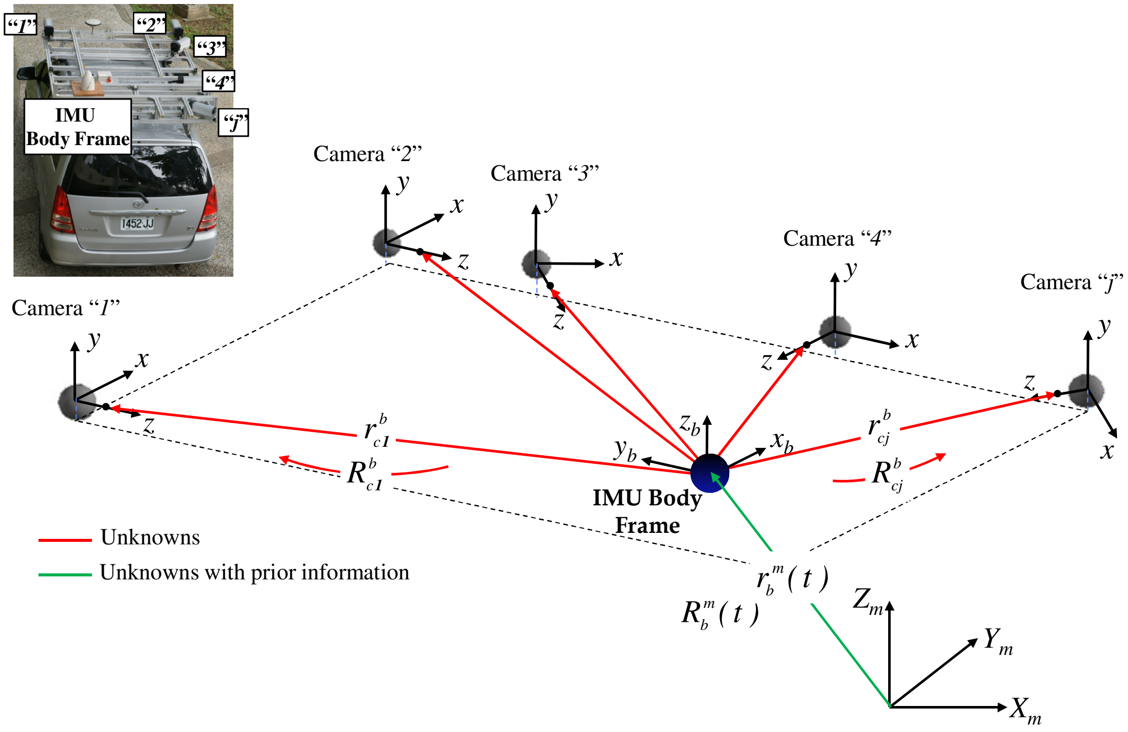

Figure 5.1. Involved quantities and coordinate systems in the proposed single-step procedure for the estimation of the system parameters.

$$r_i^{cj} = \begin{bmatrix} x_i^{cj} - x_p^{cj} - \Delta x^{cj} \\ y_i^{cj} - y_p^{cj} - \Delta y^{cj} \\ -c^{cj} \end{bmatrix} = \frac{1}{\lambda_i^{cj}} R_b^{cj} \left(R_m^b(t)\left[r_I^m - r_b^m(t)\right] - r_{cj}^b \right) = \frac{1}{\lambda_i^{cj}} \begin{bmatrix} N_x^{cj} \\ N_y^{cj} \\ D^{cj} \end{bmatrix} \tag{5.2}$$

$$x_i^{cj} = x_p^{cj} - c^{cj}\frac{N_x^{cj}}{D^{cj}} + \Delta_x^{cj} \tag{5.3a}$$

$$y_i^{cj} = y_p^{cj} - c^{cj}\frac{N_y^{cj}}{D^{cj}} + \Delta_y^{cj} \tag{5.3b}$$

$$r_b^m(t)_{GPS/INS} = \begin{bmatrix} X \\ Y \\ Z \end{bmatrix}_b^m (t)_{GPS/INS} = \begin{bmatrix} X \\ Y \\ Z \end{bmatrix}_b^m (t) + \begin{bmatrix} e_X \\ e_Y \\ e_Z \end{bmatrix}_b^m (t) \tag{5.4a}$$

$$R_b^m(t)_{GPS/INS}: \begin{bmatrix} \omega \\ \varphi \\ \kappa \end{bmatrix}_b^m (t)_{GPS/INS} = \begin{bmatrix} \omega \\ \varphi \\ \kappa \end{bmatrix}_b^m + \begin{bmatrix} e_\omega \\ e_\varphi \\ e_\kappa \end{bmatrix}_b^m \tag{5.4b}$$

The final form of the observation equations (Equations 5.3 – 5.4) expresses the observations ($\vec{Y}$) as a function of the unknown parameters ($\vec{x}$), as shown in Equation 5.5. Such observation equations can be linearized using Taylor series expansion while ignoring higher order terms to get the Gauss Markov stochastic model in Equation 5.6. The corrections to the approximate values of the unknown parameters $\left(\hat{\vec{x}}\right)$ can be derived through Equation 5.7.

$$\vec{Y} = f(\vec{x}) + \vec{e} \tag{5.5}$$

$$\vec{y} = A\vec{x} + \vec{e} \tag{5.6}$$

where:

- $\vec{y}$: is the $n \times 1$ vector of differences between the measured and computed observations using the approximate values of the unknown parameters;
- $\vec{x}$: is the $m \times 1$ correction vector to the approximate values of the unknown parameters;
- A: is the $n \times m$ design matrix (i.e., partial derivative matrix w.r.t. the unknown parameters), and
- $\vec{e}$: is the $n \times 1$ vector of random noise, which is normally distributed with a zero mean and $\Sigma = \sigma_o^2 P^{-1}$ variance-covariance matrix, where σ_o^2 is the a-priori variance factor and P is the $n \times n$ weight matrix of the noise vector.

$$\hat{\vec{x}} = (A^T P A)^{-1} A^T P \vec{y} = N^{-1} \vec{c} \tag{5.7}$$

To treat a specific parameter as a constant (e.g., the parameter corresponding to the i^{th} row of $\vec{x}$), zero values are set for all the elements occupying the i^{th} row and i^{th} column of the normal matrix N in Equation 5.7, except for the element occupying the i^{th} diagonal element, which is set as a one. Also, the i^{th} row of the $\vec{c}$ vector in Equation 5.7 is also set to zero.

5.3 Utilization of the Proposed Single-Step Photogrammetric System Calibration for the Estimation of the ROP among the Cameras

The use of the general LSA concept allows for the possibility of utilizing the same implementation for the direct estimation of the ROP among the cameras in the absence of GPS/INS data while enforcing the ROC among the different cameras in an indirect geo-referencing procedure. More specifically, one of the cameras can be used as a reference for defining the position and the orientation of the platform. This would be equivalent to having a virtual IMU body frame in the same position and orientation of the reference camera (Figure 5.2), i.e., the lever arm offset and boresight angles relating the reference camera and the IMU body frame should be fixed to zero (Equations 5.8a and 5.8b). In such a case, there is no prior information on the position and orientation of the IMU body frame (Equations 5.4a and 5.4b). In this case, the terms $r_b^m(t)$ and $R_b^m(t)$ in Equation 5.1 should be regarded as the position and orientation of the reference camera (cr) relative to the mapping frame: $r_{cr}^m(t)$ and $R_{cr}^m(t)$, respectively. Similarly, the terms r_{cj}^b and R_{cj}^b in Equation 5.1 should be regarded as the ROP of the j^{th} camera (cj) w.r.t. the reference one: r_{cj}^{cr} and R_{cj}^{cr}, respectively. Equation 5.9 shows the final form of the mathematical model. Such a procedure is denoted in this research work as "Indirect Geo-referencing with ROC", which is a single-step procedure for the estimation of the ROPs among the cameras while enforcing the ROC.

$$r_{cr}^b = \begin{bmatrix} \Delta X \\ \Delta Y \\ \Delta Z \end{bmatrix}_{cr}^b = \begin{bmatrix} 0 \\ 0 \\ 0 \end{bmatrix} \quad \text{(treated as constant)} \tag{5.8a}$$

$$R_{cr}^b : \begin{bmatrix} \Delta \omega \\ \Delta \varphi \\ \Delta \kappa \end{bmatrix}_{cr}^b = \begin{bmatrix} 0 \\ 0 \\ 0 \end{bmatrix} \quad \text{(treated as constant)} \tag{5.8b}$$

$$r_I^m = r_{cr}^m(t) + R_{cr}^m(t)\, r_{cj}^{cr} + \lambda_i^{cj} R_{cr}^m(t)\, R_{ci}^{cr} r_i^{cj} \tag{5.9}$$

In contrast to the method of adding constraint equations (illustrated in Tables 2.1 and 2.2) to enforce the invariant relationship among the cameras in traditional bundle adjustment procedure, the proposed indirect geo-referencing with ROC is much simpler. More specifically, it does not require extensive partial derivatives as well as manual formatting of the camera pairs to be utilized in the ROC, which might be cumbersome especially when the number of utilized cameras and the number of involved stations get larger. Moreover, in the proposed method, the ROP among the cameras are explicitly estimated. One should note that a reduction in the size of the normal equation matrix is obtained due to decreased number of unknown parameters. More specifically, the proposed implementation decreases the number of unknown geo-referencing parameters from *n_cam*n_epoch*6* to *n_epoch*6+6*(n_cam-1)* (where *n_cam* is the number of cameras and *n_epoch* is the number of epochs). As a result, the storage and execution time requirements are reduced as well. In the traditional bundle adjustment with constraint equations, the number of utilized constraints is *6 * (n_cam – 1) * (n_epoch – 1)*. In such a procedure, the number of independent geo-referencing parameters will be equal to the number of unknown EOP (i.e., *n_cam*n_epoch*6*) minus the number of constraints (i.e., *6 * (n_cam – 1) * (n_epoch – 1)*). It should be noted that the number of independent geo-referencing parameters in the traditional bundle adjustment with constraint equations is equivalent to the number of unknown geo-referencing parameters in the indirect geo-referencing with ROC method, i.e., both are equivalent to *n_epoch*6+6*(n_cam-1)*, which demonstrates the equivalence of the two methods.

In summary, the mounting parameters relating the cameras to the IMU body frame can be directly estimated through the proposed single-step procedure, which utilizes Equation 5.1 for incorporating the prior GPS/INS position and orientation information and the system mounting parameters in the bundle adjustment. The same procedure can be used in an indirect geo-referencing mode to directly estimate the ROP among the cameras (Equation 5.9).

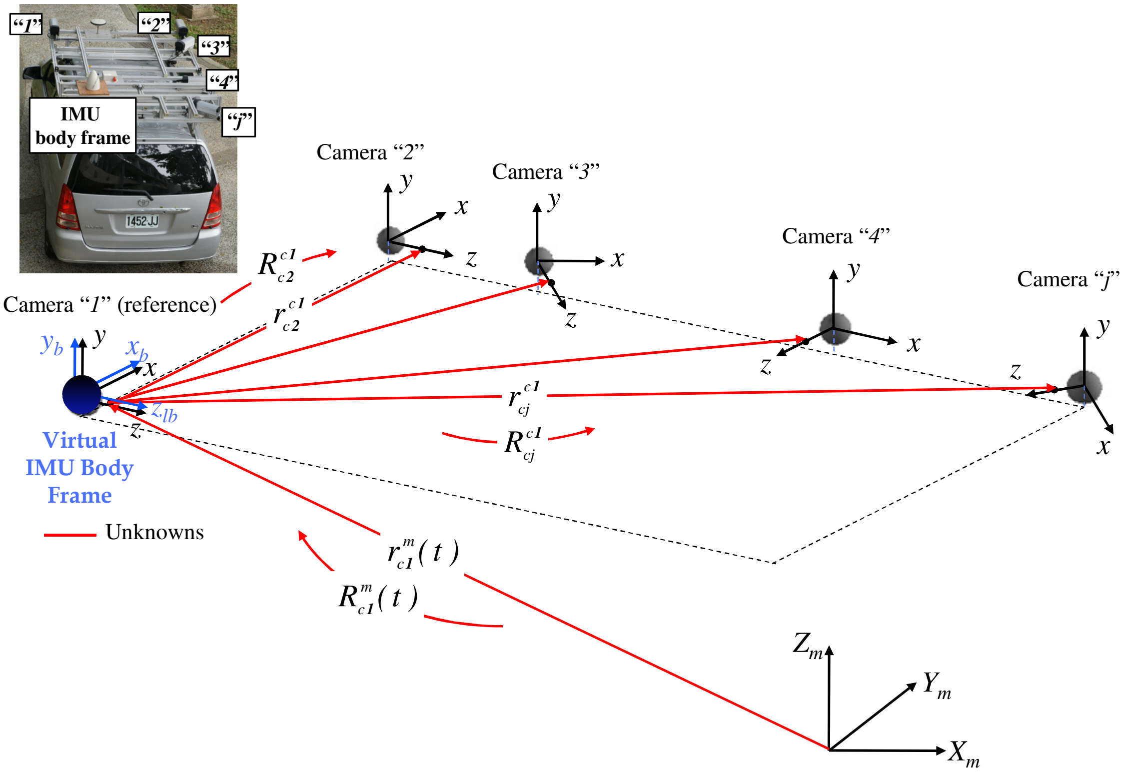

Figure 5.2. Virtual IMU body frame (placed in the same position and orientation of the reference camera) and the unknown parameters in the single-step procedure denoted as "indirect geo-referencing with ROC".

5.4 Proposed General Model for the Incorporation of Prior ROP Information among the Cameras in the Photogrammetric System Calibration

So far, a single-step procedure for the estimation of the photogrammetric system parameters has been introduced. For multi-camera systems, the proposed method can be used for the estimation of the lever arm offset and boresight angles relating the camera (s) and the IMU body frame as well as the ROP among the cameras. Now, the possibility of having a model for the ISO procedure, which can incorporate prior information on the ROP among the cameras, will be investigated. The proposed mathematical model is shown in Equation 5.10. This mathematical model is obtained through the summation of four vectors, $r_b^m(t)$, r_{cr}^b , r_{cj}^{cr} ,and r_i^{cj}, after applying the appropriate rotation matrices, $R_b^m(t)$, R_{cr}^b, and R_{cj}^{cr} as well as the scale factor (λ_i^{cj}), as illustrated in Figure 5.3.

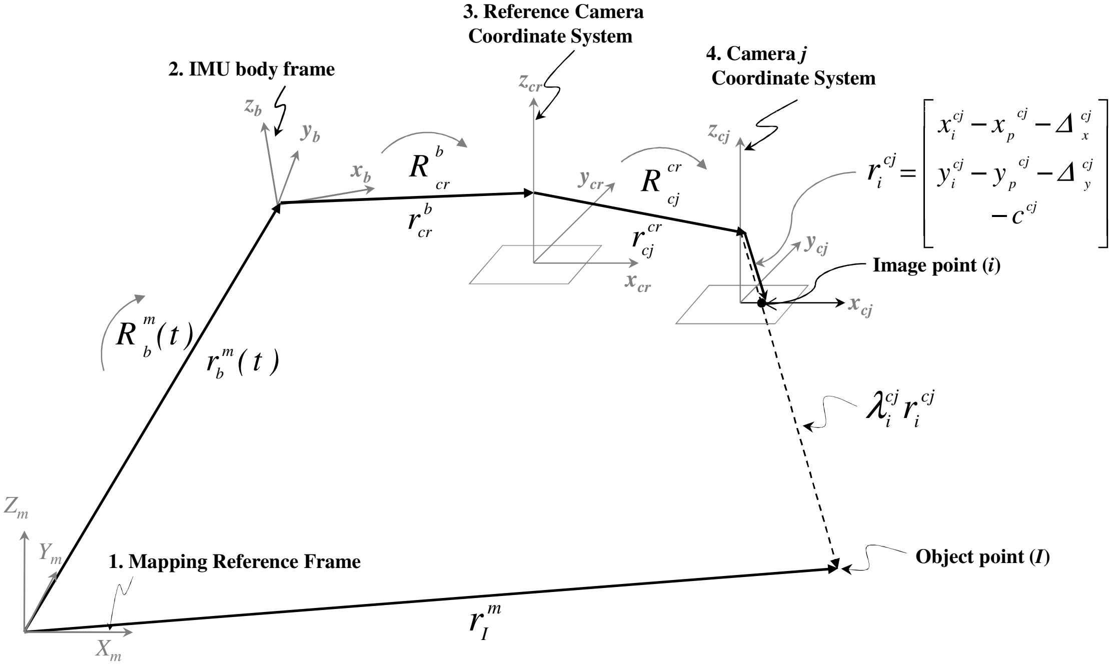

Figure 5.3. Involved parameters in the vector summation process to derive the general mathematical model for the incorporation of prior information on the ROP among the cameras in the ISO procedure.

$$r_I^m = r_b^m(t) + R_b^m(t) r_{cr}^b + R_b^m(t) R_{cr}^b r_{cj}^{cr} + \lambda_i^{cj} R_b^m(t) R_{cr}^b R_{cj}^{cr} r_i^{cj} \tag{5.10}$$

where:

- r_{cr}^b : is the lever arm offset, i.e., the vector from the origin of the IMU body frame to the reference camera (*cr*) perspective center, defined relative to the IMU body frame;
- R_{cr}^b : is the rotation matrix relating the IMU and the reference camera coordinate systems;
- r_{cj}^{cr} : is the spatial offset between the reference camera (*cr*) and the *j*th camera perspective centers, defined relative to the reference camera coordinate system;
- R_{cj}^{cr} : is the rotation matrix relating the reference camera and the *j*th camera coordinate systems.

This model can incorporate prior information on the ROP between the reference camera and the other cameras through the use of the pseudo-observations in Equations 5.11a and 5.11b. Figure 5.4 illustrates the geo-referencing parameters involved in the general model. One should note that if available, prior information on the mounting parameters relating the reference camera and the IMU body frame can be added as well (refer to the pseudo-observations in Equations 5.12a and 5.12b).

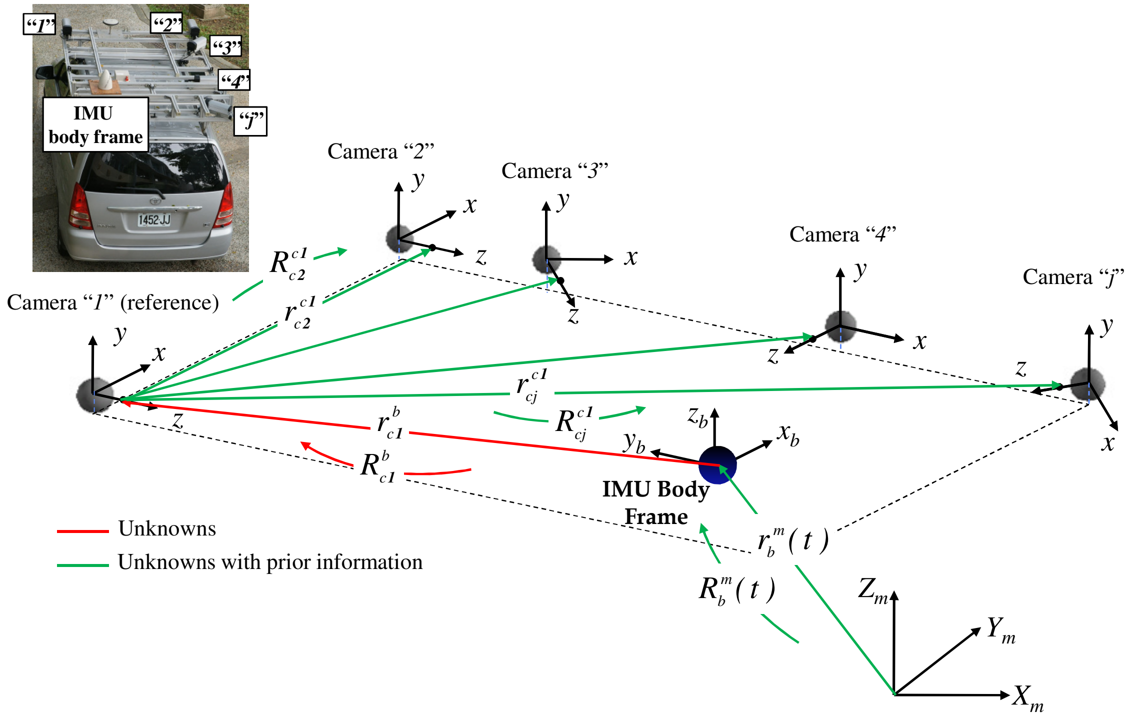

Figure 5.4. Involved geo-referencing parameters in the general model.

$$r_{cj}^{cr}(prior) = \begin{bmatrix} \Delta X \\ \Delta Y \\ \Delta Z \end{bmatrix}_{cj}^{cr} (prior) = \begin{bmatrix} \Delta X \\ \Delta Y \\ \Delta Z \end{bmatrix}_{cj}^{cr} + \begin{bmatrix} e_{\Delta X} \\ e_{\Delta Y} \\ e_{\Delta Z} \end{bmatrix}_{cj}^{cr} \tag{5.11a}$$

$$R_{cj}^{cr}(prior) : \begin{bmatrix} \Delta \omega \\ \Delta \varphi \\ \Delta \kappa \end{bmatrix}_{cj}^{cr} (prior) = \begin{bmatrix} \Delta \omega \\ \Delta \varphi \\ \Delta \kappa \end{bmatrix}_{cj}^{cr} + \begin{bmatrix} e_{\Delta \omega} \\ e_{\Delta \varphi} \\ e_{\Delta \kappa} \end{bmatrix}_{cj}^{cr} \tag{5.11b}$$

$$r_{cr}^{b}(prior) = \begin{bmatrix} \Delta X \\ \Delta Y \\ \Delta Z \end{bmatrix}_{cr}^{b} (prior) = \begin{bmatrix} \Delta X \\ \Delta Y \\ \Delta Z \end{bmatrix}_{cr}^{b} + \begin{bmatrix} e_{\Delta X} \\ e_{\Delta Y} \\ e_{\Delta Z} \end{bmatrix}_{cr}^{b} \tag{5.12a}$$

$$R_{cr}^{b}(prior): \begin{bmatrix} \Delta\omega \\ \Delta\varphi \\ \Delta\kappa \end{bmatrix}_{cr}^{b} (prior) = \begin{bmatrix} \Delta\omega \\ \Delta\varphi \\ \Delta\kappa \end{bmatrix}_{cr}^{b} + \begin{bmatrix} e_{\Delta\omega} \\ e_{\Delta\varphi} \\ e_{\Delta\kappa} \end{bmatrix}_{cr}^{b} \tag{5.12b}$$

5.5 Derivation of the Models for the Estimation of the Two Sets of ROP as Special Cases of the General Model

In this section, the derivation of the model for the estimation of the mounting parameters relating the cameras and the IMU body frame as well as the model for the estimation of the ROP among the cameras as special cases of the general devised model will be demonstrated. More specifically, the previous presented models in Equations 5.1 and 5.9, will be derived as special cases of the model in Equation 5.10 (i.e., it will be demonstrated that the same implementation can be used for all models).

To derive the model for the estimation of the mounting parameters relating the cameras and the IMU body frame from the general model, a virtual reference camera is placed in the same position and orientation of the IMU body frame (as illustrated in Figure 5.5). In this case, the lever arm offset and the boresight angles relating the reference camera and the IMU body frame must be fixed to zero, as shown in Equations 5.13a and 5.13b, respectively. By doing so, the term $R_b^m(t)r_{cr}^b$ in Equation 5.10 is eliminated and the rotation matrix R_{cr}^b becomes identity resulting in the form in Equation 5.14. Since the reference camera coordinate system coincides with the IMU body frame, all the terms referring to the reference camera in Equation 5.14 should be read as referring to the IMU body frame (i.e., $cr \equiv b$) to get the form in Equation 5.15. One can note that the final derived expression in Equation 5.15 is identical to the mathematical model in Equation 5.1.

$$r_{cr}^{b} = \begin{bmatrix} \Delta X \\ \Delta Y \\ \Delta Z \end{bmatrix}_{cr}^{b} = \begin{bmatrix} 0 \\ 0 \\ 0 \end{bmatrix} \quad \text{(treated as constant)} \tag{5.13a}$$

$$R_{cr}^{b}: \begin{bmatrix} \Delta\omega \\ \Delta\varphi \\ \Delta\kappa \end{bmatrix}_{cr}^{b} = \begin{bmatrix} 0 \\ 0 \\ 0 \end{bmatrix} \quad \text{(treated as constant)} \tag{5.13b}$$

$$r_I^m = r_b^m(t) + R_b^m(t) r_{cj}^{cr} + \lambda_i^{cj} R_b^m(t) R_{cj}^{cr} r_i^{cj} \tag{5.14}$$

$$r_I^m = r_b^m(t) + R_b^m(t) r_{cj}^{b} + \lambda_i^{cj} R_b^m(t) R_{cj}^{b} r_i^{cj} \tag{5.15}$$

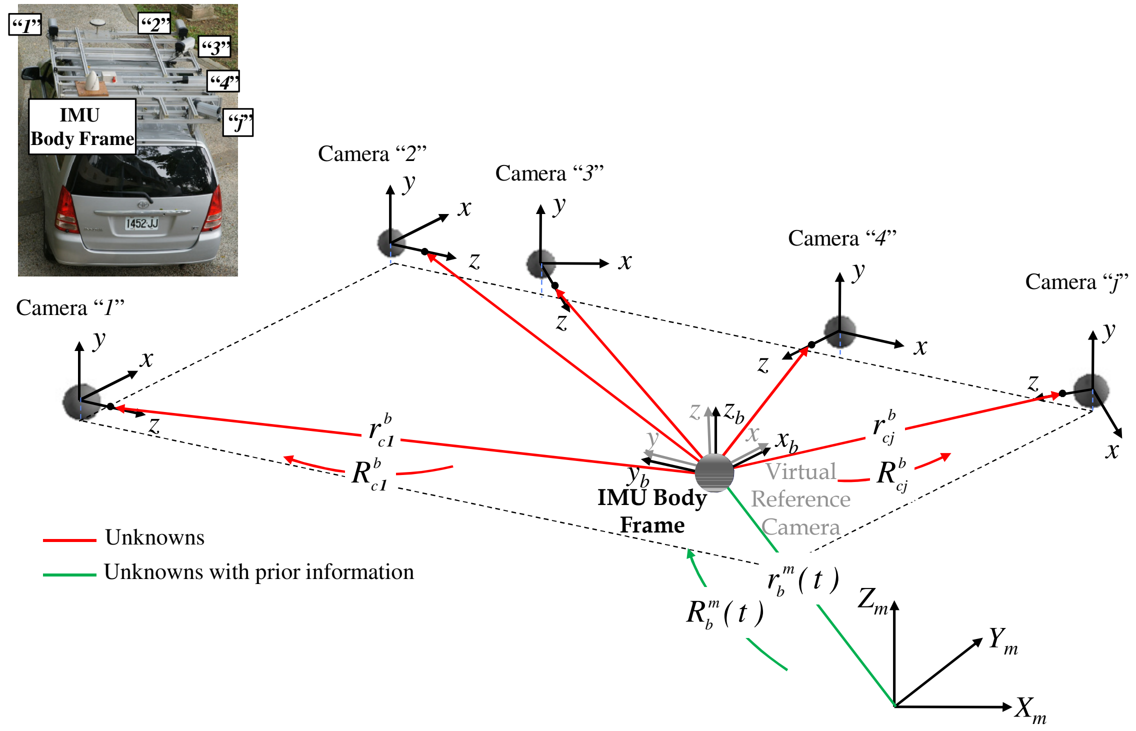

Figure 5.5. Virtual reference camera placed in the same position and orientation of the IMU body frame to derive the model for the estimation of the mounting parameters relating the cameras and the IMU body frame from the general model.

Now, the derivation of the model for the estimation of the ROP among the cameras (indirect geo-referencing with ROC) as a special case of the general model will be demonstrated. Such derivation can be performed by placing a virtual IMU body frame in the same position and orientation of the reference camera as illustrated in Figure 5.2. In this case, the lever arm offset and boresight angles relating the reference camera and the IMU body frame should be fixed to zero, as shown in Equations 5.16a and 5.16b, respectively. By doing so, the term $R_b^m(t) r_{cr}^b$ in Equation 5.10 is eliminated and the rotation matrix R_{cr}^b becomes identity resulting in the form in Equation 5.17. In such a case, there is no prior information on the position and orientation of the IMU body frame. The terms $r_b^m(t)$ and $R_b^m(t)$ in Equation 5.17 should be regarded as the position and orientation of the reference camera (cr) relative to the mapping frame: $r_{cr}^{m}(t)$ and $R_{cr}^{m}(t)$, respectively. Equation 5.18 shows the final form of the derived model. One can note that the expression in Equation 5.18 is equivalent to the model in Equation 5.9.

$$r_{cr}^{b} = \begin{bmatrix} \Delta X \\ \Delta Y \\ \Delta Z \end{bmatrix}_{cr}^{b} = \begin{bmatrix} 0 \\ 0 \\ 0 \end{bmatrix} \quad \text{(treated as constant)} \tag{5.16a}$$

$$R_{cr}^{b} : \begin{bmatrix} \Delta \omega \\ \Delta \varphi \\ \Delta \kappa \end{bmatrix}_{cr}^{b} = \begin{bmatrix} 0 \\ 0 \\ 0 \end{bmatrix} \quad \text{(treated as constant)} \tag{5.16b}$$

$$r_{I}^{m} = r_{b}^{m}(t) + R_{b}^{m}(t) r_{cj}^{cr} + \lambda_{i}^{cj} R_{b}^{m}(t) R_{cj}^{cr} r_{i}^{cj} \tag{5.17}$$

$$r_{I}^{m} = r_{cr}^{m}(t) + R_{cr}^{m}(t) r_{cj}^{cr} + \lambda_{i}^{cj} R_{cr}^{m}(t) R_{cj}^{cr} r_{i}^{cj} \tag{5.18}$$

5.6 Summary

In this chapter, a single-step photogrammetric system calibration suitable for single and multi-camera systems has been introduced. The contributions of the proposed method are as follows:

- The modified collinearity equations concept, which have been implemented in previous work for single-camera systems, is expanded in this research work to handle multi-camera systems;
- The introduced method is developed to allow for a single-step estimation of two sets of ROP (i.e., the ROP among the cameras (when GPS/INS is not available) and the ROP among the cameras and the IMU body frame) as well as the incorporation of prior information on the ROP among the cameras in the ISO;
- In contrast to the method of adding constraint equations, the proposed indirect geo-referencing with ROC allows for explicit estimation of the ROP among the cameras while enforcing the invariant relationship among the cameras. Also, the implementation of the proposed method is much simpler. Moreover, a reduction in the size of the normal equation matrix is obtained due to decreased number of

unknown geo-referencing parameters. As a result, reduction in the storage and execution time requirements is obtained.

The general hypothesis that has been demonstrated in this chapter is that the proposed method is simpler to implement when compared with existing methods. The following specific hypotheses will be tested/ verified in the experimental results section:

- It is hypothesized that for single-camera systems, the proposed single-step procedure and the commonly used added observation method in previous work yield compatible results;
- It is hypothesized that the proposed single-step procedure is also suitable for multi-camera systems;
- It is hypothesized that for multi-camera systems, the proposed implementation can be used for the estimation of the two sets of ROP: the ROP relating the cameras and the IMU body frame and the ROP among the cameras;
- It is hypothesized that the devised model, which can incorporate prior information on the ROP among the cameras, can be used as a general model (i.e., the models for the estimation of the two sets of ROP can be derived as special cases);
- It is hypothesized that the incorporation of prior information on the ROP among the cameras will improve the quality of the estimated parameters.

CHAPTER 6

LIDAR SYSTEM CALIBRATION

6.1 Introduction

In this chapter, a rigorous LiDAR system calibration method is introduced. In contrast to the photogrammetric system calibration, where point primitives can be identified in overlapping imagery, LiDAR surfaces pose an additional challenge due to its irregular nature. Correspondence between LiDAR surfaces demands the utilization of higher order primitives. In this research work, suitable primitives, which do not require specific features in the calibration site (e.g., linear and planar features), are implemented. Also, no pre-processing of the data such as pre-classification of LiDAR data into terrain and off-terrain features or segmentation of planar objects is needed. The correspondence between conjugate primitives is established in the calibration procedure using a robust matching procedure. The utilized primitives allow for similar approach to deal with overlapping LiDAR strips and overlapping LiDAR and control points. Sparse control information, which does not need to be identifiable in the LiDAR strips, can be incorporated. Although higher order primitives are utilized, simplicity in the implementation of the calibration procedure is obtained through the utilization of point-based observation equations. For that purpose, a modification to the traditional Gauss Markov stochastic model is introduced.

The conceptual basis of the proposed method is to estimate the system parameters that minimize the discrepancies between conjugate surface elements in overlapping LiDAR strips and overlapping LiDAR and control surfaces. The implementation details of the proposed method are described in the remainder of this chapter. First, the derivation of the point-based observation equations, which are based on the rigorous LiDAR point positioning equation (Equation 3.3), is demonstrated. The utilized primitives are presented next along with the proposed modification to the traditional Gauss Markov stochastic model that would allow for the utilization of these conjugate primitives while using the established point-based mathematical model. Finally, the overall calibration workflow is described.

6.2 Point-Based Observation Equations

The deterministic LiDAR model for point positioning presented in Equation 6.1 can be represented in a symbolic form by Equation 6.2. This equation indicates that the true coordinates of a given point I ($r_I^m(True)$) are derived using the true values of the system parameters ($\vec{x}$) (i.e., ΔX , ΔY , ΔZ , $\Delta\omega$, $\Delta\varphi$, $\Delta\kappa$, $\Delta\rho$ and S) and the noise-free measurements ($\vec{l}_{nf}$). The true values of the system parameters are unknown (i.e., they are determined in the calibration procedure) while the system measurements ($\vec{l}_n$) are contaminated with noise ($\vec{e}$) whose magnitude depends on the system's measurements precision.

$$r_I^m = r_b^m + R_b^m(t)\begin{bmatrix} \Delta X \\ \Delta Y \\ \Delta Z \end{bmatrix} + R_b^m(t)R_{lu}^b\begin{bmatrix} \cos S\beta & 0 & \sin S\beta \\ 0 & 1 & 0 \\ -\sin S\beta & 0 & \cos S\beta \end{bmatrix}\begin{bmatrix} 0 \\ 0 \\ -(\rho + \Delta\rho) \end{bmatrix} \quad (6.1)$$

$$r_I^m(True) = f(\vec{x}, \vec{l}_{nf}) \quad (6.2)$$

where:

- $\vec{l}_{nf} = \vec{l}_n - \vec{e}.$

If one has two conjugate points in overlapping strips, which will be denoted by subscripts A and B here forth, the difference between the true coordinates of these points can be expressed by Equation 6.3. In case of the availability of conjugate points in overlapping strips, the true coordinates of the respective points in strips A and B (i.e., $r_A^m(True)$ and $r_B^m(True)$) should be identical. In a similar fashion, if one is dealing with conjugate points in a LiDAR strip and control surface, the difference between the coordinates of the control point and the true coordinates of the LiDAR point in the strip denoted by the subscript B can be expressed as in Equation 6.4. Equations 6.3 and 6.4 represent the mathematical model (observation equations) when dealing with overlapping strips and control data, respectively.

$$r_A^m(True) - r_B^m(True) = f\left(\vec{x}, \vec{l}_{n_A} - \vec{e}_A\right) - f\left(\vec{x}, \vec{l}_{n_B} - \vec{e}_B\right) = 0 \tag{6.3}$$

$$(r_{control}^m - \vec{e}_{control}) - r_B^m(True) = (r_{control}^m - \vec{e}_{control}) - f\left(\vec{x}, \vec{l}_{n_B} - \vec{e}_B\right) = 0 \tag{6.4}$$

Since these equations are not linear with respect to the unknown system parameters and measurement noise, a linearization process through Taylor series expansion is required for the LSA. The linearized equations when using overlapping strips and control information are presented in Equations 6.5 and 6.6, respectively. These equations are obtained using the noise-contaminated system measurements $(\vec{l}_n)$ and the initial approximations for the unknown system parameters $(\vec{x}_o)$ as the point of expansion while ignoring second and higher order terms.

$$\begin{aligned} r_A^m(True) - r_B^m(True) \cong\ & f(\vec{x}_o, \vec{l}_{n_A}) + \partial f/\partial \vec{x}|_{\vec{x}_o, \vec{l}_{n_A}} \delta\vec{x} + \partial f/\partial \vec{l}\big|_{\vec{x}_o, \vec{l}_{n_A}} (-\vec{e}_A) \\ & -f(\vec{x}_o, \vec{l}_{n_B}) - \partial f/\partial \vec{x}|_{\vec{x}_o, \vec{l}_{n_B}} \delta\vec{x} - \partial f/\partial \vec{l}\big|_{\vec{x}_o, \vec{l}_{n_B}} (-\vec{e}_B) = 0 \end{aligned} \tag{6.5}$$

$$\begin{aligned} & (r_{control}^m - \vec{e}_{control}) - r_B^m(True) \\ & \quad \cong (r_{control}^m - \vec{e}_{control}) - f(\vec{x}_o, \vec{l}_{n_B}) - \partial f/\partial \vec{x}|_{\vec{x}_o, \vec{l}_{n_B}} \delta\vec{x} \\ & \quad - \partial f/\partial \vec{l}\big|_{\vec{x}_o, \vec{l}_{n_B}} (-\vec{e}_B) = 0 \end{aligned} \tag{6.6}$$

Rearranging the terms in Equations 6.5 and 6.6, one can get the final form of the linearized observations equations (Equations 6.7 and 6.8) according to the traditional Gauss Markov stochastic model (Equation 6.9).

$$\begin{aligned} & f(\vec{x}_o, \vec{l}_{n_A}) - f(\vec{x}_o, \vec{l}_{n_B}) \\ & \quad = - \left[\partial f/\partial \vec{x}|_{\vec{x}_o, \vec{l}_{n_A}} - \partial f/\partial \vec{x}|_{\vec{x}_o, \vec{l}_{n_B}}\right] \delta\vec{x} \\ & \quad + \left[\partial f/\partial \vec{l}\big|_{\vec{x}_o, \vec{l}_{n_A}} \vec{e}_A - \partial f/\partial \vec{l}\big|_{\vec{x}_o, \vec{l}_{n_B}} \vec{e}_B\right] \end{aligned} \tag{6.7}$$

$$r_{control}^m - f(\vec{x}_o, \vec{l}_{n_B}) = \left[\partial f/\partial \vec{x}|_{\vec{x}_o, \vec{l}_{n_B}}\right] \delta\vec{x} + \left[\vec{e}_{control} - \partial f/\partial \vec{l}\big|_{\vec{x}_o, \vec{l}_{n_B}} \vec{e}_B\right] \tag{6.8}$$

$$\vec{y} = A\,\delta\vec{x} + \vec{e} \qquad \vec{e} \sim (0, \Sigma) \qquad where\ \ \Sigma = \sigma_o^2 P^{-1} \tag{6.9}$$

where:

- $\vec{y}$ is the *nx1* vector of observations:
  - When using overlapping LiDAR strips, the observations correspond to the discrepancy between the predicted coordinates of conjugate points in overlapping strips using the noise-contaminated system measurements and the approximate values of the system parameters $\{f(\vec{x}_o, \vec{l}_{n_A}) - f(\vec{x}_o, \vec{l}_{n_B})\}$;
  - When using overlapping LiDAR and control points, the observations correspond to the discrepancy between the control point coordinates and the predicted LiDAR point coordinates using the noise-contaminated system measurements and the approximate values of the system parameters $\{r^m_{control} - f(\vec{x}_o, \vec{l}_{n_B})\}$.
- $\delta\vec{x}$ is the *mx1* vector of unknown corrections to the approximate values of the system parameters;
- A is the *nxm* design matrix:
  - $A = -\left[\partial f/\partial\vec{x}|_{\vec{x}_o,\vec{l}_{n_A}} - \partial f/\partial\vec{l}\big|_{\vec{x}_o,\vec{l}_{n_B}}\right]$ when using overlapping LiDAR strips;
  - $A = \partial f/\partial\vec{x}|_{\vec{x}_o,\vec{l}_{n_B}}$ when using overlapping LiDAR and control points.
- $\vec{e}$ is the *nx1* combined vector of random noise (normally distributed with a zero mean and variance-covariance matrix $\Sigma = \sigma_o^2 P^{-1}$), which represents the random error in the discrepancy vector among conjugate points as a function of the random error in the system measurements:
  - $\vec{e} = \partial f/\partial\vec{l}\big|_{\vec{x}_o,\vec{l}_{n_A}} \vec{e}_A - \partial f/\partial\vec{l}\big|_{\vec{x}_o,\vec{l}_{n_B}} \vec{e}_B$ when using overlapping LiDAR strips;
  - $\vec{e} = \vec{e}_{control} - \partial f/\partial l|_{\vec{x}_o,\vec{l}_{n_B}} \vec{e}_B$ when using overlapping LiDAR and control points;
  - Σ variance-covariance matrix of $\vec{e}$, derived through error propagation:
    - When using overlapping LiDAR strips:

$$\Sigma = \begin{bmatrix} \partial f/\partial \vec{l}\big|_{\vec{x}_o,\vec{l}_{n_A}} & -\partial f/\partial \vec{l}\big|_{\vec{x}_o,\vec{l}_{n_B}} \end{bmatrix} \begin{bmatrix} \Sigma_{\vec{e}_A} & 0 \\ 0 & \Sigma_{\vec{e}_B} \end{bmatrix} \begin{bmatrix} \partial f/\partial \vec{l}\big|_{\vec{x}_o,\vec{l}_{n_A}} \\ -\partial f/\partial \vec{l}\big|_{\vec{x}_o,\vec{l}_{n_B}} \end{bmatrix}$$

where:

- $\Sigma_{\vec{e}_A}$ and $\Sigma_{\vec{e}_B}$ are the variance-covariance matrices of the system measurements utilized to derive the coordinates of points *A* and *B*, respectively.

- When using overlapping LiDAR and control points:

$$\Sigma = \begin{bmatrix} I & -\partial f/\partial \vec{l}\big|_{\vec{x}_o,\vec{l}_{n_B}} \end{bmatrix} \begin{bmatrix} \Sigma_{\vec{e}_{control}} & 0 \\ 0 & \Sigma_{\vec{e}_B} \end{bmatrix} \begin{bmatrix} I \\ -\partial f/\partial \vec{l}\big|_{\vec{x}_o,\vec{l}_{n_B}} \end{bmatrix}$$

where:

- $\Sigma_{\vec{e}_{control}}$ is the variance-covariance matrix of the control points.

- σ_o^2 a-priori variance factor;
- P weight matrix of the noise vector.

The mathematical model that has been developed so far is based on the availability of conjugate points in overlapping LiDAR surfaces (Equation 6.7) or conjugate points in control and LiDAR surfaces (Equation 6.8). Assuming that such conjugate points exist, observations representing the discrepancy between these points follow the traditional Gauss Markov stochastic model in Equation 6.9. The LSA procedure aims at estimating the correction to the approximate values of the unknown parameters, which minimize the sum of squares of weighted residuals (Equation 6.10), which would lead to the solution in Equations 6.11, 6.12, 6.13, and 6.14 (Mikhail and Ackerman, 1976).

$\vec{e}^T P \vec{e} = min|_{\delta \vec{x}}$ (LSA Target Function) (6.10)

$\delta\hat{\vec{x}} = (A^T P A)^{-1} A^T P \vec{y} = N^{-1} A^T P \vec{y}$ (Solution Vector) (6.11)

$\tilde{\vec{e}} = \vec{y} - A\delta\hat{\vec{x}}$ (Predicted Residuals) (6.12)

$\Sigma\{\delta\hat{\vec{x}}\} = \hat{\sigma}_o^2 (A^T P A)^{-1} = \hat{\sigma}_o^2 N^{-1}$ (Variance-Covariance Matrix) (6.13)

$\hat{\sigma}_o^2 = (\tilde{\vec{e}}^T P \tilde{\vec{e}})/(n - m)$ (A-posteriori Variance Factor) (6.14)

For LiDAR data, there is no point-to-point correspondence among the point clouds in overlapping strips or between a given strip and a control surface. Therefore, the abovementioned LSA solution cannot be directly used to come up with an estimate of the system parameters. Therefore, in the following sections, the conjugate primitives that could be identified in overlapping LiDAR strips will be discussed. Then, the modification to the stochastic model that would allow for the utilization of these conjugate primitives for the estimation of the system parameters while using the point-based observation equations will be introduced.

6.3 Proposed Primitives

As already mentioned, one cannot assume point-to-point correspondence in overlapping strips due to the irregular nature of the LiDAR points. Instead, one can assume point-to-patch correspondence due to the high density of the LiDAR data as well as the relatively smooth characteristics of terrain and man-made structures. In this research work, as in Habib et al. (2009) and Habib et al. (2010a), one of the strips, denoted by S_1, is represented by the original points while the second strip, denoted by S_2, is represented by triangular patches, which can be derived from a TIN generation procedure. When a control surface is used, it will be represented by the original points (due to its sparse nature) and the LiDAR strips will be represented by triangular patches. It is important to note that the control points need not be identifiable in the LiDAR strips. The correspondence between points in S_1 and patches in S_2 is established using the Closest Patch procedure proposed in Habib et al. (2009). In this procedure, a TIN patch is deemed conjugate to a given point if it is the closest patch to this point and the projection of the point onto the patch should be inside the patch (Figure 6.1a).

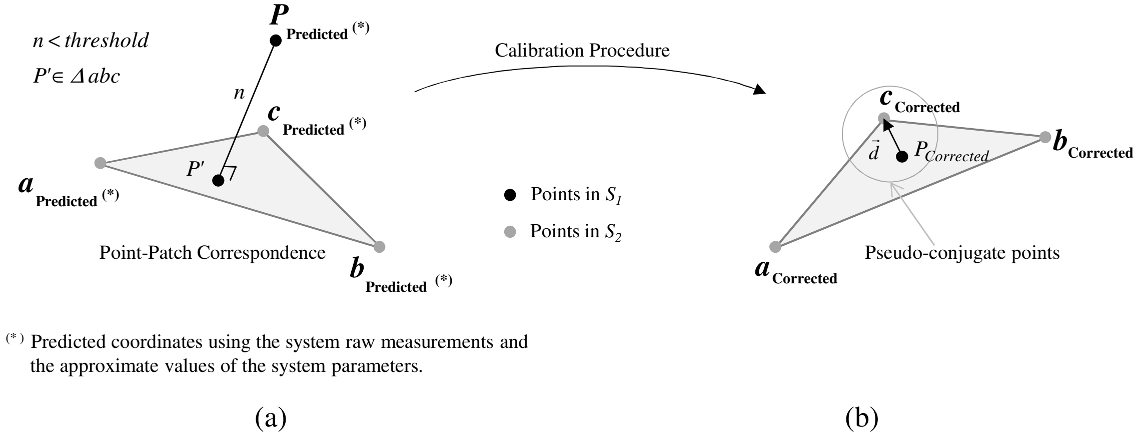

Figure 6.1. Point-patch correspondence procedure (a) and the additional unknown vector following the calibration procedure (b)

Also, a pre-defined threshold for the point-patch separation (normal distance *n*) is implemented to avoid the matching of points and patches corresponding to non-physical surfaces (i.e., points within vegetations and at building boundaries – see Figure 6.2a). Figure 6.2b shows the non-matched points among overlapping strips through the exclusion of instances where the TIN patches do not represent the physical surface (vegetation and building boundaries), which demonstrates the robustness of the matching procedure in terms of avoiding the use of point-patch pairs corresponding to non-physical surfaces in the calibration procedure.

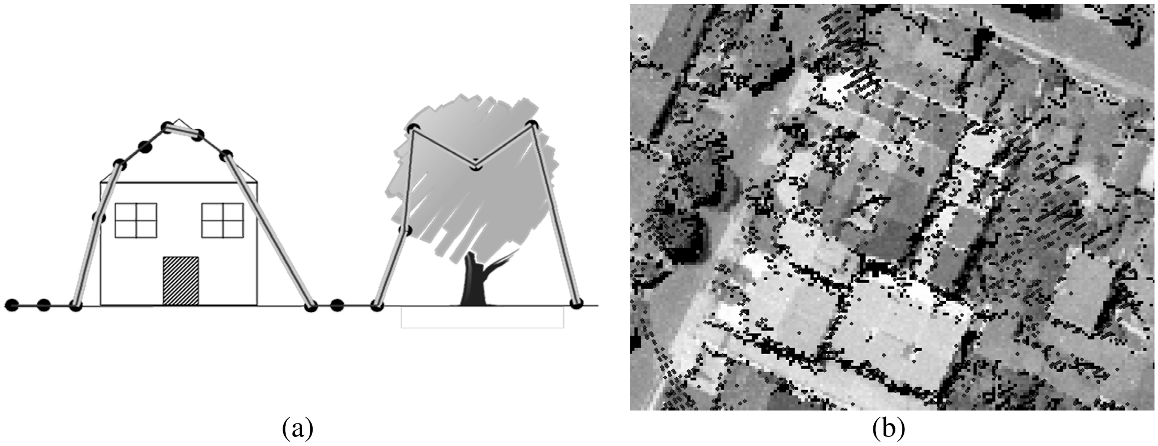
(a) (b)

Figure 6.2. Exceptions where the TIN patches do not represent the physical surface (highlighted in grey) (a) and non-matched points along edges of buildings and around areas with vegetations (b)

For a given point-patch pair, it will be assumed that one of the vertices of the TIN patch in S_2 is conjugate to the corresponding point in S_1. The TIN vertex in S_2 and the point in S_1 for a point-patch pair are denoted as pseudo-conjugate points (Figure 6.1b). Starting from Equation 6.5, the mathematical model describing the discrepancy between pseudo-conjugate points in overlapping strips will take the form in Equation 6.15. Similarly, the mathematical model describing the discrepancy between pseudo-conjugate control and LiDAR points will take the form in Equation 6.16. The stochastic model describing the discrepancies in Equations 6.15 and 6.16 can be represented by the Gauss Markov stochastic model in Equation 6.17. The difference between this model and the one in Equation 6.9 is the additional unknown vector $(\vec{d})$ resulting from using non-conjugate points along a point-patch pair (Figure 6.1b). It should be noted that the additional unknown vector $(\vec{d})$ is in the plane of the TIN patch under consideration (i.e., the component of this vector along the normal to the TIN patch is zero).

$$r_A^m(True) - r_B^m(True) = f\left(\vec{x}_o + \delta\vec{x}, \vec{l}_{n_A} - \vec{e}_A\right) - f\left(\vec{x}_o + \delta\vec{x}, \vec{l}_{n_B} - \vec{e}_B\right) = \vec{d} \qquad (6.15)$$

$$\begin{aligned}&(r_{control}^m - \vec{e}_{control}) - r_B^m(True) = \\ &= (r_{control}^m - \vec{e}_{control}) - f\left(\vec{x}_o + \delta\vec{x}, \vec{l}_{n_B} - \vec{e}_B\right) = \vec{d}\end{aligned} \qquad (6.16)$$

$$\vec{y} = A\,\delta\vec{x} + \vec{d} + \vec{e} \qquad \vec{e} \sim (0, \Sigma) \qquad where\ \Sigma = \sigma_o^2 P^{-1} \qquad (6.17)$$

6.4 Modified Least Squares Adjustment

The main objective for the development of the modified LSA is to deal with the model in Equation 6.17 while eliminating the unknown vector $(\vec{d})$ from the parameters to be estimated. To explain the modification process, the stochastic properties of the random noise vector as represented by Equation 6.18 will be changed first. The new weight matrix $(P^{`})$ of the noise vector is chosen such that $P^{`}\vec{d} = 0$ – i.e., the unknown vector $(\vec{d})$ belongs to the null space of the weight matrix $(P^{`})$. Such a condition signifies that the modified weight matrix is not positive-definite (i.e., the inverse matrix $(P^{`-1})$ does not exist). Therefore, the modified variance-covariance matrix will be represented as follows $\Sigma^{`}\{e\} = \sigma_o^2 P^{`+}$, where the plus sign indicates the Moore-Penrose pseudo-inverse (Koch, 1988).

$$\Sigma^{`}\{e\} = \sigma_o^2 P^{`+} \quad where \quad P^{`}\vec{d} = 0 \qquad (6.18)$$

Using the modified weight matrix, the LSA target function can be redefined as per Equation 6.19. Since the additional unknown vector ($\vec{d}$) belongs to the null space of the modified weight matrix, then the LSA target function in Equation 6.19 reduces to the form in Equation 6.20. Thus, the solution ($\delta\hat{\vec{x}}$) to the LSA target function is defined by Equation 6.21 (refer to Appendix *A* for detailed derivation). Using the law of error propagation, the variance-covariance matrix of the solution vector ($\Sigma\{\delta\hat{\vec{x}}\}$) is shown in Equation 6.22 (refer to Appendix *A* for the detailed derivation).

$$\vec{e}^T P^{`} \vec{e} = \left(\vec{y} - A\,\delta\vec{x} - \vec{d}\right)^T P^{`}\left(\vec{y} - A\,\delta\vec{x} - \vec{d}\right) = min|_{\delta\vec{x},\vec{d}} \quad \text{LSA Target Function} \qquad (6.19)$$

$$\vec{e}^T P^{`} \vec{e} = (\vec{y} - A\,\delta\vec{x})^T P^{`}(\vec{y} - A\,\delta\vec{x}) = min|_{\delta\vec{x}} \quad \text{LSA Target Function} \qquad (6.20)$$

$$\delta\hat{\vec{x}} = (A^T P^{`} A)^{-1} A^T P^{`} \vec{y} = N^{-1} A^T P^{`} \vec{y} \quad \text{Estimated Unknowns} \qquad (6.21)$$

$$\Sigma\{\delta\hat{\vec{x}}\} = \sigma_o^2 N^{-1} \quad \text{Variance-Covariance Matrix} \qquad (6.22)$$

The last step is to estimate the a-posteriori variance factor ($\hat{\sigma}_o^2$) by deriving the expected value of the sum of squares of weighted predicted residuals. Starting from Equation 6.23, one can derive an estimate for the a-posteriori variance factor according to Equation 6.24, where q is the rank of the modified weight matrix ($P^{`}$) – refer to Appendix *A* for the detailed derivation.

$$\begin{aligned} E\left(\tilde{\vec{e}}^T P^{`} \tilde{\vec{e}}\right) &= E\{(\vec{y} - A\,\delta\hat{\vec{x}} - \vec{d})^T P^{`}\left(\vec{y} - A\,\delta\hat{\vec{x}} - \vec{d}\right)\} = \\ &= E\left\{\left(\vec{y} - A\,\delta\hat{\vec{x}}\right)^T P^{`}\left(\vec{y} - A\,\delta\hat{\vec{x}}\right)\right\} = (q - m)\sigma_o^2 \end{aligned} \qquad (6.23)$$

$$\hat{\sigma}_o^2 = (\vec{y} - A\delta\hat{\vec{x}})^T P^{`}(\vec{y} - A\delta\hat{\vec{x}})/(q - m) \qquad (6.24)$$

In summary, from an implementation point of view, the LSA solution to the stochastic model in Equation 6.25 can be derived using Equations 6.21, 6.22, and 6.24. This solution is similar to the solution of the traditional Gauss Markov model (Equations 6.11, 6.13, and 6.14) with the exception that the redundancy is evaluated as the difference between the rank of the modified weight matrix and the number of unknowns. One should note that in order to have a solution, the rank of the modified weight matrix should be larger than the number of unknowns. This should not be a concern given the large number of point-patch pairs utilized in the calibration procedure. The modification in the weights of the noise vector allows for the elimination of the additional unknown vector ($\vec{d}$) while having almost no impact on the traditional LSA (i.e., the system parameters are obtained using the traditional solution for the Gauss Markov model in the absence of the additional unknown vector). It is important to note that the proposed weight modification process will nullify the unknown vector ($\vec{d}$). The modified LSA will deal with pseudo-conjugate points, after the weight modification process, in the same way it would deal with true conjugate points, which makes the implementation much simpler.

$$\vec{y} = A\,\delta\vec{x} + \vec{d} + \vec{e} \qquad \vec{e}\sim\left(0, \Sigma^{`}\right) \qquad where\ \Sigma^{`} = \sigma_o^2 P^{`+}\ and\ P^{`}\vec{d} = 0 \tag{6.25}$$

So far, it was established that by modifying the weight matrix to satisfy the condition in Equation 6.18, one can derive an estimate of the corrections to the approximate values of the unknown parameters while dealing with non-conjugate points along corresponding point-patch pairs. The question now is how to derive the modified weight matrix ($P^{`}$). This can be established according the following procedure. First, one starts by defining a new coordinate system (UVW), where the UV axes are aligned along the TIN patch (i.e., W is parallel to the TIN patch normal). One should note that this will be done for each TIN patch in the matched point-patch pairs. Figure 6.3 illustrates how the UVW system is defined using the TIN patch vertices (abc). The U axis is defined along the vector r_b^a, the W axis is defined along the normal to the TIN patch, and the V axis is defined in order to have a right-handed coordinate system. In Figure 6.3, one should note that the symbol × denotes cross product. The relationship between the XYZ and UVW coordinates – assuming that the two systems share the same origin – can be expressed by Equation 6.26. The rotation matrix M is obtained using the components of the unit vectors $\vec{u}$, $\vec{v}$, and $\vec{w}$ along the UVW axes (illustrated in Figure 6.3), which are defined relative to the XYZ system, as shown in Equation 6.27.

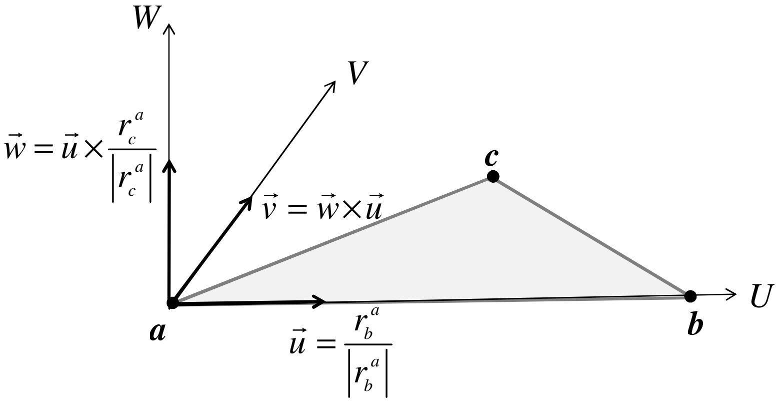

Figure 6.3. Local UVW coordinate system defined for a given TIN patch *abc*.

$$\begin{bmatrix} U \\ V \\ W \end{bmatrix} = M \begin{bmatrix} X \\ Y \\ Z \end{bmatrix} \tag{6.26}$$

$$M = \begin{bmatrix} u_x & u_y & u_z \\ v_x & v_y & v_z \\ w_x & w_y & w_z \end{bmatrix} \tag{6.27}$$

The weight matrix of the transformed coordinates in the UVW system can be derived from the law of error propagation using the rotation matrix M and the weight matrix in the XYZ system (P_{XYZ}), according to Equation 6.28. This weight matrix is then modified according to Equation 6.29.

$$P_{UVW} = MP_{XYZ}M^T = \begin{bmatrix} P_U & P_{UV} & P_{UW} \\ P_{VU} & P_V & P_{VW} \\ P_{WU} & P_{WV} & P_W \end{bmatrix} \tag{6.28}$$

$$\grave{P}_{UVW} = \begin{bmatrix} 0 & 0 & 0 \\ 0 & 0 & 0 \\ 0 & 0 & P_W \end{bmatrix} \tag{6.29}$$

Finally, the modified weight matrix in the XYZ coordinate system is defined by Equation 6.30. Using the modified weight matrix in Equation 6.30, one can show that $\grave{P}_{XYZ}\,\vec{d} = 0$ (refer to Equation 6.31) while noting that the unknown vector ($\vec{d}$) is aligned along the TIN patch (refer to Figure 6.1b). In Equation 6.31, dX, dY, and dZ represent the components of the unknown vector ($\vec{d}$) w.r.t. the XYZ system while dU, dV, and dW are the components of the unknown vector $(\vec{d})$ w.r.t. the UVW system, and therefore dW will equal to zero (non-conjugate points lie on the same TIN patch). It is important to note that the proposed weight modification process will nullify the unknown vector $(\vec{d})$ while maintaining the respective weight in the normal direction to the TIN patch (i.e., the normal distance between a point and its corresponding TIN patch is the only relevant quantity for minimizing the discrepancies among the involved surfaces).

$$\grave{P}_{XYZ} = M^T \, \grave{P}_{UVW} M \tag{6.30}$$

$$\grave{P}_{XYZ}\vec{d} = M^T \, \grave{P}_{UVW} M \begin{bmatrix} dX \\ dY \\ dZ \end{bmatrix} = M^T \, \grave{P}_{UVW} \begin{bmatrix} dU \\ dV \\ dW \end{bmatrix} = M^T \begin{bmatrix} 0 & 0 & 0 \\ 0 & 0 & 0 \\ 0 & 0 & P_W \end{bmatrix} \begin{bmatrix} dU \\ dV \\ 0 \end{bmatrix} = 0 \tag{6.31}$$

One should note that each pair of pseudo-conjugate points provides three observations of the form in Equation 6.25. However, these three observations increase the redundancy by only one (the rank of the modified weight matrix for these three equations is one – refer to Equation 6.29). In other words, the three observations would increase the redundancy by three if and only if the 3D discrepancy between the pseudo-conjugate points is considered. After the weight modification process, the 2D discrepancy between the pseudo-conjugate points along the TIN plane (i.e., the unknown vector $(\vec{d})$) is ignored during the minimization process. Therefore, only the discrepancy between the pseudo-conjugate points along the TIN normal is minimized during the modified LSA (thus, the three observations only increase the redundancy by one). Since the modified LSA only minimizes the normal distance between a point in S_1 and the corresponding TIN in S_2, the topography in the overlap area should have different slope and aspect values to ensure reliable estimates of the system parameters. Another requirement to have a solution would be, as already mentioned, having the rank of the modified weight matrix larger than the number of unknowns. Such a requirement is quite straightforward to meet due to the large number of point-patch pairs utilized in the calibration procedure.

6.5 Calibration Procedure: Workflow

Figure 6.4 illustrates the flowchart of the proposed rigorous calibration procedure. First, the predicted coordinates of the LiDAR point cloud are computed using the system raw measurements and the initial approximations for the system parameters $(\vec{x}_o)$. Then, overlapping strip pairs, following the optimum configuration devised in Chapter 4 – section 4.3, are selected for the calibration procedure. For each overlapping strip pair, one of the strips S_1 is represented by points (with their associated raw measurements) and the second strip S_2 represented by TIN patches (TIN indices and the vertices coordinates with their associated raw measurements). When using LiDAR strip and control surface pairs, the control surface S_1 is represented by points while the LiDAR surface S_2 is represented by TIN patches. The initial correspondence (matching) between points in S_1 and patches in S_2 is established using the Closest Patch procedure, as described in section 6.3. Using the established point-patch pairs, the modified LSA procedure can be performed to come up with an updated estimate for the system parameters. Since the observation equations are non-linear, the LSA would follow an iterative procedure (this iterative procedure is denoted by the "inside loop" – *il* – in Figure 6.4). After estimating the system parameters, one can derive a better prediction of the point cloud coordinates in the different strips. Since the correspondence between point-patch pairs might change after updating the point/vertices coordinates, a new set of correspondences is established using the updated point cloud coordinates. Using these correspondences, one can iteratively proceed to derive better estimate of the system parameters (this iterative procedure is referred to as the "outside loop" – *ol* – in Figure 6.4). In summary, within the outside loop, an iterative matching and parameter estimation is conducted until the change in the estimated system parameters or the estimated a-posteriori variance factor is below pre-specified thresholds.

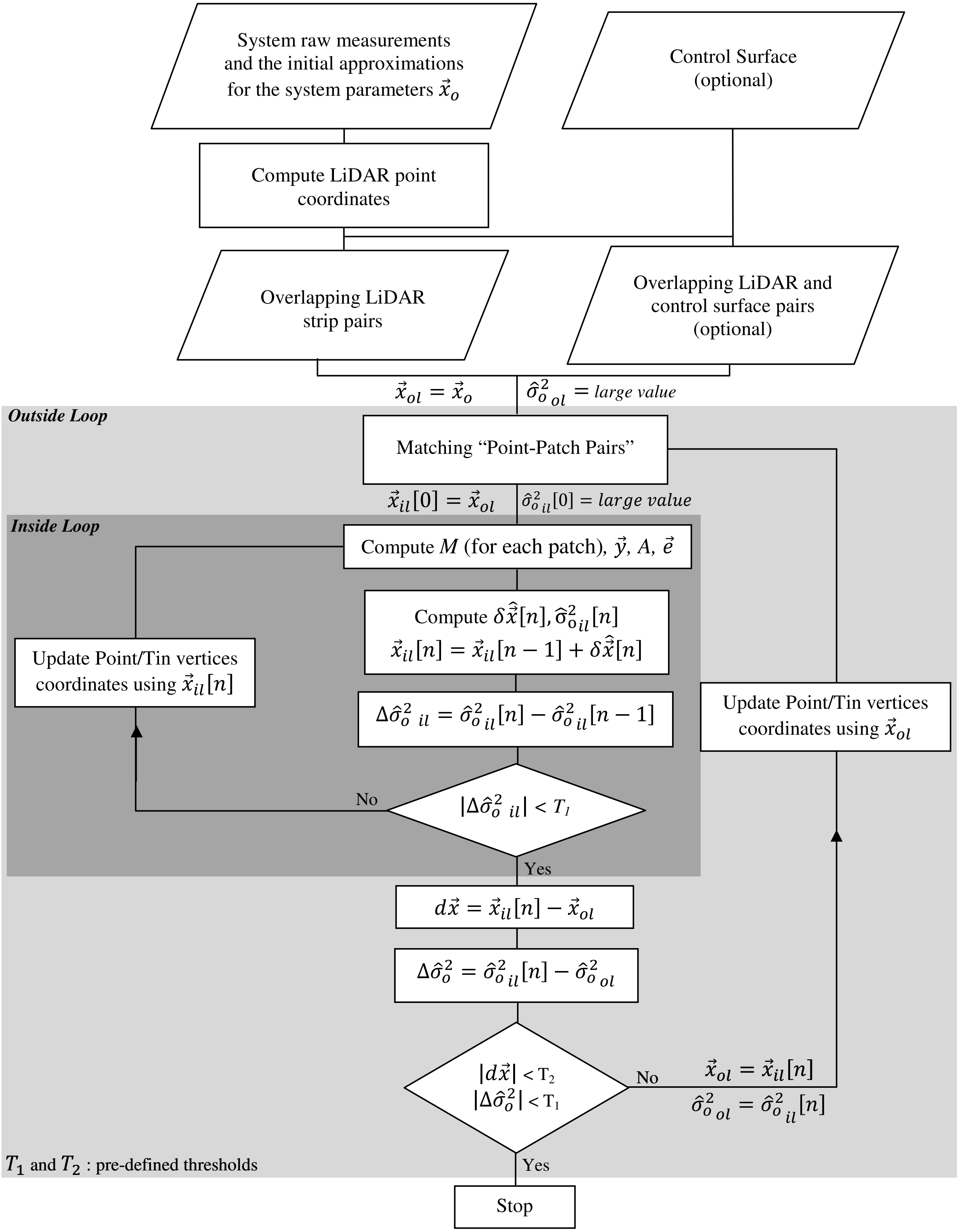

Figure 6.4. Flowchart of the proposed calibration procedure.

6.6 Summary

In this chapter, a rigorous LiDAR system calibration has been introduced. The contributions of the proposed method can be summarized as follows:

- The proposed method is fully automated and does not require specific features in the covered area (e.g., planar or linear features) as long as good topography with varying slope and aspect is available, which would be a requirement for any surface-based calibration method;
- Suitable primitives, which can deal with the irregular nature of the LiDAR point cloud, are implemented. It is important to note that the utilized primitives do not involve pre-processing of the data (i.e., classification or segmentation of the dataset);
- The parameters associated with the utilized primitives are not part of the unknowns, which significantly decreases the storage and execution time requirements due to the manageable size of the normal equation matrix;
- Control and tie features can be equally utilized in the calibration procedure without enforcing any constraints about the nature of the control data (i.e., a collection of control points that need not be physically identified in the LiDAR data can be incorporated);
- The correspondence between conjugate primitives is determined within the calibration process using a robust automated matching procedure that filters out instances where the TIN patches do not represent the physical surface;
- Although higher order primitives are used in the proposed method, simplicity in its implementation is maintained by utilizing point-based observation equations. For that purpose, a modification to the traditional Gauss Markov stochastic model is introduced together with a rigorous analysis of the impact of such modification.

The hypothesis, which will be tested/verified in the experimental results section is that the proposed method can achieve comparable results with existing rigorous approaches, which are also based on appropriate primitives, while providing all the benefits above listed.

CHAPTER 7

EXPERIMENTAL RESULTS

7.1 Introduction

In this chapter, experimental results to test the validity of the proposed photogrammetric and LiDAR system calibration methods are demonstrated.

7.2 Photogrammetric System Calibration Experimental Results

The experiments presented in this section have the following objectives:

- Test the validity of the proposed methodology for determining the distortion model adequacy.
- Verify the hypothesis that inappropriate distortion model would negatively affect the estimation of the mounting parameters, and therefore, would also affect the quality of the object space reconstruction.
- Demonstrate the validity of the devised optimum flight and control configuration for the estimation of the system parameters (i.e., the principal point coordinates, the principal distance, and the mounting parameters) of airborne single-camera systems.
- Verify the hypothesis that the principal point coordinates and the principal distance determined in laboratory/indoor calibration might experience variations under operational conditions (while considering different flying heights) for airborne systems.
- Demonstrate the feasibility of the proposed single-step procedure for the photogrammetric system calibration. The experimental results aim at verifying the following hypotheses:
    - It is hypothesized that for single-camera systems, the proposed single-step procedure (based on the direct incorporation of the GPS/INS position and orientation and the mounting parameters in the collinearity equations) and

the commonly used added observations method in previous work yield compatible results.

- It is hypothesized that the proposed single-step procedure is also suitable for multi-camera systems.
- It is hypothesized that for multi-camera systems, the proposed single-step procedure can be also used for the estimation of the ROP among the cameras. Such procedure has been denoted as the “indirect geo-referencing with ROC”.
- It is hypothesized that the devised general ISO model, which can incorporate prior information on the ROP among the cameras, can be used to derive the previous models (i.e., the model for the estimation of the ROP among the cameras as well as the model for the estimation of the mounting parameters relating the cameras and the IMU body frame) as special cases.
- It is hypothesized that the incorporation of prior information on the ROP among the cameras in the ISO procedure will improve the quality of the estimated parameters.
- It is already established for GPS/INS-assisted systems that the two-step procedure for the estimation of the system mounting parameters has an inferior performance (less accuracy) when compared to the single-step procedure for single camera systems (Jacobsen, 1999; Cramer et al., 2000) as well as for multi-camera systems (Rau et al., 2011). In the absence of GPS/INS data, some studies have been performed to compare the quality of the object space reconstruction using the conventional bundle adjustment procedure and the bundle adjustment while enforcing the relative orientation constraints among the cameras for a two-camera system (King, 1992) while having a good imaging configuration. In the study performed by (King, 1992), where a good imaging geometry is

utilized, no significant improvements in the object space reconstruction have been observed. In the current research work, it is hypothesized that in case of having a weak imaging geometry, the proposed indirect geo-referencing with ROC method will yield better results than the traditional bundle adjustment in terms of the quality of the object space reconstruction. It is also hypothesized that the estimated ROP among the cameras using the proposed indirect geo-referencing with ROC method will be of better quality than the estimated ROP using the outcome from the traditional bundle adjustment in a two-step procedure.

The sets of experiments to satisfy these objectives have been performed using real and/or simulated datasets and are presented in the following subsections.

7.2.1 Indoor Camera Calibration

To test the feasibility of the proposed methodology for determining the distortion model adequacy, an indoor camera calibration procedure utilizing a 2D test field and the Brown-Conrady model (Equation 3.1) was performed. The utilized geometric configuration for the bundle adjustment with self-calibration consisted of twelve convergent images taken from six camera stations at two different heights in landscape and portrait orientation. The utilized camera – a MFDC Rollei P-65 – has an array dimension of 8984x6732 pixels, a pixel size of 6 μm, and a nominal principal distance of 60 mm.

The adequacy of three distortion models is investigated in this work. The first model, denoted as *A*, includes the parameter K_1 only. The second model is denoted as *B* and includes the parameters K_1 and K_2. Finally, the third model, denoted as *C*, includes the parameters K_1, K_2, P_1, P_2, A_1, and A_2.

Table 7.1 reports the calibration results (i.e., the a-posteriori variance factor, the estimated calibration parameters, and the standard deviations) using the three different distortion models. It can be noticed in Table 7.1 that there is a significant improvement in the a-posteriori variance factor $(\hat{\sigma}_o)^2$ when utilizing the distortion model *B* instead of model *A*. In other words, model *B* leads to a better fit between the observations and the estimated parameters, including the IOP, more than that resulting from model *A*. The same significant improvement can be observed in the standard deviations of the estimated parameters in model *B* when compared with those derived from model *A*. The improvement in the a-posteriori variance factor $(\hat{\sigma}_o)^2$, on the other hand, is less significant when using the distortion model *C* instead of model *B*. A closer look at the results also reveals that even though the a-posteriori variance factor $(\hat{\sigma}_o)^2$ of model *C* is slightly better than that in model *B*, the standard deviation of some of the estimated parameters (e.g., x_p, y_p) using model *B* is better than that in model *C*. This is explained by the over-parameterization in model *C* that leads to correlation among the IOP and among the IOP and EOP. The correlation within the IOP is mainly between the x_p, y_p and P_1, P_2 (note the significant deviations between the estimates of x_p, y_p in models *B* and *C*). As a result, model *B* leads to better estimate of the IOP when compared with model *C*.

Based on the presented results, the following conclusions can be made:

- Model *A* is an **inadequate/insufficient** model for representing the inherent distortions in the implemented camera.
- Model *B* is the most **adequate** model from the investigated ones for representing the inherent distortions in the implemented camera. Therefore, differently from what is usually assumed for MFDCs, K_1 is not sufficient to model the lens distortion of the used MFDC in this research work.
- Model *C* is an **over-parameterized** model that leads to correlation among the elements of the IOP as well as correlation between the IOP and EOP.

Table 7.1. Calibration results (i.e., the estimated a-posteriori variance factor, the estimated calibration parameters, and the standard deviations) using indoor technique and the distortion models under investigation.

	Model *A*	Model *B*	Model *C*
$(\sigma_o)^2$ $(\mathrm{mm})^2$	$(0.0019)^2$	$(0.0011)^2$	$(0.0010)^2$
x_p (mm±mm)	0.0653 ±0.0050	0.0649 ±0.0028	0.0058 ±0.0069
y_p (mm±mm)	0.1484 ±0.0049	0.1541 ±0.0027	0.0829 ±0.0069
c (mm±mm)	60.686 ±0.0123	60.678 ±0.0070	60.681 ±0.0065
K_1 (mm^{-2}± mm^{-2})	-2.0137e-007 ±7.5957e-008	-4.2737e-006 ±9.5110e-008	-4.2090e-006 ±9.1696e-008
K_2 (mm^{-4}± mm^{-4})	-	5.5041e-009 ±1.1476e-010	5.4768e-009 ±1.0631e-010
P_1 (mm^{-1}± mm^{-1})	-	-	-5.4675e-006 ±6.0061e-007
P_2 (mm^{-1}± mm^{-1})	-	-	-6.5251e-006 ±6.0055e-007
A_1	-	-	1.1723e-005 ±5.5275e-006
A_2	-	-	-3.0024e-005 ±9.0786e-006

Now, it will be verified whether one can use the bundle similarity approach to prove the adequacy of model *B*. For that purpose, distortion model adequacy is verified for the three different models according to the ZROT, ROT, and SPR bundle similarity methods. The results are presented in Table 7.2. One can observe in the reported $\mathrm{RMSE}_{\mathrm{offset}}$ values in Table 7.2 that models *A* and *B* define two different bundles regardless of the utilized similarity model ($\mathrm{RMSE}_{\mathrm{offset}}$ larger than 1/2 pixel for all methods). Models *B* and *C*, on the other hand, are deemed similar according to the ROT and SPR methods and deemed different according to the ZROT method. The non-similarity between models *B* and *C* according to ZROT can be explained by the over-parameterization introduced by model *C*, which leads to some correlation among the IOP as well as among the IOP and the EOP while keeping the same shape of the bundles defined by model *B*. In other words, models *B* and *C* produce bundles with similar shape (i.e., the bundles are in agreement with each other after applying some rotations) and therefore are similar according to ROT and SPR methods. Therefore, model *C* does not lead to variation in the shape of the bundle when compared with model *B*. These results confirm model *B* as the most adequate model among the investigated ones to represent the distortions inherent in the implemented camera.

In section 7.2.2.1 (real dataset I), the adequacy of the distortion model *B* will be verified by checking the quality of the estimated mounting parameters in the system calibration procedure.

Table 7.2. Analysis of the distortion models adequacy using bundle similarity methods.

	$RMSE_{offset}$		
	ZROT	ROT	SPR
Indoor (*A*) vs. Indoor (*B*)	0.009714 mm (1.619 pixel)	0.008798 mm (1.466 pixel)	0.003611 mm (0.602 pixel)
Indoor (*B*) vs. Indoor (*C*)	0.069173 mm (11.529 pixel)	0.001506 mm (0.251 pixel)	0.001205 mm (0.200 pixel)

7.2.2 System Calibration

In this section, experiments using simulated and real datasets are performed to test the performance of the proposed methodology for the photogrammetric system calibration of single and multi-camera systems.

7.2.2.1 Airborne Single-Camera Systems

The main objective of the experiments using airborne single-camera systems is, besides testing the feasibility of the proposed single-step procedure, to demonstrate the validity of the devised optimum flight and control configuration for the photogrammetric system calibration. To test the feasibility/effectiveness of the proposed method/flight and control configuration one should look into the (i) a-posteriori variance factor, (ii) precision of the estimated parameters and correlations among them, (iii) proximity of the estimated lever arm offset components to the physically measured ones (for real datasets), (iv) closeness of the estimated parameters with the simulated ones (in case of simulated data), and (v) quality of the object space reconstruction (through RMSE analysis using check points).

Experiment Set I

In this set of experiments, simulated and real datasets are utilized. The simulated and real datasets have the same configuration, which is illustrated in Figure 7.1. As shown in this figure, the flight configuration consists of a total of six flight lines: four flown in the E-W direction and two in the N-S direction, (in opposite directions) with 60% overlap. The flight lines flown in the E-W direction (L1, L2, L3, and L4) were acquired from a flying height of ~550 m (above MSL) and 50% side lap. The flight lines flown in the N-S direction (L5 and L6) were obtained from a flying height of approximately 1200 m (above MSL) and 100% side lap. The average base-height ratio for both flying heights is approximately 0.26. This dataset has been acquired using the Rollei P-5 MFDC, which has been calibrated in section 7.2.1. As already mentioned, this camera has an array dimension of 8984x6732 pixels (53.904x40.392 mm) with a pixel size of 6 μm. The GPS/INS-derived position and attitude accuracy are ±10 cm and ±10 sec, respectively. It is important to mention that the provided navigation solution refers to the GPS antenna phase center. The accuracy of the GCP is ± 10 cm.

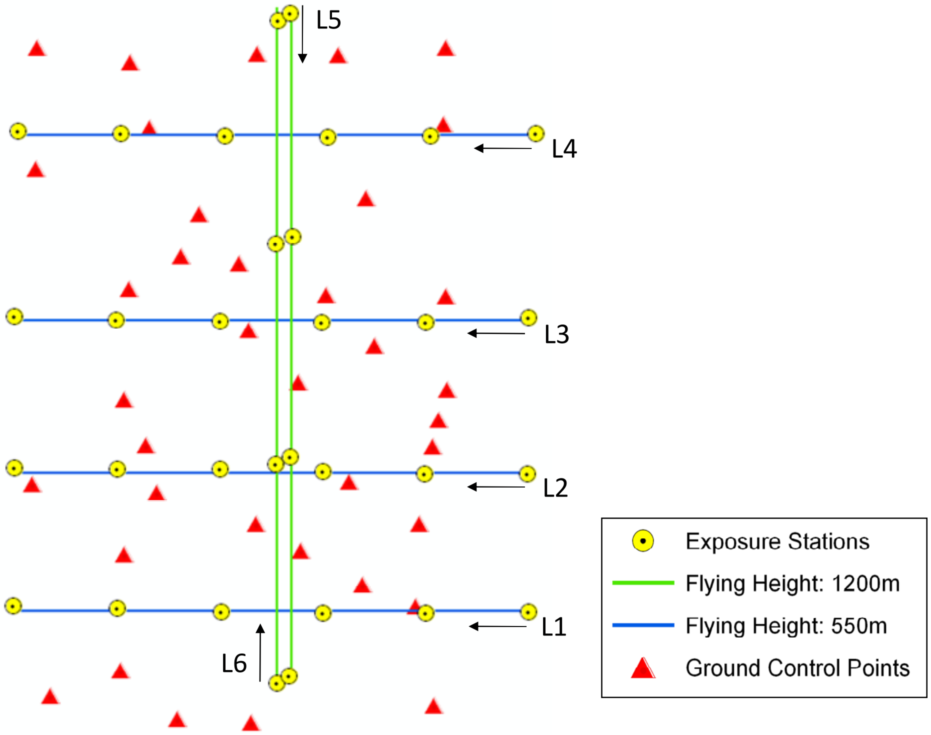

Figure 7.1. Flight and control configuration of the datasets used in experiment set I.

Simulated Dataset I

The objectives of using synthetic data in this set of experiments are as follows: (i) verify the performance of the devised flight configuration and the available camera geometry, as it relates to the estimation of the system parameters (i.e., the mounting parameters, the principal point coordinates, and the principal distance) and the photogrammetric reconstruction, in a controlled environment, (ii) investigate whether the system parameters are significantly different when adding more flight lines to the minimum recommended configuration, (iii) perform a comparative analysis with the results obtained from the commonly used single-step procedure in previous work (i.e., the added observations method), and (iv) infer problems in the real dataset with equivalent configuration (i.e., wherever the obtained results deviate significantly from the expected ones based on the simulation results).

For the purpose of investigating whether the system parameters are significantly different when adding more flight lines to the optimum recommended configuration, two configurations are tested:

- Configuration I: includes flight lines L1 and L2 (same direction with 50% side lap), L5 and L6 (opposite directions with 100% side lap), which comply with the optimum recommended configuration.
- Configuration II: includes all the flight lines (i.e., L1 – L6).

The mounting parameters were simulated as 0.50, 0.50, and 1.00 m for the lever arm offset components ΔX, ΔY, and, ΔZ, respectively; and 0.50º, 0.50º, and 181º for the boresight angles $\Delta\omega$, $\Delta\varphi$, and $\Delta\kappa$, respectively. The principal distance (c) and the principal point coordinates (x_p and y_p) were simulated as 60.6786 mm, 0.1541 mm, and -0.0649 mm, respectively. The simulated noise in the image measurements is ±3 μm, while the noise in the camera IOP is ±1 μm. The GPS/INS derived position and attitude accuracy was simulated with the same accuracy of the real data (i.e., ±10 cm and ±10 sec, respectively). The accuracy of the simulated vertical control point is ± 10 cm.

The experiments involved the estimation of the system mounting parameters only and the estimation of the system mounting parameters along with the principal point coordinates and the principal distance. Also, the two single-step methods (i.e., the added observations method and the proposed method, based on the direct incorporation of GPS/INS position and orientation and the system mounting parameters in the collinearity equations) have been tested. Table 7.3 presents the calibration results (i.e., the a-posteriori variance factor, the estimated system parameters, the standard deviations, and the RMSE analysis) using one vertical control point, the two single-step methods while using the optimum recommended configuration (configuration I). On the other hand, Table 7.4 presents the calibration results while using the redundant configuration (configuration II). In both tables, one can observe that the estimated system parameters are quite compatible with the introduced ones. Also, the reported precision of the estimated parameters and the RMSE values comply with the expected ones based on the accuracy of the navigation data and geometry of the data acquisition system.

The average correlation (for both investigated configurations) among the estimated parameters, when solving for the mounting parameters only, was 0.13 and 0.09 for the added observations and the proposed single-step procedure, respectively. The highest correlation found in the added observations method was 0.98 among the Z_o of some of the images. Also, correlations of 0.97 among the EOP and the mounting parameters were observed. In the proposed method, the highest correlation was 0.93 between the coordinates of some of the tie points. The average correlation among the estimated parameters, when solving for the mounting parameters, the principal point coordinates, and the principal distance, was 0.13 and 0.09 for the added observations method and the proposed single-step procedure, respectively. Here again, correlations of 0.98 among the Z_o of some of the images and correlations of 0.97 among EOP and the mounting parameters were found in the added observations method. In the proposed method, the highest correlation was 0.96 between the Y coordinates of some of the tie points.

As expected, the reported values in Tables 7.3 and 7.4 reveal that both approaches provide compatible estimates for the system parameters, which demonstrate the equivalency of these two methods. The RMSE values, which are computed by comparing the reconstructed object space using the estimated system parameters with the ground truth, confirm such finding. One should note that although satisfactory results were obtained with the utilized simulated dataset, the correlation among the exterior orientation parameters and among the exterior orientation parameters and the mounting parameters observed in the added observations method might be a concern when the utilized data do not comply with the optimum configuration.

In both methods, correlation of 0.85 were observed between ΔX and x_p and correlation of 0.86 between ΔY and y_p, which demonstrates that having flight lines flown at different flying heights allows for the decoupling of these parameters.

Table 7.3. Calibration results (a-posteriori variance factor, estimated system parameters, standard deviations, and RMSE analysis) using simulated data, one vertical control point, the added observations, the different approaches for the photogrammetric system calibration, and configuration I.

	Added Observations Method		**Direct Incorporation (Proposed) Method**	
	Mounting Parameters Only	Mounting Parameters + x_p, y_p, c	Mounting Parameters Only	Mounting Parameters + x_p, y_p, c
$(\hat{\sigma}_o)^2$ $(mm)^2$	$(0.0026)^2$	$(0.0026)^2$	$(0.0026)^2$	$(0.0026)^2$
x_p (mm±mm)	-	0.15565±0.0046	-	0.15565±0.0046
y_p (mm±mm)	-	-0.06588±0.0044	-	-0.06588±0.0044
c(mm±mm)	-	60.68031±0.0057	-	60.68031±0.0057
ΔX (m±m)	0.578±0.03	0.560±0.07	0.578±0.03	0.560±0.07
ΔY (m±m)	0.462±0.03	0.475±0.07	0.462±0.03	0.475±0.07
ΔZ (m±m)	1.091±0.11	1.076±0.12	1.091±0.11	1.076±0.12
$\Delta\omega$ (deg±sec)	0.50058±5.5	0.50062±5.6	0.4994±5.5	0.5001±5.6
$\Delta\varphi$ (deg±sec)	0.50192±6.2	0.50212±6.5	0.4976±6.2	0.5007±6.5
$\Delta\kappa$ (deg±sec)	180.99815±13.2	180.99812±13.4	181.0036±13.2	181.0036±13.3
RMS_X (m)	0.035	0.036	0.035	0.036
RMS_Y (m)	0.027	0.029	0.027	0.029
RMS_Z (m)	0.130	0.130	0.130	0.128
Number of check points	170	170	170	170

The findings of the performed experiments can be summarized as follows:

- Given that an appropriate flight/control configuration is utilized, the added observations method and the proposed single-step procedure will yield compatible results;
- A comparison of the reported estimated system parameters in Tables 7.3 and 7.4 reveals that adding more flight lines to the recommended optimum configuration do not significantly improve the results, confirming the hypothesis that the devised optimum configuration can reliably estimate the system parameters;

- The performed experiments demonstrate the possibility of the simultaneous estimation of the system mounting parameters, the principal point coordinates, and the principal distance.

Table 7.4. Calibration results (i.e., a-posteriori variance factor, estimated system parameters, standard deviations, and RMSE analysis) using simulated data, one vertical control point, the added observations, the different approaches for the photogrammetric system calibration, and configuration II.

	Added Observations Method		**Direct Incorporation (Proposed) Method**	
	Mounting Parameters Only	Mounting Parameters + x_p, y_p, c	Mounting Parameters Only	Mounting Parameters + x_p, y_p, c
$(\hat{\sigma}_o)^2$ (mm)^2	(0.0026)^2	(0.0026)^2	(0.0026)^2	(0.0026)^2
x_p (mm±mm)	-	0.15713±0.0042	-	0.15713±0.0042
y_p (mm±mm)	-	-0.06661±0.0040	-	-0.06661±0.0040
c (mm±mm)	-	60.68201±0.0047	-	60.68201±0.0047
ΔX (m±m)	0.561±0.03	0.527±0.06	0.561±0.03	0.527±0.06
ΔY (m±m)	0.467±0.03	0.490±0.06	0.467±0.03	0.490±0.06
ΔZ (m±m)	1.021±0.10	0.997±0.10	1.021±0.10	0.997±0.10
$\Delta\omega$ (deg±sec)	0.50081±5.0	0.50086±5.1	0.50081±5.0	0.50086±5.1
$\Delta\varphi$ (deg±sec)	0.50187±5.5	0.50223±5.7	0.50187±5.5	0.50223±5.7
$\Delta\kappa$ (deg±sec)	180.99903±10.1	180.99915±10.2	180.99903±10.1	180.99915±10.2
RMS_X (m)	0.019	0.019	0.019	0.019
RMS_Y (m)	0.017	0.021	0.017	0.021
RMS_Z (m)	0.058	0.058	0.058	0.058
Number of check points	170	170	170	170

Real Dataset I

Besides testing the feasibility of the proposed photogrammetric system calibration and the devised optimum flight and control configuration, the main purpose of the set of experiments performed in this section is to check the validity of the camera calibration parameters determined in the indoor calibration (section 7.2.1). More specifically, the adequacy of the distortion model *B* will be verified. Such verification will be performed by looking into the quality of the estimated system mounting parameters as well as the quality of the object space reconstruction. Moreover, it will be verified whether the quality of the estimated system parameters would improve significantly with the increase in the number of utilized GCP.

In the performed experiments using real data, it could be observed that the given a-priori standard deviation of the available attitude (±10 sec) was too optimistic in the adjustment procedure. Such finding was made by inspecting the a-posteriori variance factor. When using the given standard deviation for the attitude information of ±10 sec, the obtained a-posteriori variance factor was much higher than the expected one, which is based on the accuracy of the image measurements. When running the calibration in a GPS-assisted mode (i.e., considering the attitude information as unknown), the obtained a-posteriori variance factor was close to the expected one, thus revealing problems with the given a-priori standard deviation for the attitude information. The realistic standard deviation of ±100 sec was established after several trials.

The performed experiments involved the estimation of the system mounting parameters while using the different IOP sets (*A*, *B*, and *C*) and varying the number of implemented vertical GCP. Table 7.5 presents the system calibration results (i.e., the a-posteriori variance factor, the estimated mounting parameters, and the standard deviations) using the different IOP sets (*A*, *B*, and *C*) and different number of vertical GCP. Table 7.5 also presents the physically measured lever arm offset. Table 7.6 presents the RMSE analysis for all the investigated scenarios.

It can be noted in the reported values in Table 7.5 that the inadequacy of model *A* in describing the inherent distortions in the involved camera is manifested in the worst a-posteriori variance factor among the tested models. Moreover, the inadequacy of model *A* results in unrealistic estimate of the lever arm offset when compared with the physically measured, the worst precision for the estimated mounting parameters as well as the worst RMSE values. Model *B* leads to the closest estimate of the lever arm offset when compared to the physically measured one (refer to the highlighted cells in Table 7.5) as well as the best precision for the estimated mounting parameters. In addition, it leads to the best RMSE results when compared with the other tested models (highlighted cells in Table 7.6). On the other hand, the over-parameterized model *C* leads to unrealistic estimate of the lever arm offset as well as worse estimate of the RMSE values when compared with the outcome from the model *B*, Table 7.6. The performed experiments confirm model *B* as the most adequate model from the investigated ones. Another conclusion that can be drawn from the results reported in Table 7.5 is that increasing the number of implemented GCP does not lead to significant changes in the estimated mounting parameters given that an appropriate configuration is used. This indicates that a single vertical GCP is sufficient for the estimation of the mounting parameters given that an appropriate flight configuration is available and that the utilized vertical GCP is visible in a reasonable number of images (in the performed experiments the GCP was visible/measured in 8 images). Moreover, it can be concluded that for the utilized dataset, the principal point coordinates and the principal distance did not experience variations under operational conditions. Such finding has been made by inspecting the closeness of the estimated lever arm offset components to the physically measured ones. Experiments, solving for the system mounting parameters, the principal point coordinates, and the principal distance simultaneously, have not been performed due to the degraded precision of the available attitude information.

The conclusions from the performed experiments in this section can be summarized as follows:

- The hypothesis that inadequate distortion models will negatively affect the estimation of the mounting parameters and as a consequence will affect the quality of the object space reconstruction has been confirmed;
- The performed experiments have demonstrated that a single vertical GCP is sufficient for the estimation of the mounting parameters given that an appropriate flight configuration is available and that the utilized vertical GCP is visible in a reasonable number of images;

- For the utilized dataset, where the implemented flying heights were not too high (i.e., 550 and 1200 m), the principal point coordinates and the principal distance did not experience variations from those evaluated through indoor calibration.

Table 7.5. Calibration results (i.e., a-posteriori variance factor, estimated mounting parameters, and the standard deviations) using the different distortion models.

	$(\hat{\sigma}_o)^2$	Lever arm offset			Boresight Angles		
		ΔX (m±m)	ΔY (m±m)	ΔZ (m±m)	$\Delta\omega$ (deg±sec)	$\Delta\varphi$ (deg±sec)	$\Delta\kappa$ (deg±sec)
Model *A* + 1 vert. GCP	$(0.0074)^2$	0.31 ±0.15	-0.14 ±0.14	0.32 ±0.41	-0.11022 ±55.7	0.85668 ±54.7	179.58027 ±65.7
Model *B* + 1 vert. GCP	$(0.0025)^2$	-0.09 ±0.05	-0.13 ±0.05	1.14 ±0.14	-0.12534 ±18.9	0.83663 ±18.6	179.54752 ±22.3
Model *B* + 37 vert. GCP	$(0.0024)^2$	-0.08 ±0.05	-0.13 ±0.04	1.11 ±0.05	-0.12198 ±17.0	0.83871 ±17.2	179.54706 ±21.1
Model *B* + 37 full GCP	$(0.0024)^2$	-0.03 ±0.03	-0.15 ±0.03	1.23 ±0.03	-0.12296 ±17.0	0.83754 ±17.4	179.54489 ±16.1
Model *C* + 1 vert. GCP	$(0.0032)^2$	0.26 ±0.07	-1.73 ±0.06	1.21 ±0.18	-0.07466 ±24.3	0.79344 ±23.9	179.54027 ±28.7
Physically measured values		-0.180	-0.170	1.065			

Table 7.6. RMSE analysis using the different distortion models.

	Model (*A*) + 1 vertical GCP	Model (*B*) + 1 vertical GCP	Model (*B*) + 37 vertical GCP	Model (*B*) + 37 full GCP	Model (*C*) + 1 vertical GCP
RMS_X (mean±std) (m)	0.19 (-0.10±0.17)	0.09 (0.06±0.07)	0.10 (0.09±0.06)	NA	0.07 (-0.01±0.07)
RMS_Y (mean±std) (m)	0.25 (-0.17±0.18)	0.09 (-0.01±0.09)	0.09 (-0.04±0.08)	NA	0.42 (0.41±0.07)
RMS_Z (mean±std) (m)	0.27 (-0.22±0.16)	0.13 (0.05±0.12)	NA	NA	0.20 (0.08±0.19)

Experiment Set II

In this set of experiments, simulated and the real datasets are also utilized. The main objective of the experiments in this section is to verify the performance of the available flight configuration for the estimation of the system parameters as well as to check whether the principal point coordinates and the principal distance might experience changes under operational conditions (for the real dataset).

The synthetic data was simulated following the same configuration of the utilized real dataset. The flight configuration of the available dataset consists of 4 flight lines with a total of fifty images. The dataset was acquired from two different flying heights. Flight lines “1” and “2” were flown in opposite directions (E-W and W-E, respectively) with 100% side lap from a flying height of approximate 1500 m. Flight lines “3” and “4” were also flown in opposite directions (E-W and W-E, respectively) with 100% side lap from a flying height of approximately 2000 m. In the surveyed area, sixteen control points were established (accuracy ±10 cm). The flight configuration and the available ground control points are illustrated in Figure 7.2. The average base-height ratio for both flying heights is approximately 0.26. The GPS/INS-derived position and attitude accuracy, given by the data provider, is ±10 cm and ±10 sec, respectively. The utilized camera is the same as the one utilized in the experiment set I. Different from the previously utilized dataset, the provided navigation solution now refers to the IMU body frame. It should be noted that the available dataset comply with the optimum configuration discussed in Chapter 4 except for the parallel flight line with minimum side lap, which would be useful for better estimation of the boresight yaw angle. The estimation of the boresight yaw angle, using the available dataset, is obtained through the minimization of the *y*-parallax between conjugate light rays.

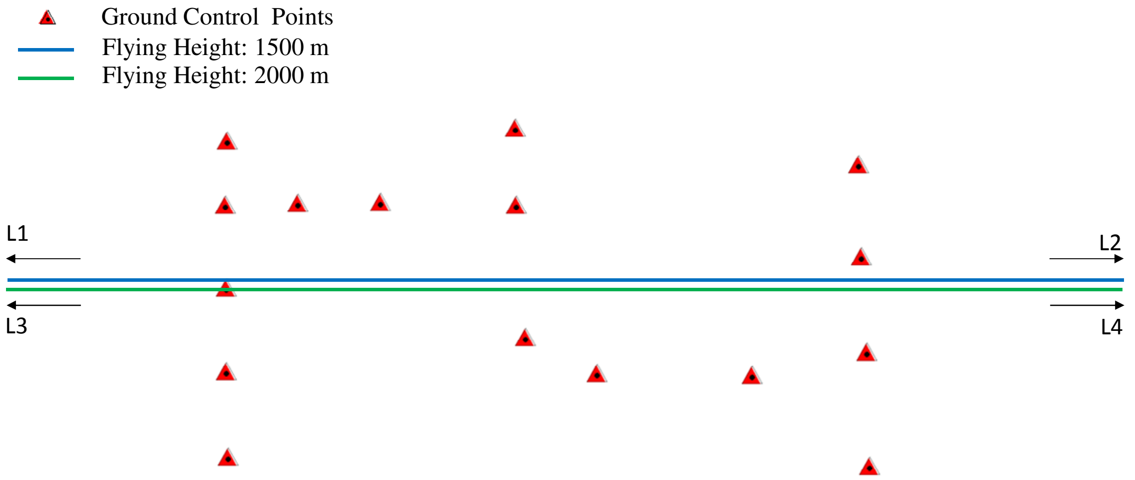

Figure 7.2. Flight and control configuration of the real dataset used in the experiment set II.

Simulated Dataset II

The objectives of using synthetic data in this set of experiments are (i) test the performance of the available flight configuration and camera geometry for the estimation of the system parameters (i.e., the mounting parameters, the principal point coordinates, and the principal distance) in a controlled environment, (ii) check whether a small increase in the number of utilized GCP would promote improvements when the utilized configuration slightly deviate from the optimum recommended configuration, and (iii) check the impact on the quality of the estimated system mounting parameters while having biased principal point coordinates and principal distance.

The mounting parameters were simulated as 0.10, 0.50, and 0.10 m for the lever arm offset components ΔX, ΔY, and, ΔZ, respectively; and 0.0500°, 0.18075°, and 179.97826° for the boresight angles $\Delta\omega$, $\Delta\varphi$, and $\Delta\kappa$, respectively. The camera IOP parameters were simulated as 0.15412 mm, -0.06488 mm, and 60.67857 mm for the x_p, y_p, and c respectively. In terms of the noise level, the image measurement noise was simulated as ½ of the pixel size (i.e., ±3 µm) while the camera IOP noise was simulated as ±1 µm. The GPS/INS-derived position/attitude and the control points' accuracy were simulated with the same accuracy of the real data (i.e., ±10 cm/±10 sec and ±10 cm, respectively).

The experiments involved the estimation of the system mounting parameters only and the estimation of the system mounting parameters along with the principal point coordinates and the principal distance under different control configurations. The outcome from these experiments (i.e., the a-posteriori variance factor and the system parameters as well as the RMSE analysis) is reported in Table 7.7. The first conclusion that can be drawn is that, when using a configuration with less flight lines than the optimum recommended configuration, a small increase in the number of implemented vertical GCP might lead to some improvement in the estimated vertical lever arm offset component (refer to the highlighted values in Table 7.7). The utilized control point was visible (measured) in 6 images. Moreover, the reported values using full control when compared to the results using only vertical control do not show significant improvements, which confirms the requirement of vertical control only. Overall, the reported accuracy of the estimated mounting parameters and the RMSE values comply with the expected ones based on the accuracy of the navigation data and geometry of the data acquisition system. Also, one can observe that the estimated system parameters (in Table 7.7) are quite compatible with the introduced ones.

Correlations of -0.96 and -0.97 were observed between x_p and ΔX and between y_p and ΔY, respectively. Such correlation might be due to an insufficient flying height difference between the flight lines flown at different flying heights. To confirm such hypothesis, Table 7.8 reports the results (i.e., the estimated a-posteriori variance factor, the system parameters as well as the RMSE analysis) when using a higher flying height difference (800 m) while utilizing flying heights 1200 m and 2000 m and three vertical control points. The correlations between x_p and ΔX and between y_p and ΔY dropped to -0.87 and -0.89, respectively, while leading to closer estimates for such parameters when compared to the simulated ones.

Table 7.7. Calibration results (i.e., a-posteriori variance factor, estimated system parameters, standard deviations, and RMSE analysis) using simulated data and different control configurations.

	Mounting Parameters Only			Mounting Parameters + x_p, y_p, and c		
	1 vertical GCP	3 vertical GCP	3 full GCP	1 vertical GCP	3 vertical GCP	3 full GCP
$(\hat{\sigma}_o)^2$ (mm)^2	$(0.0027)^2$	$(0.0027)^2$	$(0.0027)^2$	$(0.0027)^2$	$(0.0027)^2$	$(0.0027)^2$
x_p (mm±mm)	-	-	-	0.15257 ±0.0042	0.15250 ±0.0042	0.15259 ±0.0042
y_p (mm±mm)	-	-	-	-0.06961 ±0.0041	-0.06964 ±0.0041	-0.06960 ±0.0041
c (mm±mm)	-	-	-	60.68071 ±0.0037	60.68068 ±0.0037	60.68046 ±0.0037
ΔX (m±m)	0.09 ±0.03	0.09 ±0.03	0.09 ±0.03	0.13 ±0.12	0.14 ±0.12	0.14 ±0.12
ΔY (m±m)	0.49 ±0.03	0.49 ±0.03	0.49 ±0.03	0.62 ±0.12	0.62 ±0.12	0.62 ±0.12
ΔZ (m±m)	0.25 ±0.16	0.15 ±0.11	0.17 ±0.11	0.30 ±0.19	0.20 ±0.15	0.22 ±0.14
$\Delta\omega$ (deg±sec)	0.05042 ±3.1	0.05042 ±3.1	0.05042 ±3.1	0.05058 ±3.1	0.05059 ±3.1	0.05058 ±3.1
$\Delta\varphi$ (deg±sec)	0.18042 ±3.7	0.18042 ±3.7	0.18042 ±3.7	0.18040 ±3.8	0.18040 ±3.8	0.18039 ±3.8
$\Delta\kappa$ (deg±sec)	179.97719 ±2.8	179.97721 ±2.8	179.97721 ±2.7	179.97707 ±2.8	179.97708 ±2.8	179.97708 ±2.7
RMS_X (m)	0.05	0.05	0.05	0.05	0.05	0.05
RMS_Y (m)	0.06	0.06	0.06	0.06	0.06	0.06
RMS_Z (m)	0.22	0.18	0.18	0.22	0.18	0.18
# Check Points	200	197	197	200	197	197

Table 7.8. Calibration results (i.e., a-posteriori variance factor, estimated system parameters, standard deviations, and RMSE analysis – 197 check points) using simulated data with a larger flying height difference (800 m) and three vertical control points.

x_p (mm ±mm)	y_p (mm ±mm)	c (mm ±mm)	ΔX (m±m)	ΔY (m±m)	ΔZ (m±m)	$\Delta\omega$ (°±sec)	$\Delta\varphi$ (°±sec)	$\Delta\kappa$ (°±sec)
0.15202 ±0.0027	-0.06680 ±0.0026	60.68234 ±0.0024	0.18 ±0.06	0.56 ±0.06	0.13 ±0.12	0.049428 ±3.7	0.18127 ±4.2	179.97958 ±2.8
$(\hat{\sigma}_o)^2$ (mm)^2: $(0.0026)^2$ RMS_X (m): 0.04 RMS_Y (m): 0.07 RMS_Z (m): 0.20								

To verify the impact of biases in the principal point coordinates and principal distance on the quality of the estimated system mounting parameters, biases of 70 µm, 34 µm, and 70 µm, have been introduced in the x_p, y_p, and c, respectively, while keeping them fixed in the calibration procedure. The results are reported in Table 7.9. In this table, it can be noted that biases in the principal point coordinates and principal distance led to unreasonable estimates for the estimated lever arm offset components for the two investigated flying height differences. The RMSE results reveal that there is almost no impact of biases in the IOP on the reconstructed object space. For the biases in the principal point coordinates, such phenomenon can be explained by the utilized flight configuration (opposite flight lines) and the nature of impact of such biases. The impact of biases in the principal point coordinates on the derived object space consists of constant shifts, which are flying direction dependent (refer to Table 4.6). Since the utilized dataset was acquired from flight lines flown in opposite directions the impact on the object points reconstructed from backward and forward strips will be in opposite directions. In the bundle adjustment the final estimate will be the average of the two, which will therefore coincide with the true location (since there is equal number of flight lines in opposite directions). The incompatibility of reconstruction from different flight lines can be observed in the a-posteriori variance factor, which gets worse. On the other hand, the impact of a bias in the principal distance on the object space consists of a vertical shift, which is flying direction independent. One should note that in order to obtain best fit at the location of the vertical control points in the bundle adjustment, the impact of the bias in the principal distance on the object space (which would be the average of the impact for the two available flying heights – e.g., for the flying heights 2000m and 1500m the impact would be 2.33m and 1.75m, respectively) led to unreasonable estimation for the vertical lever arm offset. One should note that the isolated analysis of RMSE results might lead to misleading conclusions. All the evaluation criteria should be always utilized in the analysis.

The following conclusions can be drawn from the performed experiments in this section:

- When using a configuration with less flight lines than the minimum recommended configuration, a small increase in the number of implemented vertical GCP might lead to some improvement in the precision of the estimated vertical lever arm offset component;
- The principal point coordinates and the planimetric lever arm offset can be simultaneously estimated given that an appropriate flying height difference among the utilized flight lines is available;
- Inaccurate principal point coordinates and principal distance will lead to unreasonable estimates for the lever arm offset components.

Table 7.9. Calibration results (i.e., a-posteriori variance factor, estimated system mounting parameters, standard deviations, and RMSE analysis – 197 check points) using three vertical control points, the original simulated data with biases in the principal point coordinates and in the principal distance.

$(\hat{\sigma}_o)^2$ (mm)^2	ΔX (m±m)	ΔY (m±m)	ΔZ (m±m)	$\Delta\omega$ (°±sec)	$\Delta\varphi$ (°±sec)	$\Delta\kappa$ (°±sec)	RMS_X (m)	RMS_Y (m)	RMS_Z (m)
Flying heights: 1500 and 2000 m									
$(0.0029)^2$	-1.71 ±0.04	-0.47 ±0.03	2.11 ±0.12	0.05035 ±3.4	0.18600 ±4.1	179.97802 ±3.1	0.06	0.07	0.20
Flying heights: 1200 and 2000 m									
$(0.0034)^2$	-1.28 ±0.04	-0.25 ±0.03	1.75 ±0.12	0.04615 ±4.5	0.19408 ±5.1	179.98031 ±3.6	0.12	0.10	0.25

Real Dataset II

Similar to the simulated data, the conducted experiments using real data involved the estimation of the system mounting parameters only and the estimation of the system mounting parameters along with the principal point coordinates and the principal distance under different control configurations. The outcome from the experiments (i.e., the a-posteriori variance factor, the estimated system parameters, the standard deviations, and the RMSE analysis) is reported in Table 7.10. Once again, it can be concluded that when using a configuration with less flight lines than the optimum recommended configuration, a small increase the number of implemented vertical GCP might lead to some improvement in the precision of the estimated vertical lever arm offset component (refer to the highlighted values in Table 7.10). One should note that in the experiment using a single vertical control point, the utilized point was visible (measured) in 6 images. The reported values using full control when compared to the results using vertical control only do not show significant improvements, which confirms the requirement of vertical control only. One can observe in Table 7.10, where only the mounting parameters are determined in the system calibration, that the estimated lever arm offset components are quite different from the expected physical ones. More specifically, since the trajectory refers to the IMU body frame, which is mounted close to the camera, the lever arm offset components should be very small, i.e., < 0.5m. Unreasonable estimates for the lever arm offset components might be an indication of instability of the principal point coordinates and the principal distance determined from the indoor calibration or an indication that such parameters have experienced changes under operational conditions. Such hypothesis has been validated in the results using simulated data and is now validated by the results obtained when the principal point coordinates and the principal distance are estimated along with the system mounting parameters, which are presented in Table 7.10. More specifically, when releasing the principal point coordinates and the principal distance, reasonable results for the lever arm offset components are obtained. In these experiments, correlations of -0.94 were observed between x_p and ΔX and between y_p and ΔY. Here again, such correlation is due to an insufficient flying height difference between the flight lines flown at different flying heights.

The conclusions from the performed experiments using real dataset can be summarized as follows:

- As has been already observed in the experiments with simulated data, when using a configuration with less flight lines than the optimum recommended configuration, a small increase in the number of implemented vertical GCP might lead to some improvement in the precision of the estimated vertical lever arm offset component;

– The results have demonstrated that the principal point coordinates and the principal distance determined through an indoor calibration procedure might undergo changes under operational conditions (for flying heights of 1500 and 2000 m).

Table 7.10. Calibration results (i.e., a-posteriori variance factor, estimated system parameters, standard deviations, and RMSE analysis) using real data and different control configurations.

	Mounting Parameters Only			Mounting Parameters + x_p, y_p, and c		
	1 vertical GCP	3 vertical GCP	3 full GCP	1 vertical GCP	3 vertical GCP	3 full GCP
$(\hat{\sigma}_o)^2$ (mm)^2	$(0.0043)^2$	$(0.0043)^2$	$(0.0043)^2$	$(0.0040)^2$	$(0.0040)^2$	$(0.0040)^2$
x_p (mm±mm)	-	-	-	0.08115 ±0.0067	0.08125 ±0.0067	0.08141 ±0.0067
y_p (mm±mm)	-	-	-	-0.10350 ±0.0067	-0.10345 ±0.0067	-0.10358 ±0.0068
c (mm±mm)	-	-	-	60.68259 ±0.0074	60.68263 ±0.0074	60.68281 ±0.0074
ΔX (m±m)	-1.82 ±0.07	-1.82 ±0.07	-1.82 ±0.07	0.10 ±0.18	0.09 ±0.18	0.09 ±0.18
ΔY (m±m)	-0.56 ±0.06	-0.56 ±0.06	-0.56 ±0.06	0.50 ±0.18	0.50 ±0.18	0.50 ±0.18
ΔZ (m±m)	0.01 ±0.28	0.12 ±0.19	0.10 ±0.18	-0.04 ±0.33	0.12 ±0.27	0.12 ±0.27
$\Delta\omega$ (deg±sec)	0.02984 ±7.0	0.02983 ±7.0	0.02984 ±7.0	0.03079 ±6.8	0.03078 ±6.8	0.03080 ±6.9
$\Delta\varphi$ (deg±sec)	0.18073 ±7.7	0.18072 ±7.6	0.18070 ±7.6	0.17597 ±7.5	0.17596 ±7.5	0.17596 ±7.5
$\Delta\kappa$ (deg±sec)	179.97853 ±4.8	179.97852 ±4.8	179.97771 ±4.7	179.97761 ±4.6	179.97759 ±4.6	179.97676 ±4.5
RMS_X (m)	0.17	0.17	0.16	0.16	0.16	0.15
RMS_Y (m)	0.28	0.28	0.26	0.29	0.29	0.26
RMS_Z (m)	0.18	0.22	0.21	0.19	0.17	0.17
Number of check points	15	13	13	15	13	13

Experiment Set III

In this set of experiments, a real dataset captured by a large format digital camera, Vexcel UltraCamX, is utilized. The objective of this set of experiments is to demonstrate the performance of the proposed photogrammetric system calibration using such camera. Moreover, it will be checked whether a small increase in the number of utilized vertical ground control points will promote improvements in the estimated vertical lever arm offset component.

The utilized dataset consists of six flight lines acquired from a flying height of approximately 1390 m following the configuration shown in Figure 7.3. This figure also illustrates the sixteen ground control points available, which were used for the check point analysis. The images have been acquired with 60% overlap and 30% side lap. The average base-height ratio is 0.28. The camera IOP was obtained from the camera calibration certificate, which was provided by the camera manufacturer (Table 7.11).

Table 7.11. Camera IOP from the camera calibration certificate (CCC).

CCD array size	Pixel Size (μm)	Camera IOP		
		x_p (mm± mm)	y_p (mm± mm)	c (mm± mm)
67.824 x 103.896 mm	7.2	0.000 ±0.002	0.216 ±0.002	100.500 ±0.002

Note: The camera has no inherent distortions.

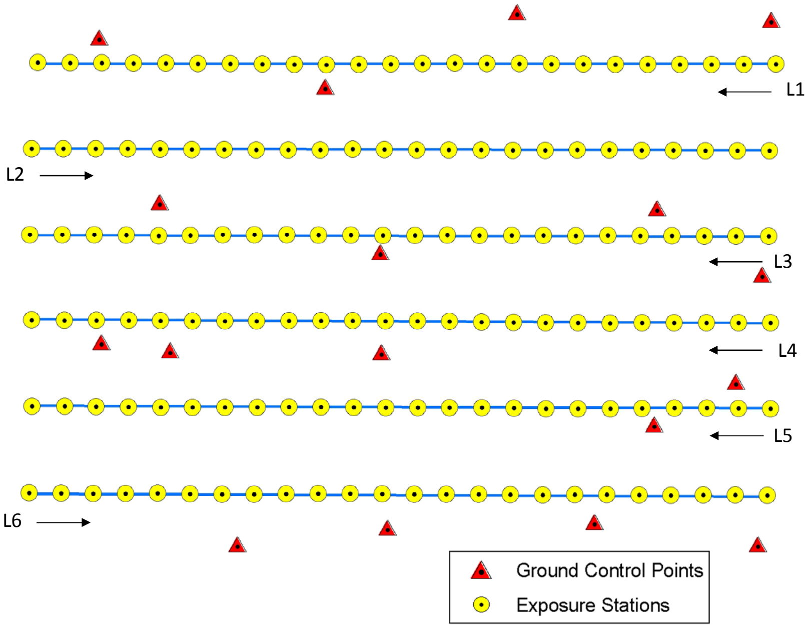

Figure 7.3. Flight and control configuration of the real dataset used in the experiment set III.

The conducted experiments involved the estimation of the system mounting parameters under different control configurations while using the IOP provided by the camera manufacturer. Note that the principal point coordinates and the principal distance are not estimated along with the mounting parameters since only one flying height was available. The outcome from the experiments (i.e., the a-posteriori variance factor, the estimated system mounting parameters, and the standard deviations) is reported in Table 7.12. Table 7.13 presents the RMSE analysis for the performed experiments. Once again, one can see improvements in the estimated vertical lever arm offset component with a small increase in the number of implemented vertical control points (refer to the highlighted values in Table 7.12). Such improvement can also be seen in the reported RMSE values in the vertical direction (refer to the highlighted cells in Table 7.13). The utilized ground control point was visible in only two images. Therefore, in such cases, it is recommended to use more than one vertical control point. A closer look at Table 7.12 also reveals that the estimated mounting parameters are very compatible to the physically measured ones, which demonstrates the validity of the proposed system calibration as well as the validity of the camera IOP from the camera calibration certificate. The standard deviations of the estimated parameters in Table 7.12 as well as the reported RMSE values in Table 7.13 are also an indication of the validity of the proposed system calibration.

Table 7.12. Calibration results (i.e., a-posteriori variance factor, system parameters, and standard deviations) using real data captured by a large format digital camera and different control configurations.

	$(\hat{\sigma}_o)^2$ (mm)^2	Lever arm offset			Boresight angles		
		ΔX (m±m)	ΔY (m±m)	ΔZ (m±m)	$\Delta\omega$ (deg±sec)	$\Delta\varphi$ (deg±sec)	$\Delta\kappa$ (deg±sec)
1 vertical	$(0.0078)^2$	-0.178	-0.110	-0.659	0.00554	-0.00210	179.98151
GCP		±0.03	±0.08	±0.38	±11.3	±4.8	±1.6
4 vertical	$(0.0078)^2$	-0.180	-0.104	-0.322	0.00509	-0.00212	179.98139
GCP		±0.03	±0.08	±0.17	±11.3	±4.9	±1.6
Physically measured values		-0.174	-0.005	-0.474			

Table 7.13. RMSE analysis for the experiments using different control configuration in Table 7.12.

	Number of check points	RMS_X (mean±std) (m)	RMS_Y (mean±std) (m)	RMS_Z (mean±std) (m)
1 vertical	15	0.328	0.177	0.543
GCP		0.07±0.33	0.07±0.17	0.50±0.22
4 vertical	12	0.333	0.186	0.298
GCP		0.14±0.31	0.06±0.18	0.19±0.24

The following statements can be made based on the performed experiments:

- When the utilized vertical control point is visible/measured in very few images (low redundancy), it is recommended to increase the number of implemented vertical control points;
- For a large format digital camera, considering a flying height of 1390 m, the principal point coordinates and the principal distance did not experience variations under operational conditions.

7.2.2.2 Land-Based/Airborne Multi-Camera Systems

The main objective of the set of experiments presented in this section is to demonstrate the feasibility of the proposed single-step procedure for the estimation of the mounting parameters of multi-camera systems. As already mentioned, multi-camera systems entail two sets of ROP: the ROP among the cameras as well as the ROP between the cameras and the IMU body frame. One should note that these two sets of parameters are not independent. The proposed procedure has the ability of estimating these two sets of ROP. Moreover, prior information on the ROP can be incorporated in the ISO procedure when using the most general devised model. The presented experiments will demonstrate the performance of the proposed procedure for these different purposes. To test the feasibility/effectiveness of the proposed method, similar to what was done for single-camera systems, it will be looked into the (i) a-posteriori variance factor, (ii) precision of the estimated parameters and correlations among them (iii) proximity of the estimated lever arm offset components to the physically measured ones (for real datasets) (iv) closeness of the estimated parameters with the simulated ones (in case of simulated data) (iii) quality of the object space reconstruction (through RMSE analysis using check points).

Land-Based Multi-Camera Systems

The objectives of the experiments using simulated and real datasets are as follows:

- Test the possibility of using the proposed single-step method for the estimation of the ROP among the cameras. Such procedure is denoted as “indirect geo-referencing with ROC”;
- Perform a comparative analysis between the estimated mounting parameters using the proposed indirect geo-referencing with ROC method and the two-step procedure (which makes use of the outcome from the traditional bundle adjustment procedure and Equations 2.9 and 2.10) while considering: strong/weak data acquisition geometries and good/poor distribution of the points in the imagery. A comparative analysis in terms of the quality of object space reconstruction obtained using indirect geo-referencing with ROC method and the traditional bundle adjustment will be also performed;
- Test the feasibility of the proposed single-step method for the estimation of the mounting parameters relating the cameras and the IMU body frame (ISO procedure);

- Check the feasibility of the devised general ISO procedure, which is capable of incorporating ROP prior information;
- Check whether the utilization of prior information on the ROP among the cameras improves the quality of the estimated mounting parameters in the ISO for different scenarios;
- Check whether the general devised ISO model can derive the previous models as special cases. More specifically, check whether the models for the estimation of the ROP among the cameras (indirect geo-referencing with ROC) and the mounting parameters relating the cameras and the IMU body frame (ISO procedure) can be derived from the general ISO model;
- Test the performance of the investigated multi-camera systems under a direct geo-referencing procedure (simple intersection of multiple conjugate light rays). This hasn't been an objective for airborne single-camera systems since this has already been the topic of investigation of previous research work (e.g., Jacobsen, 2000; Wegman, 2002).

Simulated Dataset

The simulated land-based multi-camera mobile mapping system is illustrated in Figure 7.4. One should note that the coordinate systems definition shown in Figure 7.4 would lead to correlation between the rotation angles $\Delta\omega$ and $\Delta\kappa$ relating camera "1" (reference camera) and camera "4" in the indirect geo-referencing with ROC method as illustrated in Figure 7.5. Moreover, it would also lead to correlations between ω and κ in the conventional bundle adjustment (indirect geo-referencing) procedure as illustrated for camera "1" in Figure 7.6. For these reasons, the coordinate systems' definition shown in Figure 7.7 was employed instead.

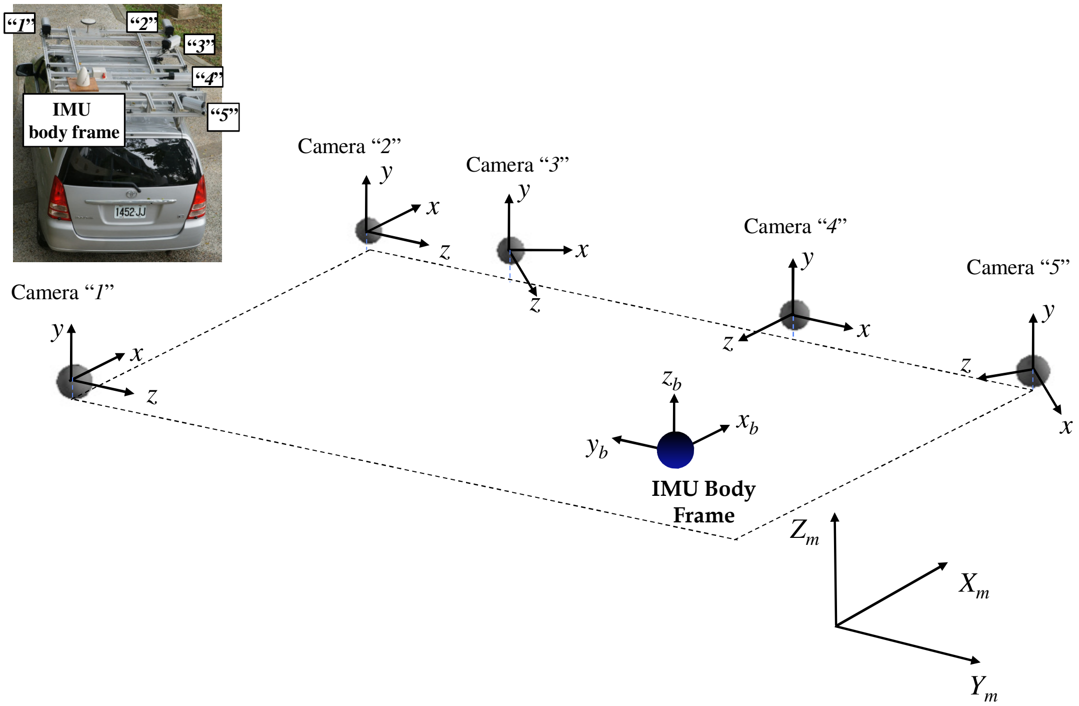

Figure 7.4. Configuration of the simulated land-based MMS and the original definition for the ground, IMU, and camera coordinate systems.

The system consists of five cameras whose characteristics and interior orientation parameters are described in Table 7.14. The utilized values for the simulated parameters were based on the values of an operational system. In the experiments, cameras with small and large Field Of View (FOV) are utilized (Table 7.14).

Table 7.14. Simulated IOP (small FOV and large FOV).

Camera	CCD array size	Pixel Size (μm)	Small FOV			Large FOV		
			x_p (mm)	y_p (mm)	c (mm)	x_p (mm)	y_p (mm)	c (mm)
"1"	7.1456 x 5.4296 mm	4.4	-0.0643	-0.0166	10.833	-0.0643	-0.0166	4.8691
"2"			-0.0588	-0.0923	10.833	-0.0588	-0.0923	4.8809
"3"			-0.1110	0.0911	10.833	-0.1110	0.0911	6.1710
"4"			0.0224	0.0308	10.833	0.0224	0.0308	6.1729
"5"			0.0815	-0.0635	10.833	0.0815	-0.0635	6.1750

Note: The simulated cameras have no inherent distortions.

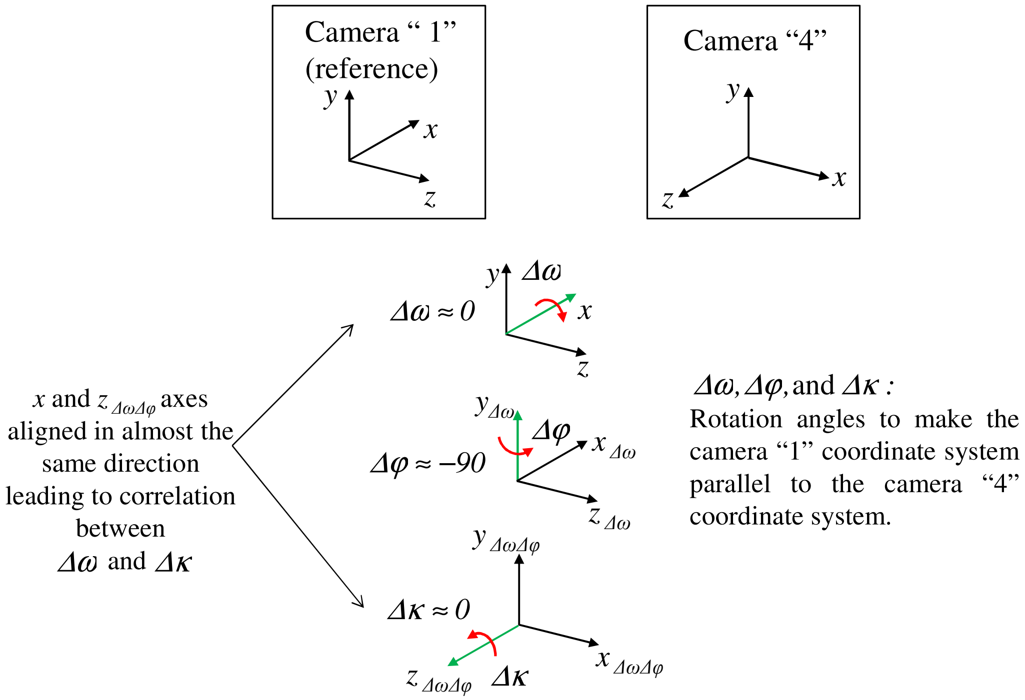

Figure 7.5. Correlation between the rotation angles $\Delta\omega$ and $\Delta\kappa$ relating camera "1" (reference camera) and camera "4".

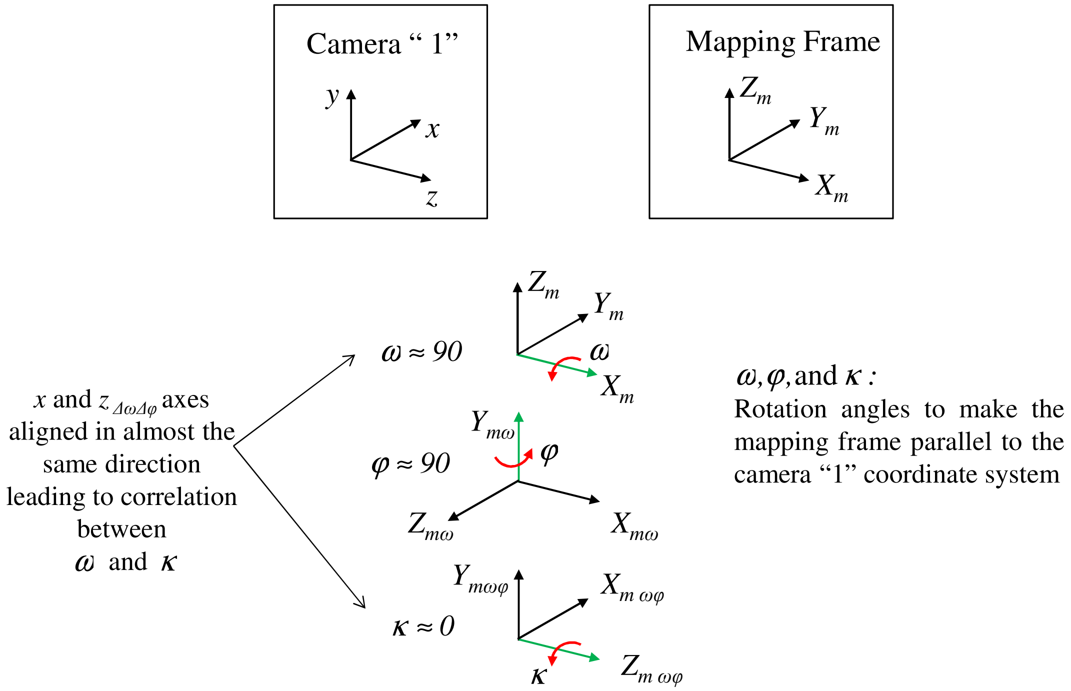

Figure 7.6. Correlation between omega and kappa (illustration for camera "1").

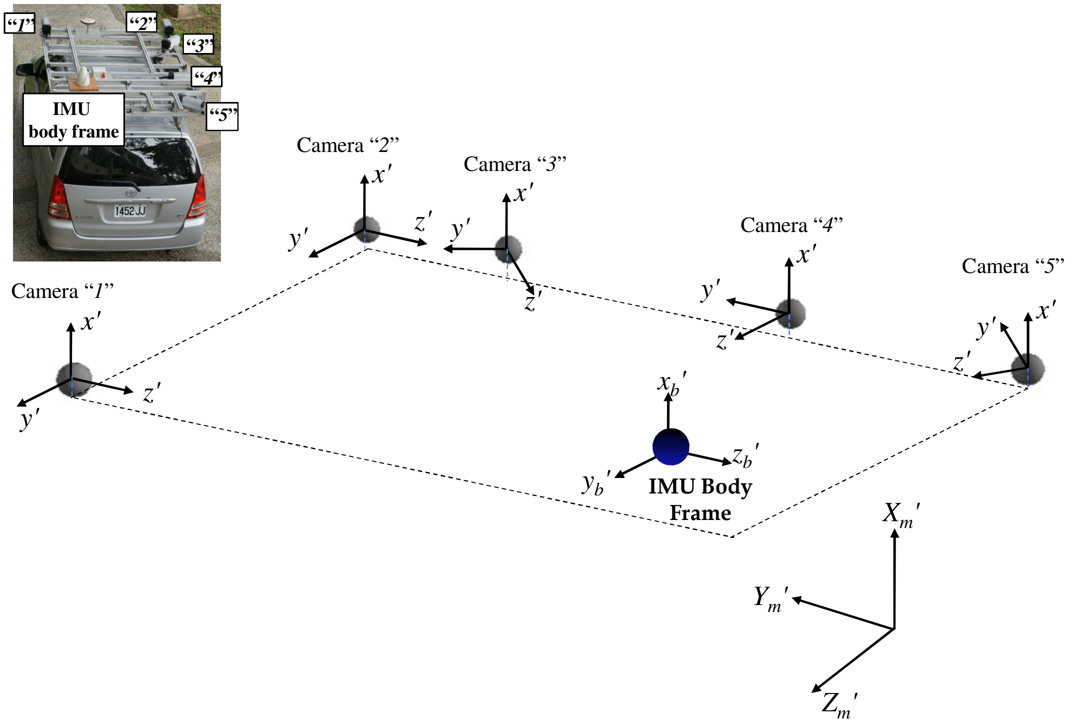

Figure 7.7. Configuration of the simulated land-based MMS and the utilized definition for the ground, IMU, and camera coordinate systems to avoid correlations among the parameters.

The simulated ROP of the cameras w.r.t. camera "1" are reported in Table 7.15, while the simulated lever arm offset and boresight angles of camera "1" w.r.t. the IMU body frame are reported in Table 7.16. The lever arm offset and boresight angles of the other cameras w.r.t. the IMU body frame, reported in Table 7.17, have been computed using the parameters in Tables 7.15 and 7.16. The simulated noise for the camera IOP, image measurements, control points, and GPS/INS-derived position/orientation are ±1 μm, ±0.0044 mm (1 pixel), ±5 cm, and ±10 cm/100 sec, respectively.

Table 7.15. Simulated ROP of the cameras w.r.t. camera "1".

Camera	$\Delta\omega$ (deg)	$\Delta\varphi$ (deg)	$\Delta\kappa$ (deg)	ΔX (m)	ΔY (m)	ΔZ (m)
"2"	1.00000	-0.500000	-2.00000	-0.05	-1.45	0.05
"3"	-41.00000	-0.20000	-1.00000	-0.05	-1.50	0.60
"4"	-89.00000	2.00000	-0.70000	-0.05	-1.50	1.70
"5"	-128.00000	0.50000	-0.40000	-0.05	-1.45	2.45

Table 7.16. Simulated lever arm offset and boresight angles of camera “1” w.r.t. the IMU body frame.

$\Delta\omega$ (deg)	$\Delta\varphi$ (deg)	$\Delta\kappa$ (deg)	ΔX (m)	ΔY (m)	ΔZ (m)
-1.00000	-0.50000	1.30000	0.10	0.50	-1.55

Table 7.17. Lever arm offset and boresight angles of the cameras w.r.t. IMU body frame derived from parameters in Tables 7.15 and 7.16.

Camera	$\Delta\omega$ (deg)	$\Delta\varphi$ (deg)	$\Delta\kappa$ (deg)	ΔX (m)	ΔY (m)	ΔZ (m)
“2”	0.011197	-0.977107	-0.691329	0.08	-0.95	-1.47
“3”	-41.99638	-1.430203	-0.346807	0.08	-0.99	-0.92
“4”	-89.994463	0.691450	-1.177272	0.07	-0.97	0.18
“5”	-129.002719	-0.216588	-1.594356	0.06	-0.91	0.92

The simulated dataset has been derived using cameras with small and large FOV as well as two different imaging configurations. Both imaging configurations comprise 60 images acquired at 12 epochs from 4 different directions (refer to Figure 7.8). In configuration I (Figure 7.8a), the distance between the cameras and the object points is in the range of 10 to 30m, while in configuration II (Figure 7.8b) the distance between the cameras and the object points is in the range of 100 to 300 m. The simulated object space is composed of well distributed points along four walls. Five control points are used in the experiments while the remaining points are used for check point analysis.

In the first half of Table 7.18, the estimated ROPs among the cameras using the proposed indirect geo-referencing with ROC procedure, while using the simulated dataset with configuration I and the camera with large FOV (strong geometry), are presented. Camera “1” was considered as the reference camera to define the position and orientation of the platform. The standard deviations of the estimated parameters, the difference between the estimated and simulated system parameters, the a-posteriori variance factor, as well as the RMSE analysis (using 600 check points) are also reported in the first half of Table 7.18. The reported results demonstrate the feasibility of the proposed indirect geo-referencing with ROC procedure.

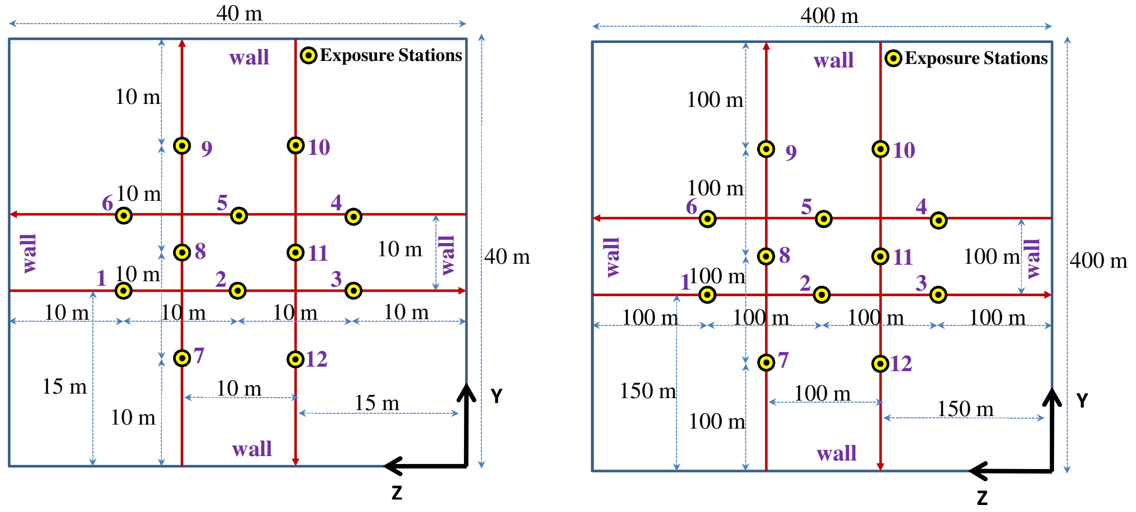

(a) (b)

Figure 7.8. Tested imaging configurations (a) configuration I: object distances of 10-30m (b) configuration II: object distances of 100-300m.

A conventional indirect geo-referencing procedure, using the same dataset, was performed to estimate the ROP among the cameras using the two-step procedure. The two-step procedure results were obtained using the derived EOP from the conventional indirect geo-referencing procedure and Equations 2.9 and 2.10, while considering camera “1” as the reference camera. One should note that the derived ROP are time dependent since each exposure station instance will give an estimate for the ROP. An averaging process was then performed. Table 7.18 (second half) reports the estimated ROP of the cameras w.r.t. camera “1”, the standard deviation, and the difference between the estimated and simulated ROP. The a-posteriori variance factor of the traditional indirect geo-referencing procedure and the RMSE analysis (using 600 check points) are also reported in the second half of Table 7.18.

A closer look at the reported values in Table 7.18 reveals a significant reduction in the standard deviations of the estimated parameters when using the indirect geo-referencing with ROC procedure. Such an improvement should be expected since the relative orientation constraint is explicitly enforced in the proposed single-step procedure. It should be noted that the impact of such improvement in the object space would be in the order of 1~3cm (for an object at a 10-30 m distance). Therefore, such improvement might not be discerned in the reconstructed object space given that the accuracy of the ground control points is ±5cm.

The same set of experiments has been repeated using the simulated data with weaker geometry (configuration II using camera with narrow FOV). The calibration results (i.e., the a-posteriori variance factor, the estimated ROP of the cameras w.r.t. to camera “1”, the standard deviations, the difference between the estimated and simulated parameters, and the RMSE analysis – 700 check points) using the two methods, are presented in Table 7.19. From the reported results in Table 7.19, one can note that in the presence of a weaker geometry, the proposed indirect geo-referencing with ROC procedure leads to significant improvements in the quality of the estimated parameters (in term of closeness to the simulated parameters and their standard deviations) as well as in the quality of the object space reconstruction (refer to the highlighted cells in Table 7.19).

Table 7.18. Calibration results (i.e., estimated ROP of the cameras w.r.t. to camera "1", standard deviations, difference between the estimated and simulated parameters, a-posteriori variance factor, and RMSE analysis – 600 check points) using 5GCP, strong geometry (configuration I – large FOV), and the different methods.

	Camera	$\Delta\omega$ (deg± sec) Diff (sec)	$\Delta\varphi$ (deg± sec) Diff (sec)	$\Delta\kappa$ (deg± sec) Diff (sec)	ΔX (m± m) Diff. (m)	ΔY (m± m) Diff. (m)	ΔZ (m± m) Diff. (m)
Indirect Geo-ref. with ROC "Single-Step"	Camera "2"	1.00184	-0.51613	-2.00218	-0.05	-1.45	0.05
		±27.8	±33.9	±13.7	±0.0020	±0.0025	±0.0033
		6.6	-58.1	-7.9	0.00	0.00	0.00
	Camera "3"	-40.99705	-0.19873	-1.01387	-0.05	-1.50	0.60
		±36.9	±37.7	±28.4	±0.0026	±0.0033	±0.0040
		10.6	4.6	-49.9	0.00	0.00	0.00
	Camera "4"	-88.99962	2.01870	-0.71304	-0.04	-1.51	1.69
		±40.5	±41.6	±38.5	±0.0036	±0.0045	±0.0045
		1.4	67.3	-46.9	0.01	-0.01	-0.01
	Camera "5"	-127.99131	0.51642	-0.41363	-0.05	-1.45	2.45
		±42.0	±50.3	±33.6	±0.0036	±0.0049	±0.0045
		31.3	59.1	-49.1	0.00	0.00	0.00
	$(\hat{\sigma}_o)^2$: $(0.0039)^2$ mm^2 **RMS$_X$**: 0.1121m **RMS$_Y$**: 0.1655 m **RMS$_Z$** :0.1376 m **RMS$_{TOTAL}$:** 0.2426 m						
Indirect Geo-ref. "Two-Step"	"2"	1.01005	-0.49422	-2.00270	-0.04	-1.44	0.05
		±161.4	±302.3	±28.0	±0.0209	±0.0165	±0.0050
		36.2	20.8	-9.7	0.01	0.01	0.00
	"3"	-41.01252	-0.20950	-1.01332	-0.05	-1.49	0.61
		±215.5	±152.5	±130.6	±0.0218	±0.0191	±0.0157
		-45.1	-34.2	-48.0	0.00	0.01	0.01
	"4"	-89.01333	2.04740	-0.72737	-0.04	-1.50	1.70
		±288.3	±253.4	±174.1	±0.0297	±0.0176	±0.0230
		-48.00	170.62	-98.54	0.01	0.00	0.00
	"5"	-128.00727	0.52917	-0.42276	-0.05	-1.45	2.45
		±227.7	±191.9	±153.1	±0.0170	±0.0195	±0.0116
		-26.2	105.0	-81.9	0.00	0.00	0.00
	$(\hat{\sigma}_o)^2$: $(0.0039)^2$ mm^2 **RMS$_X$**: 0.1143 m **RMS$_Y$**: 0.1661 m **RMS$_Z$**: 0.1401 m **RMS$_{TOTAL}$**: 0.2455 m						

Table 7.19. Calibration results (i.e., estimated ROP of the cameras w.r.t. to camera “1”, standard deviations, difference between the estimated and simulated parameters, a-posteriori variance factor, and the RMSE analysis – 700 check points) using 5GCP, weak geometry (configuration II – narrow FOV), and the different methods.

	Camera	$\Delta\omega$ (deg± sec) Diff (sec)	$\Delta\varphi$ (deg± sec) Diff (sec)	$\Delta\kappa$ (deg± sec) Diff (sec)	ΔX (m± m) Diff. (m)	ΔY (m± m) Diff. (m)	ΔZ (m± m) Diff. (m)
Indirect Geo-ref. with ROC “Single-Step”	“2”	1.01128	-0.50614	-2.00737	-0.04	-1.46	0.03
		±24.7	±25.6	±19.4	±0.0110	±0.0110	±0.0272
		40.6	-22.1	-26.5	0.01	-0.01	-0.02
	“3”	-40.97882	-0.19118	-1.00276	-0.02	-1.55	0.55
		±31.3	±33.1	±44.6	±0.0223	±0.0290	±0.0399
		76.2	31.8	-9.9	0.03	-0.05	-0.05
	“4”	-88.96109	2.00386	-0.69907	-0.02	-1.60	1.65
		±48.2	±56.6	±59.5	±0.0336	±0.0484	±0.0491
		140.1	13.9	3.3	0.03	-0.10	-0.05
	“5”	-127.97382	0.51399	-0.39765	0.01	-1.49	2.40
		±43.8	±85.5	±48.2	±0.0380	±0.0619	±0.0402
		94.3	50.4	8.5	0.06	-0.04	-0.05
	$(\hat{\sigma}_o)^2$: $(0.0039)^2$ mm^2 **RMS$_X$**: 0.0900 m **RMS$_Y$**: 0.1543 m **RMS$_Z$**: 0.1877 m **RMS$_{TOTAL}$**: 0.2591 m						
Indirect Geo-ref. “Two-Step”	“2”	1.04940	-0.50650	-2.01320	-0.03	-1.56	0.04
		±429.9	±586.6	±160.0	±0.4658	±0.3413	±0.0548
		177.8	-23.4	-47.5	0.02	-0.11	-0.01
	“3”	-41.02659	-0.18949	-1.01359	-0.17	-1.41	0.47
		±858.2	±669.5	±441.1	±0.6092	±0.5348	±0.2629
		-95.7	37.8	-48.9	-0.12	0.09	-0.13
	“4”	-88.98599	2.08992	-0.73285	-0.04	-1.49	1.76
		±986.0	±898.2	±849.0	±0.8560	±0.4368	±0.6050
		50.4	323.7	-118.3	0.01	0.01	0.06
	“5”	-128.01051	0.56057	-0.39532	-0.11	-1.43	2.47
		±832.6	±588.3	±775.9	±0.6666	±0.6068	±0.3584
		-37.8	218.0	16.8	-0.06	0.02	0.02
	$(\hat{\sigma}_o)^2$: $(0.0039)^2$ mm^2 **RMS$_X$**: 0.1094 m **RMS$_Y$**: 0.3118 m **RMS$_Z$**: 0.3881 m **RMS$_{TOTAL}$**: 0.5097 m						

To verify the performance of the indirect geo-referencing with ROC and the two-step procedures while having poor distribution of the points in the imagery, experiments involving different scenarios have been carried out. The investigated scenarios are as follows (note that the image coordinates x_{min}/x_{max} and y_{min}/y_{max} are: -2.7148 mm / +2.7148 mm and -3.5728 mm/+3.5728 mm, respectively):

- **Scenario I:** Only the points with image coordinates |x| < 1.5 mm and |y| < 2.5 mm in all the images are considered in the calibration.
- **Scenario II:** Only the points with image coordinates |x| < 1.9 mm and |y| < 2.9 mm in all the images are considered in the calibration procedure.
- **Scenario III:** Only the points with image coordinates |x| < 2.4 mm and |y| < 3.2 mm in all the images are considered in the calibration procedure.

For scenario I, in both experiments (conventional indirect geo-referencing and the indirect geo-referencing with ROC), we have singularity, i.e., the geometry is insufficient and no solution is obtained. On the other hand, in the scenario II, for the conventional indirect geo-referencing singularity takes place, while for the indirect geo-referencing with ROC such problem is eliminated due to the enforced ROC among the cameras. The results obtained using the indirect geo-referencing with ROC are reported in Table 7.20.

Table 7.20. Calibration results (i.e., estimated ROP of the cameras w.r.t. to camera "1", standard deviations, difference between the estimated and simulated parameters, a-posteriori variance factor, RMSE analysis – 120 check points) using 5GCP, the weak geometry (configuration II – narrow FOV) under scenario II, and the indirect geo-referencing with ROC method.

Camera	$\Delta\omega$ (deg± sec) Diff (sec)	$\Delta\varphi$ (deg± sec) Diff (sec)	$\Delta\kappa$ (deg± sec) Diff (sec)	ΔX (m± m) Diff. (m)	ΔY (m± m) Diff. (m)	ΔZ (m± m) Diff. (m)
"2"	1.01720	-0.50177	-1.97758	-0.02	-1.48	0.05
	±32.8	±33.5	±70.6	±0.0209	±0.0208	±0.0609
	61.9	-6.4	80.7	0.03	-0.03	0.00
"3"	-40.92666	-0.26845	-0.91867	-0.12	-1.87	0.16
	±81.7	±105.2	±150.6	±0.0845	±0.1110	±0.1278
	264.0	-246.4	292.8	-0.07	-0.37	-0.44
"4"	-88.89413	1.90522	-0.61856	0.07	-1.86	1.43
	±145.8	±189.2	±193.1	±0.1086	±0.1454	±0.1531
	381.1	-341.2	293.2	0.12	-0.36	-0.27
"5"	-127.87016	0.34895	-0.34600	0.04	-1.75	2.30
	±126.4	±278.8	±159.9	±0.1237	±0.2134	±0.1151
	467.4	-543.8	194.4	0.09	-0.3	-0.15

$(\hat{\sigma}_o)^2$: $(0.0037)^2$ mm^2 **RMS$_X$**: 0.1198 m **RMS$_Y$**: 0.2848 m **RMS$_Z$**: 0.2694 m
RMS$_{TOTAL}$: 0.4099 m

In the experiment carried out under scenario III, both methods were able to produce some results, which are reported in Table 7.21. However, significant improvement in terms of the quality of the estimated system parameters (closeness to the simulated parameters and their standard deviations) and the quality of the reconstructed object space (RMSE results) can be observed when using the proposed indirect geo-referencing with ROC method (refer to the highlighted cells in Table 7.21).

The proposed single-step procedure has also been tested for the estimation of lever arm offset and boresight angles relating the cameras and the IMU body frame in the presence of GPS/INS data. The experiment has been performed using the imaging configuration II and the cameras with narrow FOV. The reason for using configuration II is that it yields more similarity to open areas, representing scenarios where a good GPS signal is available. The calibration results (i.e., the estimated mounting parameters relating the cameras and the IMU body frame, the standard deviations, the difference between the estimated and the simulated parameters, the a-posteriori variance factor, and the RMSE analysis – using 700 check points) are reported in Table 7.22. The closeness of the parameters to the simulated ones and their standard deviations comply with the expected based on the accuracy of the navigation data. The same comment can be made for the a-posteriori variance factor and the RMSE values.

Table 7.21. Calibration results (i.e., estimated ROP of the cameras w.r.t. to camera “1”, standard deviations, difference between the estimated and simulated parameters, a-posteriori variance factor, RMSE analysis – 340 check points) using 5GCP, the different methods, and weak geometry (configuration II – narrow FOV) under scenario III.

	Camera	*Δω* (deg± sec) Diff (sec)	*Δφ* (deg± sec) Diff (sec)	*Δκ* (deg± sec) Diff (sec)	*ΔX* (m± m) Diff. (m)	*ΔY* (m± m) Diff. (m)	*ΔZ* (m± m) Diff. (m)
Indirect Geo-ref. ROC “Single-Step”	“2”	1.01283	-0.50670	-1.99722	-0.04	-1.47	0.05
		±27.0	±27.5	±30.8	±0.0141	±0.0140	±0.0349
		46.2	-24.1	10.0	0.01	-0.02	0.00
	“3”	-40.98009	-0.20274	-0.99045	-0.06	-1.57	0.53
		±42.1	±47.6	±69.4	±0.0372	±0.0484	±0.0571
		71.7	-9.9	34.4	-0.01	-0.07	-0.07
	“4”	-88.95254	1.99412	-0.68926	-0.03	-1.64	1.65
		±67.4	±84.3	±89.0	±0.0523	±0.0699	±0.0691
		170.8	-21.2	38.7	0.02	-0.14	-0.05
	“5”	-127.97038	0.50564	-0.38261	0.03	-1.54	2.37
		±62.0	±127.8	±74.2	±0.0584	±0.0898	±0.0565
		106.6	20.3	62.6	0.08	-0.09	-0.08
	$(\hat{\sigma}_o)^2$: (0.0039)^2 mm^2 **RMS$_X$**: 0.1873 m **RMS$_Y$**: 0.1381 m **RMS$_Z$**: 0.1905 m **RMS$_{TOTAL}$**: 0.3007 m						
Indirect Geo-ref. “Two-Step”	“2”	0.98442	-0.47660	-2.00772	0.00	-1.37	0.08
		±784.1	±560.0	±175.3	±0.6727	±0.6486	±0.0870
		-56.07	84.23	-27.78	0.05	0.08	0.03
	“3”	-40.95439	-0.18395	-0.96404	-0.19	-1.71	0.64
		±1762.1	±894.4	±727.1	±0.8791	±1.5332	±0.7694
		164.2	57.8	129.5	-0.14	-0.21	0.04
	“4”	-88.91740	2.05908	-0.67460	0.00	-1.85	1.87
		±1839.8	±1330.6	±1036.1	±1.4548	±1.5422	±1.1744
		297.4	212.7	91.4	0.05	-0.35	0.17
	“5”	-127.89998	0.49168	-0.34501	0.08	-1.83	2.42
		±1650.9	v493.4	±1056.3	±1.5114	±1.6952	±0.6852
		360.1	-30.0	198.0	0.13	-0.38	-0.03
	$(\hat{\sigma}_o)^2$: (0.0040)^2 mm^2 **RMS$_X$**: 0.6879 m **RMS$_Y$**: 1.1955 m **RMS$_Z$**: 1.0032 m **RMS$_{TOTAL}$**: 1.7055 m						

Table 7.22. Calibration results (i.e., estimated lever arm offset and boresight angles relating the cameras and the IMU body frame, standard deviations, difference between the estimated and simulated parameters, a-posteriori variance factor, and RMSE analysis –700 check points), using 5GCP, and weak geometry (configuration II – narrow FOV).

	Camera	$\Delta\omega$ (deg± sec) Diff (sec)	$\Delta\varphi$ (deg± sec) Diff (sec)	$\Delta\kappa$ (deg± sec) Diff (sec)	ΔX (m± m) Diff. (m)	ΔY (m± m) Diff. (m)	ΔZ (m± m) Diff. (m)
ISO "single-step"	"1"	-1.02037 ±50.4 -73.3	-0.52277 ±52.4 -82.0	1.29626 ±32.1 -13.5	0.09 ±0.0582 -0.01	0.51 ±0.0456 0.01	-1.48 ±0.0371 0.07
	"2"	0.00251 ±50.5 -31.3	-1.00629 ±52.5 -105.0	-0.70170 ±31.8 -37.3	0.07 ±0.0582 -0.01	-0.95 ±0.0457 0.00	-1.43 ±0.0371 0.04
	"3"	-42.00052 ±47.0 -14.9	-1.43880 ±51.1 -30.9	-0.35733 ±30.3 -37.9	0.10 ±0.0591 0.02	-1.01 ±0.0407 -0.02	-0.90 ±0.0385 0.02
	"4"	-89.97866 ±54.7 56.9	0.68997 ±49.1 -5.3	-1.18427 ±31.5 -25.2	0.11 ±0.0556 0.04	-1.05 ±0.0368 -0.08	0.20 ±0.0485 0.02
	"5"	-129.00843 ±47.8 -20.6	-0.20500 ±49.7 41.7	-1.59402 ±31.4 1.2	0.13 ±0.0559 0.07	-0.94 ±0.0406 -0.03	0.92 ±0.0393 0.00
	$(\hat{\sigma}_o)^2$: $(0.0039)^2$ mm^2 **RMS**$_X$: 0.0682 m **RMS**$_Y$: 0.1448 m **RMS**$_Z$: 0.1794 m **RMS**$_{TOTAL}$: 0.2404 m						

The estimated lever arm offset and boresight angles of the cameras w.r.t. to the IMU body frame presented in Table 7.22 were used in a direct geo-referencing procedure, i.e., simple intersection using multiple light rays and an independent dataset. The independent dataset was also simulated using configuration II, but using an independent set of tie points). The RMSE analysis using 600 check points is reported in Table 7.23.

Table 7.23. RMSE analysis (600 check points) of the reconstructed object space from the direct geo-referencing procedure using the mounting parameters in Table 7.22.

RMS$_X$ mean±std. dev. (m)	RMS$_Y$ mean±std. dev. (m)	RMS$_Z$ mean±std. dev. (m)	RMS$_{TOTAL}$ (m)
0.12 -0.02±0.12	0.29 0.07±0.28	0.37 -0.04±0.37	0.49

The incorporation of prior ROP information in the ISO procedure can be done by using the most general mathematical model presented in Equation 5.10. Such model has been denoted as “general ISO model”. Besides testing the performance of the most general mathematical model, it will be verified whether the utilization of prior information about the ROP among the cameras improves the quality of the estimated mounting parameters in the ISO for different scenarios. To do so, two sets of experiments have been performed. In the first set, good distribution of the points in the imagery is utilized while in the second set of experiments, the distribution of the points is degraded leading to a poor tying among the images. More specifically, only the points located in the center of the image ($|x| < 1.5$mm and $|y|<2.5$mm) in all the images are considered in the calibration procedure. The outcome from the general ISO procedure is the lever arm offset and boresight angles of the reference camera (i.e., camera “1”) w.r.t. to the IMU body frame and the adjusted or estimated (if no prior information is used) values for the ROP among the cameras. The accuracy of the prior information on the ROP relating cameras to the reference one is ±1cm for the spatial offset and ±20sec for the relative rotation angles. Table 7.24 presents the estimated/adjusted mounting parameters, the standard deviations, the difference between the estimated and the simulated parameters, the a-posteriori variance factor, and the RMSE values (700 check points) obtained from the experiments with and without prior information on the ROP among the cameras, while having a good distribution of the points in the imagery. Table 7.25, on the other hand, presents the same set of results for the scenario with a poor distribution of the points in the imagery. One can observe in Table 7.24 that compatible results are observed with and without prior ROP information when a good distribution of the points in the imagery is available. In such a case, the use of prior information on the ROP among the cameras hasn’t led to improvements in the estimated parameters. One should note that the proposed ISO implicitly enforces the invariant geometric relationship among the cameras, and therefore, for a reasonable imaging configuration it is expected that the use of prior information on the ROP among the cameras will not lead to significant improvements. On the other hand, the results from the second set of experiments (presented in Table 7.25) reveals that in the scenario where we have a poor tying among the images, the use of prior ROP information leads to significant improvements in the estimated parameters (refer to the highlighted cells in Table 7.25) although almost no improvement can be noted in the quality of the object space reconstruction (refer to the RMSE values in Table 7.25).

The estimated parameters, from the two set of experiments with and without ROP prior information, have been used in a direct geo-referencing procedure using simple intersection of multiple conjugate light rays using the independent dataset. The RMSE analysis is presented in Table 7.26. The reported values in Table 7.26 demonstrate that no improvement in the object space reconstruction is observed when using prior ROP information in the presence of a good point distribution in the imagery. In case of poor distribution of the points in the imagery, although improvements could be noted in the estimated parameters (refer to Table 7.25); very little improvement in terms of object space reconstruction can be observed in Table 7.26. This might be explained by the fact that the object points are reconstructed from the intersection of multiple light rays from images captured by several cameras (i.e., cameras with good and poor estimation for the mounting parameters). Therefore, the impact of bad estimates for the mounting parameters of some of the cameras on the object space is minimized in such case.

Table 7.24. Calibration results (i.e., estimated mounting parameters of the reference camera w.r.t. to the IMU body frame and adjusted/estimated values for the ROP among the cameras, standard deviations, difference between the estimated and simulated parameters, a-posteriori variance factor, and RMSE analysis – 700 check points) using 5GCP, weak geometry (configuration II – narrow FOV), the most general ISO model with/without ROP prior information, and good distribution of the points in the imagery.

	Camera	$\Delta\omega$ (deg± sec) Diff (sec)	$\Delta\varphi$ (deg± sec) Diff (sec)	$\Delta\kappa$ (deg± sec) Diff (sec)	ΔX (m± m) Diff. (m)	ΔY (m± m) Diff. (m)	ΔZ (m± m) Diff. (m)
General ISO model without ROP prior inform.	“1”	-1.02037	-0.52277	1.29626	0.09	0.51	-1.48
		±50.0	±52.1	±31.9	±0.0578	±0.0453	±0.0369
		-73.3	-82.0	-13.5	-0.01	0.01	0.07
	“2”	1.01157	-0.50661	-2.00714	-0.04	-1.46	0.03
		±24.7	±25.6	±19.5	±0.0111	±0.0111	±0.0273
		41.6	-23.8	-25.7	0.01	-0.01	-0.02
	“3”	-40.98329	-0.19405	-0.99312	-0.01	-1.53	0.55
		±30.6	±31.7	±38.7	±0.0212	±0.0278	±0.0388
		60.2	21.4	24.8	0.04	-0.03	-0.05
	“4”	-88.96407	1.99550	-0.68499	0.00	-1.59	1.65
		±46.0	±48.0	±48.7	±0.0318	±0.0454	±0.0473
		129.3	-16.2	54.1	0.05	-0.09	-0.05
	“5”	-127.98520	0.49494	-0.38421	0.03	-1.49	2.37
		±41.4	±66.7	±41.8	±0.0349	±0.0574	±0.0392
		53.3	-18.2	56.9	0.08	-0.04	-0.08
	$(\hat{\sigma}_o)^2$: $(0.0039)^2$ mm^2 **RMS$_X$**: 0.0682 m **RMS$_Y$**: 0.1448 m **RMS$_Z$**: 0.1794 m **RMS$_{TOTAL}$**: 0.2404 m						
General ISO model with ROP prior inform.	“1”	-0.99957	-0.50688	1.29701	0.16	0.45	-1.53
		±37.4	±28.1	±27.9	±0.0420	±0.0281	±0.0287
		1.5	-24.8	-10.8	0.06	-0.05	0.02
	“2”	1.00003	-0.50102	-1.99915	-0.05	-1.46	0.05
		±13.6	±13.8	±12.6	±0.0066	±0.0067	±0.0083
		0.1	-3.7	3.0	0.00	-0.01	0.00
	“3”	-40.99790	-0.19356	-1.00318	-0.03	-1.50	0.61
		±13.5	±13.8	±13.0	±0.0076	±0.0080	±0.0082
		7.6	23.2	-11.5	0.02	0.00	0.01
	“4”	-88.99617	1.99999	-0.69842	-0.05	-1.51	1.70
		±14.4	±14.2	±13.9	±0.0079	±0.0085	±0.0082
		13.8	0.0	5.7	0.00	-0.01	0.00
	“5”	-128.00221	0.50729	-0.39904	-0.04	-1.45	2.47
		±14.7	±15.0	±14.0	±0.0081	±0.0085	±0.0083
		-8.0	26.3	3.5	0.01	0.00	0.02
	$(\hat{\sigma}_o)^2$: $(0.0039)^2$ mm^2 **RMS$_X$**: 0.0703 m **RMS$_Y$**: 0.1372 m **RMS$_Z$**: 0.1760 m **RMS$_{TOTAL}$**: 0.2340 m						

Table 7.25. Calibration results (i.e., estimated mounting parameters of the reference camera w.r.t. to the IMU body frame and adjusted/estimated values for the ROP among the cameras, standard deviations, difference between the estimated and simulated parameters, a-posteriori variance factor, and RMSE analysis – 700 check points) using 5GCP, weak geometry (configuration II – narrow FOV), the most general ISO model with/without ROP prior information, and poor distribution of the points in the imagery.

	Camera	$\Delta\omega$ (deg± sec) Diff (sec)	$\Delta\varphi$ (deg± sec) Diff (sec)	$\Delta\kappa$ (deg± sec) Diff (sec)	ΔX (m± m) Diff. (m)	ΔY (m± m) Diff. (m)	ΔZ (m± m) Diff. (m)
General ISO model without ROP prior inform.	"1"	-1.01261	-0.54072	1.31125	-0.01	0.50	-1.35
		±83.6	±79.1	±140.7	±0.0810	±0.0851	±0.1327
		-45.4	-146.6	40.5	-0.11	0.00	0.20
	"2"	1.01825	-0.49631	-1.99811	0.00	-1.47	-0.10
		±44.9	±46.5	±136.7	±0.0335	±0.0327	±0.1049
		65.7	13.3	6.8	0.05	-0.02	-0.15
	"3"	-41.01139	-0.19463	-1.01321	0.01	-1.34	0.36
		±131.3	±137.3	±165.7	±0.1257	±0.2002	±0.1942
		-41.0	19.3	-47.6	0.06	0.16	-0.24
	"4"	-88.94687	2.03304	-0.67732	0.15	-1.65	1.59
		±135.5	±181.9	±136.9	±0.1126	±0.1533	±0.1923
		191.3	118.9	81.6	0.20	-0.15	-0.11
	"5"	-127.96319	0.48415	-0.38947	0.08	-1.72	2.44
		±126.3	±182.9	±154.4	±0.1135	±0.1663	±0.1849
		132.5	-57.1	37.9	0.13	-0.27	-0.01
	$(\hat{\sigma}_o)^2$: $(0.0036)^2$ mm^2 **RMS$_X$**: 0.0624 m **RMS$_Y$**: 0.1764 m **RMS$_Z$**: 0.1875 m **RMS$_{TOTAL}$**: 0.2649 m						
General ISO model with ROP prior inform.	"1"	-0.98192	-0.51156	1.30811	0.10	0.41	-1.53
		±45.6	±32.5	±42.2	±0.0437	±0.0356	±0.0481
		65.1	-41.6	29.2	0.00	-0.09	0.02
	"2"	0.99956	-0.50046	-1.99199	-0.05	-1.46	0.05
		±13.5	±13.5	±15.5	±0.0073	±0.0073	±0.0078
		-1.6	-1.7	28.8	0.00	-0.01	0.00
	"3"	-40.99696	-0.19499	-1.00202	-0.03	-1.49	0.61
		±14.4	±14.1	±15.4	±0.0077	±0.0078	±0.0078
		10.9	18.0	-7.3	0.02	0.01	0.01
	"4"	-89.00064	2.00299	-0.69806	-0.05	-1.50	1.70
		±14.8	±14.1	±15.5	±0.0076	±0.0078	±0.0077
		-2.3	10.8	7.0	0.00	0.00	0.00
	"5"	-128.00085	0.50711	-0.39812	-0.04	-1.45	2.47
		±15.2	±14.9	±15.5	±0.0077	±0.0078	±0.0078
		-3.1	25.6	6.8	0.01	0.00	0.02
	$(\hat{\sigma}_o)^2$: $(0.0034)^2$ mm^2 **RMS$_X$**: 0.0593 m **RMS$_Y$**: 0.1561 m **RMS$_Z$**: 0.1819 m **RMS$_{TOTAL}$**: 0.2470 m						

Table 7.26. RMSE analysis (600 check points) of the reconstructed object space from the direct geo-referencing procedure using the estimated parameters in Tables 7.24 and 7.25.

Scenario	Prior ROP information	RMS_X mean±std. dev. (m)	RMS_Y mean±std. dev. (m)	RMS_Z mean±std. dev. (m)	RMS_{TOTAL} (m)
Good distribution	without	0.12 -0.02±0.12	0.29 0.07±0.28	0.37 -0.04±0.37	0.49
	with	0.12 -0.01±0.12	0.28 0.07±0.28	0.36 -0.04±0.36	0.48
Poor distribution	without	0.13 -0.02±0.13	0.33 0.07±0.32	0.42 -0.04±0.42	0.55
	with	0.12 -0.02±0.12	0.29 0.07±0.28	0.37 -0.04±0.37	0.49

Experiments have also been performed to check whether the general devised ISO model can be used to derive the previous models, i.e., the model for the estimation of the ROP among the cameras and the ISO model for the estimation of the mounting parameters relating the cameras and the IMU body frame. For that purpose, the experiments previously performed to test these models using the simulated dataset with configuration II and the camera with narrow FOV are now repeated using the general devised model. The results are reported in Table 7.27. By comparing the results in Table 7.27 with the indirect geo-referencing with ROC results in Table 7.19 and with the ISO results reported in Table 7.22 one can note the equivalence of the results, which demonstrates that the general devised model has the capability of deriving the previous models properly.

Table 7.27. Calibration results (i.e., estimated ROP of the cameras w.r.t. to camera “1” and the mounting parameter relating the cameras and the IMU body frame, standard deviations, difference between the estimated and simulated parameters, a-posteriori variance factor, and RMSE analysis – 700 check points) using 5GCP, weak geometry (configuration II – narrow FOV), and the general devised ISO model.

	Camera	$\Delta\omega$ (deg± sec) Diff (sec)	$\Delta\varphi$ (deg± sec) Diff (sec)	$\Delta\kappa$ (deg± sec) Diff (sec)	ΔX (m± m) Diff. (m)	ΔY (m± m) Diff. (m)	ΔZ (m± m) Diff. (m)
ROP of the cameras w.r.t. camera “1” (Indirect Geo-ref. with ROC)	“2”	1.01128	-0.50614	-2.00737	-0.04	-1.46	0.03
		±24.7	±25.6	±19.4	±0.0110	±0.0110	±0.0272
		40.6	-22.1	-26.5	0.01	-0.01	-0.02
	“3”	-40.97882	-0.19118	-1.00276	-0.02	-1.55	0.55
		±31.3	±33.1	±44.6	±0.0223	±0.0290	±0.0399
		76.2	31.8	-9.9	0.03	-0.05	-0.05
	“4”	-88.96109	2.00386	-0.69907	-0.02	-1.60	1.65
		±48.2	±56.6	±59.5	±0.0336	±0.0484	±0.0491
		140.1	13.9	3.3	0.03	-0.10	-0.05
	“5”	-127.97382	0.51399	-0.39765	0.01	-1.49	2.40
		±43.8	±85.5	±48.2	±0.0380	±0.0619	±0.0402
		94.3	50.4	8.5	0.06	-0.04	-0.05
	$(\hat{\sigma}_o)^2$: $(0.0039)^2$ mm^2 **RMS$_X$**: 0.0900 m **RMS$_Y$**: 0.1543 m **RMS$_Z$**: 0.1877 m **RMS$_{TOTAL}$**: 0.2591 m						
Mounting parameters relating the cameras and the IMU body frame (ISO single-step)	“1”	-1.02037	-0.52277	1.29626	0.09	0.51	-1.48
		±50.4	±52.4	±32.1	±0.0582	±0.0456	±0.0371
		-73.3	-82.0	-13.5	-0.01	0.01	0.07
	“2”	0.00251	-1.00629	-0.70170	0.07	-0.95	-1.43
		±50.5	±52.5	±31.8	±0.0582	±0.0457	±0.0371
		-31.3	-105.0	-37.3	-0.01	0.00	0.04
	“3”	-42.00052	-1.43880	-0.35733	0.10	-1.01	-0.90
		±47.0	±51.1	±30.3	±0.0591	±0.0407	±0.0385
		-14.9	-30.9	-37.9	0.02	-0.02	0.02
	“4”	-89.97866	0.68997	-1.18427	0.11	-1.05	0.20
		±54.7	±49.1	±31.5	±0.0556	±0.0368	±0.0485
		56.9	-5.3	-25.2	0.04	-0.08	0.02
	“5”	-129.00843	-0.20500	-1.59402	0.13	-0.94	0.92
		±47.8	±49.7	±31.4	±0.0559	±0.0406	±0.0393
		-20.6	41.7	1.2	0.07	-0.03	0.00
	$(\hat{\sigma}_o)^2$: $(0.0039)^2$ mm^2 **RMS$_X$**: 0.0682 m **RMS$_Y$**: 0.1448 m **RMS$_Z$**: 0.1794 m **RMS$_{TOTAL}$**: 0.2404 m						

Real Dataset

The utilized system configuration for the acquisition of the real dataset as well as the coordinate systems' definition are the same as the ones used for the simulated data shown in Figure 7.7. The dataset was acquired over an established test field with 67 surveyed targets. Figure 7.9 shows the imaging configuration of the acquired dataset, illustrating the location of the exposure stations (total of 21), the surveyed control points, as well as the tie points. The accuracy of the surveyed points is ±5 cm. From the available points, 34 were used as control points in the performed experiments while the remaining 33 points were used for check point analysis. The nominal accuracy of the GPS/INS-derived position and orientation information is ±10cm and ±100sec, respectively. A total of 105 images were taken by the 5 cameras at 21 epochs. The first 12 epochs were used for estimating the mounting parameters while the remaining 9 epochs were used for evaluating the system performance under a direct geo-referencing procedure.

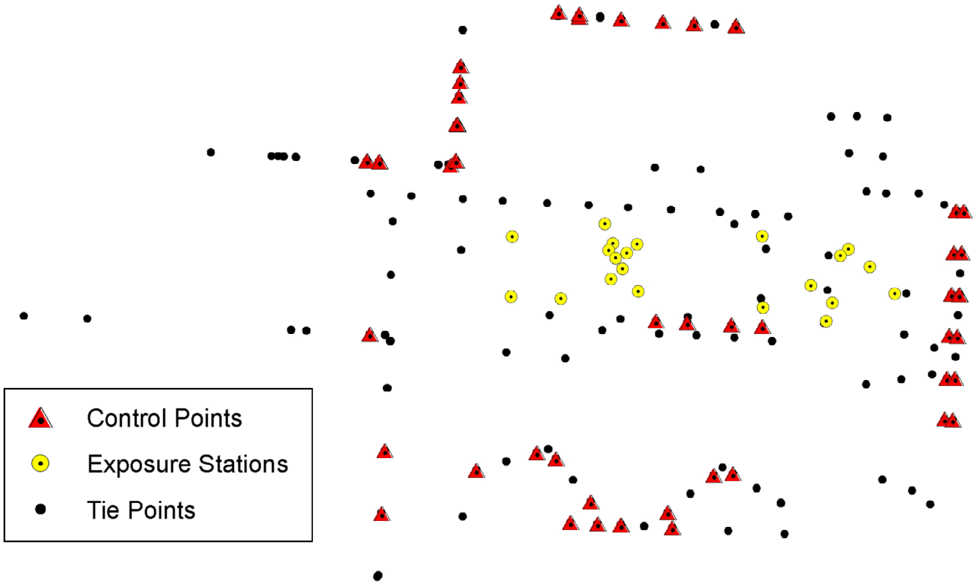

Figure 7.9. Top view of the imaging configuration of the real dataset illustrating the location of the exposure stations, the surveyed control points, and the tie points.

The proposed indirect geo-referencing with ROC has been performed to estimate the ROP among the cameras. As in the performed experiments using simulated data, camera "1" was considered as the reference camera to define the position and orientation of the platform. The estimated ROP of the cameras w.r.t. camera "1" are reported in the first half of Table 7.28. The standard deviations of the estimated parameters as well as the estimated a-posteriori variance factor and the RMSE analysis (using 33 check points) are also reported in Table 7.28 (first half). The reported results comply with the expected ones based on the available camera geometry and data acquisition configuration.

A conventional indirect geo-referencing procedure was performed to estimate the ROP among the cameras using the two-step procedure. The two-step procedure results were obtained using the derived EOP from the conventional indirect geo-referencing procedure using Equations 2.9 and 2.10, while considering camera "1" as the reference camera. One should note that the derived ROP are time dependent since each exposure station instance will give an estimate for the ROP. An averaging process was then performed. The second half of Table 7.28 reports the estimated ROP of the cameras w.r.t. camera "1" and the standard deviation using the two-step procedure. The estimated a-posteriori variance factor of the traditional indirect geo-referencing procedure and the RMSE analysis (using 33 check points) are also reported in the second half of Table 7.28. A closer look at the reported values in Table 7.28 reveals a significant reduction in the standard deviations of the estimated parameters when using the indirect geo-referencing with ROC procedure. Such an improvement should be expected since the relative orientation constraint is explicitly enforced in the proposed single-step procedure. It should be noted that the impact of such improvement in the object space would be in the order of 2~3cm (for an object at a 20 m distance). Therefore, such improvement might not be discerned in the reconstructed object space given that the accuracy of the ground control points is ±5 cm.

Table 7.28. Calibration results (i.e., estimated ROP of the cameras w.r.t. to the reference camera (camera “1”), standard deviations, a-posteriori variance factor, and RMSE analysis – 33 check points) using 34GCP and the different methods.

	Camera	$\Delta\omega$ (deg± sec)	$\Delta\varphi$ (deg± sec)	$\Delta\kappa$ (deg± sec)	ΔX (m± m)	ΔY (m± m)	ΔZ (m± m)
Indirect Geo-ref. ROC “Single-Step”	“2”	0.93444 ±14.6	-0.40842 ±17.1	-2.00061 ±20.0	-0.03 ±0.0013	-1.48 ±0.0019	0.06 ±0.0014
	“3”	-41.66469 ±17.5	-0.09493 ±23.3	-1.06639 ±31.4	-0.03 ±0.0017	-1.50 ±0.0022	0.63 ±0.0024
	“4”	-88.91613 ±25.0	1.95771 ±43.2	-0.69984 ±36.8	-0.04 ±0.0021	-1.49 ±0.0026	1.72 ±0.0031
	“5”	-128.10779 ±25.1	0.54875 ±52.1	-0.32753 ±38.0	-0.05 ±0.0021	-1.48 ±0.0028	2.47 ±0.0035
	$(\hat{\sigma}_o)^2$: $(0.0032)^2$ mm^2 **RMS$_X$**: 0.007 m **RMS$_Y$**: 0.016 m **RMS$_Z$**: 0.013 m **RMS$_{TOTAL}$**: 0.022 m						
Indirect Geo-ref. “Two-Step”	“2”	0.92777 ±285.5	-0.38012 ±100.1	-2.00209 ±85.2	-0.03 ±0.01	-1.47 ±0.01	0.06 ±0.01
	“3”	-41.65608 ±144.7	-0.05911 ±140.8	-1.05843 ±198.3	-0.02 ±0.01	-1.49 ±0.01	0.62 ±0.01
	“4”	-88.95329 ±235.1	1.98176 ±237.6	-0.69070 ±200.0	-0.04 ±0.01	-1.48 ±0.02	1.71 ±0.02
	“5”	-128.10177 ±321.9	0.52740 ±130.3	-0.33972 ±85.9	-0.06 ±0.01	-1.48 ±0.01	2.47 ±0.01
	$(\hat{\sigma}_o)^2$: $(0.0025)^2$ mm^2 **RMS$_X$**: 0.006 m **RMS$_Y$**: 0.014 m **RMS$_Z$**: 0.013 m **RMS$_{TOTAL}$**: 0.020 m						

The proposed single-step procedure has also been tested for the estimation of lever arm offset and boresight angles relating the cameras and the IMU body frame in the presence of GPS/INS data (ISO model). The outcome from the experiment (i.e., the estimated mounting parameters relating the cameras and the IMU body frame, the standard deviations, the a-posteriori variance factor, and the RMSE analysis – using 33 check points), is reported in Table 7.29. One should note that the magnitude of the standard deviations of the estimated boresight angles is ranging from ±125 to ±456 sec, which is an indication that the provided nominal attitude accuracy (i.e., ±100 sec) is too optimistic. The impact of an optimistic a-priori accuracy for the attitude angles is also made evident by the deterioration in the a-posteriori variance factor $(\hat{\sigma}_o)^2$, which is expected to be at the image measurement accuracy level $(0.003)^2$. After several trials it has been found that the realistic accuracy for the attitude information is approximately ±500 sec. The results using the realistic accuracy for the attitude information are reported in Table 7.30.

Table 7.29. Calibration results (i.e., estimated lever arm offset and boresight angles relating the cameras and the IMU body frame, the standard deviations, the a-posteriori variance factor, and the RMSE analysis – 33 check points) using 34GCP and a-priori accuracy for the attitude information of ±100 sec.

	Camera	*Δω* (deg± sec)	*Δφ* (deg± sec)	*Δκ* (deg± sec)	*ΔX* (m± m)	*ΔY* (m± m)	*ΔZ* (m± m)
ISO "Single-Step"	"1"	-0.90343	0.05174	1.28972	0.07	0.50	-1.55
		±454.4	±125.7	±119.1	±0.12	±0.10	±0.10
	"2"	0.06634	-0.31522	-0.70938	0.08	-0.98	-1.48
		±454.7	±125.1	±120.3	±0.12	±0.10	±0.10
	"3"	-42.53492	-0.92732	0.00765	0.08	-0.99	-0.92
		±454.7	±128.6	±119.3	±0.12	±0.10	±0.10
	"4"	-89.83526	0.55968	-0.53241	0.06	-0.96	0.17
		±455.9	±131.7	±117.4	±0.12	±0.10	±0.10
	"5"	-129.0088	-0.64709	-1.07301	0.05	-0.94	0.93
		±456.0	±129.3	±119.4	±0.12	±0.10	±0.10
	$(\hat{\sigma}_o)^2$: $(0.0077)^2$ mm^2 **RMS$_X$**: 0.454 m **RMS$_Y$**: 0.070 m **RMS$_Z$**: 0.044 m **RMS$_{TOTAL}$**: 0.461 m						

Table 7.30. Calibration results (i.e., estimated lever arm offset and boresight angles relating the cameras and the IMU body frame, standard deviations, a-posteriori variance factor, and RMSE analysis – 33 check points) using 34GCP and a-priori accuracy for the attitude information of ±500 sec.

	Camera	*Δω* (deg± sec)	*Δφ* (deg± sec)	*Δκ* (deg± sec)	*ΔX* (m± m)	*ΔY* (m± m)	*ΔZ* (m± m)
ISO "Single-Step"	"1"	-0.95957	-0.06757	1.33466	0.08	0.50	-1.57
		305.7	237.1	237.5	0.05	0.05	0.05
	"2"	0.00903	-0.43523	-0.66640	0.08	-0.98	-1.48
		305.8	237.0	237.7	0.05	0.05	0.05
	"3"	-42.58210	-1.01526	-0.11133	0.08	-0.99	-0.92
		305.8	238.3	236.7	0.05	0.05	0.05
	"4"	-89.87329	0.63720	-0.73457	0.07	-0.96	0.17
		306.1	239.1	236.2	0.05	0.05	0.05
	"5"	-129.05394	-0.45571	-1.19828	0.06	-0.94	0.92
		306.2	238.0	237.2	0.05	0.05	0.05
	$(\hat{\sigma}_o)^2$: $(0.0035)^2$ mm^2 **RMS$_X$**: 0.248 m **RMS$_Y$**: 0.041 m **RMS$_Z$**: 0.027 m **RMS$_{TOTAL}$**: 0.253 m						

The estimated lever arm offset and boresight angles relative to the IMU (presented in Table 7.30) were then used in a direct geo-referencing procedure (simple intersection of multiple conjugate light rays) for an independent dataset (the 9 remaining epochs of the acquired dataset). The direct geo-referencing results (i.e., accuracy analysis – RMSE analysis – using 67 check points) are presented in Table 7.31.

Table 7.31. RMSE analysis (67 check points) of the reconstructed object space from the direct geo-referencing procedure using the estimated mounting parameters in Table 7.30.

RMS_X mean±std. dev. (m)	RMS_Y mean±std. dev. (m)	RMS_Z mean±std. dev. (m)	RMS_{TOTAL} (m)
0.47 -0.01±0.48	0.61 0.08±0.61	0.82 0.00±0.83	1.13

Now, it will be verified the performance of the general ISO model, which can incorporate prior ROP information. The utilized prior ROP information consists of the estimated ROP of the cameras w.r.t. camera “1”, using the indirect geo-referencing with ROC method, presented in Table 7.28. Besides testing the performance of the most general mathematical model, it will be verified whether the utilization of prior information on the ROP among the cameras improves the quality of the estimated mounting parameters in the ISO for different scenarios. Similar to what was done for the simulated data, two sets of experiments have been performed. In the first set, good distribution of the points in the imagery is utilized, i.e., all the available points are utilized, while in the second set of experiments the distribution of the points is degraded leading to a poor tying among the images. More specifically, only the points located in the center of the image ($|x| < 1.9$mm and $|y|<2.9$mm) in all the images are considered in the calibration procedure. As already mentioned, the outcome from the general ISO model is the lever arm offset and boresight angles of the reference camera (i.e., camera “1”) w.r.t. to the IMU body frame and the adjusted or estimated (if no prior information is used) values for the ROP among the cameras. Table 7.32 presents the estimated/adjusted mounting parameters and the standard deviations with and without prior information on the ROP among the cameras, while having a good distribution of the points in the imagery. Table 7.33, on the other hand, presents the same set of results obtained using a poor distribution of the points in the imagery. One should note that the reduced number of utilized control points (7 points) and check points (7 points) in the results reported in Table 7.33 is due to the fact that the other available surveyed points where filtered out. More specifically, their coordinates where not in the center of the images (i.e., |x| > 1.9mm or |y|>2.9mm). It can be observed in Table 7.32 that compatible results are observed with or without prior ROP information when a good distribution of the points in the imagery is available. In such a case, the use of prior information on the ROP among the cameras has not led to improvements in the estimated parameters. Here again, one should note that the proposed ISO implicitly enforces the invariant geometric relationship among the cameras, and therefore, for a reasonable imaging configuration it is expected that the use of prior information on the ROP among the cameras will not promote significant improvements. On the other hand, the results from the second set of experiments, reported on Table 7.33 reveals that, in the scenario with poor tying among the images, the use of prior ROP information leads to more significant improvements in the estimated parameters (refer to the highlighted cells in Table 7.33). On the other hand, no improvement could be observed in the object space (refer to the RMSE values in Table 7.33).

The estimated parameters, from the two set of experiments with and without ROP prior information, have been used in a direct geo-referencing procedure using simple intersection of multiple conjugate light rays using the independent dataset. The RMSE analysis is presented in Table 7.34. This table demonstrates that no improvement in the object space reconstruction is observed when using prior ROP information in the presence of a good point distribution in the imagery. In case of poor distribution of the points in the imagery, although improvements could be noted in the estimated parameters (refer to Table 7.33), the impact of such improvement in the object space is in the order of 1~2cm (for an object at a 20 m distance).

Table 7.32. Calibration results (i.e., estimated lever arm offset and boresight angles of the reference camera (i.e., camera “1”) w.r.t. to the IMU body frame and the adjusted/estimated values for the ROP among the cameras, standard deviations, a-posteriori variance factor, and RMSE analysis – 33 check points) using 34GCP, the general ISO model with/without ROP prior information, and good distribution of the points in the imagery.

	Camera	$\Delta\omega$ (deg± sec)	$\Delta\varphi$ (deg± sec)	$\Delta\kappa$ (deg± sec)	ΔX (m± m)	ΔY (m± m)	ΔZ (m± m)
General ISO model without ROP prior inform.	“1”	-0.95957 ±301.4	-0.06757 ±233.8	1.33466 ±234.3	0.08 ±0.05	0.50 ±0.05	-1.57 ±0.05
	“2”	0.95976 ±15.7	-0.39013 ±18.3	-2.00204 ±21.5	-0.03 ±0.00	-1.48 ±0.00	0.06 ±0.00
	“3”	-41.63084 ±18.8	-0.07816 ±25.0	-1.06413 ±33.7	-0.03 ±0.00	-1.50 ±0.00	0.62 ±0.00
	“4”	-88.91390 ±26.8	1.97290 ±46.3	-0.69230 ±39.5	-0.04 ±0.00	-1.49 ±0.00	1.71 ±0.00
	“5”	-128.09433 ±26.9	0.55300 ±55.9	-0.32169 ±40.7	-0.05 ±0.00	-1.48 ±0.00	2.46 ±0.00
	$(\hat{\sigma}_o)^2$: $(0.0034)^2$ mm^2 **RMS$_X$**: 0.248 m **RMS$_Y$**: 0.041 m **RMS$_Z$**: 0.027 m **RMS$_{TOTAL}$**: 0.253 m						
General ISO model with ROP prior inform.	“1”	-0.95195 ±303.1	-0.07536 ±234.2	1.33617 ±235.4	0.07 ±0.05	0.49 ±0.05	-1.58 ±0.05
	“2”	0.95475 ±9.7	-0.39394 ±9.1	-1.99873 ±17.3	-0.03 ±0.00	-1.48 ±0.00	0.06 ±0.00
	“3”	-41.63157 ±10.6	-0.08391 ±12.7	-1.06148 ±23.4	-0.03 ±0.00	-1.50 ±0.00	0.63 ±0.00
	“4”	-88.92025 ±16.3	1.98046 ±26.4	-0.68858 ±27.0	-0.04 ±0.00	-1.49 ±0.00	1.72 ±0.00
	“5”	-128.09832 ±18.8	0.55877 ±35.0	-0.31290 ±27.0	-0.05 ±0.00	-1.48 ±0.00	2.47 ±0.00
	$(\hat{\sigma}_o)^2$: $(0.0034)^2$ mm^2 **RMS$_X$**: 0.246 m **RMS$_Y$**: 0.090 m **RMS$_Z$**: 0.050 m **RMS$_{TOTAL}$**: 0.266 m						

Table 7.33. Calibration results (i.e., estimated lever arm offset and boresight angles of the reference camera (i.e., camera "1") w.r.t. to the IMU body frame and the adjusted/estimated values for the ROP among the cameras, standard deviations, a-posteriori variance factor, and RMSE analysis – 7 check points) using 7GCP, the general ISO model with/without ROP prior information, and poor distribution of the points in the imagery.

	Camera	$\Delta\omega$ (deg± sec)	$\Delta\varphi$ (deg± sec)	$\Delta\kappa$ (deg± sec)	ΔX (m± m)	ΔY (m± m)	ΔZ (m± m)
General ISO model without ROP prior inform.	"1"	-0.92614 ±525.5	-0.08593 ±337.3	1.21929 ±315.4	0.01 ±0.09	0.49 ±0.06	-1.58 ±0.06
	"2"	0.94255 ±65.2	-0.39028 ±65.2	-1.97964 ±93.5	-0.03 ±0.01	-1.48 ±0.01	0.06 ±0.01
	"3"	-41.64694 ±89.9	-0.10498 ±112.9	-0.94938 ±182.6	-0.02 ±0.01	-1.49 ±0.01	0.64 ±0.03
	"4"	-88.92340 ±221.8	1.78863 ±263.8	-0.51971 ±230.4	-0.03 ±0.01	-1.48 ±0.02	1.73 ±0.03
	"5"	-128.12491 ±210.9	0.27605 ±332.6	-0.28269 ±205.3	-0.05 ±0.01	-1.47 ±0.02	2.47 ±0.03
	$(\hat{\sigma}_o)^2$: $(0.0041)^2$ mm^2 **RMS$_X$**: 0.333 m **RMS$_Y$**: 0.032 m **RMS$_Z$**: 0.023 m **RMS$_{TOTAL}$**: 0.336 m						
General ISO model with ROP prior inform.	"1"	-0.93359 ±505.1	0.02958 ±274.2	1.28894 ±281.3	0.03 ±0.09	0.49 ±0.05	-1.58 ±0.05
	"2"	0.93627 ±20.4	-0.40319 ±20.6	-1.99655 ±32.3	-0.03 ±0.00	-1.48 ±0.00	0.06 ±0.00
	"3"	-41.65260 ±23.7	-0.08999 ±29.5	-1.06084 ±48.3	-0.03 ±0.00	-1.50 ±0.00	0.63 ±0.00
	"4"	-88.91913 ±35.3	1.95984 ±49.9	-0.68737 ±55.9	-0.04 ±0.00	-1.49 ±0.00	1.72 ±0.00
	"5"	-128.11100 ±38.2	0.54006 ±62.4	-0.32802 ±58.5	-0.05 ±0.00	-1.48 ±0.00	2.47 ±0.00
	$(\hat{\sigma}_o)^2$: $(0.0039)^2$ mm^2 **RMS$_X$**: 0.338 m **RMS$_Y$**: 0.059 m **RMS$_Z$**: 0.041 m **RMS$_{TOTAL}$**: 0.346 m						

Table 7.34. RMSE analysis (33 check points) of the reconstructed object space from the direct geo-referencing procedure using the estimated mounting parameters in Tables 7.32 and 7.33.

Scenario	ROP prior information	RMS_X mean±std. dev. (m)	RMS_Y mean±std. dev. (m)	RMS_Z mean±std. dev. (m)	RMS_{TOTAL} (m)
Good distribution	without	0.48 0.00±0.48	0.60 0.07±0.60	0.84 0.01±0.85	1.13
	with	0.47 -0.01±0.47	0.61 0.07±0.61	0.82 -0.01±0.82	1.12
Poor distribution	without	0.51 0.04±0.51	0.56 0.04±0.57	0.90 0.05±0.91	1.18
	with	0.49 0.03±0.49	0.56 0.03±0.57	0.86 0.03±0.86	1.14

As has been done using simulated data, experiments using real data have also been performed to check whether the general devised ISO model can be used to derive the previous models, i.e., the model for the estimation of the ROP among the cameras (indirect geo-referencing with ROC) and the model for the estimation of the mounting parameters relating the cameras and the IMU body frame (ISO). For that purpose, the experiments previously performed to test these models are now repeated using the general devised model. The results are reported in Table 7.35. By comparing the results in Table 7.35 with the indirect geo-referencing with ROC results in Table 7.28 and with the ISO results reported in Table 7.30 one can note the equivalence of the results, which demonstrates that the general devised model has the capability of properly deriving the previous models.

Table 7.35. Calibration results (i.e., estimated ROP of the cameras w.r.t. to camera “1” and the mounting parameter relating the cameras and the IMU body frame, standard deviations, a-posteriori variance factor, and RMSE analysis – 33 check points) using 34GCP and the general devised ISO model.

	Camera	$\Delta\omega$ (deg± sec) Diff (sec)	$\Delta\varphi$ (deg± sec) Diff (sec)	$\Delta\kappa$ (deg± sec) Diff (sec)	ΔX (m± m) Diff. (m)	ΔY (m± m) Diff. (m)	ΔZ (m± m) Diff. (m)
ROP of the cameras w.r.t. camera “1” (Indirect Geo-ref. ROC)	“2”	0.93444 ±14.6	-0.40842 ±17.1	-2.00061 ±20.0	-0.03 ±0.0013	-1.48 ±0.0019	0.06 ±0.0014
	“3”	-41.66469 ±17.5	-0.09493 ±23.3	-1.06639 ±31.4	-0.03 ±0.0017	-1.50 ±0.0022	0.63 ±0.0024
	“4”	-88.91613 ±25.0	1.95771 ±43.2	-0.69984 ±36.8	-0.04 ±0.0021	-1.49 ±0.0026	1.72 ±0.0031
	“5”	-128.10779 ±25.1	0.54875 ±52.1	-0.32753 ±38.0	-0.05 ±0.0021	-1.48 ±0.0028	2.47 ±0.0035
	$(\hat{\sigma}_o)^2$: $(0.0032)^2$ mm^2 **RMS**$_X$: 0.007 m **RMS**$_Y$: 0.016 m **RMS**$_Z$: 0.013 m **RMS**$_{TOTAL}$: 0.022 m						
Mounting parameters relating the cameras and the IMU body frame (ISO single-step)	“1”	-0.95957 305.7	-0.06757 237.1	1.33466 237.5	0.08 0.05	0.50 0.05	-1.57 0.05
	“2”	0.00903 305.8	-0.43523 237.0	-0.66640 237.7	0.08 0.05	-0.98 0.05	-1.48 0.05
	“3”	-42.58210 305.8	-1.01526 238.3	-0.11133 236.7	0.08 0.05	-0.99 0.05	-0.92 0.05
	“4”	-89.87329 306.1	0.63720 239.1	-0.73457 236.2	0.07 0.05	-0.96 0.05	0.17 0.05
	“5”	-129.05394 306.2	-0.45571 238.0	-1.19828 237.2	0.06 0.05	-0.94 0.05	0.92 0.05
	$(\hat{\sigma}_o)^2$: $(0.0035)^2$ mm^2 **RMS**$_X$: 0.248 m **RMS**$_Y$: 0.041 m **RMS**$_Z$: 0.027 m **RMS**$_{TOTAL}$: 0.253 m						

Airborne Multi-Camera Systems

In this section, the performance of the proposed single-step procedure for the estimation of the two sets of ROP as well as the proposed general ISO model are tested for airborne multi-camera systems. Also, it will be investigated whether the inclusion of prior ROP information would improve the quality of the estimated mounting parameters. The performance of the studied airborne multi-camera system under a direct geo-referencing procedure (simple intersection of multiple conjugate light rays) will be investigated as well.

The simulated airborne MMS consists of five cameras arranged as illustrated in Figure 7.10, which shows a real system. The simulated system parameters (IOP and mounting parameters) were based on such real system (developed by the National Cheng-Kung University). The simulated IOP for the cameras are listed in Table 7.36. The simulated ROP of the cameras w.r.t. camera “5” are reported in Table 7.37, while the simulated lever arm offset and boresight angles of camera “5” w.r.t. the IMU body frame are reported in Table 7.38. The lever arm offset and boresight angles of the other cameras w.r.t. the IMU body frame can be computed from the parameters in Tables 7.37 and 7.38 and are reported in Table 7.39.

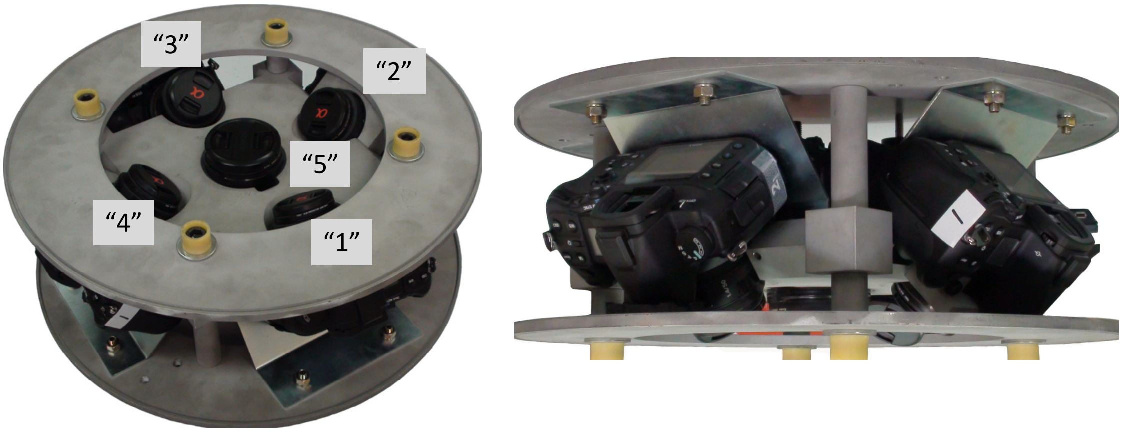

Figure 7.10. Configuration of the simulated airborne MMS.

Table 7.36. Simulated IOP for the airborne MMS.

	CCD array size (mm)	Pixel Size (µm)	x_p (mm)	y_p (mm)	c (mm)
Camera “1”	36 x 24	5.9	0.086200	-0.257700	51.127800
Camera “2”			0.014300	-0.146900	51.118600
Camera “3”			0.020900	-0.023000	51.075300
Camera “4”			-0.065200	-0.056200	51.138100
Camera “5”			0.063100	0.224500	20.456700

Obs.: The simulated cameras have no inherent distortions.

Table 7.37. Simulated ROP of the cameras w.r.t. camera “5” for the airborne MMS.

	$\Delta\omega$ (deg)	$\Delta\varphi$ (deg)	$\Delta\kappa$ (deg)	ΔX (m)	ΔY (m)	ΔZ (m)
Camera “1”	-44.00000	1.00000	-1.20000	0.00	0.15	0.00
Camera “2”	-2.50000	36.50000	-89.00000	0.10	0.00	0.00
Camera “3”	44.00000	-1.10000	179.00000	0.00	-0.10	0.00
Camera “4”	-1.50000	-38.00000	88.00000	-0.10	0.00	0.00

Table 7.38. Simulated lever arm offset and boresight angles of camera “5” w.r.t. the IMU body frame for the airborne MMS.

$\Delta\omega$ (deg)	$\Delta\varphi$ (deg)	$\Delta\kappa$ (deg)	ΔX (m)	ΔY (m)	ΔZ (m)
0.50000	1.00000	-2.00000	0.165	0.000	0.195

Table 7.39. Lever arm offset and boresight angles w.r.t. IMU body frame derived from parameters in Tables 7.37 and 7.38 for the airborne MMS.

	$\Delta\omega$ (deg)	$\Delta\varphi$ (deg)	$\Delta\kappa$ (deg)	ΔX (m)	ΔY (m)	ΔZ (m)
Camera “1”	-43.490758	3.108518	-1.944662	0.170234	0.149904	0.196217
Camera “2”	-0.532445	37.561258	-91.465456	0.264924	-0.003475	0.193225
Camera “3”	44.429111	-1.768772	176.865698	0.161511	-0.099936	0.194189
Camera “4”	-2.518742	-36.921837	85.532023	0.065076	0.003475	0.196775

The simulated flight configuration is shown in Figure 7.11. The flying height is 700 m above the ground level and the distance between the exposure stations is approximately 240 m in the along flight direction and approximately 270 m in the across flight direction. The utilized ground control points are also illustrated in Figure 7.11. One should note that the simulated dataset follows the configuration of a real dataset, which is the reason for the non-uniform distribution of the utilized ground control points in the surveyed area. The simulated noise for the image measurements, camera IOP, ground control points, and GPS/INS position and orientation are ±3 μm, ±1 μm, ±10 cm, and ±10 cm/100 sec, respectively.

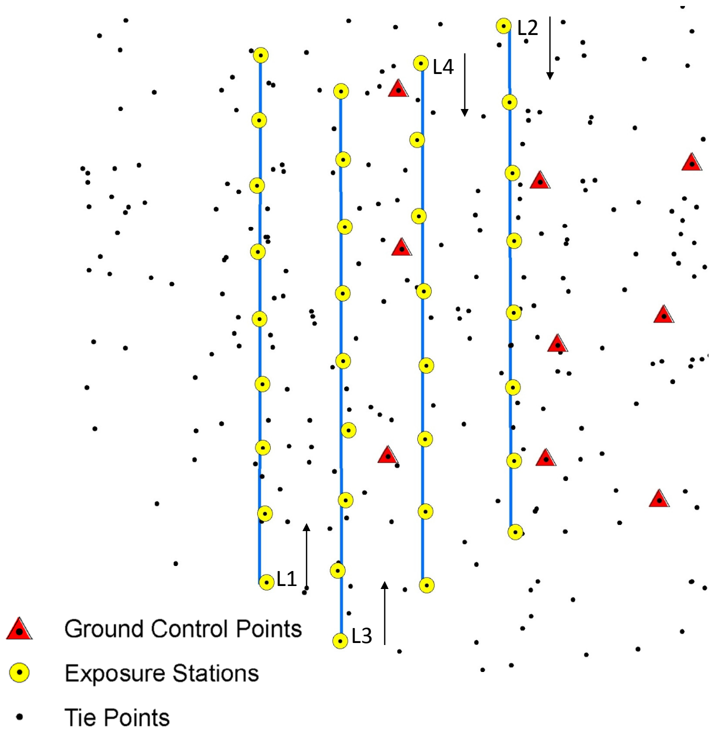

Figure 7.11. Simulated flight configuration, location of the exposure stations, control points, and tie points.

The proposed indirect geo-referencing with ROC has been performed to estimate the ROP among the cameras. Camera “5” was considered as the reference camera to define the position and orientation of the platform. The estimated ROP of the cameras w.r.t. camera “5” are reported in Table 7.40. The standard deviations of the estimated parameters as well as the estimated a-posteriori variance factor and the RMSE analysis (using 247 check points) are also reported in Table 7.40. The reported results demonstrate the feasibility of the proposed indirect geo-referencing with ROC procedure for airborne multi-camera systems.

Table 7.40. Calibration results (i.e., estimated ROP of the cameras w.r.t. to the reference camera (camera “5”), standard deviations, difference between the simulated and true parameters, a-posteriori variance factor, and RMSE analysis – 247 check points) using 9GCP and the proposed indirect geo-referencing with ROC method.

	$\Delta\omega$ (deg± sec) Diff (sec)	$\Delta\varphi$ (deg± sec) Diff (sec)	$\Delta\kappa$ (deg± sec) Diff (sec)	ΔX (m± m) Diff. (m)	ΔY (m± m) Diff. (m)	ΔZ (m± m) Diff. (m)
Camera “1”	-44.00270	0.99962	-1.20043	-0.02	0.14	0.03
	±9.9	±6.7	±3.8	±0.0405	±0.0419	±0.0406
	-9.7	-1.4	-1.6	-0.02	-0.01	0.03
Camera “2”	-2.50287	36.50444	-88.99943	0.15	-0.03	0.03
	±8.9	±9.0	±4.8	±0.0395	±0.0382	±0.0390
	-10.3	16.0	2.0	0.05	-0.03	0.03
Camera “3”	43.99839	-1.09964	178.99933	-0.03	-0.12	0.07
	±10.0	±5.1	±4.0	±0.0322	±0.0426	±0.0416
	-5.8	1.3	-2.4	-0.03	-0.02	0.07
Camera “4”	-1.50161	-38.00368	88.00050	-0.19	-0.01	0.05
	±6.9	±8.6	±3.6	±0.0393	±0.0331	±0.0358
	-5.8	-13.3	1.8	-0.09	-0.01	0.05
$(\hat{\sigma}_o)^2$: $(0.0025)^2$ mm^2 **RMS$_X$**: 0.074 m **RMS$_Y$**: 0.054 m **RMS$_Z$**: 0.163 m **RMS$_{TOTAL}$**: 0.188 m						

The lever arm offset and boresight angles of the cameras w.r.t. the IMU body frame have also been estimated using the proposed ISO procedure. Table 7.41 reports the estimated mounting parameters, the standard deviations, the a-posteriori variance factor, and the RMSE analysis (using 247 check points). The estimated mounting parameters have been used in a direct geo-referencing procedure (simple intersection of multiple conjugate light rays) using an independent set of tie points (220 points). The RMSE analysis of the direct geo-referencing procedure is presented in Table 7.42.

Table 7.43 reports the calibration results (i.e., the estimated mounting parameters of the camera “5” (reference) w.r.t. to the IMU body frame and the adjusted/estimated values for the ROP among the cameras, the standard deviations, the difference between the estimated and the simulated parameters, and the RMSE analysis – 247 check points) using the most general devised model with and without prior information on the ROP among the cameras. The utilized prior information on the ROP of the cameras w.r.t. camera “5” are the estimated ROP using the indirect geo-referencing with ROC method reported in Table 7.40. Here again, we can observe in the reported values in Table 7.43 that no significant improvement when using prior ROP information is noted since a strong data acquisition geometry is available. The mounting parameters estimated with and without prior ROP information have been used in a direct geo-referencing procedure to evaluate the system performance on a simple intersection of multiple conjugate light rays using an independent set of tie points. The RMSE results are reported in Table 7.44.

Table 7.41. Calibration results (i.e., estimated mounting parameters of the cameras w.r.t. to the IMU body frame, standard deviations, difference between the simulated and true parameters, a-posteriori variance factor, and RMSE analysis – 247 check points) using 9GCP and the proposed single-step ISO procedure.

	$\Delta\omega$ (deg± sec) Diff (sec)	$\Delta\varphi$ (deg± sec) Diff (sec)	$\Delta\kappa$ (deg± sec) Diff (sec)	ΔX (m± m) Diff. (m)	ΔY (m± m) Diff. (m)	ΔZ (m± m) Diff. (m)
Camera "1"	-43.48852	3.11622	-1.95100	0.16	0.19	0.25
	±16.4	±16.3	±15.3	±0.0316	±0.0303	±0.0486
	8.1	27.7	-22.8	-0.01	0.04	0.05
Camera "2"	-0.52170	37.56651	-91.47737	0.31	-0.01	0.25
	±20.5	±17.7	±19.8	±0.0373	±0.0343	±0.0505
	38.7	18.9	-42.9	0.04	-0.01	0.05
Camera "3"	44.43457	-1.77380	176.85623	0.16	-0.11	0.28
	±16.5	±16.0	±15.1	±0.0281	±0.0335	±0.0466
	19.6	-18.1	-34.1	-0.01	-0.01	0.09
Camera "4"	-2.52225	-36.92086	85.51997	0.02	0.03	0.29
	±19.1	±15.6	±19.4	±0.0270	±0.0248	±0.0475
	-12.6	3.5	-43.4	-0.05	0.03	0.09
Camera "5"	0.50596	1.00209	-2.00999	0.18	0.03	0.22
	±14.8	±14.9	±15.3	±0.0333	±0.0330	±0.0514
	21.5	7.5	-36.0	0.02	0.03	0.03
$(\hat{\sigma}_o)^2$: (0.0025)^2 mm^2 **RMS$_X$**: 0.081 m **RMS$_Y$**: 0.048 m **RMS$_Z$**: 0.116 m **RMS$_{TOTAL}$**: 0.149 m						

Table 7.42. RMSE analysis (220 check points) of the reconstructed object space from the direct geo-referencing procedure using the estimated mounting parameters in Table 7.41.

RMS$_X$ mean±std. dev. (m)	RMS$_Y$ mean±std. dev. (m)	RMS$_Z$ mean±std. dev. (m)	RMS$_{TOTAL}$ (m)
0.46 -0.12±0.45	0.20 0.02±0.20	0.49 0.07±0.48	0.70

Table 7.43. Calibration results (i.e., estimated lever arm offset and boresight angles of the reference camera (i.e., camera “5”) w.r.t. to the IMU body frame and the adjusted/estimated values for the ROP among the cameras, standard deviations, difference between the estimated and simulated parameters, a-posteriori variance factor, and RMSE analysis – 247 check points) using 9GCP, simulated dataset, and the general ISO model with and without prior information on the ROP among the cameras.

		$\Delta\omega$ (deg± sec) Diff (sec)	$\Delta\varphi$ (deg± sec) Diff (sec)	$\Delta\kappa$ (deg± sec) Diff (sec)	ΔX (m± m) Diff. (m)	ΔY (m± m) Diff. (m)	ΔZ (m± m) Diff. (m)
General ISO model without ROP prior inform.	Camera “1”	-44.00384 ±8.8 -13.8	0.99921 ±6.6 -2.9	-1.20074 ±3.6 -2.7	-0.03 ±0.04 -0.03	0.16 ±0.04 0.01	0.03 ±0.04 0.03
	Camera “2”	-2.50281 ±8.8 -10.1	36.50288 ±8.6 10.4	-88.99933 ±4.8 2.4	0.13 ±0.04 0.03	-0.03 ±0.04 -0.03	0.03 ±0.04 0.03
	Camera “3”	43.99992 ±8.2 -0.3	-1.09961 ±4.9 1.4	178.99918 ±3.7 -3.0	-0.02 ±0.03 -0.02	-0.14 ±0.04 -0.04	0.06 ±0.04 0.06
	Camera “4”	-1.50182 ±6.8 -6.6	-38.00171 ±8.0 -6.1	88.00030 ±3.6 1.1	-0.17 ±0.04 -0.07	0.00 ±0.03 0.00	0.06 ±0.04 0.06
	Camera “5”	0.50596 ±14.7 21.5	1.00209 ±14.8 7.5	-2.00999 ±15.2 -36.0	0.18 ±0.03 0.02	0.03 ±0.03 0.03	0.22 ±0.05 0.03
	$(\hat{\sigma}_o)^2$: (0.0025)^2 mm^2 **RMS**$_X$: 0.081 m **RMS**$_Y$: 0.048 m **RMS**$_Z$: 0.116 m **RMS**$_{TOTAL}$: 0.149 m						
General ISO model with ROP prior inform.	Camera “1”	-44.00283 ±4.5 -10.2	0.99961 ±1.1 -1.4	-1.20046 ±1.2 -1.7	-0.02 ±0.01 -0.02	0.14 ±0.01 -0.01	0.03 ±0.02 0.03
	Camera “2”	-2.50299 ±4.3 -10.8	36.50367 ±6.0 13.2	-88.99941 ±1.5 2.1	0.14 ±0.02 0.04	-0.03 ±0.02 -0.03	0.03 ±0.02 0.03
	Camera “3”	43.99861 ±3.7 -5.0	-1.09965 ±1.1 1.3	178.99933 ±1.7 -2.4	-0.03 ±0.02 -0.03	-0.12 ±0.01 -0.02	0.07 ±0.03 0.07
	Camera “4”	-1.50154 ±3.1 -5.5	-38.00249 ±5.9 -9.0	88.00048 ±1.3 1.7	-0.18 ±0.03 -0.08	-0.01 ±0.01 -0.01	0.05 ±0.02 0.05
	Camera “5”	0.50593 ±14.5 21.3	1.00224 ±14.6 8.1	-2.01014 ±15.1 -36.5	0.19 ±0.02 0.02	0.03 ±0.02 0.03	0.21 ±0.04 0.02
	$(\hat{\sigma}_o)^2$: (0.0025)^2 mm^2 **RMS**$_X$: 0.080 m **RMS**$_Y$: 0.047 m **RMS**$_Z$: 0.116 m **RMS**$_{TOTAL}$: 0.149 m						

Table 7.44. RMSE analysis (220 check points) of the reconstructed object space from the direct geo-referencing procedure using the estimated mounting parameters in Table 7.43.

ROP prior information	RMS_X mean±std. dev. (m)	RMS_Y mean±std. dev. (m)	RMS_Z mean±std. dev. (m)	RMS_{TOTAL} (m)
without	0.46 -0.12±0.45	0.20 0.02±0.20	0.49 0.07±0.48	0.70
with	0.46 -0.12±0.45	0.20 0.02±0.20	0.49 0.07±0.48	0.70

To illustrate a situation where we could see more improvement in the quality of the estimated mounting parameters when using ROP prior information, the quality of the flight configuration/ camera geometry was degraded to some extent. Two flight lines were used only (1&3, flown in the same direction) and the focal length of the cameras were increased to 85mm (all the cameras). The results with and without prior ROP information for that scenario are reported in Table 7.45. One can observe in the reported results in Table 7.45 that more improvements take place when utilizing prior information on the ROP among the cameras (refer to highlighted cells in Table 7.45) in the presence of a weaker geometry. In the object space, on the other hand, the improvement is superseded by the GPS/INS accuracy. The estimated mounting parameters with and without prior ROP information reported in Table 7.45 have been used in a direct geo-referencing procedure. The RMSE results are presented in Table 7.46. Here again since the intersection is done using multiple light rays from images captured by several cameras the impact of poor estimates for the mounting parameters in some of the cameras is minimized on the reconstructed object space.

Table 7.45. Calibration results (i.e., estimated lever arm offset and boresight angles of the reference camera (i.e., camera “5”) w.r.t. to the IMU body frame and the adjusted/estimated values for the ROP among the cameras, standard deviations, difference between the estimated and simulated parameters, a-posteriori variance factor, and RMSE analysis – 173 check points) using 3GCP, simulated dataset, weaker geometry, and the most general ISO model with/without prior information on the ROP among the cameras.

		$\Delta\omega$ (deg± sec) Diff (sec)	$\Delta\varphi$ (deg± sec) Diff (sec)	$\Delta\kappa$ (deg± sec) Diff (sec)	ΔX (m± m) Diff. (m)	ΔY (m± m) Diff. (m)	ΔZ (m± m) Diff. (m)
ISO “single-step” without ROP prior inform.	Camera “1”	-44.00967	1.00029	-1.20339	-0.03	0.18	-0.08
		±54.0	±34.1	±28.3	±0.15	±0.19	±0.08
		-34.8	1.1	-12.2	-0.03	0.03	-0.08
	Camera “2”	-2.49278	36.49425	-89.01223	0.08	-0.09	0.10
		±54.8	±48.9	±17.7	±0.17	±0.19	±0.10
		26.0	-20.7	-44.0	-0.02	-0.09	0.10
	Camera “3”	44.01214	-1.10911	179.00161	-0.12	-0.11	-0.28
		±51.5	±29.1	±29.2	±0.15	±0.19	±0.08
		43.7	-32.8	5.8	-0.12	-0.01	-0.28
	Camera “4”	-1.48809	-37.98217	88.00362	0.11	-0.14	0.17
		±57.7	±47.4	±16.4	±0.17	±0.20	±0.08
		42.9	64.2	13.0	0.21	-0.14	0.17
	Camera “5”	0.51067	1.00442	-2.00755	0.19	-0.09	0.26
		±51.4	±46.1	±17.9	±0.17	±0.19	±0.08
		38.4	15.9	-27.2	0.02	-0.09	0.06
	$(\hat{\sigma}_o)^2$: (0.0018)^2 mm^2 **RMS$_X$**: 0.168 m **RMS$_Y$**: 0.108 m **RMS$_Z$**: 0.206 m **RMS$_{TOTAL}$**: 0.287 m						
ISO “single-step” with ROP prior inform.	Camera “1”	-44.00237	0.99959	-1.20048	-0.01	0.14	0.02
		±4.1	±0.8	±1.0	±0.01	±0.01	±0.02
		-8.5	-1.5	-1.7	-0.01	-0.01	0.02
	Camera “2”	-2.50200	36.50485	-88.99945	0.16	-0.02	0.03
		±4.5	±6.2	±1.2	±0.02	±0.02	±0.02
		-7.2	17.5	2.0	0.06	-0.02	0.03
	Camera “3”	43.99920	-1.09970	178.99939	-0.01	-0.11	0.04
		±3.1	±0.8	±1.4	±0.01	±0.01	±0.03
		-2.9	1.1	-2.2	-0.01	-0.01	0.04
	Camera “4”	-1.50063	-38.00230	88.00046	-0.13	-0.01	0.03
		±2.7	±6.4	±1.1	±0.03	±0.01	±0.03
		-2.3	-8.3	1.6	-0.03	-0.01	0.03
	Camera “5”	0.50785	1.00462	-2.00879	0.16	-0.03	0.36
		±15.9	±25.7	±16.1	±0.09	±0.06	±0.07
		28.3	16.6	-31.6	-0.01	-0.03	0.16
	$(\hat{\sigma}_o)^2$: (0.0018)^2 mm^2 **RMS$_X$**: 0.176 m **RMS$_Y$**: 0.107 m **RMS$_Z$**: 0.238 m **RMS$_{TOTAL}$**: 0.315 m						

Table 7.46. RMSE analysis (217 check points) of the reconstructed object space from the direct geo-referencing procedure using the estimated mounting parameters in Table 7.45.

ROP prior information	RMS_X mean±std. dev. (m)	RMS_Y mean±std. dev. (m)	RMS_Z mean±std. dev. (m)	RMS_{TOTAL} (m)
without	0.46 -0.07±0.46	0.31 0.00±0.32	0.54 0.00±0.54	0.78
with	0.42 -0.05±0.42	0.31 0.00±0.31	0.55 0.07±0.55	0.76

7.3 LiDAR System Calibration Experimental Results

In this section, experimental results related to the LiDAR system calibration are presented. Experiments involving simulated and real datasets are presented in the next subsections.

7.3.1 Simulated Dataset

The objectives of the experiments using a simulated dataset are (i) test the feasibility of the proposed rigorous LiDAR system calibration in a controlled environment, (ii) demonstrate the validity of the devised optimum flight and control configuration for the LiDAR system calibration, and (iii) check whether an increase in the number of implemented vertical control points significantly improves the results. To test/demonstrate the feasibility/effectiveness of the proposed method/flight and control configuration, the closeness of the estimated parameters to the simulated ones will be analyzed. Also, the improvement in the relative accuracy of the LiDAR point cloud after the calibration process is evaluated qualitatively and quantitatively.

The simulated data was produced using a LiDAR system with a pulse repetition rate of 50 kHz, a scan frequency of 20 Hz, and a scan angle varying from -25^{o} to $+25^{o}$. A total of 5 strips, following the devised optimum flight configuration, have been simulated. Figure 7.12 shows the simulated flight configuration and the location of the control points. The optimum flight configuration, as mathematically demonstrated in Chapter 4, should consist of three side lap cases: four strips which are captured from two flying heights in opposite directions with 100% side lap, and two flight lines, which are flown in the same direction with the least side lap possible. This testing configuration allows for the maximization of the impact of systematic biases and has the ability to decouple the different biases from each other. The characteristics of the simulated strip pair cases are presented in Table 7.47. The simulated surface has topography with varying slope and aspect (Figure 7.13).

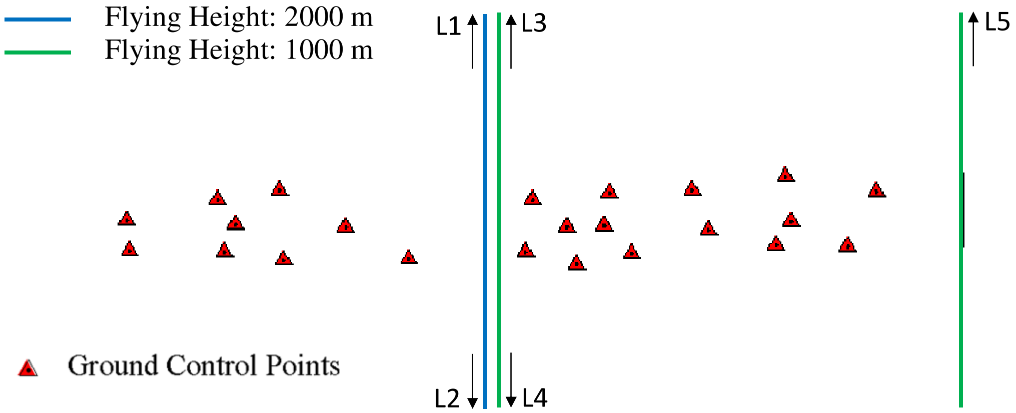

Figure 7.12. Flight and control configuration of the simulated dataset.

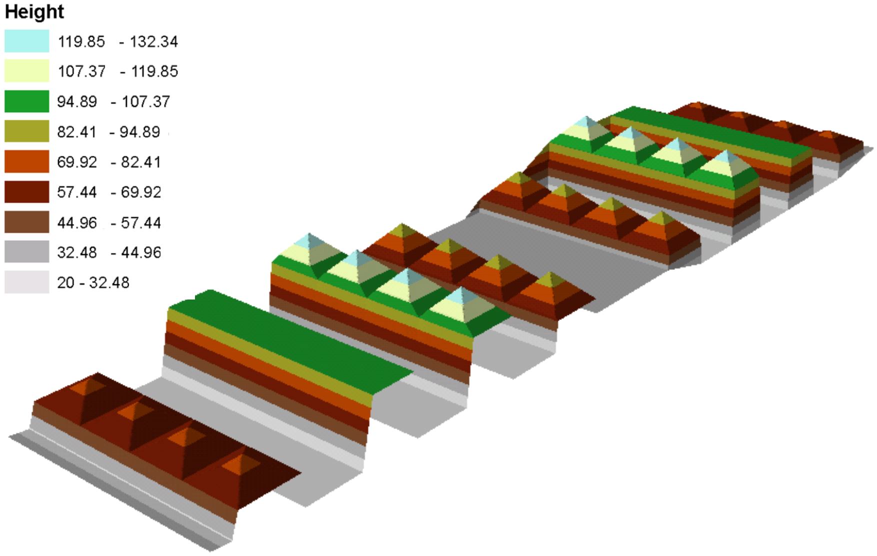

Figure 7.13. Simulated calibration site consisting of topography with varying slope and aspect.

Table 7.47. Characteristics of the strip pairs used in the calibration.

Strip-pairs	Flying Direction	% Side lap	Flying Height (m)
1&2	opposite	100	2000
3&4	opposite	100	1000
5&4	parallel	50	1000

The considered system parameters in the LiDAR point positioning equation include the lever arm offset components $\Delta X, \Delta Y,$ and ΔZ, the boresight angles $\Delta\omega, \Delta\varphi,$ and $\Delta\kappa$, bias in the measured ranges $\Delta\rho$, and the mirror angle scale S. One should note that the proposed approach can be utilized for the estimation of any other set of systematic errors as long as: i) their impact is explicitly modeled in the LiDAR point positioning equation, ii) they are not correlated, and iii) there is adequate flight and control configuration for their estimation.

Using the simulated surface, flight line trajectories, and the system parameters, the LiDAR measurements were derived. The simulated system parameters are listed in Table 7.48 while the simulated random noise in the trajectory and the LiDAR measurements are listed in Table 7.49.

Table 7.48. Simulated system parameters.

$\Delta\omega$ (deg)	$\Delta\varphi$ (deg)	$\Delta\kappa$ (deg)	ΔX (m)	ΔY (m)	ΔZ (m)	$\Delta\rho$ (m)	S
0.02000	0.02000	0.02000	0.15	0.15	0.15	0.20	0.999

Table 7.49. Simulated random noise in the system measurements.

ω_b (deg)	φ_b (deg)	κ_b (deg)	X_b (m)	Y_b (m)	Z_b (m)	ρ (m)	β (deg)
±0.00500	±0.00500	±0.00800	±0.05	±0.05	±0.10	±0.02	±0.009

The calibration procedure has been performed using overlapping strips only (the overlapping pairs listed in Table 7.47) and using overlapping strips along with control points, while varying the number of utilized ground control points. Table 7.50 lists the investigated scenarios. The estimated calibration parameters for the investigated scenarios are reported in Table 7.51. One should note that for reliable estimation of the range bias, control information should be used since the magnitude of the discrepancies among overlapping strips caused by the range bias is very small. Therefore, when using overlapping strips only, the range bias is not estimated. Also note that the vertical lever arm offset component has not been included in the calibration procedure since it is highly correlated with the range bias. In all test scenarios, we can observe that the estimated parameters are quite close to the simulated ones (refer to Tables 7.48 and 7.51). Also, no significant improvement in the estimated parameters is observed when increasing the number of utilized control points.

Table 7.50. Performed experiments.

Experiment	Characteristics
I	Overlapping Strips only
II	Overlapping Strips + 1 Ground Control Point
III	Overlapping Strips + 8 Ground Control Point
IV	Overlapping Strips + 23 Ground Control Point

Table 7.51. Estimated system parameters using the proposed method.

Experiment	$\Delta\omega$ (deg± sec)	$\Delta\varphi$ (deg± sec)	$\Delta\kappa$ (deg± sec)	ΔX (m± m)	ΔY (m± m)	$\Delta\rho$ (m± m)	S
I	0.01969 ±0.25	0.02015 ±0.10	0.01870 ±1.02	0.143 ±0.001	0.157 ±0.002	-	0.99883 ±0.00000
II	0.01970 ±0.25	0.02014 ±0.10	0.01861 ±1.02	0.144 ±0.001	0.157 ±0.002	0.197 ±0.009	0.99899 ±0.00001
III	0.01980 ±0.25	0.02014 ±0.10	0.01851 ±1.01	0.144 ±0.001	0.155 ±0.002	0.216 ±0.003	0.99901 ±0.00001
IV	0.01999 ±0.25	0.02014 ±0.10	0.01888 ±0.94	0.144 ±0.001	0.151 ±0.002	0.204 ±0.002	0.99901 ±0.00000

The qualitative analysis of the calibration results is performed by visual inspection of profiles generated before and after the calibration procedure (using no control and using 1 ground control point) to check any improvements in the quality of fit between overlapping strips (an illustration of one profile is shown in Figure 7.14). The before calibration profile is derived using the predicted coordinates while using the nominal values for the system parameters $- \Delta\omega = \Delta\varphi = \Delta\kappa = \Delta\rho = 0$ and $S = 1$. Through visual inspection of the profile in Figure 7.14, significant improvement in the compatibility of reconstructed point cloud using the estimated system parameters can be noticed. To quantitatively evaluate the performance of the proposed calibration procedure, the discrepancies (i.e., three shifts (X_T,Y_T,Z_T) and three rotations $(\omega, \varphi, \kappa)$) between conjugate surface elements in overlapping strips are computed before the calibration and after reconstructing the LiDAR point cloud using the estimated system parameters. Table 7.52 reports the estimated discrepancies before and after applying the calibration parameters determined using the different test scenarios. It can be observed large discrepancies among the strip pairs before the calibration procedure. Significant improvement can be noted in the compatibility among conjugate surface elements in overlapping strips for all scenarios. One can also note that there is almost no improvement in the compatibility of the strips when adding the control information. The reason is that control data is only necessary for the estimation of the range bias, whose impact does not significantly affect the compatibility among the strips.

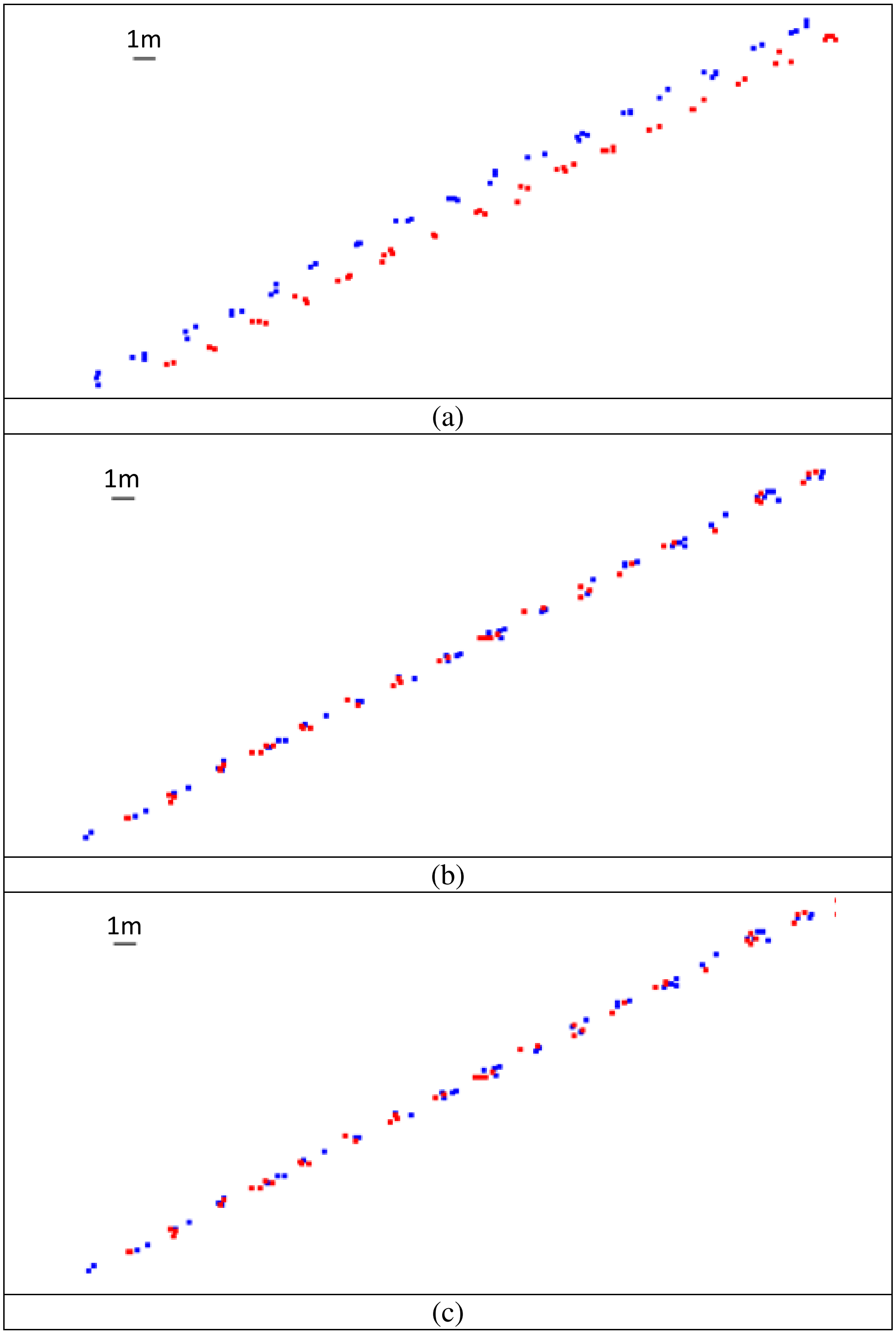

Figure 7.14. Profiles (along the N-S direction) over strips “1” and “2” before the calibration (a), after the calibration procedure using overlapping strips only (b), after the calibration procedure using overlapping strips only and 1 ground control point (c).

Table 7.52. Discrepancies (i.e., three shifts and three rotations) between overlapping strips before and after the calibration (with and without control points) using the nominal and estimated system parameters, respectively.

Before Calibration			Overlapping Strips Only			Overlapping Strips + 1 Control Point			Overlapping Strips + 8 Control Points / Overlapping Strips + 23 Control Points		
1&2											
X_T(m)	**Y_T(m)**	**Z_T(m)**	**X_T(m)**	**YT(m)**	**ZT(m)**	**X_T(m)**	**Y_T(m)**	**Z_T(m)**	**X_T(m)**	**Y_T(m)**	**Z_T(m)**
0.9186	-0.3719	-0.0027	-0.0883	-0.0036	0.0003	-0.0945	0.0009	0.0002	-0.0918/ -0.089	-0.0026/ -0.011	0.0002/ 0.0002
ω(°)	**φ(°)**	**κ(°)**	**ω(°)**	**φ(°)**	**κ(°)**	**ω(°)**	**φ(°)**	**κ(°)**	**ω(°)**	**φ(°)**	**κ(°)**
0.0025	-0.0391	-0.0006	0.0006	0.0003	0.0024	0.0006	0.0004	0.0025	0.0005/ 0.0005	0.0004/ 0.0003	0.0025/ 0.0024
3&4											
X_T(m)	**Y_T(m)**	**Z_T(m)**	**X_T(m)**	**Y_T(m)**	**Z_T(m)**	**X_T(m)**	**Y_T(m)**	**Z_T(m)**	**X_T(m)**	**Y_T(m)**	**Z_T(m)**
0.3527	-0.9125	-0.0003	0.0095	-0.001	-0.0011	0.0054	0	-0.0011	0.0056/ 0.0079	-0.0004/ 0.0019	-0.0011/ -0.001
ω(°)	**φ(°)**	**κ(°)**	**ω(°)**	**φ(°)**	**κ(°)**	**ω(°)**	**φ(°)**	**κ(°)**	**ω(°)**	**φ(°)**	**κ(°)**
-0.0009	-0.0389	0.0104	0.0012	0.0012	0.0005	0.0011	0.0012	0.0005	0.001/ 0.0008	0.0012/ 0.0012	0.0005/ 0.0005
4&5											
X_T(m)	**Y_T(m)**	**Z_T(m)**	**X_T(m)**	**Y_T(m)**	**Z_T(m)**	**X_T(m)**	**Y_T(m)**	**Z_T(m)**	**X_T(m)**	**Y_T(m)**	**Z_T(m)**
0.5781	0.1921	0.4181	0.0225	0.0266	-0.0158	0.0051	0.0265	-0.0001	0.0022/ 0.0077	0.0258/ 0.0283	0.0013/ 0.0024
ω(°)	**φ(°)**	**κ(°)**	**ω(°)**	**φ(°)**	**κ(°)**	**ω(°)**	**φ(°)**	**κ(°)**	**ω(°)**	**φ(°)**	**κ(°)**
0.0042	-0.0598	0.0014	0.0042	0.0039	0.0048	0.0042	0.0001	0.0048	0.0042/ 0.0042	-0.0003/ -0.0005	0.0049/ 0.0047

7.3.2 Real Dataset

In this section, experimental results using a real LiDAR dataset are presented. The objectives are as follows: (i) demonstrate the feasibility of the proposed calibration method, (ii) check whether adding more strip pairs than the optimum recommended configuration significantly improves the results, and (iii) perform a comparative analysis with the calibration results obtained using an existing calibration method (Skaloud and Lichti, 2006). The results are evaluated qualitatively and quantitatively by checking the improvement in the relative accuracy of the LiDAR point cloud after the calibration process.

The real dataset used to perform the experiments was captured by a compact LiDAR system built at École Polytechnique Fédérale de Lausanne (EPFL) (Skaloud et al., 2005). The system is operated from the side of a helicopter. The sensor head incorporates an LN200/A1 tactical grade IMU with 400 Hz measurement rate from Northtrop Grumann and a dual-frequency GPS receiver. The laser scanner is a short-range 2D scanner (Riegl LMS-Q240) with a scanning angle of 60° and maximal range of 450m at 80% reflectance (Skaloud and Lichti, 2006). The flight lines used in the calibration process and the available ground control points (10 signalized targets located along roads in the covered area) are illustrated in Figure 7.15.

It is important to mention that in order to reliably estimate the system parameters, the calibration site should have topography with varying slope and aspect and/or an area that has gable roof buildings with varying slope and aspect. Figure 7.16 illustrates the calibration site utilized in this research, which covers an urban area with several gable roof buildings at different orientation.

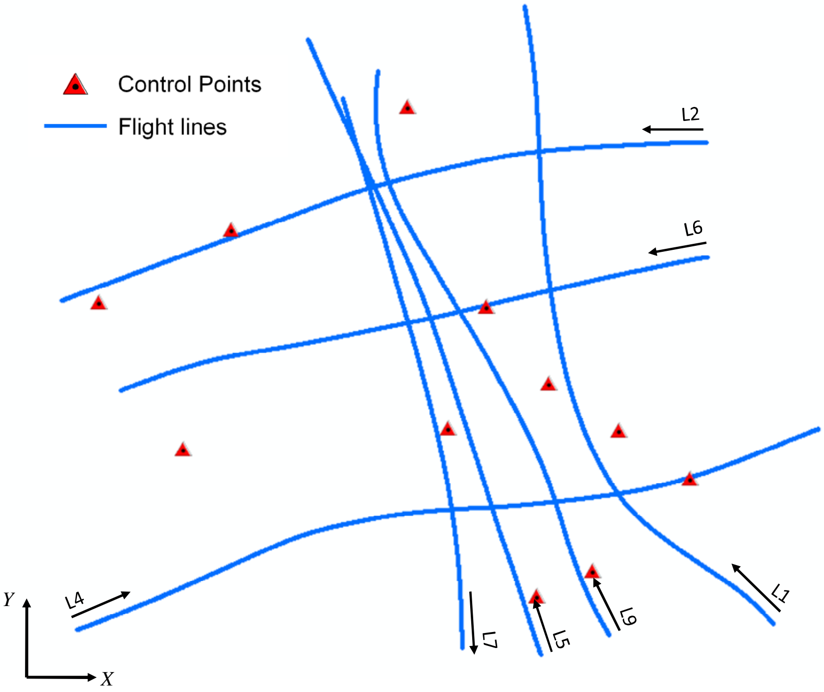

Figure 7.15. Flight and control configuration of the utilized real dataset.

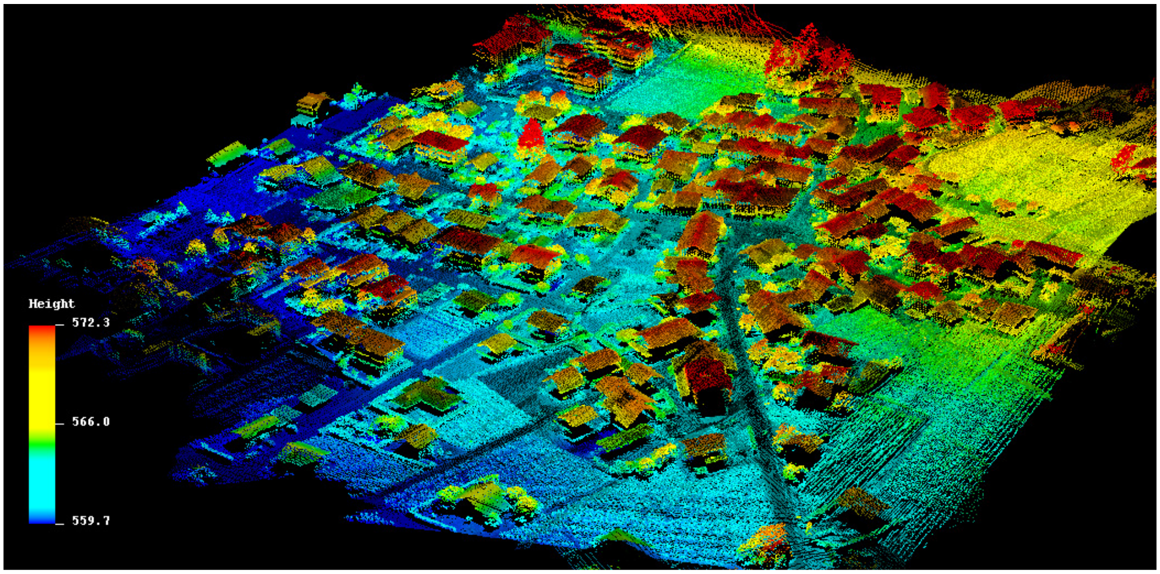

Figure 7.16. Perspective view of the calibration site over an area that includes gable roofs with varying slope and aspect.

Table 7.53 shows the overlapping strip pairs utilized in the calibration procedure. For the pairs 1&9, 2&4, and 5&7, the strips are approximately parallel (flown in opposite and same directions) while in the pair 5&6, the strips are perpendicular (cross direction). One should note that the overlap percentages in Table 7.53 are just approximate values since the flight lines are neither exactly straight nor parallel. Table 7.53 also reports the average point density of the utilized LiDAR strips.

Table 7.53. Characteristics of the LiDAR overlapping strip pairs used in the calibration procedure.

Strip-pairs	**Flying Direction**	**% Overlap**	**Strip Average Point Density (pts/m^2)**	**Flying Height (m)**	**Number of Matched Point-Patch Pairs out of the Total Number of Points in S_1**
1&9	approx. parallel	75	7&6	130	16545 out of 20608
2&4	approx. opposite	70	5&6	130	8039 out of 11677
5&6	cross	-	4&5	230	12842 out of 17123
5&7	approx. opposite	75	4&6	230	10783 out of 13690

To simultaneously estimate the planimetric lever arm offset components and the boresight angles, overlapping strip pairs flown in opposite directions at different flying heights must be available. For this dataset, the flying height difference between the overlapping strip pairs 2&4 and 5&7 is very small (~100m) and therefore they do not allow for the decoupling of the planimetric lever arm offset components and the boresight angles, which would reduce the reliability of the estimated parameters. For the utilized LiDAR system, the lever arm offset have been determined by a laboratory calibration with accuracy better than ±1 cm and are independent of the system installation. Therefore, there is no need for refining the lever arm offset during the in-flight calibration. For this reason, only the boresight angles, the range bias, and the mirror angle scale are considered in the calibration procedure. Here again, one should note that for reliable estimation of the range bias, control information should be used since the magnitude of the discrepancies among overlapping strips caused by the range bias is very small. Also, for reliable estimation of the mirror angle scale, well distributed data in the across flight direction should be used.

The calibration procedure has been performed using overlapping strips only and using overlapping strips along with the 11 control points illustrated in Figure 7.15. To check whether adding more strip pairs in the calibration procedure would significantly improve the results, the experiments involving overlapping strips only have been performed for two scenarios. In the first scenario, strip pairs 1&9, 2&4, and 5&7 are used. Note that the first scenario complies with the optimum devised flight configuration. In the second scenario, the strip pair 5&6 is also added. The number of matched point-patch pairs in the calibration process is reported in Table 7.53. It should be noted that the matched point-patch pairs include not only points on man-made features but also on the terrain surface while excluding points which do not represent physical surfaces (vegetation and building boundaries). In the experiments involving overlapping strips only, the range bias is not estimated. The estimated calibration parameters using the established method for the different experiments together with the estimated parameters using the calibration method proposed by Skaloud and Lichti (2006), which entails the boresight angles only, are reported in Table 7.54. One can note in Table 7.54 that the largest estimated parameter is the boresight roll angle followed by the boresight yaw and pitch angles. On the other hand, the mirror angle scale and range bias estimated using the proposed method are not significantly large. It can be noticed in the experiments involving overlapping strips only that adding one more overlapping strip pairs to the devised optimum configuration do not lead significant improvement in the quality of the estimated parameters. A closer look at the reported values in Table 7.54 also reveals that the estimated boresight angles using the proposed calibration are quite comparable to the estimated parameters using the Skaloud and Lichti (2006) method. These results demonstrate that accurate estimation of the calibration parameters can be obtained using the proposed method without the need for pre-processing techniques (i.e., classification of LiDAR data into terrain and off-terrain features or segmentation of planar patches) or the need for specific features (e.g., planar and/or linear features).

Table 7.54. Estimated system parameters.

	$\Delta\omega$ (sec±sec)	$\Delta\varphi$ (sec±sec)	$\Delta\kappa$ (sec±sec)	S	$\Delta\rho$ (m±m)
Proposed Calibration (Overlapping Strips Only: Scenario I)	-342.2 ±0.5	104.3 ±0.7	226.8 ±2.7	1.00009 ±0.00001	-
Proposed Calibration (Overlapping Strips Only: Scenario II)	-336.9 ±0.5	114.7 ±0.6	230.0 ±2.2	1.00017 ±0.00001	-
Proposed Calibration (Overlapping Strips – Scenario II – + Control Data)	-340.8 ±0.5	115.6 ±0.6	227.9 ±2.2	1.00005 ±0.00001	0.023 ±0.001
Skaloud and Lichti (2006) method	-324.0 ±NA	115.2 ±NA	237.6 ±NA	-	-

The qualitative analysis of the calibration results is performed by visual inspection of profiles generated before and after the calibration procedure to check any improvements in the quality of fit between overlapping strips (an illustration of one profile is shown in Figure 7.17). The before calibration profile is derived using the predicted coordinates while using the nominal values for the system parameters – $\Delta\omega = \Delta\varphi = \Delta\kappa = \Delta\rho = 0$ and $S = 1$. Through visual inspection of the profile in Figure 7.17, significant improvement in the compatibility of reconstructed point cloud using the estimated system parameters from the proposed method and the Skaloud and Lichti (2006) method can be noticed.

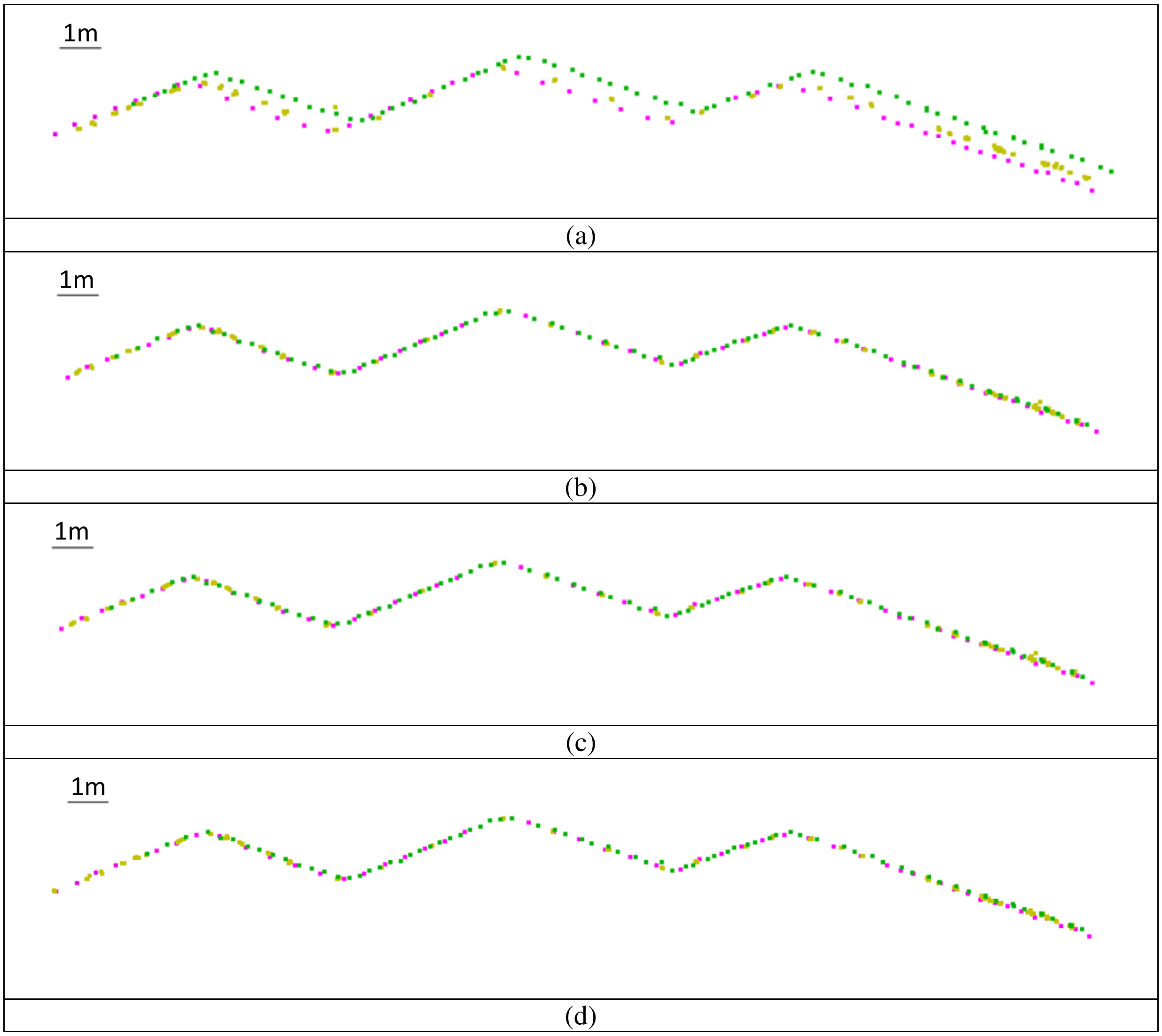

Figure 7.17. Profiles (along the N-S direction) before the calibration (a), after the calibration procedure using the proposed method with overlapping strips only (scenario II) (b), the proposed method with overlapping strips (scenario II) and control data (c), and Skaloud and Lichti (2006) method (d).

To quantitatively evaluate the performance of the proposed calibration procedure, the discrepancies, i.e., three shifts (X_T, Y_T, Z_T) and three rotations $(\omega, \varphi, \kappa)$ between conjugate surface elements in overlapping strips, are computed before the calibration and after reconstructing the LiDAR point cloud using the estimated system parameters. Table 7.55 reports the estimated discrepancies before and after applying the calibration parameters determined using the different test scenarios and the method proposed by Skaloud and Lichti (2006). One can observe large discrepancies among the overlapping strip pairs before the calibration procedure. For instance, the overlapping strip pair 2&4 (flown in opposite directions approximately East-West) has a large shift in the Y-axis, which is approximately the across flight direction. Such discrepancy can be attributed to large deviation between the nominal and estimated boresight roll angle, which mainly affects the across-flight direction, i.e., constant shift across the flight direction and a rotation around the flight direction. Similarly, the overlapping strip pair 5&7 (also flown in opposite directions approximately North-South) has a large shift in the X-axis, which is approximately the across flight direction. The impact of the boresight roll angle is larger for the overlapping strip pair 5&7 due to the fact that it was flown at higher flying height. One should note that for the overlapping strip pair 1&9, no significant discrepancy in the across flight direction is observed before the calibration process. This is due to the fact that for strips flown in the same direction, inaccurate boresight roll angle only causes a constant vertical shift between conjugate surfaces elements with a much smaller magnitude (the magnitude increases with an increased lateral distance between the strips – which is not the case for this strip pair). The slightly larger shift in the Y-axis for the strip pair 1&9, which is approximately along the flight direction of these strips, can be attributed to inaccurate nominal value for the boresight yaw angle. Similar to the other strip pairs, a significant improvement after the calibration process is noticeable. When compared to the results using Skaloud and Lichti (2006) method, one can observe compatible results using the proposed method. Since the estimated mirror angle scale and range bias are quite small, one should not expect improvement in the compatibility between the strip pairs when comparing the proposed calibration and the Skaloud and Lichti (2006) method. Also, no significant improvements are observed when using control data when compared to the results using overlapping LiDAR strips only.

Although the utilized dataset might not be a typical one in terms of the flying height and point density when compared to those datasets captured by a fixed wing aircraft, this dataset is better for illustrating the performance of the proposed approach for two reasons. First, for a lower flying height, the impact of boresight angles would be quite small. Therefore, if the proposed methodology is capable of deriving an accurate estimate of the system parameters in such a case, it would be also capable of dealing with higher altitude systems where the impact of the boresight angles would be much larger. Second, for this dataset, a higher point density is available (i.e., the point spacing is smaller than the discrepancies caused by the approximate values of the system parameters). Therefore, if the system is eventually capable of providing the correct correspondences and accurate estimate of the system parameters for this high point density, it would be also capable of dealing with datasets with a smaller point density.

Table 7.55. Discrepancies (i.e., three shifts and three rotations) between overlapping strips before and after the calibration using the nominal and estimated system parameters.

Before Calibration			**Skaloud and Lichti (2006) Method**			**Proposed Calibration Overlapping Strips Only (Scenario I / Scenario II)**			**Proposed Calibration Overlapping Strips (Scenario II) + Control**		
1&9											
X_T(m)	**Y_T(m)**	**Z_T(m)**	**X_T(m)**	**Y_T(m)**	**Z_T(m)**	**X_T(m)**	**Y_T(m)**	**Z_T(m)**	**X_T(m)**	**Y_T(m)**	**Z_T(m)**
0.0685	-0.1989	-0.0719	0.0132	-0.0179	0.0124	0.0084/ 0.0163	-0.0059/ 0.0012	0.0152/ 0.0136	0.0173	-0.004	0.0145
$\omega(^o)$	**$\varphi(^o)$**	**$\kappa(^o)$**	**$\omega(^o)$**	**$\varphi(^o)$**	**$\kappa(^o)$**	**$\omega(^o)$**	**$\varphi(^o)$**	**$\kappa(^o)$**	**$\omega(^o)$**	**$\varphi(^o)$**	**$\kappa(^o)$**
-0.0224	0.0098	0.0432	0.012	0.0174	0.0228	0.0139/ 0.0137	0.014/ 0.0116	0.0173/ 0.0155	0.0137	0.0128	0.0176
2&4											
X_T(m)	**Y_T(m)**	**Z_T(m)**	**X_T(m)**	**Y_T(m)**	**Z_T(m)**	**X_T(m)**	**Y_T(m)**	**Z_T(m)**	**X_T(m)**	**Y_T(m)**	**Z_T(m)**
0.0517	0.5642	0.0639	-0.0419	0.0723	-0.0018	-0.0167/ -0.0367	0.0614/ 0.0694	-0.003/ -0.0006	-0.0402	0.0767	-0.0013
$\omega(^o)$	**$\varphi(^o)$**	**$\kappa(^o)$**	**$\omega(^o)$**	**$\varphi(^o)$**	**$\kappa(^o)$**	**$\omega(^o)$**	**$\varphi(^o)$**	**$\kappa(^o)$**	**$\omega(^o)$**	**$\varphi(^o)$**	**$\kappa(^o)$**
0.1408	0.0572	0.0008	-0.0115	0.0219	-0.0068	-0.0137/ -0.0058	0.021/ 0.0226	-0.0081/ -0.006	-0.009	0.0223	-0.0084
5&6											
X_T(m)	**Y_T(m)**	**Z_T(m)**	**X_T(m)**	**Y_T(m)**	**Z_T(m)**	**X_T(m)**	**Y_T(m)**	**Z_T(m)**	**X_T(m)**	**Y_T(m)**	**Z_T(m)**
0.3349	-0.4631	0.0095	0.0146	-0.05	0.0217	-0.0102/ NA	-0.0184/ NA	0.0222/ NA	-0.0114	-0.0191	0.0227
$\omega(^o)$	**$\varphi(^o)$**	**$\kappa(^o)$**	**$\omega(^o)$**	**$\varphi(^o)$**	**$\kappa(^o)$**	**$\omega(^o)$**	**$\varphi(^o)$**	**$\kappa(^o)$**	**$\omega(^o)$**	**$\varphi(^o)$**	**$\kappa(^o)$**
-0.0626	-0.1021	-0.0083	0.0001	0.0025	0.0014	0.0011/ NA	0.0069/ NA	0.0018/ NA	0.0018	0.0078	0.0019
5&7											
X_T(m)	**Y_T(m)**	**Z_T(m)**	**X_T(m)**	**Y_T(m)**	**Z_T(m)**	**X_T(m)**	**Y_T(m)**	**Z_T(m)**	**X_T(m)**	**Y_T(m)**	**Z_T(m)**
0.7591	-0.1461	0.0961	0.0561	-0.0005	0.0299	0.0068/ 0.0127	-0.0152/ 0.0058	0.025/ 0.027	0.0115	0.0071	0.027
$\omega(^o)$	**$\varphi(^o)$**	**$\kappa(^o)$**	**$\omega(^o)$**	**$\varphi(^o)$**	**$\kappa(^o)$**	**$\omega(^o)$**	**$\varphi(^o)$**	**$\kappa(^o)$**	**$\omega(^o)$**	**$\varphi(^o)$**	**$\kappa(^o)$**
0.0832	-0.1677	0.0032	0.0063	0.0058	0.025	0.0033/ 0.0028	0.0158/ 0.0135	0.0223/ 0.0229	0.0024	0.0141	0.0229

CHAPTER 8

CONCLUSIONS AND RECOMMENDATIONS FOR FUTURE WORK

8.1 Research Contributions

In this research work, methodologies for the calibration of photogrammetric and LiDAR systems have been introduced. The contributions and the research findings are detailed next.

Distortion Model Adequacy

A methodology for evaluating the adequacy of the distortion model has been introduced. In the proposed method, the adequacy of the distortion model is evaluated by incrementally increasing the model parameters while checking: (i) the outcome of the bundle adjustment with self-calibration procedure, (ii) the bundle similarity, and (iii) the validity of the estimated lever arm offset, i.e., the proximity of the physically measured lever arm offset components to the estimated ones in the system calibration. Experiments using a real dataset have demonstrated the feasibility of the proposed methodology. Also, the hypothesis that insufficient/overparameterized distortion models could have an adverse impact on the estimation of the system mounting parameters and in the quality of the object space reconstruction has been confirmed in the performed experiments.

Analysis of Flight and Control Requirements for the Calibration of Airborne GPS/INS-Assisted Single-Camera Photogrammetric and LiDAR Systems

A rigorous analysis of flight and control requirements for airborne GPS/INS-assisted single-camera photogrammetric and LiDAR Systems has been introduced. The outcome from the proposed analyses for photogrammetric and LiDAR systems and the research findings are summarized in the next paragraphs.

Photogrammetric Systems: Two mathematical analyses have been introduced for photogrammetric system calibration. The first analysis investigated which biased system parameters under different flight configurations would introduce *y*-parallax (i.e., impact on the reconstruction process). The second analysis is restricted to stereo-pairs from the same flight line for the *y*-parallax analysis but also allowed the investigation of the impact of biases in the system parameters on the reconstructed object space. In other words, the second analysis allowed the analysis of the impact of biased system parameters on the reconstruction process as well as on the precision and accuracy of the reconstructed object space. The mathematical analysis was verified through a simulation process. The outcome from the proposed analysis is summarized in Table 8.1. Based on such impact, the minimum and optimum requirement for the estimation of the parameters could be devised (reported in Table 8.1). One should note that the planimetric lever arm offset components and the principal point coordinates can only be simultaneously estimated if two different flying heights are available (refer to highlighted text in Table 8.1). Based on the proposed analysis, it could be concluded that the optimum flight and control configuration for reliable estimation of the parameters should consist of three side lap cases, i.e., four strips captured from two flying heights in opposite directions with 100% side lap, and two strips, which are flown in the same direction with the least side lap possible (while having proper tying among the images from different flight lines) and one vertical control point (as long as it is visible/measured in a reasonable number of images). Experiments from simulated and real datasets have demonstrated the feasibility of the proposed optimum flight and control configuration.

Table 8.1. Summary of the outcome from the two proposed analyses as well as the devised minimum and optimum requirement for the estimation of the parameters.

Parameter		***Y*-Parallax**	**Discrepancies: Flying Direction/ Flying Height/ Point coord. dependent?**	**Control Required?**	**Minimum Requirement**	**Optimum Requirement**
Lever arm offset	along flight direction (ΔX)	Yes*	Yes/No/No	No	Two flight lines in opposite directions (flying height H_1)	Two flight lines in opposite directions with 100% side lap (flying height H_1)
	across flight direction (ΔY)	Yes*	Yes/No/No	No		
	vertical (ΔZ)	No	No/No/No	Yes	One vertical control point	One vertical control point
Boresight roll angle ($\Delta\omega$)		Yes*	Yes/Yes/Yes	No	Two flight lines with some percentage of side lap	Two flight lines in opposite directions with 100% side lap
Boresight pitch angle ($\Delta\varphi$)		Yes	Yes/Yes/Yes	No	stereo-pair (from the same flight line)	Two flight lines in opposite directions with 100% side lap
Boresight yaw angle ($\Delta\kappa$)		Yes	Yes/Yes/Yes	No	stereo-pair (from the same flight line)	Two flight lines in the same direction with minimum side lap
Principal point coord. (along flight direction) (x_p)		Yes*	Yes/Yes/No	No	Two flight lines in opposite directions (flying height H_2)	Two flight lines in opposite directions with 100% side lap (flying height H_2)
Principal point coord. (across flight direction) (y_p)		Yes*	Yes/Yes/No	No		
Principal distance (c)		No	No/Yes/No	No	Flight lines at diff. flying heights (H_1 and H_2)	Flight lines at diff. flying heights (H_1 and H_2)

*Considering stereo-pairs from different flight lines.

<u>LiDAR Systems</u>: A mathematical analysis has been presented to derive the impact of biases in the system parameters on the reconstructed object space. Such mathematical analysis has been verified through a simulation process. A summary of the outcome from the performed analysis is presented in Table 8.2. One should note that it is not possible to simultaneously estimate the vertical lever arm offset component and the range bias. Also, in order to simultaneously estimated the lever arm offset component in the along flight direction and the boresight pitch angle, two different flying heights should be available (refer to highlighted text in Table 8.2). From the proposed analysis, it could be concluded that the optimum flight and control configuration for reliable estimation of the parameters should consist of three side lap cases, i.e., four strips captured from two flying heights in opposite directions with 100% side lap, and two strips, which are flown in the same direction with the least side lap possible (while having enough conjugate surface elements among the strips), and one vertical control point. Experiments using simulated and real datasets have demonstrated the feasibility of the devised flight and control configuration.

Table 8.2. Summary of the impact of biases in the LiDAR system parameters on the reconstructed object space along with the devised minimum and optimum requirements for the estimation of the parameters.

Parameter		Discrepancies: Flying Direction/ Flying Height/ Scan Angle dependent?	Control Required?	Minimum Requirement	Optimum Requirement
Lever arm offset	across flight direction ΔX	Yes/No/No	No	Two flight lines in opposite directions	Two flight lines in opposite directions with 100% side lap
	along flight direction ΔY	Yes/No/No	No	Two flight lines in opposite directions (flying height H_1)	Two flight lines in opposite directions with 100% side lap (flying height H_1)
	vertical ΔZ*	No/No/No	Yes	One vertical control point	One vertical control point
Boresight pitch angle $\Delta\omega$		Yes/Yes/Yes	No	Two flight lines in opposite directions (flying height H_2)	Two flight lines in opposite directions with 100% side lap (flying height H_2)
Boresight roll angle $\Delta\varphi$		Yes/Yes/Yes	No	Two flight lines with some percentage of side lap	Two flight lines in opposite directions with 100% side lap
Boresight yaw angle $\Delta\kappa$		No/No/Yes	No	Two flight lines with some percentage of side lap	Two flight lines in the same direction with minimum side lap
Range bias $\Delta\rho$*		No/No/Yes	Yes	One vertical control point	One vertical control point
Mirror scan angle scale S		No/Yes/Yes	No	Two flight lines with some percentage of side lap	Two flight lines in the same direction with minimum side lap

*The vertical lever arm offset component and the range bias cannot be simultaneously estimated.

Photogrammetric System Calibration

A single-step photogrammetric system calibration for the calibration of single and multi-camera systems has been introduced. The contributions of the proposed method can be summarized as follows:

- The modified collinearity equations concept, which has been implemented in previous work for single-camera systems, is expanded in this research work to handle multi-camera systems.
- The proposed single-step procedure is implemented in such a way to allow for the estimation of two sets of ROP for multi-camera systems. More specifically, besides the estimation of the mounting parameters relating the cameras and the IMU body frame (ISO model), the proposed method can also be used to estimate the ROP among the cameras. Such a procedure has been denoted as "indirect geo-referencing with ROC". Experiments using simulated and real datasets have demonstrated the performance of the proposed single-step procedure for the estimation of these two sets of parameters.
- The proposed indirect geo-referencing with ROC is of simpler implementation when compared to the commonly used method of adding constraint equations to the traditional bundle adjustment procedures, i.e., it does not require extensive partial derivatives as well as manual formatting of the camera pairs to be utilized in the ROC. Such complexities are amplified when the number of utilized cameras and the number of involved stations get larger. Moreover, a reduction in the size of normal equations matrix is obtained due to decreased number of unknown parameters, thus, reducing the storage and execution time requirements.
- A general ISO model capable of incorporating prior information on the ROP among the cameras has been devised. The outcome of such model includes the mounting parameters relating a reference camera to the IMU body frame and the adjusted or estimated (if no prior information is utilized) ROP among the cameras. Experimental results from simulated and real datasets have verified the validity of the devised general model. Moreover, it has been demonstrated that the utilization of prior ROP information leads to more significant improvements in the estimated parameters in the presence of a poor distribution of the points in the imagery.
- The general devised ISO model has the ability of deriving the previous models, i.e., the model for the estimation of the ROP among the cameras (indirect geo-

referencing with ROC) and the model for the estimation of the mounting parameters relating the cameras and the IMU body frame. Such ability has been verified through experiments using simulated and real datasets.

LiDAR System Calibration

A LiDAR system calibration method, based on the rigorous LiDAR point positioning equation, has been introduced. The proposed method utilizes raw LiDAR data in overlapping strips where the system parameters are determined by minimizing the discrepancies among conjugate surface elements. The developed method utilizes appropriate primitives (i.e., point-patch pairs) to cope with the irregular nature of the LiDAR surfaces. The contributions of the proposed method can be summarized as follows: (i) the proposed method is fully automated, (ii) it doesn't require specific features in the calibration site (e.g., planar or linear features), (iii) the utilized primitives do not involve pre-processing of the data (i.e., classification or segmentation of the dataset), (iv) the parameters associated with the utilized primitives are not part of the unknowns, which significantly decreases the storage and execution time requirements due to the manageable size of the normal equation matrix, (v) control and tie features can be equally utilized in the calibration procedure without enforcing any constraints about the nature of the control data, (vi) the approach can deal with sparse control data (discrete points), (vii) the utilized control points need not be physically identified in the LiDAR data, (viii) a robust automated matching procedure is utilized to establish the correspondence between conjugate primitives, and (ix) simplicity in the implementation of higher order primitives is maintained by utilizing point-based observation equations and a modified Gauss Markov stochastic model while providing a rigorous analysis of the impact of such modification. The performance of the proposed rigorous LiDAR system calibration has been tested using simulated and real datasets. It has been demonstrated that the proposed method can yield comparable results when compared to existing rigorous approach while enjoying the above benefits.

8.2 Recommendations for Future Work

Recommendations/suggestions for future work related to the calibration of photogrammetric and LiDAR systems are as follows:

(i) Investigate the optimum flight and control configuration for airborne multi-camera systems.

(ii) Perform more testing with simulated and real datasets from operational multi-camera systems using the proposed single-step procedure for the estimation of the two sets of ROP.

(iii) More testing with real datasets using the proposed methodology based on a two-step process for the calibration of land-based GPS/INS-assisted multi-camera systems. In the first step, the ROP among the cameras would be estimated. One should note that in such step, GPS/INS data is not necessary. Therefore, the availability of GPS signal would not be a requirement. Thus, areas with high buildings, which would provide a good distribution of tie points, can be utilized. The second step would entail the ISO procedure, using the most general devised ISO model capable of incorporating prior ROP information. One should note that the second step should be performed in open areas to ensure good GPS signal. It is important to mention that the availability of tie points in open areas is reduced and a good tying among the images (i.e., good distribution of the points in the imagery) cannot be always guaranteed. In such cases, the use of prior ROP information will play an important role.

(iv) Investigate other possible system parameters to be considered in the system calibration of operational LiDAR systems as well as the necessary flight and control configuration for estimating such parameters.

(v) Implementation of an automated procedure for the identification of useful areas within the LiDAR data (areas with topography that has a good variety of slopes and aspects) for reliable and faster estimation of the parameters.

(vi) Investigate whether the utilization of the raw measurements (scan angles and ranges) significantly improves the LiDAR system calibration results. More specifically, investigate the use of existing data, such as trajectory position/orientation and the LiDAR point coordinates, to synthesize the raw measurements (scan angles and ranges) to be utilized in the calibration procedure.

(vii) Investigate the benefits of using data from LiDAR systems with full-waveform digitization capability in the system calibration.

(viii) Investigate the utilization of photogrammetric data in the calibration of airborne and land-based laser scanner systems and vice versa.

REFERENCES

Baltsavias, E., 1999. Airborne laser scanning: existing systems and firms and other resources, *ISPRS Journal of Photogrammetry and Remote Sensing*, 54(2-3):164–198.

Bang, K., 2010. *Alternative Methodologies for LiDAR System Calibration,* Ph.D. dissertation, Department of Geomatics Engineering, University of Calgary, Canada, 160 p.

Baron, A., W. Kornus, and J. Talaya, 2003. ICC Experiences on Inertial/GPS Sensor Orientation, *Proceedings of Workshop: Theory, Technology and Realities of Inertial/GPS/Sensor Orientation*, ISPRS WG I/5, Barcelona 2003, on CD-ROM, 5 p.

Bretar, F., A. Chauve, C. Mallet, and B. Jutzi, 2008. Managing full waveform Lidar data: A challenging task for the forthcoming years, *The International Archives of the Photogrammetry, Remote Sensing and Spatial Information Sciences,* 37(Part B1):415420.

Brown, D., 1966. Decentring distortion of lenses, *Photogrammetric Engineering*, 32(3):444–462.

Brown, D., 1971. Close range camera calibration, *Photogrammetric Engineering*, 37(8):855–866.

Burman, H., 2000. *Calibration and Orientation of Airborne Image and Laser Scanner Data Using GPS and INS*, Ph.D. dissertation, Royal Institute of Technology, Stockholm, 125 p.

Casella, V., R. Galetto, and M. Franzini, 2006. An Italian Project on the Evaluation of Direct Georeferencing in Photogrammetry, *Proceedings Eurocow 2006*, unpaginated CD-ROM.

Chauve, A., C. Mallet, F. Bretar, S. Durrieu, M. Pierrot-Deseilligny, and W. Puech, 2007. Processing full waveform lidar data: modelling raw signals, *International Archives of Photogrammetry, Remote Sensing and Spatial Information Sciences*, 39(Part3/W52):102–107.

Coetsee, J., A. Brown, J. Bossler, 1994. GIS Data Collection Using the GPSVan Supported by a GPS/Inertial Mapping System, *Proceedings of the 7th International Technical Meeting of the Satellite Division of The Institute of Navigation (ION GPS 1994)*, Salt Lake City, UT, September 1994, pp. 85–93.

Coren, F., and P. Sterzai, 2006. Radiometric correction in laser scanning, *International Journal of Remote Sensing*, 27(15):3097–3014.

Cramer, M., 1999. Direct geocoding – is aerial triangulation obsolete? *Photogrammetric Week 1999* (D. Fritsch, and R. Spiller, editors), Wichmann Verlag, Heidelberg, Germany, pp. 59–70.

Cramer, M., D. Stallmann, and N. Haala, 1999. Sensor Integration and Calibration of Digital Airborne Three-line Camera Systems, *Proceedings of the International Workshop on Mobile Mapping Technology*, Bangkok, Thailand, April 21–23, pp. 451–458.

Cramer, M., D. Stallmann, and N. Haala, 2000. Direct georeferencing using GPS/inertial exterior orientations for photogrammetric applications, *International Archives of Photogrammetry and Remote Sensing*, 33 (B3): 198–205.

Cramer, M., and D. Stallmann, 2001. On the use of GPS/inertial exterior orientation parameters in airborne photogrammetry, *ISPRS Workshop "High Resolution Mapping from Space 2001"*, Hannover, Germany, pp. 32–44.

Cramer, M., and D. Stallmann, 2002. System Calibration for Direct Georeferencing, *International Archives of Photogrammetry, Remote Sensing and Spatial Information Sciences,* 34(3/A):79–84.

Cramer, M., 2004. EUROSDR Network on digital camera calibration, *International Archives of Photogrammetry and Remote Sensing*, XXth ISPRS Congress, Istanbul, 35(Part B3):210–215.

Crombaghs, M., E. De Min, and R. Bruegelmann, 2000. On the Adjustment of Overlapping Strips of Laser Altimeter Height Data, *International Archives of Photogrammetry and Remote Sensing*, 33(B3/1):230–237.

Csanyi, N., 2008. *A Rigorous Approach to Comprehensive Performance Analysis of State-of-the-Art Airborne Mobile Mapping Systems*, Ph.D. dissertation, The Ohio State University, 217 p.

Ellum, C., 2001. *The Development of a Backpack Mobile Mapping System*, M.Sc. Thesis, Department of Geomatics Engineering, University of Calgary, Canada, 158 p.

El-Sheimy, N., 1996a. A Mobile Multi-Sensor System for GIS Applications in Urban Centers, *International Archives of Photogrammetry and Remote Sensing*, 31(PartB2):95–100.

El-Sheimy, N., 1996b. *The Development of VISAT - A Mobile Survey System for GIS Applications*, Ph.D. dissertation, Department of Geomatics Engineering, University of Calgary, Canada, 179 p.

El-Sheimy, N., C. Valeo, and A. Habib, 2005. *Digital Terrain Modeling: Acquisition, Manipulation And Applications*, Artech House Remote Sensing Library, 257 p.

El-Sheimy, N., 2008. Land mobile mapping systems, *Advances in Photogrammetry, Remote Sensing and Spatial Information Sciences* (Z. Li, J. Chen, and E. Baltsavias, editors), 2008 ISPRS Congress Book, ISPRS Book Series, CRC Press, 2008, pp. 85–100.

Filin, S., 2001. *Calibration of Spaceborne and Airborne Laser Altimeters Using Natural Surfaces*, Ph.D. dissertation, Department of Civil and Environmental Engineering and Geodetic Science, the Ohio-State University, Columbus, OH, 129 p.

Filin S., and G. Vosselman, 2004. Adjustment of airborne laser altimetry strips, *International Archives of Photogrammetry and Remote Sensing*, 35(Part B3):285–289.

Fraser, C., 1997. Digital camera self-calibration, *ISPRS Journal of Photogrammetry and Remote Sensing*, 52(4):149–159.

Friess, P., 2006. Toward a rigorous methodology for airborne laser mapping, *Proceedings of EuroCOW,* Castelldefels, Spain, unpaginated CD-ROM.

Goad, C., 1991. The Ohio State University Highway Mapping System: The Positioning Component, *Proceedings of the Institute of Navigation Conference*, Williamsburg, VA, pp. 117–120.

Grejner-Brzezinska, D. A., 1997. Airborne Integrated Mapping System: Positioning component, *Proceedings 53rd ION Annual Meeting*, 30 June-02 July, Albuquerquue, New Mexico (Institute of Navigation, Fairfax, Virginia), pp. 225–235.

Grejner-Brzezinska, D. A., 2001. Direct Sensor Orientation in Airborne and Land-based Mapping Applications, *Report No. 461*, Geodetic GeoInformation Science, Department of Civil and Environmental Engineering and Geodetic Science, The Ohio State University.

Habib, A., and T. Schenk, 2001. Accuracy Analysis of Reconstructed Points in Object Space from Direct and Indirect Exterior Orientation Methods, *OEEPE Workshop on Integrated Sensor Orientation*, Institute for Photogrammetry and Engineering Surveying, University of Hannover, 17–18 September, 2001.

Habib, A., A. Pullivelli, E. Mitishita, M. Ghanma, and E. Kim, 2006. Stability analysis of low-cost digital cameras for aerial mapping using different georeferencing techniques, *The Photogrammetric Record*, 21 (113): 29–43.

Habib, A., 2006. *Advanced photogrammetric and ranging techniques* (ENGO 531), Course Note of Department of Geomatics Engineering, University of Calgary, Canada.

Habib, A., A. Jarvis, I. Detchev, G. Stensaas, D. Moe, and J. Christopherson, 2008. Standards and specifications for the calibration and stability of amateur digital cameras for close-range mapping applications, *The International Archives of Photogrammetry, Remote Sensing and Spatial Information Sciences*, ISPRS Congress Beijing 2008, 37(B1):1059–1064.

Habib, A., K. Bang, A. P. Kersting, and D. C. Lee, 2009. Error budget of LiDAR Systems and Quality Control of the Derived Data, *Photogrammetric Engineering and Remote Sensing*, 75(9):1093–1108.

Habib, A., A. P. Kersting, K. Bang, and D. C. Lee, 2010a. Alternative methodologies for the internal quality control of parallel LiDAR strips, *IEEE Transactions on Geoscience and Remote Sensing*, 48(1): 221–236.

Habib A., K. Bang, A. P. Kersting, and J. Chow, 2010b. Alternative Methodologies for LiDAR System Calibration, *Remote Sensing*, 2(3): 874–907.

Huising, E. J., and L. M. G. Pereira, 1998. Errors and Accuracy Estimates of Laser Data Acquired by various Laser Scanning Systems for Topographic Applications, *ISPRS Journal of Photogrammetry and Remote Sensing*, 53(5): 245–261.

He, G., K. Novak, W. Feng, 1992. On the Integrated Calibration of a Digital Stereo-Vision System, *The International Archives of Photogrammetry and Remote Sensing*, 29(Part B5):139–145.

He, G., G. Orvets, and R. Hammersley, 1996. Capturing Urban Infrastructure Data Using Mobile Mapping System, *Proceedings of the 52nd Annual Meeting of The Institute of Navigation*, Cambridge, MA, June 1996, pp. 667–674.

Heipke, C., K. Jacobsen, and H. Wegmann, 2001. The OEEPE test on integrated sensor orientation – Results of phase I, *Photogrammetric Week 2001* (D. Fritsch and R. Spiller, editors), Wichmann Verlag, Heidelberg, Germany, pp. 195–204.

Heipke, C., K. Jacobsen, and H. Wegmann, 2002. Analysis of the Results of the OEEPE Test "Integrated Sensor Orientation", *Integrated Sensor Orientation, Test Report and Workshop Proceedings* (C. Heipke, K. Jacobsen, and H. Wegmann, editors), OEEPE Official Publication No. 43, pp. 31–49.

Hock, C., W. Caspary, H. Heister, J. Klemm, and H. Sternberg, 1995. Architecture and design of the kinematic survey system KiSS, *Proceedings of the 3rd International Workshop on High Precision Navigation*, Stuttgart, Germany, April 1995, pp. 569–576.

Höfle, B., and N. Pfeifer, 2007. Correction of laser scanning intensity data: Data and model-driven approaches, *ISPRS Journal of Photogrammetry and Remote Sensing*, 62(6):415–433.

Honkavaara, E., 2003. Calibration Field Structures for GPS/IMU/Camera-system Calibration, *The Photogrammetric Journal of Finland*, 18(2):3–15.

Honkavara, E., R. Ilves, and J. Jaakkola, 2003. Practical results of GPS/IMU camera system calibration, *Proceedings of International Workshop: Theory, Technology and Realities of Inertial/GPS Sensor Orientation*, ISPRS WG I/5, Castelldefels, Spain, unpaginated CD-ROM.

Honkavaara, E., 2004. In-Flight Camera Calibration for Direct Georeferencing, *International Archives of Photogrammetry, Remote Sensing and Spatial Information Sciences*, 35(1):166–171.

Jakobsen, K., 1999. Determination of Image Orientation Supported by IMU and GPS, *Joint Workshop of ISPRS Working Groups I/1, I/3 and IV/4 – Sensors and Mapping from Space*, Hannover.

Jakobsen, K., 2000. Combined Bundle Block Adjustment versus Direct Sensor Orientation, *ASPRS Annual Convention 2000*, Washington, unpaginated CD-ROM.

Jacobsen, K., 2001. Aspects of Handling Image Orientation by Direct Sensor Orientation, *ASPRS annual convention St. Louis 2001*, unpaginated CD-ROM.

Jacobsen, K. 2003. Issues and Method for In-Flight and On-Orbit Calibration, *Workshop on Radiometric and Geometric Calibration*, December 2-5, Gulfport, Mississippi, USA.

Jacobsen, K., 2004. Direct/ Integrated Sensor Orientation – Pros and Cons, *The International Archives of Photogrammetry and Remote Sensing*, 35(Part B3):829–835.

Jutzi, B., and U. Stilla, 2003. Laser pulse analysis for reconstruction and classification of urban objects, *International Archives of Photogrammetry, Remote Sensing and Spatial Information Sciences*, 34 (Part 3/W8):151–156.

Kaasalainen, S., J. Hyyppä, P. Litkey, H. Hyyppä, E. Ahokas, A. Kukko, and H. Kaartinen, 2007. Radiometric calibration of ALS intensity, *International Archives of* *the Photogrammetry, Remote Sensing and Spatial Information Sciences*, 36(3/W52):201–205.

Kager, H. and K. Kraus, 2001. Height Discrepancies between Overlapping Laser Scanner Strips, *Optical 3-D Measurement Techniques V* (A. Grün and H. Kahmen, editors), Vienna, Austria, pp.103–110.

Kager, H., 2004. Discrepancies Between Overlapping Laser Scanning Strips-Simultaneous Fitting of Aerial Laser Scanner Strips, *Proceedings of the International Society for Photogrammetry and Remote Sensing XXth Congress*, Istanbul, 34(B/1):555–560.

Kenefick, J. F., M. S. Gyer, and B. F. Harp, 1972. Analytical self-calibration, *Photogrammetric Engineering*, 38(11):1117–1126.

Kilian, J., N. Haala, and M. Englich, 1996. Capture and evaluation of airborne laser scanner data, *International Archives of Photogrammetry and Remote Sensing*, 31(PartB3): 383–388.

King, B., 1992. Optimisation of Bundle Adjustments for Stereo Photography, *International Archives of Photogrammetry and Remote Sensing*, 29(Part B5):168–173.

Khoshelham, K., M. Saadatseresht, and B.G. Gorte, 2007. Influence of tie point distribution on integrated sensor orientation, *Proceedings of the 5th International Symposium on Mobile Mapping Technology MMT '07*, Padua, Italy, pp. 1–6.

Koch, K. R., 1988. *Parameter estimation and hypothesis testing in linear models*, Springer-Verlag New York, Inc. New York, NY, USA, 378 p.

Krauss, K., 1993. *Photogrammetry*, Volume 1: Fundamentals and Standard Processes, Dummler/Bonn, 397 p.

Lerma, J.L., S. Navarro, M. Cabrelles, and A. E. Seguí, 2010. Camera Calibration with Baseline Distance Constraints, *The Photogrammetric Record*, 25(130):140–158.

Maas H. G., 2002. Method for measuring height and planimetry discrepancies in airborne laserscanner data, *Photogrammetric Engineering and Remote Sensing*, 68(9):933–940.

Merchant, D.C., 1974. Calibration of the air photo system, *Photogrammetric Engineering and Remote Sensing*, 40(5): 605–617.

Merchant, D.C, A. Schenk, A. Habib, T. Yoon, 2004. USGS/OSU progress with digital camera in situ calibration methods, *International Archives of Photogrammetry and Remote Sensing*, 35(2):19–24.

Morin, K. W., 2002. *Calibration of Airborne Laser Scanners*, M.S. thesis, University of Calgary, Department of Geomatics Engineering, Calgary, AB, 125 p.

Mikhail, E. M., and F. Ackerman, 1976. *Observations and Least Squares*, New York: University Press of America, 497 p.

Novak, K., 1991. The Ohio State University Highway Mapping System: The Stereo Vision System Component, *Proceedings of the Institute of Navigation Conference*, Williamsburg, VA, pp.121–124.

Optech Inc. 2002. Data Processing Manual for the ALTM Laser System. Canada.

Pinto, L., and G. Forlani, 2002. A single step calibration procedure for IMU/GPS in aerial photogrammetry, *International Archives of Photogrammetry and Remote Sensing*, 34(Part B3): 210–213.

Rau, J., A. Habib, A. P. Kersting, K. Bang, K. Chiang, Y. Li, and Y. Tseng, 2011. Direct Sensor Orientation of a Land-Based Mobile Mapping System, *Sensors*, 11(7):7243–7261.

Schenk, T., 2001. Modeling and Analyzing Systematic Errors in Airborne Laser Scanners, *Technical Report in Photogrammetry No. 19*, Ohio Sate University.

Scherzinger, B., 1997. A Position and Orientation Post-Processing Software Package for Inertial/GPS Integration (POSProc), *International Symposium on Kinematic Systems in Geodesy, Geomatics and Navigation – KIS97*, Banff, Alberta, Canada, June 3-6, pp. 197–204.

Schwarz, K. P., 1995. Integrated airborne navigation systems for photogrammetry, *Photogrammetric Week 1995* (D. Fritsch and D. Hobbie, editors), Wichmann Verlag, Heidelberg, Germany, pp. 139–154.

Schwarz, K.P., M. Chapman, M. E. Cannon, and P. Gong, 1993. An integrated INS/GPS approach to the georeferencing of remotely sensed data, *Photogrammetric Engineering and Remote Sensing*, 59(11): 1667–1674.

Skaloud, J., 1999. *Optimizing Georeferencing of Airborne Survey Systems by INS/DGPS*, Ph.D. dissertation, Department of Geomatics Engineering, University of Calgary, Calgary, Canada, 179 p.

Skaloud, J., J. Vallet, K. Keller, G. Veyssiere, and O. Koelbl, 2005. HELIMAP: Rapid large scale mapping using handheld LiDAR/CCD/GPS/INS sensors on helicopters, *Proceedings ION GNSS 2005*, Long Beach, CA, USA, 13–16 September, pp. 2461–2467.

Skaloud, J., and D. Lichti, 2006. Rigorous Approach to Bore-Sight Self-Calibration in Airborne Laser Scanning, *ISPRS Journal of Photogrammetry and Remote Sensing*, 61(6): 47–59.

Smith, M. J., K. S. Qtaishat, D.W.G. Park, and A. Jamieson, 2006. IMU and Digital Aerial Camera Misalignment Calibration, *Proceedings EuroCow 2006*, unpaginated CD-ROM.

Sullivan, D., and A., Brown, 2002. High Accuracy Autonomous Image Georeferencing Using a GPS/Inertial-Aided Digital Imaging System, *Proceedings of the 2002 National Technical Meeting of The Institute of Navigation*, San Diego, CA, January 2002, pp. 598–603.

Toth, C. K., 1998. Direct Platform orientation of multi-sensor data acquisition systems, *International Archives of Photogrammetry and Remote Sensing*, 32(Part 4): 629–634.

Toth, C. K., 1999. Experiences with frame CCD Arrays and Direct Georeferencing, *Photogrammetric Week 1999* (D. Fritsch and R. Spiller, editors), Wichmann Verlag, Heidelberg, Germany, pp. 95–109.

Toth, C.K., 2002. Calibrating airborne lidar systems, *Proceedings of ISPRS Commission II Symposium*, Xi'an, China, pp. 475–480.

Toth, C. 2010. Airborne Lidar Technology: The state –of-the-art and future trends, *Proceedings of the LARS – Latin American Remote Sensing Week*, October 4 – 8, Santiago – Chile.

Vain, A., X. Yu, S. Kaasalainen, and J. Hyyppä, 2010. Correcting airborne laser scanning intensity data for automatic gain control effect, *IEEE Geoscience and Remote Sensing letters* , 7(3):511–514.

Wagner, W., A. Ullrich, V. Ducic, T. Melzer, and N. Studnicka, 2006. Gaussian decomposition and calibration of a novel small-footprint full-waveform digitising airborne laser scanner, *ISPRS Journal of Photogrammetry and Remote Sensing*, 60(2):100–112.

Wegmann, H., 2002. Image Orientation by Combined (A) AT with GPS and IMU, *ISPRS Com. I, Midterm Symposium, Integrated Remote Sensing at the Global, Regional, and Local Scale*, Denver, U.S.A., 10-15 November 2002.

Wehr, A., and Lohr, U., 1999. Airborne laser scanning - an introduction and overview, *ISPRS Journal of Photogrammetry and Remote Sensing*, 54(2-3): 68–82.

Yuan, X., 2008. A novel method of systematic error compensation for a position and orientation system, *Progress in Nature Science*, 18(8): 953–963.

Yan, W.Y., A. Shaker, A. Habib, A. P. Kersting, 2012. Improving classification accuracy of airborne LiDAR intensity data by geometric calibration and radiometric correction, *ISPRS Journal of Photogrammetry and Remote Sensing*, 67:35–44.

Yastikli, N., and K. Jacobsen, 2005. Direct Sensor Orientation for Large Scale Mapping-Potential, Problems, and Solutions, *The Photogrammetric Record*, 20(111): 274–284.

APPENDIX A

Modified Least Squares

1. Model

$$\vec{y} = A\delta\vec{x} + \vec{d} + \vec{e} \qquad \vec{e} \sim \left(0, \Sigma^{`}\right) \qquad where\ \ \Sigma^{`} = \sigma_o^2 P^{`+}\ and\ \ P^{`}\vec{d} = 0 \tag{A.1}$$

2. LSA Target Function $\phi(\delta\vec{x}, \vec{d})$

$$\phi(\delta\vec{x}, \vec{d}) = \vec{e}^T P^{`}\vec{e} = \left(\vec{y} - A\,\delta\vec{x} - \vec{d}\right)^T P^{`}\left(\vec{y} - A\,\delta\vec{x} - \vec{d}\right) = min|_{\delta\vec{x},\vec{d}} \tag{A.2}$$

Since $P^{`}\vec{d} = 0$:

$$\phi(\delta\vec{x}, \vec{d}) = \phi(\delta\vec{x}) = \vec{e}^T P^{`}\vec{e} = (\vec{y} - A\delta\vec{x})^T P^{`}(\vec{y} - A\delta\vec{x}) = min|_{\delta\vec{x}} \tag{A.3}$$

Expanding Equation A.3 we get:

$$\begin{aligned} \phi(\delta\vec{x}) &= (\vec{y} - A\,\delta\vec{x})^T P^{`}(\vec{y} - A\,\delta\vec{x}) \\ &= \vec{y}^T P^{`}\vec{y} - \vec{y}^T P^{`} A\,\delta\vec{x} - \delta\vec{x}^T A^T P^{`}\vec{y} + \delta\vec{x}^T A^T P^{`} A\,\delta\vec{x} = min|_{\delta\vec{x}} \end{aligned} \tag{A.4}$$

Equation A.3 can be simplified to:

$$\phi(\delta\vec{x}) = \vec{y}^T P^{`}\vec{y} + \delta\vec{x}^T A^T P^{`} A\,\delta\vec{x} - 2\delta\vec{x}^T A^T P^{`}\vec{y} = min|_{\delta\vec{x}} \tag{A.5}$$

3. Solution Vector $(\delta\hat{\vec{x}})$

The solution vector $(\delta\hat{\vec{x}})$ that minimizes $\phi(\delta\vec{x})$ can be obtained by differentiating $\phi(\delta\vec{x})$ w.r.t. $\delta\vec{x}$ and equating it to zero:

$$\frac{\partial\phi}{\partial\delta\vec{x}} = 2A^T P^{`} A\,\delta\vec{x} - 2A^T P^{`}\vec{y} = 0 \tag{A.6}$$

$$\delta\hat{\vec{x}} = \left(A^T P^{`} A\right)^{-1} A^T P^{`}\vec{y} = N^{-1} A^T P^{`}\vec{y} \quad \text{where } N = A^T P^{`} A \tag{A.7}$$

4. Variance-covariance matrix of the solution vector $(\Sigma\{\delta\hat{\vec{x}}\})$

Using the law of error propagation, the variance-covariance matrix of the solution vector $(\Sigma\{\delta\hat{\vec{x}}\})$ can be obtained as follows:

$$\Sigma\{\delta\hat{\vec{x}}\}=\sigma_o^2 N^{-1}A^T P^{`} P^{`+} P^{`} A N^{-1} \qquad \text{A.8}$$

Since for a Moore-Penrose pseudo-inverse, $P^{`} P^{`+} P^{`} = P^{`}$ (Koch, 1988):

$$\Sigma\{\delta\hat{\vec{x}}\} = \sigma_o^2 N^{-1} N N^{-1} = \sigma_o^2 N^{-1} \qquad \text{A.9}$$

5. A-posteriori variance factor ($\hat{\sigma}_o^2$)

The a-posteriori variance factor ($\hat{\sigma}_o^2$) is obtained by deriving the expected value of the sum of squares of the weighted predicted residuals:

$$E\left(\tilde{\vec{e}}^T P^{`} \tilde{\vec{e}}\right) = E\{(\vec{y} - A\delta\hat{\vec{x}} - \vec{d})^T P^{`} \left(\vec{y} - A\widehat{\delta\vec{x}} - \vec{d}\right)\} \qquad \text{A.10}$$

Since $P^{`}\vec{d} = 0$, Equation A.10 gets the form:

$$E\left(\tilde{\vec{e}}^T P^{`} \tilde{\vec{e}}\right) = E\left\{\left(\vec{y} - A\delta\hat{\vec{x}}\right)^T P^{`} \left(\vec{y} - A\delta\hat{\vec{x}}\right)\right\} \qquad \text{A.11}$$

Expanding Equation A.11 while using the derived solution for $\delta\hat{\vec{x}}$ in Equation A.7 we get:

$$E\left(\tilde{\vec{e}}^T P^{`} \tilde{\vec{e}}\right) = E\left\{\vec{y}^T P^{`} \vec{y} - \vec{y}^T P^{`} A N^{-1} A^T P^{`} \vec{y}\right\} \qquad \text{A.12}$$

Given that the trace of a scalar equals to the scalar, i.e., *tr(S)* = *S* and that the trace operation is commutative, i.e., *tr(AB)* = *tr(BA)* (Koch, 1988), Equation A.12 can be manipulated as follows:

$$E\left(\tilde{\vec{e}}^T P^{`} \tilde{\vec{e}}\right) = E\left\{tr\left(P^{`} \vec{y}\vec{y}^T\right) - tr(P^{`} A N^{-1} A^T P^{`} \vec{y}\vec{y}^T)\right\} \qquad \text{A.13}$$

Based on the properties that *tr(A)* + *tr(B)* = *tr(A+B)* and that $E\{tr(A)\} = trE(A)$ (Koch, 1988), Equation A.13 can be rewritten as follows:

$$\begin{aligned} E\left(\tilde{\vec{e}}^T P^{`} \tilde{\vec{e}}\right) &= trP^{`}\left[E(\vec{y}\vec{y}^T) - AN^{-1}A^T P^{`} E(\vec{y}\vec{y}^T)\right] \\ &= trP^{`}\left(I_n - AN^{-1}A^T P^{`}\right)E(\vec{y}\vec{y}^T) \end{aligned} \qquad \text{A.14}$$

where:

I_n is an nxn identity matrix.

The term $E(\vec{y}\vec{y}^T)$ can be derived from the variance-covariance matrix of the observations vector ($\Sigma\{\vec{y}\}$) as follows:

$$\Sigma\{\vec{y}\} = \sigma_o^2 P^{`+} = E\left\{\left(\vec{y} - A\,\delta\vec{x} - \vec{d}\right)\left(\vec{y} - A\,\delta\vec{x} - \vec{d}\right)^T\right\} \tag{A.15}$$

Expanding Equation A.15, we get:

$$\begin{aligned} E(\vec{y}\vec{y}^T) &= \sigma_o^2 P^{`+} + \left(A\,\delta\vec{x} + \vec{d}\right)\left(A\,\delta\vec{x} + \vec{d}\right)^T \\ &= \sigma_o^2 P^{`+} + A\delta\vec{x}\delta\vec{x}^T A^T + A\delta\vec{x}\vec{d}^T + \vec{d}\delta\vec{x}^T A^T + \vec{d}\vec{d}^T \end{aligned} \tag{A.16}$$

Substituting Equation A.16 in Equation A.14 yields:

$$\begin{aligned} E\left(\tilde{\vec{e}}^T P^{`} \tilde{\vec{e}}\right) = trP^{`}\left(I - AN^{-1}A^T P^{`}\right)\big[&\sigma_o^2 P^{`+} + A\delta\vec{x}\delta\vec{x}^T A^T + A\delta\vec{x}\vec{d}^T + \vec{d}\delta\vec{x}^T A^T \\ &+ \vec{d}\vec{d}^T\big] \end{aligned} \tag{A.17}$$

Given that P$^{`}\vec{d} = 0$, Equation A.17 can be simplified to:

$$E\left(\tilde{\vec{e}}^T P^{`} \tilde{\vec{e}}\right) = \sigma_o^2 trP^{`}\left(I - AN^{-1}A^T P^{`}\right)P^{`+} = \sigma_o^2 trP^{`}P^{`+} - \sigma_o^2 trN^{-1}A^T P^{`}P^{`+}P^{`}A \tag{A.18}$$

Based on the property that $tr(AB) = rank(AB)$ (given that AB is idempotent) and $rank(AB) \leq$ min $(rankA, rankB)$ (Koch, 1988), the following can be stated:

$$tr(P^{`}P^{`+}) = rank(P^{`}P^{`+}) = min\left(rankP^{`}, rankP^{`+}\right) = rankP^{`} = q \tag{A.19}$$

Given that $tr(P^{`}P^{`+}) = q$ (as shown in Equation A.19) and that $P^{`}P^{`+}P^{`} = P^{`}$, Equation A.18 can be simplified to:

$$E\left(\tilde{\vec{e}}^T P^{`} \tilde{\vec{e}}\right) = \sigma_o^2 q - \sigma_o^2 trN^{-1}N = \sigma_o^2 q - \sigma_o^2 trI_m = \sigma_o^2 q - \sigma_o^2 m \tag{A.20}$$

where,

m $is\ the\ number\ of\ unknwon\ parameters.$

Finally, we can get the expression for the estimated a-posteriori variance factor ($\hat{\sigma}_o^2$) from Equation A.20 as follows:

$$\hat{\sigma}_o^2 = \frac{\tilde{\vec{e}}^T P^{`} \tilde{\vec{e}}}{(q-m)} \tag{A.21}$$